Integrated Electrocardiographic Mapping

Combined Analysis of Multichannel Endocardial and Body Surface ECG Data

Integrated Electrocardiographic Mapping; Combined Analysis of Multichannel Endocardial and Body Surface ECG Data

Printed by Thela Thesis, Amsterdam.

Cover: The "Klein bottle," a geometric object whose inner and outer surface are one, symbolizes the unity of inside and outside, as well as the way a balloon and a basket reflect on the surface.

Cover design by André Linnenbank

ISBN 90–9015342–X

Integrated Electrocardiographic Mapping

Combined Analysis of Multichannel Endocardial and Body Surface ECG Data

ACADEMISCH PROEFSCHRIFT

ter verkrijging van de graad van doctor
aan de Universiteit van Amsterdam
op gezag van de Rector Magnificus
prof. dr. J.J.M. Franse
ten overstaan van een door het college voor promoties
ingestelde commissie, in het openbaar te verdedigen in de Aula
der Universiteit
op 3 december 2001, te 14.00 uur
door

Mark Potse

geboren te Zaandam

Promotiecommissie

promotores	Prof. Dr. Ir. C.A. Grimbergen
	Prof. Dr. Ir. J.M.T. de Bakker
co-promotores	Dr. A.C. Linnenbank
	Dr. A. Sippens Groenewegen
overige leden	Prof. Dr. N.M. van Hemel
	Prof. Dr. A. van Oosterom
	Prof. Dr. A.A.M. Wilde
	Prof. Dr. Ir. J.A.E. Spaan
	Prof. Dr. J. Strackee

Faculteit Geneeskunde

Financial support by the Technology Foundation STW for the publication of this thesis is gratefully acknowledged.

Contents

could be filled with perfusion fluid and evacuated at will. The results indicated that the differences between basket and balloon recordings are largely attributable to the presence and absence of blood. Activation maps obtained in the presence and absence of blood were usually similar and only differed in a minority of cases at sites where electrograms revealed multiple deflections. — Submitted for publication [204].

Characterization and comparison of body surface maps is necessary for the localization of cardiac arrhythmias, diagnosis of ischaemia, dysplasia, hypertrophy, and conduction abnormalities. Various methods for comparison have been used, the choice of a method depending on the application. An overview of these methods is given in this chapter. An improvement for one of these methods, the "nondipolar content," is also presented. — Presented in part at the *World Congress on Med. Phys. and Biom. Eng.*, 1997 [211].

adjacent pacing sites in individual patients are localized relative to each other. Important advantages of the new method are the objectivity and reproducibility of the localization results. — *IEEE Trans. Biomed. Eng.* 47(5) pp. 682–689, May 2000 [212];

The continuous localization method for the normal left ventricle, described in chapter 7, can be adapted for infarcted left ventricles, and yield a comparable performance. In addition, it can be used to quantify the differences in the relation between site of origin and surface ECG pattern between normal and infarcted hearts. — Presented in part at the *NFSI* symposium, September 2001 [201]; *World Congress on Medical Physics and Biomedical Engineering*, July 2000 [214]; *20th Annu. Int. Conf. IEEE EMBS*, October 1998 [206].

The BSM-based localization methods described in previous chapters provide their results in a coordinate system relative to the heart. It is preferable to present these results in the biplane fluoroscopic views that are routinely used to monitor catheter positioning. We investigated how well cardiac coordinates can be converted into fluoroscopic projections with the limited anatomical data available in clinical practice. Endocardial surfaces from MRI scans of 24 healthy volunteers

were used to create an appropriate model of the left ventricular endocardium. Methods for estimation of model parameters from biplane fluoroscopic images were evaluated using simulated biplane data created from these surfaces. In addition, the conversion method was evaluated using 107 catheter positions obtained from 8 patients. The median distance between reconstructed positions and measured positions was 4.3 mm. — *Med. & Biol. Eng. & Comput.*, 2001 (in press) [197];

Analysis of multichannel ECG recordings requires special software. We created a software package and a user interface on top of a commercial data analysis package (Matlab) by a combination of high-level and low-level programming. Our software was created to satisfy the needs of a diverse group of researchers. It can handle a large variety of recording configurations. It allows for interactive usage through a fast and robust user interface and batch processing for the analysis of large amounts of data. The package is user-extensible, includes routines for both common and experimental data processing tasks, and works on several computer platforms. The source code is made intelligible using software for structured documentation and is available to the users. — *Comp. Meth. Prog. Biomed.* (in press) [208].

"Read them," said the King. The White Rabbit put on his spectacles.
"Where shall I begin, please your Majesty?" he asked.

"Begin at the beginning," the King said, very gravely, "and go on till you come to the end: then stop."

—Lewis Carroll, *Alice's Adventures in Wonderland*

Chapter 1

Introduction

1.1 Electrocardiography

Electricity plays an important role in biological systems. Interestingly, biological systems also played an important role in the development of our understanding of electricity itself when by the end of the eighteenth century the physician Galvani discovered that the muscles of a dissected frog's leg contract if the leg is touched with an arc made of two different metals. Galvani explained this phenomenon, in accordance with the theory of electricity of his time, as caused by electricity of physiological origin. The discovery also prompted the physicist Volta to revise the whole eighteenth-century theory of electricity, to allow a physical rather than a physiological explanation. The ensuing dispute between Galvani and Volta concerning the physical or the physiological origin of electricity was never settled: Galvani demonstrated that electricity could be generated without metals while Volta demonstrated that it could be generated without frogs. Galvani's method was interesting from a physiological point of view, but due to the lack of accurate instruments could not be fully appreciated until the end of the nineteenth century. Volta's method on the other hand found immediate application leading to the invention of the electrical battery or "Voltaic pile," which provided continuous electrical current.

Today, biology no longer has such a profound influence on the development of pure physics. Instead, biology is now considered an *application* of physics—though not of physics alone [138]. What did not change, however, is the possible fruitfulness of the collaboration between a physician and a physicist [154, 260].

Besides illustrating the strength of combining physiological and physical talents, the account of the Galvani–Volta controversy given above intro-

duces the topic of this thesis: the electrical activation of (heart) muscle. It was known for several decades before Galvani performed his experiments that muscles are activated electrically [195], but the experiments of Galvani demonstrated that this stimulation could be far more subtle than the pulses from electrical engines commonly applied in his time. What sets the heart aside from other muscles is the fact that its activation takes place in a single wave, moving essentially from one end of the heart to the other. This organization makes it possible that the minute currents generated by all individual myocytes (muscle cells) add up to generate potential differences that can be observed even with rather crude instruments. Together with technical developments this accounts for the fact that the first bioelectrical signal that was obtained noninvasively was an electrocardiogram (ECG), recorded by Waller in 1887, and not an electromyogram, by Galvani in the eighteenth century [24, 67].

1.2 Conventional Electrocardiography

In 1901 Einthoven developed the string galvanometer, with which the first faithful recording of a human surface ECG was made in 1902 [67]. Subsequently, Einthoven and his contemporaries carried out extensive research of the ECG in normal and diseased hearts and provided the basis for our understanding of the relation between cardiac activation and the surface ECG. Since this pioneering work the ECG has evolved into one of the most important diagnostic tools in cardiology.

The standards for lead placement that were introduced by Einthoven are still in use today for bipolar extremity lead recordings. Usually three electrodes are applied, which are attached to the arms and the left leg of the subject (figure 1.1). If it is assumed that the heart generates a dipole field, the strenght and direction of the part of the dipole that lies in the frontal plane can be derived from the amplitude of the potentials measured between pairs of these three electrodes.

The average of the potentials of these three electrodes is termed Wilson's Central Terminal (WCT) and is commonly used as a reference potential for unipolar leads from additional electrodes. Wilson proposed six additional electrodes, placed on the left anterior chest and termed "precordial leads," in order to observe the horizontal component of the assumed cardiac dipole (figure 1.1).

It is customary to have as extremity leads not only the three Einthoven leads I, II, and III but also the linear combinations aVR, aVL, and aVF. Together with Wilson's six precordial leads these constitute the "standard 12-lead ECG."

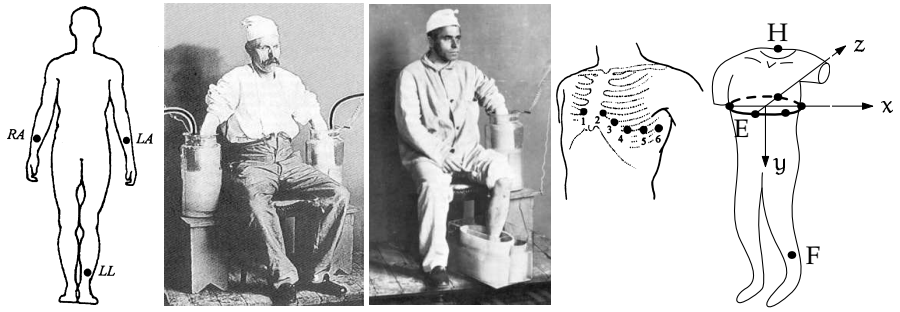

Figure 1.1: (a) *Einthoven's electrode positions left arm (LA), left leg (LL), and right arm (RA).* **(b)** *Einthoven lead I, defined as LA − RA.* **(c)** *Einthoven lead III, defined as LL − LA.* **(d)** *Wilson's precordial leads V1–V6.* **(e)** *Orthogonal Frank leads X, Y, and Z.*

Another lead system, which gives a more accurate description of the cardiac dipole in three dimensions, is the orthogonal lead system proposed by Frank [69] (see figure 1.1). The three orthogonal leads, termed X, Y and Z, are used to create the so-called "vector cardiogram."

1.3 Body Surface Mapping

Electrocardiographic body surface mapping, or multichannel electrocardiography, comprises the recording of many (32 up to several hundred) ECGs simultaneously from the body surface (figure 1.2). This technique aims at collecting as much information about the electrical behaviour of the heart as can possibly be obtained by surface potential measurements. Efforts have been made to determine the optimal number of leads where practically no extra information can be obtained if more leads are added.

A lower limit can be derived from the number of independent signals, which is estimated to be about 8–10 for individual subjects [96, 264–266]. In order to record all information, the number of leads must be substantially larger than the number of independent signals.

Using recordings with many leads (about 200), estimates can be made of the minimum number of leads that is needed to obtain the same accuracy. By application of the spatial sampling theorem to data sets of 209 leads, Zywietz determined this to be approximately 33 [285]. Another approach to determine the optimal number of leads was employed by Lux et al. [160, 162]. They demonstrated that sets of approximately 32 well-chosen

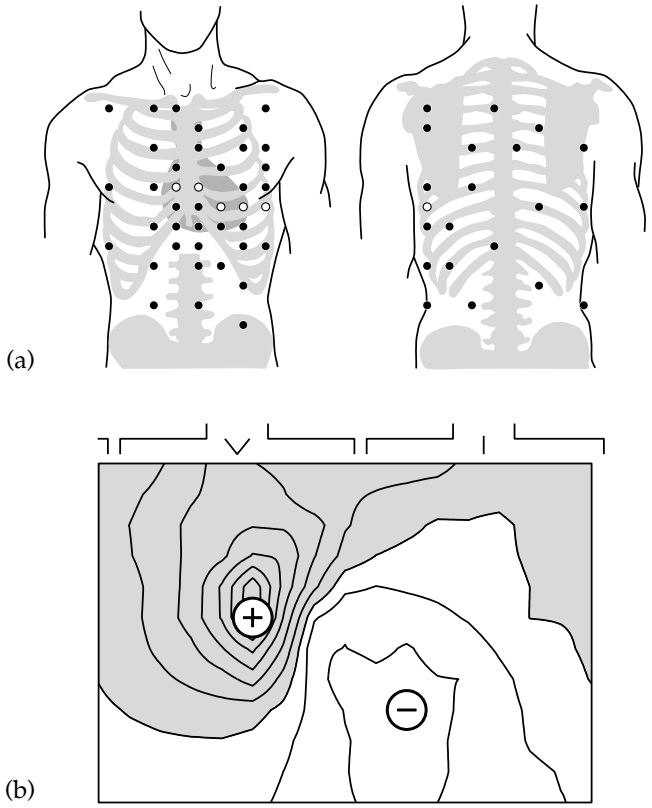

Figure 1.2: (a) *Electrodes of the Amsterdam 62-lead body surface mapping set. The set includes the standard 6 precordial electrodes, shown here with open circles. Other electrodes are indicated with solid circles.* **(b)** *Example of a body surface map recorded with the lead set shown in panel (a). This map displays the potential distribution, integrated over some time interval, over the body surface, using contour lines which connect points with equal values. Plus and minus signs indicate the extrema positions; the shaded area identifies torso sites with positive values.*

leads (figure 1.3) can predict the signals recorded in 192 leads with a very small error [160]. The Amsterdam 62-lead set used by our group includes two of these limited lead sets, known as the "Lux limited" and the "Lux anterior" set [252], and can therefore be expected to provide about the same information as 192 equally distributed leads. For visualization purposes, potentials at these 192 electrode positions are often estimated by interpolation from the 62 measured leads.

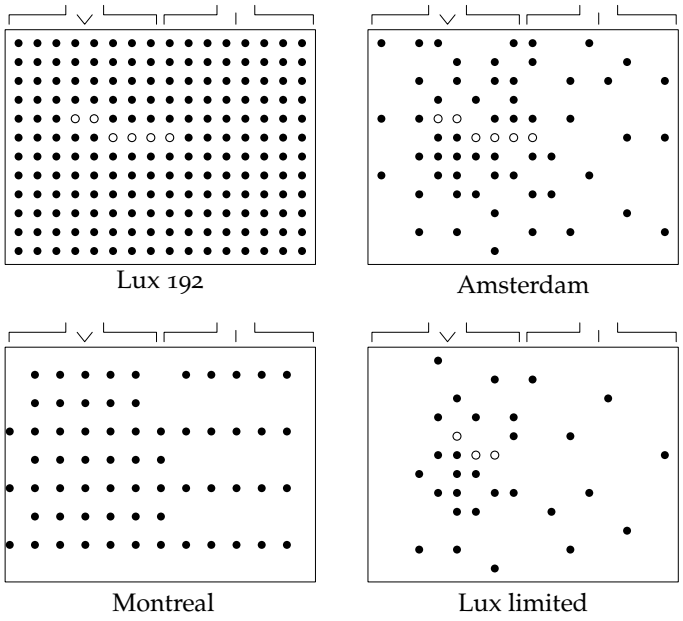

Figure 1.3: *Examples of body surface mapping electrode sets. The Lux 192-electrode set (upper left panel) consists of 16 columns and 12 rows, with equally spaced lead sites. The Amsterdam 62-electrode set (upper right panel) is a subset of this set. Its electrodes are applied in 14 flexible straps. The Amsterdam set [252] was created as a superset of the Lux limited set [160] shown in the bottom right panel. Among others, it includes approximated positions of all six standard precordial electrodes, shown with open circles in these diagrams. The Lux limited set (lower right panel) includes only three of these positions. In the lower left panel, a different electrode set, employed in Montreal, Canada, is shown [228]. This set consists of 12 columns and includes positions on the sternum and spine, while the Lux-based sets have positions adjacent to the sternum and spine. An overview of body surface mapping sets is given by Hoekema et al. [98].*

Because the difference in information content between ~ 30 leads and ~ 200 leads is already small, it is assumed that recording even more than about 200 leads does not significantly increase accuracy. If the difference in accuracy between 30 and 200 leads is considered small enough, it follows that 30 well-chosen leads are able to record all relevant information. We conclude that the Amsterdam lead set, with 62 leads incorporating the two limited lead sets published by Lux et al. [160] as well as the conventional precordial leads and several other electrodes [252], is able to record all elec-

trocardiographic information that can be obtained from the body surface.

The extra information that can be provided by a body surface map (BSM), as compared to the standard 12-lead ECG, is useful for more accurate localization of cardiac arrhythmias. It has been used to identify the exit site of ventricular tachycardia (VT) and ventricular extrasystoles (VES) [235–237, 242], pre-excitation sites in Wolff–Parkinson–White (WPW) syndrome [146, 176, 180, 191, 282], and the focal origin of atrial arrhythmias [239, 240]. It can also be applied for accurate and quantitative detection of abnormal depolarization and repolarization sequences [1, 42, 44, 190, 192, 193], for improved diagnosis of ventricular hypertrophy [136], for diagnosis of myocardial infarction [135], and for measurement of induced ischaemia [251].

1.4 Catheter Ablation

Body surface mapping can be used together with endocardial catheters, in order to speed up a catheter-ablation procedure by guiding a catheter efficiently to the site of origin of an arrhythmia [194, 235]. The arrhythmic substrate can then be destroyed by delivery of radiofrequency (RF) energy [29, 182, 225, 233], cryoablation, or ethanol infusion [53, 127]. Catheter ablation is now routinely performed for treatment of VTS, as an alternative for, or complementary to, administration of antiarrhythmic drugs or application of an implantable cardioverter-defibrillator (ICD) [29]. It is considered the treatment of choice in several situations, especially for treatment of atrial flutter [183, 196]. The application of body surface mapping to accelerate this procedure has been a subject of clinical research [194]. This thesis deals with two improvements to the techniques of BSM-guided catheter ablation. 1) Chapters 6, 7, and 8 discuss a method called continuous localization, which provides a more accurate localization of the arrhythmogenic site than the simple database lookup method that was used in the studies by SippensGroenewegen and Peeters [194, 236, 237]. 2) In chapter 9, a method is discussed to present the localization results in such a way that they can be more easily interpreted during a catheterization procedure.

1.5 Endocardial Mapping

Application of endocardial mapping during cardiac surgery as a means to treat cardiac arrhythmias has shown the importance of recording simultaneous electrograms at several endocardial sites, given the difficulty of repeated arrhythmia induction in the operating room [14]. However, cardiac surgery is a highly demanding procedure. Therefore, treatment with less invasive methods, such as administration of antiarrhythmic drugs, catheter

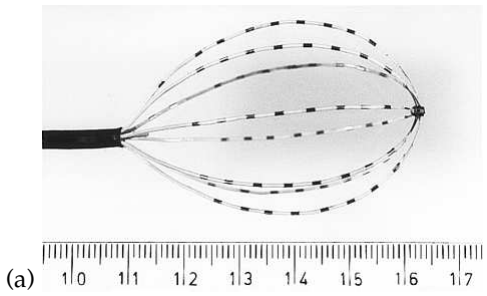

Figure 1.4: (a) *Constellation Basket catheter (Boston Scientific Inc.), consisting of eight flexible nitinol splines, each containing eight electrodes. The measuring rule is in centimetres and millimetres.* **(b)** *Fluoroscopic image of a Constellation Basket catheter positioned in the left ventricle of a patient (left anterior oblique view). The basket splines are hardly visible but the electrodes and the catheter shaft can be clearly seen. In the upper left corner of the image, two mapping catheters are also visible. Especially their tips, containing metal electrodes, are well discernible.*

ablation, or application of an implantable cardioverter-defibrillator (ICD) is preferred and antiarrhythmic surgery is performed infrequently

Multichannel mapping can also be advantageous during a catheter ablation procedure. First because it saves time, and second, because induction of arrhythmia can be difficult in the electrophysiology laboratory just like it is during surgery. Additionally, haemodynamic instability can in some cases preclude long periods of induced arrhythmia. Recently, multichannel endocardial catheter mapping has become feasible due to the introduction of "basket" catheters. For example, the Constellation Basket catheter (Boston Scientific Inc., Natick, MA, USA), illustrated in figure 1.4, which consists of eight flexible splines, each containing eight electrodes, provides simultaneous electrograms from 64 endocardial sites in a single cavity. Basket catheters have been used in animals [63,78,117], human atria [221], and the human left ventricle [47,48,229].

Chapter 3 of this thesis discusses the analysis of intracardial electrograms in general. The analysis of endocardial electrograms recorded with a basket catheter is discussed in chapter 4.

1.6 Integrated Mapping

At the St. Antonius Hospital in Nieuwegein, the Netherlands, equipment for the simultaneous acquisition of 62-channel body surface maps, 61 basket leads, and 3 extremity leads is available. This "integrated mapping"

system, which is able to record 126 surface and endocardial leads with 2 µV resolution, 16 bits (131 mV) dynamic range, and amplifier noise below 0.4 μV_{RMS}, can make continuous recordings of several hours duration which are presently unique in the world. Both mapping techniques have the capability to perform diagnosis based on a single beat; however, the basket gives more detailed and more reliable information on the electrical activity of the endocardium, whereas BSM also provides information on electrical activity in parts of the heart not covered by the basket catheter.

Simultaneous recording of multichannel endocardial electrograms and body surface electrocardiograms allows investigators to evaluate and develop noninvasive diagnostic methods based on body surface mapping, which can be used in patients where basket mapping is not performed. Applications that can be evaluated with this approach are localization of VT exit sites [47], localization of "late potentials" [148, 275], and assessment of dispersion in repolarization.

Simultaneous acquisition of many endocardial and body surface leads will be referred to as *integrated mapping*. The title of this thesis reflects the fact that it discusses body surface mapping, endocardial mapping, and integrated mapping. A software package that can be used for integrated mapping is presented in chapter 10. Specific problems of basket mapping are discussed in chapter 4.

1.7 Applications of Integrated Mapping

The clinical importance of endocardial basket mapping lies in the possibility to derive the activation pattern from a single beat, which makes it possible to identify the site of origin of VTs that cannot be localized by traditional roving catheters because they are difficult to induce, or haemodynamically unstable. Particularly in cases where the VT leads quickly to loss of consciousness, basket mapping is an option. The basket is applied for the study of VT in patients with extensive infarction scars which lead to complex activation patterns and multiple VT morphologies [47, 48].

The possibility to determine activation patterns on a beat-by-beat basis is important for research purposes as well because it may give insight in the formation of arrhythmia.

Integrated mapping can also be applied for the development and validation of body surface mapping methods. In particular, endocardial activation maps may be used to determine the exit site of a VT, which can be used as a gold standard for exit site identification using a body surface map.

The "Nieuwegein recordings" are at present the only data that make this comparison possible in a closed-chest situation. A challenge to the in-

vestigators of these data is the fact that they were recorded exclusively in patients with severely infarcted hearts—the basket catheter was not employed in patients with structurally normal hearts. The analysis of activation patterns in infarcted hearts is difficult, but on the other hand particularly interesting. Moreover, it is known that exit-site localization methods based on surface electrocardiograms perform less well in severely infarcted hearts than in structurally normal hearts. The Nieuwegein recordings are especially useful for analysis of this problem [47, 206].

Another topic of research using integrated mapping may be the relation between repolarization abnormalities of the endocardium and changes in the BSM pattern. To date this has not been investigated with integrated mapping data.

1.8 Catheter Ablation Guided by Body Surface Mapping

The work described in this thesis is part of a longer-term effort towards the creation of a system that uses noninvasive ECG data to guide the catheter quickly to the site of origin of an arrhythmia during a catheter-ablation procedure [123, 151, 154, 172, 194, 235–237, 241]. The system should automatically detect arrhythmic beats and present them to the operator. After approval and classification, the system should present the exit site localization derived from the ECG data on the displays of the fluoroscopy system, which are used to monitor the catheter position. Thus, the result can be easily compared with the catheter position. In addition, the system should automatically detect every paced beat during a pace mapping protocol, compute its site of origin, and show it in the same fluoroscopic displays. By giving an easily interpretable estimate of the relative positions of pacing sites and arrhythmia exit sites, the system should facilitate the work of the physician, to speed up the procedure and to allow treatment of more difficult arrhythmias.

The system can be thought of as subdivided into several modules: acquisition of BSM data, detection and classification of QRS complexes, estimation of the site of origin of ectopic beats, translation to fluoroscopic views, display, and interaction with physicians and operators. To date several of the tasks to be performed by these modules have not been described. Non-stop acquisition of 62-channel ECG data has only recently become feasible; this thesis is one of the first publications to describe the application of continuous multichannel ECG data. QRS detection in VT has been investigated [123] but the accuracy of this method needs to be improved. Conversion of localization results into biplane fluoroscopic projec-

tions requires a three-dimensional (3-D) model of the individual heart, or at least an approximation, which is not routinely available; a simple method is developed in chapter 9. A method for accurate automatic localization of ectopic beats, termed "continuous localization," has recently been developed [212] (chapters 6, 7, and 8). The influence of infarction on these methods is first described in chapter 8 of this thesis.

The interface between the system and the physician can only be developed experimentally, when a prototype system is clinically used. Application of this prototype system during catheter-ablation procedures is necessary to find out exactly which data must be displayed, which interaction with the physician is necessary, how to adapt the algorithms to individual patients, etc.

As indicated above, integrated mapping data can help us to test newly-developed methods for arrhythmia localization and to investigate the influence of infarct scars on the accuracy of these methods. Conversion into biplane fluoroscopic projections can be evaluated with existing data from pace mapping studies [236], as discussed in chapter 9 [213]. When the arrhythmia localization problem has been solved, a prototype guidance system can be created.

1.9 Data Exchange in the Electrophysiology Laboratory

Communication between several acquisition systems and analysis systems in the catheterization laboratory is necessary for our procedures. Various modalities like fluoroscopy, ECG, blood flow, and blood pressure all have their own recording systems, and present their results on different displays. Sometimes even the surface ECG and endocardial electrograms obtained with catheters are recorded with different systems. The same applies to the operating room, where a similar diversity of monitoring systems is used. At present, manufacturers of commercial equipment provide some communication, e.g. between a blood pressure recorder and an ECG recording system, in an ad hoc fashion. Proprietary communication protocols are used and different manufacturers have to establish bilateral agreements in order to exchange data. For every pair of communicating devices, a special connection—usually a wire—is needed. The creation of an open standard for data interchange between instruments used in the catheterization laboratory or operating room would make it much easier to combine instruments from different manufacturers and to add experimental analysis systems to an existing setup. Some ideas about a standard, which should include the instrumentation bus as well as the communication protocols,

were previously expressed by Linnenbank [154].

Easy access to the data using an open communications standard would facilitate the development of the catheter-guidance system described in this thesis, given its heavy reliance on on-line data acquired by different recording systems.

1.10 Software

Processing methods for multichannel ECG recordings, intracardial maps as well as body surface maps, differ strongly from those for single-lead or standard 12-lead ECGs. The large number of channels makes visual inspection of all waveforms almost impossible, but does enable spatial representation of parameters such as potential or activation time, using for example pseudocolour maps. In addition, specialized computer algorithms are employed to convert the large amounts of data into concise diagnostics. Standard ECG-analysis tools are therefore inadequate for multichannel ECG analysis.

Due to the variety in research purposes and available hardware, many custom software packages have been created at laboratories involved in electrocardiographic research. The creation of software that would be general enough to be applicable in many different laboratories, might prevent repetition of effort, and make implementation of difficult algorithms and a sophisticated user interface more worthwile. The MA$^{P}_{L}$AB package, which is described in chapter 10, is an attempt to create such software. It was developed during the last six years at the Medical Physics Department of the University of Amsterdam, and is now in use at about 10 research centres worldwide. This software can process both intracardial maps and body surface maps, and both at the same time, thereby facilitating research in integrated mapping.

1.11 Outline

Analysis of integrated mapping data and development of a guidance system for ablation procedures requires at least the following questions to be addressed:

- How can the pacemap databases developed by SippensGroenewegen et al. be optimally applied for relative and continuous localization. This is discussed in chapters 6, 7, and 8 [199, 201, 212, 214].
- How can arrhythmia localization results obtained from the surface ECG be presented in 3-D or RAO and LAO fluoroscopic projections in

the catheterization laboratory today and in the future. E.g., can standard models be used? Which information is useful for adaptation of a model to an individual patient? Can it be done in real-time? A method that allows conversion into fluoroscopic projections using simple information derived from angiographic images is presented in chapter 9 [197, 213].

- To what extent do infarct scars hamper BSM localization of VT, and how can this problem be handled [206, 214]. The effects of limited infarction on BSM localization are evaluated in chapter 8.

- Are electrograms recorded with a basket catheter comparable with signals obtained with standard catheters or intracardial balloon electrodes? How should basket electrograms be processed to facilitate interpretation? Some properties of basket electrograms are investigated in chapter 4.

- What software is needed for multichannel ECG analysis. The $\text{MA}^{\text{P}}_{\text{L}}\text{AB}$ software package, which can handle all kinds of multichannel ECGS, is described in chapter 10 [207, 208]. Documentation is important for the creation of such software. Appendix A illustrates the software documentation methods that were used.

The discussion of these questions involves seven of the 11 chapters in this thesis. Two introductory chapters complete the discussion: Chapter 2 describes the hardware and software needed for recording and storage of multichannel ECG data, and chapter 5 introduces methods for analysis of multichannel surface electrocardiograms.

Chapter 2

Recording, Storage, and Analysis of Electrocardiograms

This chapter discusses recording technology, datafile formats, and software for the digital recording of multichannel ECG data. — Linnenbank et al. *Selecting the optimal parameters for biomedical amplifier systems* (in preparation). Presented in part at the *13th Annu. Int. Conf. IEEE EMBS*, 1991 [151]; *14th Annu. Int. Conf. IEEE EMBS*, 1992 [149]; *Intern. Conf. on Electrocardiology*, 1995 [150].

2.1 Introduction

In the last few decades, technological progress has changed the recording of multichannel ECGs from a complex laboratory experiment into a routine clinical procedure. Miniaturization of amplifiers has made the equipment portable and made high-quality recording in an electrically noisy environment possible [172]. Fast digital computers allow the simultaneous recording of many leads, sampled at a frequency of 1 kHz or more, in such a way that the data are immediately accessible for on-line analysis.

In the 1950's and 60's, maps comprising hundreds of leads were obtained with analog recording equipment by multiplexing of signals, recording only a few of the leads at a time and using several beats—which were assumed to be identical—to obtain a complete map [58–60,256]. Nowadays, digital acquisition systems are able to record more than 500 leads simultaneously at a sampling frequency of 2 kHz [18]. Digital acquisition systems also facilitate analysis of recordings because they make the data immedi-

ately available in a computer-readable format. Recordings with in the order of a million leads, though for short durations or reduced sampling frequencies, are possible with optical mapping methods, where the intracellular potential is converted to fluorescence by voltage-sensitive dyes, and recorded with a CCD camera [75, 177, 267, 277] (see section 3.4 on page 49).

2.2 Recording Hardware Requirements

Equipment for ECG recording is in direct electrical contact with the patient. This implies that the system has to be not only technically well-designed but also safe. For multichannel recording this means that the system can best be divided into a part with amplifiers that is in contact with the patient (often called the "front-end") and a part that is connected to the mains and takes care of the processing, storage, and user interfacing (the "back-end"). The parts communicate via an electrically isolated connection. For this purpose, an optical fibre has been employed by our group [172]. This has the additional advantage of reducing the capacitive coupling between front-end and back-end.

In this design setup the front-end must be compact and use as little power as possible because it cannot be powered by the mains. Batteries are often the most convenient power source for the front-end; laser powering by optical fibres may become feasible, but it presents complicated safety problems which have to be solved before this method can be applied clinically [86]. At the moment it is technically not possible to transmit multichannel data over an analog connection in a practical way. We therefore assume that analog-to-digital (A/D) conversion is performed in the front-end and that the data are transported digitally. Typical design parameters that influence the size and power consumption of such systems are: the number of parts per channel, the number of bits of the A/D converters, and the sampling frequency.

Using an isolated recording system with high-quality amplifiers as described above, it is possible to obtain amplified signals whose noise level is dominated by the inevitable "electrode noise," which originates primarily at the electrode–skin interface and amounts $2 - 10\,\mu V_{RMS}$ [107].

2.2.1 Computation of the bit step

The next stage in the design of a digital acquisition system is the selection of a bit step (discretization level) for analog-to-digital (A/D) conversion. Discretization of a signal introduces additional noise proportional to the bit step ($V_{RMS} = 1/\sqrt{12} \cdot V_{bitstep}$) [150]. Thus the selection of a small bit step

both increases accuracy and decreases additional noise. However, a smaller bit step implies a larger number of bits, and A/D converters generally use more power for a larger number of bits. If power conservation is an issue, as is the case in a battery-powered front-end, the bit step of a system should therefore not be made unnecessarily small. Since there is an inevitable noise component arising from the electrodes, and (RMS) noise levels add quadratically, it is not functional to choose the bit step so small that the discretization noise is much smaller than the electrode noise. A bit step of about one to three times the analog RMS noise level is thus a reasonable choice. For a typical ECG this means a bit step of 2–8 µV.

The required number of bits then follows by dividing the maximal expected signal by the bit step. A typical assumed noise level for ECG data is $4\,\mu V_{RMS}$. If this value is used as a bit step, at least 14 bits are needed for endocardial electrograms with a range of approximately 50 mV. For surface ECG data, 12 bits generally suffice at this resolution.

2.2.2 Analog filtering prior to sampling

For electrocardiographic recordings, high-pass filters with cut-off frequencies of 0.05 or 0.16 Hz are employed to reduce DC offset and baseline drift originating at the interface between electrode and skin [40, 107].

In addition, analog low-pass filters are employed before the A/D conversion in order to reduce noise and distortion in the sampled signals. During sampling, signals with frequencies above half the sampling frequency (known as the Nyquist frequency and denoted f_ν) are 'folded back' into the lower frequency range. If the sampling frequency is 1 kHz then a signal with a frequency of 550 Hz will turn up in the output as a signal of 450 Hz. The 450 Hz signal is called an alias of the original frequency and this process is therefore also commonly known as *aliasing*.

In order to digitize a signal as effectively as possible, the noise and signal components with frequencies above the Nyquist frequency should be attenuated as much as possible by a low-pass filter. It is not possible to remove these unwanted signals after sampling because of the aliasing effect; the aliases will distort the signals and be virtually inseparable from them. A related function of the analog low-pass filters is to increase the signal-to-noise ratio (SNR) by attenuating those frequencies that do not contain information.

The interaction between filtering and aliasing is illustrated in figure 2.1. Because noise adds quadratically, the influence of aliases of noise on the total noise is negligible, except for frequencies close to the Nyquist frequency in the case of a second-order filter with a relatively high cut-off frequency. Moreover, both ECG and noise diminish with increasing frequency,

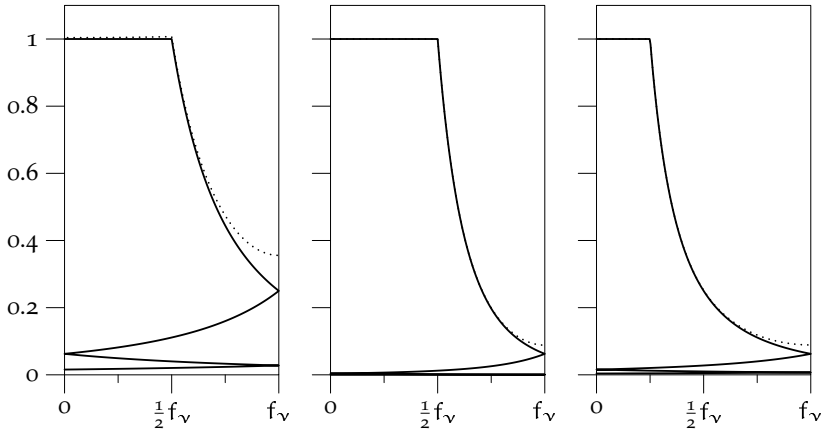

Figure 2.1: *Examples of aliasing, also called "folding back" of frequency bands due to sampling. Amplitude responses of three different filters are shown, to give an estimate of the relative contributions of noise and interference of different frequencies after filtering. Along the horizontal scale of each plot, the frequency is expressed in terms of the Nyquist frequency $f_\nu = \frac{1}{2}f_s$, where f_s is the sampling frequency. In panel (A), the filter is an idealized 2nd-order low-pass with a cut-off frequency of half the Nyquist frequency ($1/4f_s$). Panel (B) shows the results of a 4th-order filter and panel (C) demonstrates a 2nd-order filter with a low-pass frequency at a quarter of the Nyquist frequency. The drawn line represents the amplitude response in arbitrary units. The amplitude response consists of four "folds," the upper fold represents the interval 0–f_ν, the next fold the aliased frequencies in the interval f_ν–$2f_\nu$ that are folded back to the primary interval, etc. The dotted line represents the quadratic sum of all four folds. These responses can also be interpreted as those that would be obtained if the input would consist entirely of white noise.*

making aliases even less of a problem. Only aliases of interference can have a noticeable influence on the recorded signals.

2.2.3 Computation of the low-pass cut-off frequency

The value of the optimal low-pass cut-off frequency depends on the frequency spectra of the signal that is recorded, and of the noise that is superposed on it.

To estimate the spectrum of the ECG, ~ 700 complexes of sinus rhythm of

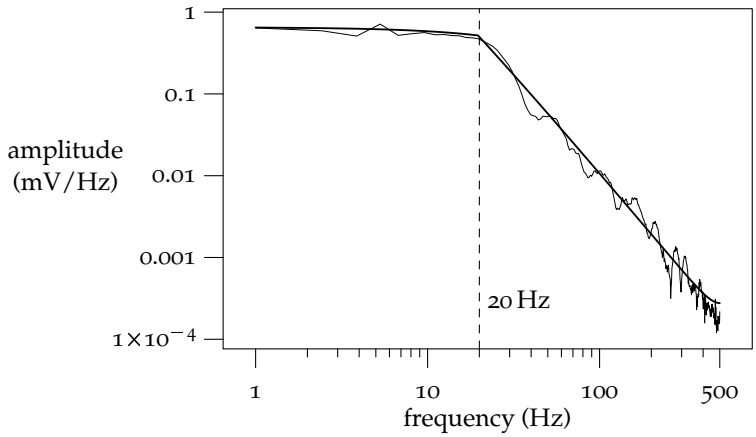

Figure 2.2: *Amplitude spectrum of an averaged 64-channel ECG of one patient. Each lead was averaged over approximately 700 beats, and the amplitude spectrum of the average signal was estimated. The thin line represents the average of the spectra of the 64 leads. The thick line is the approximation used in this chapter. Its characteristic point at 20 Hz is indicated with a dashed line.*

a multichannel ECG recording of a single patient were signal averaged. The (quadratic) average spectrum of all 64 channels was taken as an estimate of the spectrum of an ECG. It turned out that the spectrum could be approximated by a curve that decreases slowly up to about 20 Hz and then drops off with 15 dB per octave (figure 2.2). The average peak R amplitude of the ECG was 640 µV and the RMS amplitude of the signal 128 µV, at a heart rate of 85 beats per minute.

The spectrum of the noise in the ECG can be modelled by $1/f$ noise. The amplitude of the noise is about 2 μV_{RMS} for high-quality recordings to 20 μV_{RMS} in situations with much interference, bad electrode contact, or muscle artefacts. In our experience, the modal noise amplitude is about 3 to 5 μV_{RMS} (15–25 µV peak-to-peak).

Using the spectra of ECG and noise it is possible to compute the SNR of the ECG as a function of the cut-off frequency. We consider three sources of "noise." 1) The filtered noise that results from the noise present at the input, consisting mainly of electrode noise. 2) The aliases of the input ECG that fold back into the $0–f_\nu$ frequency range. 3) Those parts of the input ECG that are attenuated by the filter. The latter components also have to be taken into account as noise for the SNR computation. Phase changes in the analog filter can also cause distortions, which will be ignored here.

The SNR as a function of the cut-off frequency has a maximum because for low cut-off frequencies, the signal will be distorted as a result of the filtering, whereas at higher frequencies this distortion of the signal is small but the noise contribution is larger with increasing bandwidth of the amplifier (panel a in figure 2.3). The distortion as a result of aliased signal components in an ECG with a frequency above f_ν is negligible at a sampling frequency of 1 kHz and is not shown in the figure.

With the above-mentioned parameters for the spectra, the optimal cut-off frequency can be computed. If we assume a second-order idealized low-pass filter and a sampling frequency of 1 kHz then the optimal cut-off frequency is about 150 Hz for a noise level of 2 μV_{RMS}. In case of a tenfold noise level, the optimal frequency will be lower at 50 Hz. If, however, these signals will be used for signal averaging and after averaging only 0.2 μV_{RMS} remains, the low-pass cut-off frequency should have been at 400 Hz for optimal performance (panel b in figure 2.3).

When higher than second-order filters are employed, the bandwidth of the amplifiers can be larger. For e.g. a 4th-order filter the values are 55, 175, and 450 Hz for 20, 2, and 0.2 μV_{RMS}, respectively. In general, higher-order filters reduce the distortion in the sampled signal but they require a larger number of parts on the amplifier board.

Thus, the optimal cut-off frequency is highly dependent on the (often unknown) noise level. Since the total noise level increases little for cut-off frequencies above the optimal frequency (figure 2.3a), it is safer to choose a relatively high cut-off frequency if the noise level is not accurately known.

2.2.4 Computation of the sampling frequency

It is advantageous to have a sampling frequency that is as low as possible. Most A/D-converters are built with CMOS transistors. The power consumption of these transistors is proportional to the frequency at which they operate. Therefore, a lower sampling frequency reduces the power consumption proportionally, thus increasing the battery life.

The only noise contribuent that changes with the sampling frequency is the aliasing of signal components in the ECG signal. The spectrum of the ECG drops quickly with increasing frequency. The effect of aliasing on the SNR when selecting a certain f_ν (which will turn all frequencies higher than that into "noise") is therefore highly comparable to the distortion that results from using a low-pass filter with cut-off frequency $f_{cut} = f_\nu$. At the frequency with an optimal SNR, the distortion component is already much lower than the noise contribution. The sampling frequency can therefore be chosen as low as $2f_{cut}$ without affecting the SNR.

There may be two reasons to select a higher sampling frequency. First,

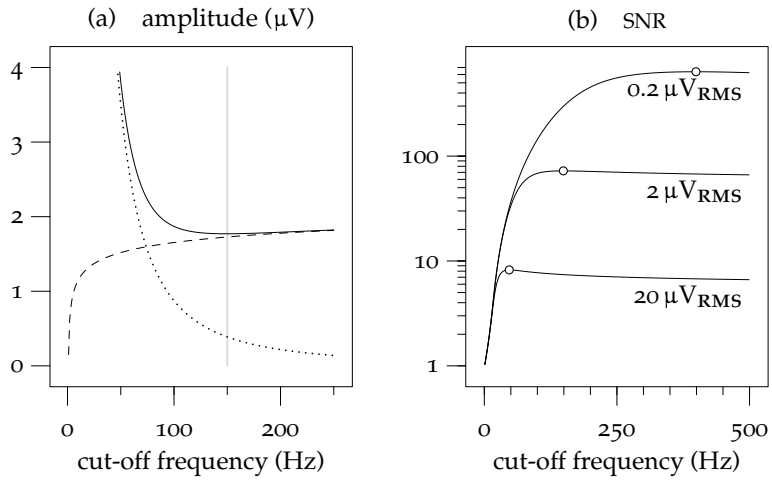

Figure 2.3: (a) *Contributions of distortion (dotted line) and input noise (dashed line) to the total noise at the output (solid line), as a function of the cut-off frequency, for an ECG with an input noise level of 2 μV_{RMS}. The sampling frequency is 1 kHz and a 2nd-order low-pass filter is applied. The distortion decreases with increasing cut-off frequency, but the contribution from the input noise increases with the cut-off frequency. The quadratic sum of these noise sources reaches a minimum at 150 Hz, indicated in the figure by the vertical line.* **(b)** *Signal-to-noise ratio (SNR) as a function of the cut-off frequency for three noise levels. The level (0.2, 2, or 20 μV_{RMS}) corresponding to each curve is indicated. The maximum of each curve is indicated with an open circle. For the 20 μV_{RMS} curve the maximal SNR is 8.2, and it slowly decreaeses for higher cut-off frequencies, to 6.4 at a cut-off frequency of 500 Hz.*

to reduce the influence of aliases. If the noise at frequencies close to the sampling frequency is not much attenuated, it can hamper further processing since it folds back as low-frequency noise. Also, one may plan to reduce the higher-frequency noise after sampling, by a digital filtering technique, instead of applying an analog filter before sampling.

The second reason for using a higher sampling frequency is when these signals will be used later for signal averaging. After averaging, smaller higher-frequency signals can be detected due to the lower noise level. In this case, one should also increase the cut-off frequency of the low-pass filter (see section 2.2.3). This decreases the SNR for the beat-to-beat analysis, but fortunately the SNR decreases but slowly with frequency, so this may be a favourable trade-off.

2.3 Computer Hardware Requirements

The number of channels, the measurement accuracy, and the sampling frequency determine the *data rate* of a system. The equipment that stores the data must be able to handle this data rate. Just a few decades ago, only photographic equipment, and to a lesser extent mechanical pen plotters, could handle the data rate of an ECG [57, 60, 256]. Later, analog magnetic tape was employed; this method is still used for portable ("Holter") ECG recording devices. For most other applications, digital computers nowadays store ECG data.

Two subtasks can be recognized in the task of computer acquisition and storage of data: 1) entering the data in short-term random access memory (RAM), and 2) storage in long-term memory (hard disc). In addition, archiving on permanent media such as CD-ROM is a task of the computer equipment. Generally, the first subtask can be performed much faster than the second, because RAM allows a much larger data rate than a hard disc. On the other hand the capacity of the hard disc is generally much larger than the capacity of the RAM. Three possible scenarios can be distinguished:

1. The data rate exceeds the speed of both short-term and long-term storage. In this case direct computer acquisition is impossible.

2. The data rate is too high for the long-term storage but not for the short-term storage. In this case, recordings may be made for a limited period by caching the data in RAM, and subsequently storing them relatively slowly on hard disc. Most acquisition systems employed in the last decade use this method.

3. Both long-term storage and short-term storage can handle the data rate. This allows continuous recordings with the recording duration only limited by the size of the long-term memory. The integrated mapping system employed in the St. Antonius hospital (section 1.6) is able to do this for 128 channels of 16-bits data recorded at a sampling frequency of either 1 or 2 kHz (yielding a data rate of 256 or 512 kB/s).

Data acquisition is a so-called "real-time task" for computer systems. This means that the device that delivers the data, which typically has limited storage capabilities, must be served in time, where "in time" may mean within milliseconds from the moment it requests service. Most operating systems are not able to guarantee this level of service without modification of their internals. Generally, data acquisition is possible if the user is careful not to keep the system too busy. Absolute guarantees can only be offered by specialized real-time operating systems. If a user interface has to run simultaneously with the acquisition, for example in order to display

and analyze the recorded data immediately, it may be preferable to run acquisition software and user interface software on different computers: one of them running a real-time or nearly real-time operating system, and the other running an operating system that facilitates user-interface programming. This solution was chosen previously for a clinically applicable BSM system [154].

2.4 Software Requirements

Some requirements for acquisition and analysis software are already mentioned in section 2.3. In addition, we may require that the analysis software is fast, robust, user-friendly, and programmer-friendly.

Speed and robustness are obvious advantages of any software system. About user-friendliness, it may be remarked that it is not necessarily the same as "beginner-friendliness." Most commercial software is beginner-friendly. This means that a novice user can find out in an intuitive way how the software is operated, for example, because the most commonly used functions can be performed by pressing virtual buttons on the screen, which are marked with easily interpretable pictograms or texts. Experienced users, however, may not need such devices: they may prefer to press special combinations on the keyboard, which can be done much faster than reaching for the mouse and pressing buttons on the screen—but requires them to remember the key combinations. Such experienced users may wish to have the unused screen buttons removed, in order to save space for more important things such as larger data displays. Of course, there are many other differences between user-friendly and beginner-friendly software systems.

This thesis concentrates on the development of an automatic system for catheter guidance during electrophysiologic study of cardiac arrhythmias in the catheterization laboratory, using multichannel surface ECG data. In short, this system should record multichannel ECG data continuously, detect and classify beats automatically, and present results of ECG-based arrhythmia localization in such a way that they can be easily interpreted by the physician. Such a system has not yet been built. Parts of the work towards it are discussed in chapters 6, 7, 8, and 9.

A software package designed for research purposes is the MAP$_{\text{L}}$AB software described in chapter 10 [207, 208]. This package was developed for off-line analysis of various kinds of multichannel electrocardiographic data. It is highly versatile and provides easy access to various sophisticated algorithms, but it is less suitable for on-line clinical application.

2.5 File Formats for Data Storage

Digitized ECG data are usually stored on disc, and archived on CD-ROM, for later analysis or re-analysis. The data must be stored in a way that allows them to be completely understood by various researchers for several decades, or perhaps centuries. For example, the re-analysis described in chapter 7 of BSM data that were recorded in 1986–1988, was perhaps never anticipated, but proved worthwhile for the research described in this thesis. Clinical data should be stored at least as long as the patient lives, or longer for the sake of diagnosis of genetic disorders in descendants, and therefore should preferably be intelligible to contemporary hardware and software. This calls for a well-documented file format that contains all information necessary for a complete understanding of the data, and that can be completely interpreted by a computer program. Examples of such information are electrode configuration, patient identity, recording time, sampling frequency, and resolution.

2.5.1 Homogeneous and inhomogeneous datasets

Multichannel recordings can be subdivided in two fundamentally different types. One has *homogeneous datasets* where all channels have the same parameters and the spatial relations of the channels are significant. Typical examples are the BSM recordings, the multielectrodes used to record data from the epicardium, and multipolar catheters. On the other hand there are *inhomogeneous datasets*. A typical example would include a few ECG signals, some electro-encefalogram (EEG) signals, a blood pressure signal, and a signal from a thermistor for respiration monitoring. In these inhomogeneous recordings the spatial relations between the channels are not important; the main emphasis is on the temporal relations of all these data. Basically, every channel can have a different bit step, a different sampling frequency and a different transducer.

Datasets can also combine homogeneous and inhomogeneous subsets, or several of each kind. An example of this type of dataset is the combined recording of a 62-channel BSM, a 61-channel endocardial basket recording, and three extremity leads, which was discussed in section 1.6. In this case, the spatial relation is important within homogeneous subsets, and may be important between the homogeneous subsets. As in purely inhomogeneous datasets, the emphasis is on the temporal relation.

These three types of datasets require slightly different file formats. For inhomogeneous datasets the file format should allow for every channel to have a different specification, whereas for homogeneous datasets the spatial relations have to be encoded. If the spatial relations are encoded ex-

ternally, a file format that allows inhomogeneous datasets can be used for the homogeneous case, but a reader program will be much more complicated (and therefore slower) because it has to allow for those cases where not all channels have the same sampling frequency and it is, therefore, not possible to read blocks of data in one pass.

For mixed homogeneous and inhomogeneous datasets, the datafile format becomes particularly complicated if the homogeneous character of subsets is to be exploited. In such cases, a choice must be made between programming efficiency and computational efficiency.

2.5.2 Requirements for datafile formats

Preferably, a file format should comply with all of the following requirements.

- The format should identify itself. It is not sufficient to encode the format in the filename, as is customary in some environments, for filenames may be changed easily and are not treated in the same way on all computer platforms. Preferably, the first few bytes of a file should contain a unique code. For example, the IFF-MCHD format (section 2.5.4) specifies that the first 4 bytes read "`FORM`" and bytes 9–12 read "`MCHD`," the JPEG format specifies that bytes 7–10 read "`JFIF`," and various types of WordPerfect files can be identified by a string beginning with "`WPC`" which starts in the second byte of the file. On UNIX systems, such unique codes are commonly used, and known as "magic numbers;" identifications of many file formats can be found in the system file `/etc/magic`.

- A datafile format must allow complete reconstruction of the signals, without knowledge of the recording hardware and software. This means that, for example, bit step, number of bits or bytes, numeric format (integer or floating-point, signed or unsigned, left- or right-aligned), order of the bytes in a machine word (Little-Endian, Big-Endian, etc. [219]), unit, and sampling frequency should either be encoded in the file, or specified by the file format. Typically, information like the byte order and numeric format are specified by the file format, while bit step and sampling frequency are encoded in the file. In general, it is the best to encode as much of the information as possible in the file—if it does not lead to excessive file sizes—because this allows employment of a file format by a wider range of equipment. For example, the free choice of byte order in IFF-MCHD files (section 2.5.4) allows these to be written efficiently on both Big-Endian and Little-Endian computers.

- It must be evident what was recorded. The required information includes the identity of the subject (a Hospital Patient Identification Number (HPIN), or a unique identifier for animal experiments). In case of ECG data, it should be clear where the electrodes were placed. If a standard lead set is used, such as the standard 12-lead set or the orthogonal Frank leads, a set identifier can be used, provided that the order of the leads in the set is standardized.

- The recording date and time should be encoded, since these may be helpful later to identify the recording and to relate it to other data that were acquired at the same time in the same subject. In order to relate recordings to each other, it is better to encode the starting time of the recording in terms of the sampling frequency, relative to some convenient time instant, e.g. the starting time of the procedure or the time the recording apparatus was switched on. Preferably the recording time should have an accuracy comparable to the sampling frequency.

  If the timing of recordings is relative to the procedure starting time, the latter should also be included, but it need not be as accurate as the recording time, provided that all recordings that need to be compared to each other are created during a single "procedure," so that they can be compared with high temporal accuracy.

  The lesser accuracy requirement for the procedure starting time is necessary because the sampling interval for electrocardiograms may be less than a millisecond; in many recording systems, time cannot be measured with millisecond accuracy over periods of hours or days. In most cases, it is not necessary to know the procedure starting time more accurately than a minute.

- If the recording system influences the recorded data, for example due to built-in filters, this should be encoded. This can be difficult, because an infinity of filter types can be devised. At least, an identification of the recording system and its configurable parameters should be included.

- In order to make tracking of errors—and perhaps compensation—possible, an identification of the recording system (type, version of software, and serial number of hardware) should be included. Although it was argued above that knowledge of the recording system should not be necessary, it still should be possible to use this knowledge, if present, to solve problems. For example, if an acquisition system is used in combination with a badly calibrated preamplifier

for a specific experiment, this setup should be identified, to allow correct reconstruction of the signals for researchers who know the experimental setup well enough.

- For most acquisition systems, integer data formats are most suitable because the precision is limited, determined by the A/D converter. Nowadays, A/D converters with precisions of 8 up to 20 bits are in use. However, it may be necessary to store also processed data in the same file format. If, for example, signal averaging is applied to an ECG, the dynamic range may increase by as much as 10 or 12 bits. If nonlinear transformations are involved, it may even be necessary to use a floating-point format.

- It must be simple for an acquisition system to create the file. This means, for example, that data should be written in the order in which it enters the system. Usually this means that samples rather than channels are contiguous. An exception has to be made if the channels are not all sampled at the same frequency; in such cases it is more convenient to let a channel be contiguous for the least common multiple of the sampling intervals. It is therefore advantageous to choose the sampling frequencies such that this common interval is small. Complicated schemes may be required in other situations as well. For example, it turns out that BSM data of arrhythmias can be successfully compressed by Huffman-encoding of the second derivative of each channel [149]. This means that the data of a channel must be contiguous, which in turn means that the recording system must be able to store all data for the length of the recording. If this is not feasible, a compromise can be to write the data in relatively short "blocks" where a channel is contiguous only within the block. This solution was chosen in the IFF-MCHD format, which will be discussed in section 2.5.4, where blocks of 256 samples are employed.

- It must be simple to extract a single sample or a single channel from a recording. For plain storage formats this is straightforward, but if a variable-length compression scheme such as Huffman-encoding [106, 149,215] is used, the location of a specific sample cannot be computed without decompressing all preceding samples. If such compression schemes are used for long recordings, it may be necessary to divide the data into small blocks whose locations in the file can be easily determined, so that only a few samples have to be decompressed to find the required sample (see section 2.5.6). This was another reason for the "block" approach used in the IFF-MCHD format.

- All information should be encoded in a way that is formal enough to allow interpretation by a computer program without sophisticated artificial intelligence. For example, the recording date should not be a free-format string: "`01/02/2001`" could be interpreted as the first of February in Europe and as the second of January in the United States. A date like "`23-Feb-2001`" would be hard to understand for a system that expects dates like "`Feb 23, 2001`," not to mention "`23e Février 2001`." An unambiguous way to encode a date would be a set of three numbers: year, month, and day. Even more accurate is to use the number of seconds elapsed since a standardized Event (midnight GMT 1st January 1970, for UNIX system software), or the Julian day number. Of course, the range of such a number should be sufficiently large for a few centuries; on UNIX systems that treat the date as a signed 32-bit integer the date will wrap around on January 19, 2038.

  Encoding of the data unit is rather uncommon. One possibility is to use Système International (SI) units only, and encode multiplication and division in case a derived unit such as the volt is needed. Since the number of SI units is fixed at seven, any derived unit can be represented as a set of seven numbers indicating the positive or negative powers with which the individual SI units contribute. Of course, the SI system can be used only for physical units, but fortunately the vast majority of signals is physical. A problem is presented by units like the decibel, Beaufort, $1/\sqrt{\text{Hz}}$, and the pH, which need complicated conversion formulas, and nonstandard units like mmHg, which should preferably not be used. For these, and for non-physical units, it may be necessary to include both the SI encoded unit and the name of the unit, and to allow one of them to be void. If the SI encoded unit is present, it can still be useful to include the unit name, for the convenience of the user. For example, a reader program may be unable to convert $\text{kg}^1\text{m}^1\text{s}^{-2}$ into N.

- In addition to the unit, either the kind of data or the transducer type has to be identified. It may be impossible to devise an encoding system that allows everything ranging from "epicardial potassium electrode (millivolts)" to "Mars Polar Lander altitude (feet)," but it should be possible for an analysis program to distinguish an epicardial potassium electrode from a Ag–AgCl surface electrode. Such information may be encoded in an external configuration definition which must then be identified in the datafile; the MAPLAB software (chapter 10) uses electrode definition files that provide some information on the type of data.

- If there is a spatial relationship between the recording electrodes, such as in a BSM or an intracardial map, it should be encoded. The datafile format can specify an encoding method or a way of referring to an external definition.

- In particular for large amounts of data, it is useful if the format specifies a way of data compression that works well for the type of data that is stored. Similarly, the JPEG format contains compression methods that work well for pictures, and the MPEG format contains compression methods that work well for movies. In contrast, the ZIP and LZW compression algorithms are byte-oriented and work reasonably for most data types, but poorly compared to JPEG when applied to images. ECG data encoded in 2-byte integers cannot be optimally compressed by a byte-oriented method because such a method would never be able to see the relation between byte n and byte $n + 2$ (they tend to be approximately equal, which provides good opportunities for compression with algorithms that *are* aware of this relation).

- The file format should be efficient both in time and space. This means binary rather than ASCII encoding, data compression, variable sizes for large parts (like a Huffman-encoding table) and fixed sizes for small parts (like a patient name).

- The format should be extensible and preferably offer both backward and forward compatibility.

  Backward compatibility means that reader software for newer versions of the format can read old versions without problems. Forward compatibility means that old software can read newer formats as well as possible. For example, adding a HPIN to the patient data should not make reading of the electrograms impossible for older software that does not handle HPINS.

  Forward compatibility cannot be maintained completely in all cases. For example, when a new compression type is introduced, it is inevitable that old software will be unable to read the data. However, it should still be able to read the patient information and basic recording information such as the number of channels. In addition, it should be able to report the nature of the problem to the user: Not "read error," but something like "This file employs compression type zoo-13f which is not implemented; please update."

It is difficult to decide which information should be completely specified in the datafile and which information should be specified by referring to an external definition. In our IFF-MCHD format, for example, the patient

name and date of birth are encoded completely, but alternatively a HPIN could be given. In contrast, this file format specifies the electrode configuration by name only, which means that analysis programs have to rely on external electrode definitions.

If datafiles are to be interchanged between hospitals or laboratories, it is preferable to select a format that is already adopted as a standard, in order not to force all centres involved in a project to implement every new file format one may invent. To make wide adoption feasible, a standard format should meet the requirements of efficiency and completeness stated above.

2.5.3 The European Data Format (EDF)

An example of a standard file format is the European Data Format (EDF) [124], which is particularly used in neurophysiology. The EDF format was published and is employed by several research groups, and at least one manufacturer of recording systems. The format can be used for highly inhomogeneous datasets (section 2.5.1), but for several reasons it is less suitable for homogeneous multichannel ECG data. Specific problems of this file format are

- The length of a data record is specified in seconds, *preferably* as a whole number of seconds. This is a very inconvenient way of encoding time. For example, it means that rounding errors in the timing occur if the sampling frequency f is not an integer fraction of an integer number of seconds ($f \notin \mathbb{Q}$, where $\mathbb{Q}$ is the set of rational numbers), which is usually the case. In the rare cases that $f \in \mathbb{Q}$, that is, $f = n/m | \{n, m\} \in \mathbb{N}$ with $\mathbb{N}$ the set of natural numbers, but n is large, data records have to be long to prevent rounding errors.

- Data records must be short, because they have the wrong order for most acquisition systems: channels rather than samples are contiguous, such that data for each sample is spread out over the data record. This means that the acquisition system must be able to store the entire record to write it out in the correct order, or must use non-sequential file access, which is rather inefficient.

- The format of the data unit is not specified. This means that an analysis program cannot, for example, automatically convert microvolts to millivolts.

- The byte order (Little-Endian/Big-Endian) is not specified.

- Compression is not included.

- The file header is rather large, requiring 256 bytes for each channel, i.e. 32 kB for a 128-channel recording. For the shortest recordings that are currently made in the catheterization laboratory (1 second, at 1 kHz and 2 bytes per sample), the header would take 12.5 % of the file size. In case of homogeneous data sets, where the header information is the same for all channels, these headers are redundant, which makes the format relatively inefficient.

- The format does not include an identification of the recording setup ("electrode grid"), although this may be added as "local information."

- The format does not identify itself in an unambiguous way.

- Apart from a few bytes reserved for "local information," the format has no provisions for extensions.

- The format is not year-2000 compliant.

Some of these problems are probably due to the specific application for which the EDF format was developed, that is, the exchange of sleep-wake recordings [124]. This application requires relatively few channels, of very different kinds (such as temperature, EEG, and ECG), with different sampling frequencies which are sometimes much lower than those common in multichannel ECG analysis. These are typical examples of inhomogeneous datasets (section 2.5.1). The EDF format can handle these reasonably well but is relatively inefficient for homogeneous datasets.

The fact that such a poorly designed format is adopted by a broad research community, even for homogeneous datasets, indicates that there is an urgent need for a well-defined public data format.

2.5.4 The IFF-MCHD format

Since 1995, our ECG data have been stored in the interchange file format (IFF) [178]. IFF is a family of file formats used by most applications on the Amiga microcomputer, but also on other platforms. Within IFF every type of data has its own format but the general file structure is the same for all types. A well-known subtype is the interleave bitmap (ILBM) format which is used to encode graphics. Other subtypes are for text, music, animations, etc. For multichannel data we use the MCHD subtype, which was carefully specified and documented at our laboratory, but not yet published or registered as a standard subtype. A compression method is part of the IFF-MCHD file standard [149].

The date and time formats of IFF-MCHD were originally not well defined. For example, the date was a free-format string of 11 characters. Later, it was specified that this string should be written as `dd-mm-yyyy` (the eleventh character is the end-of-string character).

Recently, extensions were defined to allow different data types and different bit steps in one recording, and to store a HPIN instead of a patient name. These extensions make the format more suitable for inhomogeneous datasets (section 2.5.1) than it was before. In contrast to EDF, the format still cannot handle channels with different sampling frequencies in a standardized way. The datafiles that have been recorded until now do not contain the recording time with a better resolution than 1 second, and the time is derived from the system clock instead of an accurate external source. Also parameters like the version of the hardware and software and the filter settings are not recorded yet, but due to the extensibility of the IFF format these can easily be added without breaking existing code.

2.5.5 Other formats

Other formats that we use are the local file formats developed at the Experimental Cardiology Department of the University of Amsterdam. These file formats are very much biased to the particular kind of recordings made at this department. A notable disadvantage is that they do not contain a recording time. It is our intention that these formats are some day superseded by IFF-MCHD or an other standard format. However, because these formats can be read by the MATLAB software (chapter 10) [207, 208], they can be exchanged between many research groups worldwide.

2.5.6 Data compression

Data compression means representation of data in a more compact way. Two fundamental types of compression can be recognized: *lossless* and *lossy* compression. Lossless compression means representing exactly the same information in a more compact way by removing redundancy in the original data. Lossy compression methods also omit details that are considered irrelevant, such as fine details in bitmap images that cannot be perceived by the human eye. Since medical data are generally to be stored without any data loss, we confined ourselves to lossless methods.

Lossless compression is only possible if the original data are redundant. One example of redundant digital data is text in ASCII encoding. This encoding contains only 127 different characters and can therefore be represented by 7 bits per character. However, it is convenient for a computer to represent each character in one byte (8 bits), so that one bit is wasted for

each character. Such data can be compressed by removing each 8th bit, i.e., representing characters in a noninteger number of bytes.

Variable-length encodings like Huffman and arithmetic coding employ also the fact that the 'e' and the 'n' occur more often in English texts than the 'z' or the 'q' [106, 215]). By using fewer bits for frequently occurring characters and more—possibly even more than 8—for rarer characters, it turns out to be possible to reduce the *average* number of bits per character.

Compression methods for digitized signals can be described by *forecasting* and *encoding* methods. Forecasting means that, for example, the value of a signal sample is forecasted from the values of preceding samples: the encoding and decoding program can perform this forecasting in the same way, which means that instead of the actual value, the difference between the actual value and the forecasted value must be represented. It turns out that if the data are not totally random, some of these differences (the smaller) occur much more frequently than others, like the letters in English text; therefore Huffman or arithmetic coding can be employed for compression, as discussed above.

A complication of variable-length encoding schemes is that the location of a given sample cannot be easily predicted; all preceding data have to be decoded to find its location. For long recordings, this problem can be reduced by dividing the data into blocks of limited duration, as already mentioned in section 2.5.2. Each block of data starts with a pointer to the next block, followed by compressed data for a known, limited number of samples. In order to find a given sample, a decompressing program only has to read the pointer at the beginning of a block in order to skip the data and proceed to the next block, repeating this until it arrives at the block containing the desired sample. For very long recordings, it can be advantageous to use a central directory of block addresses. Such a directory can be contained in the file or it may be created on the fly by the reading program. The latter approach is used in the MATLAB software for IFF-MCHD recordings that employ Huffman encoding for compression [149, 198].

2.6 Discussion

When the spectra of the expected signal and noise are known, the design of an isolated front-end can be tuned to give an optimal SNR while minimizing the power consumption. In sections 2.2.1, 2.2.3 and 2.2.4 the optimal bit step, low-pass filter and sampling frequency are computed for an ECG signal. For this computation a large number of sinus beats was used. For different applications, such as intracardiac signals and arrhythmia recordings, the optimal parameters may be different. When designing hardware it

is probably best to make a system useful for a large number of applications. An example is the recording system developed for combined body surface and endocardial mapping that is now in use at the St. Antonius Hospital in Nieuwegein. This system has a dynamic range that is much larger than needed for surface electrocardiograms, but allows the larger amplitudes of endocardial signals to be captured with exactly the same amplifiers and A/D converters. The methodology that is described here for computation of the design parameters for various signals, will give some solid guidelines for amplifier design.

A more general conclusion that follows from these computations, is that for biological signals, which fall off rapidly with increasing frequency, a sampling frequency far above twice the low-pass cut-off frequency is a waste of (battery) power, bandwidth and storage capacity. A second conclusion is that it is important to know what the signals will be used for. The bandwidth of an ECG system for signal averaging needs to be much larger than the bandwidth of a system for single-beat analysis.

The experience obtained by our group during the implementation and use of various acquisition and analysis systems has led to the formulation of the requirements for software and file formats in sections 2.4 and 2.5. We have not yet had the opportunity to build a system that meets all these requirements, but we have made some progress towards it. For example, the IFF-MCHD datafile format, which is used by the latest generation of integrated BSM systems developed at our laboratory, as well as by the new (2001) recording software for the "Nieuwegein system," approximates what is considered perfect in the discussion above.

Chapter 3

Analysis of Intracardial Electrograms

This chapter discusses the physiological background and methods of analysis of electrograms that are recorded in the heart, either from endocardial, epicardial, or intramural sites. A new algorithm for the creation of isochronal maps is presented.

In this chapter, methods for analysis of intracardial electrograms will be discussed. Sections 3.1–3.4 summarize the genesis of electrograms and the theoretical foundation for their analysis. Sections 3.5–3.8 discuss some practical methods for electrogram analysis. A new algorithm for the creation of isochronal maps is presented in section 3.7.

3.1 The Cell

The contraction of cardiac myocytes, which makes the heart perform its pump function, is triggered by an electrical impulse. The electrical current that is responsible for the contraction is generated by the myocyte itself, a phenomenon called the *action potential*. Action potentials also occur in nerve cells. The action potential can be triggered by electrical activity from neighbouring cells, allowing the activation to spread quickly from a few "pacemaker" cells and cover the heart in an organized fashion—a precondition for efficient pump functioning.

The electrical behaviour of the cell consists mainly of the movements of Na^+, K^+, Ca^{2+} and Cl^- ions [84]. In contrast to, for example, oxygen and alcohol, which can enter the cell by diffusion through the membrane, these ions can enter and leave only through specific ion channels, either by diffusion or by active transport. An example of an active transport mechanism

is the so-called sodium/potassium pump, which exchanges three Na^+ ions for two K^+ ion at the cost of energy.

The ion specificity, time dependence, and voltage dependence of ion channels make the cell's electrodynamic behaviour, especially the action potential, possible. There are many different kinds of ion channels. A defect in one or more channel types, for example due to a genetic disorder, may provoke depolarization or repolarization abnormalities leading to electrical dysfunction, and may cause sudden death at any stage of life. Examples are the Brugada syndrome and the long-QT syndrome [26,27,44,272]. Multichannel ECG recordings can support the diagnosis of these disorders, as discussed in chapter 5. Drugs are used to inactivate specific channels, experimentally to study the behaviour of channels, and clinically when it is desirable to change the ion balance in the cardiac cells.

In the following sections, a short discussion of the physical properties of the cell that are important for its electrophysiology, and for the measurement of electrograms, is given. A complete discussion of these subjects was published by Gulrajani [84, chapters 1, 2].

3.2 Action Potentials

A mathematical description of the dynamic electrical behaviour of the cell membrane is called a "membrane model." Such models can be used to improve our understanding of the membrane, and for computer simulation of its dynamics. The most important aspect of the membrane dynamics is the action potential, which enables signal transport in nerves and triggers the mechanical contraction of myocytes.

The Hodgkin–Huxley membrane model, created specifically for the *loligo* (squid) giant axon [94], was the first dynamic model of the cell membrane. It was based on current-potential curves measured in cells. It uses a simple description of the ion channel, which results from observations of the time- and voltage-dependent permeabilities of the membrane. From this model and several empirical constants, differential equations for the Na^+ and K^+ permeabilities can be derived, by which the action potential and several related phenomena of the squid giant axon could be simulated.

Models with the same formulation as the Hodgkin–Huxley membrane model, but parameter settings adapted to other cell types, were created later. Such models are known as "Hodgkin–Huxley type models." McAllister [170] created a model for Purkinje fibres. Beeler and Reuter [19] created one for ventricular myocytes. More elaborate models exist [51, 52, 61, 159], but for many purposes those of the Beeler–Reuter type suffice for simulation of ventricular muscle [110, 165, 247].

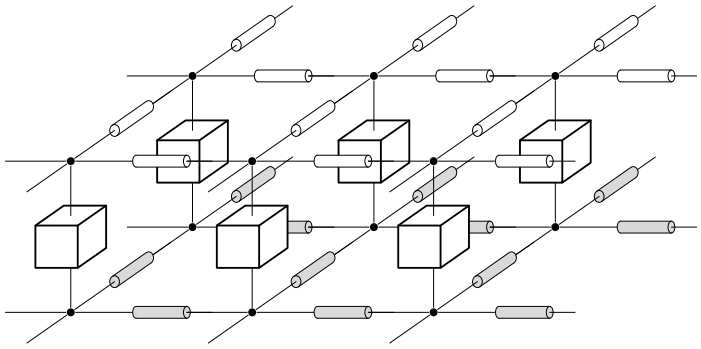

Figure 3.1: *The tissue model that is commonly used in propagation models consists of "cells" with a complicated electrical behaviour, here taken as "black boxes," connected to each other with resistances. These connections represent the intracellular conductance σ_i. The other side of the bidomain, the extracellular space or interstitium, has conductance σ_e. For computation of the activation order, the extracellular domain can be assumed to have zero resistance, i.e., $\sigma_e = \infty$.*

There are also membrane models that are not of the Hodgkin–Huxley type. Hoyt's model, for example, is an equally adequate alternative for the Hodgkin–Huxley model [101]. Models of the FitzHugh–Nagumo type are much simpler. They are intended for simulation of action potential propagation or "conduction" (section 3.3), rather than modelling of the electrical behaviour of the membrane itself [30, 75].

3.3 Propagation

The capability of cardiac cells to excite their neighbours, which leads to propagated activation, is essential for the coordinated contraction of the heart, and for the generation of measurable extracellular and body surface electrograms. Defects in this mechanism are a main cause of cardiac arrhythmias and may lead to a possibly fatal deterioration in cardiac function. For the understanding of such defects, simulation of the propagation mechanism has been used [84, 249]. In general, this is done by coupling cell models, incorporating one of the membrane models described in section 3.2, with a model of the interstitium and the electrical interface between cells. Thus, a complete tissue model is obtained (figure 3.1).

A particularly simple model was described by Van Capelle and Durrer [30]. In this model, the membrane was characterized by two functions $i_r(\phi)$ and $i_a(\phi)$ which described the voltage dependence of the transmembrane

current in the resting (maximally excitable) and active (inexcitable) states, respectively, a voltage-dependent excitability function $Y(\phi)$, a membrane capacitance C, and a time constant τ. The state of a cell was characterized by its excitability y and its membrane potential ϕ. The time-dependence was described by the equations

$$C\dot{\phi} = i_{ion} - y i_a(\phi) - (1-y) i_r(\phi) \quad (3.1)$$

$$\tau \dot{y} = Y(\phi) - y \quad (3.2)$$

Current flow between cells was limited by an adjustable resistance $R = 1/\sigma_i$. The extracellular resistance was taken zero.

In contrast to the Hodgkin–Huxley type models, the description of the membrane in terms of $i_r(\phi)$, $i_a(\phi)$, and $Y(\phi)$ was not intended to clarify the membrane gating mechanisms; rather, its purpose was to allow any desired cell type, such as infarcted cells, to be represented. The purpose of the model was to simulate propagation, assuming that the behaviour of the cells is given from experimental or theoretical data. For example, the genesis of focal arrhythmias due to injury currents could be simulated with this model [30, 116].

Maglaveras et al. employed a Beeler-Reuter membrane model, to examine the suitability of the surface Laplacian of the extracellular potential as an indicator of local activation near tissue discontinuities [165]. This is discussed in section 3.4.2. In other papers these authors describe the effect of barriers and infarction on simulated propagation [163, 166].

Propagation models without realistic modelling of the cell membrane dynamics and tissue conductance have also been described [72, 175, 261]. Many phenomena can be simulated with a model consisting of a limited number of elements, representing cardiac cells or groups of cells. The elements are finite state automata with two states: active and inactive. A larger number of states can be used to model relative refractoriness [175]. Their behaviour is characterized only by (1) an *activation delay*, the minimum interval between the activation time of an element and the time it activates its neighbours, (2) an *active time*, the maximum interval between the activation time of an element and the time it activates its neighbours, and (3) a *refractory period*, the time interval during which the element cannot be activated again. Activation delays can have fixed values, or can be computed in more complex ways. Numerous simplifications and complifications can be implemented; for example, the interval between activation of the element and its activating of other elements can be fixed, in which case the activation delay equals the active time.

Such simple models can be implemented in computer programs, but also using dedicated electronics. Therefore such models could be developed

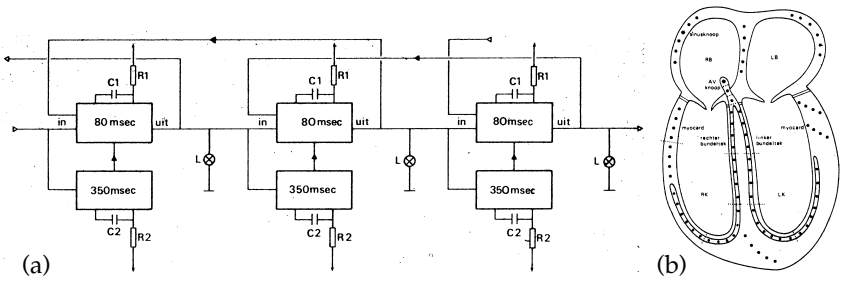

Figure 3.2: (a) *Circuit diagram of three elements of the electronic heart model described by Van der Tweel et al., reproduced from the original publication [261]. Each element consists of two timers, implementing an 80 ms activation delay, and a 350 + 80 ms refractory period, during which new activations are inhibited.* **(b)** *Overview of the model display. Each dot indicates a light, dashed lines separate groups of lights. Each group represents one element of the electronic model.*

during the nineteen-sixties and -seventies when computers were not yet common equipment. An electronic model of the entire heart, intended for demonstration and teaching purposes, was described by Van der Tweel et al. [261]. This model is illustrated in figure 3.2.

3.4 Extracellular Potentials and Activation Detection

To determine propagation of activation on a microscopic scale, measuring the transmembrane potential is very appropriate. However, for macroscopic activation mapping, i.e., mapping of areas much larger than a single cell, intracellular recordings are not practical. First, because an intracellular recording provides information on a single cell only, and the number of cells would be far too large to measure each one of them. Second, intracellular recordings are hard to obtain with conventional techniques because they require the insertion of a small and fragile glass electrode into the cell, which is difficult at least, and virtually impossible in a beating heart.

A relatively recent solution is *optical mapping* using voltage-sensitive dyes [75, 267, 277] to measure action potentials. If a video camera assesses the dye activity, thousands of "leads" are available. However, the temporal resolution of such systems is currently limited to a few hundred frames per second. This means that temporal multiplexing is required to obtain the sampling frequencies of a few kHz that are necessary for recording action

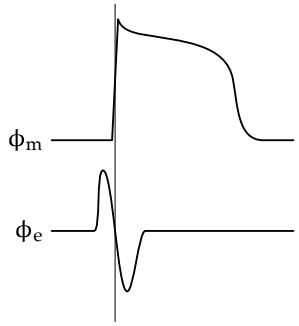

Figure 3.3: *Upper panel: stylized intracellular electrogram, representing the membrane potential ϕ_m of a healthy myocyte in normal circumstances. Lower panel: stylized unipolar extracellular electrogram ϕ_e that would be measured at a site where propagation passes, by cells with a membrane potential that behaves as in the upper panel. The instant of peak negative $\dot{\phi}_e$ corresponds to the upward slope of ϕ_m in cells directly under the extracellular electrode.*

potentials [267].

Extracellular recordings, which compare potentials at different extracellular positions, are more commonly used as an alternative for intracellular recordings. Endocardial, intramural, epicardial, and body surface leads are all examples of extracellular recordings. Propagating action potentials in intracellular recordings are accompanied by steep negative deflections in local (unipolar) extracellular recordings (figure 3.3) [115, 246, 248–250]. Such negative deflections have become the most commonly used indicator of activation passing under an electrode [4, 13].

Analysis of the extracellular electrogram is complicated because the extracellular potential is a result of activation in the entire heart. In order to understand this, we can consider the heart as consisting of two spatially coincident domains (figure 3.1). The *bidomain model* of cardiac tissue consists of the intracellular space, i.e. cell interiors and conducting links between cells (upper layer of resistors in figure 3.1), and the extracellular space (lower layer of resistors in figure 3.1). These domains are separated by the cell membrane. Potentials are measured in the extracellular space, while the intracellular domain and membrane are considered as a "black box" that injects current into the extracellular domain. This current is specified by a current density I_m. Generally, the current density varies over space; hence it is denoted $I_m(\vec{r})$. If $I_m(\vec{r})$ is given for all positions $\vec{r}$ in the

entire cardiac volume V, the potential at a point $\vec{x}$ is given by [84]

$$\phi(\vec{x}) = \frac{1}{4\pi\sigma_e} \int_V \frac{I_m(\vec{r})}{\|\vec{x} - \vec{r}\|} \, d\vec{r} \tag{3.3}$$

where the integration is over the entire cardiac volume. σ_e denotes the conductivity of the extracellular space, which must be homogeneous. The potential ϕ is defined with respect to a reference that is placed infinitely far away. In practice, either an approximation of "infinity" is used, or the difference between potentials ϕ at two locations is observed instead of the potentials themselves. From equation (3.3) it is clear that the contribution of remote tissue, represented by the injected current I_m at remote sites, to the local potential is inversely proportional to the distance. Because the amount of remote tissue is much larger than the amount of local tissue, remote tissue contributes notably to the local unipolar electrogram $\phi(t, \vec{x})$. The expression for $\phi(\vec{x})$ in case of a nonhomogeneous $\sigma_e(\vec{r})$ is much more complicated [84].

Due to the contribution of activation in tissue remote from the recording electrode, detection of local activation in unipolar electrograms can be difficult. In healthy tissue and for normal propagation, local activation generates a negative deflection that is steeper than any other part of the lead. But under less ideal circumstances, for example in (partially) infarcted tissue or when the electrode has poor contact with the tissue, a large distant source may generate a steeper deflection than a small local source [5]. A threshold for the slope can be helpful to disqualify remote activations, but it will also reject small local activations. Noise presents an additional problem: it can increase or decrease the slope of a lead and thus enhance or mask a small deflection.

Several methods to discriminate between local and remote activations were studied by different researchers. These are discussed in section 3.5. One of them uses the estimated transmembrane current; this will be discussed in section 3.4.2.

3.4.1 Unipolar versus bipolar electrograms

The potential difference between an electrode in the heart and an 'indifferent' electrode placed far away is called a unipolar potential; a signal recorded in this way is called a *unipolar electrogram*. A *bipolar electrogram* is a signal consisting of the difference of potentials measured at two closely separated electrodes. Since the position of these electrodes is almost the same, the contributions of activation in remote tissue on their potentials will be similar and therefore cancel each other in the subtraction. In contrast, unipolar signals may contain large remote components, which may

mask deflections resulting from local activation if these are relatively small, such as in surviving strands of myocardial tissue in infarcted areas. Therefore it is often easier to infer local activation from bipolar signals than from unipolar signals.

A disadvantage of bipolar leads is that the amplitude of the deflection resulting from local activation depends on the orientation of the electrode pair with respect to the activation front. If the orientation is exactly parallel to the front, activation affects the potential on both electrodes in the same way and no deflection is measured in the bipolar electrogram. Such problems do not occur with unipolar electrograms. Another disadvantage of the bipolar electrogram is that in the presence of complicated activation patterns (fractionated signals) it may be difficult to analyze. Furthermore, the cancellation of remote effects obtained by bipolar recording is not always an advantage. For example, remote components in the unipolar electrogram may help to identify the exit site of arrhythmia during endocardial catheter mapping. An overview of the advantages and disadvantages of unipolar and bipolar recording was given by De Bakker et al. [13].

3.4.2 The coaxial lead, the transmembrane current, and the surface Laplacian

An alternative way to reduce the influence of remote activity on electrograms is to subtract the potential of several neighbouring electrodes, instead of just one. De Bakker et al. used the term "coaxial lead." A sample from a coaxial lead consists of the value at the lead minus the mean of the values at its neighbours [14]. Let $\phi_{0,0}$ denote the potential at a central electrode in a square grid, $\phi_{-1,0}$ the potential at its left neighbour, etc. An implementation of the coaxial signal, using four neighbours, is

$$\gamma^{(4)}_{0,0} = \phi_{0,0} - \frac{1}{4}(\phi_{-1,0} + \phi_{1,0} + \phi_{0,-1} + \phi_{0,1}) \tag{3.4}$$

On a square grid, the coaxial signal is proportional to a second-order approximation of the *surface Laplacian* (further referred to as "Laplacian"): the second spatial derivative. The Laplacian (denoted with the squared nabla operator ∇^2) of a scalar field F, is defined as

$$\nabla^2 F = \frac{\partial^2 F}{\partial x^2} + \frac{\partial^2 F}{\partial y^2} \tag{3.5}$$

A second-order approximation of the Laplacian of a vector field ϕ in a point $(0,0)$ on a square grid is

$$\nabla^2 \phi_{0,0} \simeq \frac{1}{d^2}(\phi_{-1,0} + \phi_{1,0} + \phi_{0,-1} + \phi_{0,1} - 4\phi_{0,0}) \tag{3.6}$$

where d is the interelectrode distance. Combining (3.4) and (3.6) results in

$$\gamma^{(4)}_{o,o} \simeq -\frac{d^2}{4}\nabla^2\phi \tag{3.7}$$

Generalizing, the coaxial-lead signal can be defined as the difference between the actual signal and the signal that would be measured if the estimated Laplacian at its site were zero:

$$\gamma_{o,o} = -\frac{d^2}{4}\nabla^2\phi_{o,o} \tag{3.8}$$

The term "coaxial lead" will be used here with this interpretation. The coaxial lead is always defined for a particular interelectrode distance d. The advantage of the coaxial lead over the Laplacian itself is that it provides a potential difference, of the same order of magnitude as the original lead, rather than a combination of spatial derivatives (expressed in V/m^2). In addition, it has the same sign as the original lead. It can therefore be interpreted as a purified local lead.

It should be noted that this application of coaxial leads is rather different from the application of coaxial electrodes for Laplacian mapping at the body surface, which is advocated by some researchers as superior over potential mapping, while others demonstrated that it is technically impossible [74, 188].

Another reason for using (approximations of) the surface Laplacian is that it can be shown that it is linearly related to the local transmembrane current I_m [84, 165]:

$$I_m = -\frac{\nabla^2\phi}{\rho} \tag{3.9}$$

where ρ is the extracellular resistivity. The transmembrane current in turn is a good indicator for local activation [165]. However, for correct estimation of the Laplacian, the interelectrode distance must be smaller than the typical dimensions of the variations in the potential field, which is a fraction of a millimeter. Most grids have larger interelectrode distances. This results in erroneous values for the Laplacian. Coronel et al. showed that the Laplacian decreases with interelectrode distance 0.3, 0.6, ... 1.8 mm, but the instant of zero crossing, which is used as an estimate for the activation time, does not change [37].

In conclusion, an estimate of the surface Laplacian can be used to detect local activation. In case of large interelectrode distances, however, the term "coaxial lead" is more appropriate. Using the coaxial lead as defined in equation (3.8), a signal is obtained that can be interpreted in the same way as unipolar electrograms, but with a reduced influence of remote activation.

Several authors investigated the application of the surface Laplacian for activation detection in unipolar electrograms [165, 277, 278]; this is discussed in section 3.5.2.

3.4.3 Computation of the surface Laplacian

For a plane regular grid, relatively simple expressions for the surface Laplacian can be derived by making a two-dimensional Taylor's expansion. The second-order expansion leads to the well-known approximation given in equation (3.6) above. Bickley [21] published the expansion up to fourth order, resulting in the expression

$$\nabla^2\phi_{0,0} \simeq \frac{1}{6d^2}(4S_+ + S_\times - 20\phi_{0,0}) \tag{3.10}$$

with interelectrode distance d and

$$S_+ = \phi_{-1,0} + \phi_{1,0} + \phi_{0,-1} + \phi_{0,1} \tag{3.11}$$

$$S_\times = \phi_{-1,-1} + \phi_{-1,1} + \phi_{1,-1} + \phi_{1,1} \tag{3.12}$$

where $\phi_{i,j}$ denotes the potential at an electrode in row i and column j, counted with respect to the central electrode labelled $(0,0)$ (figure 3.4). The approximation (3.10) is more accurate than (3.6), but since it involves more electrodes it is a somewhat less "local" estimate. A method involving even more electrodes, suitable for relatively dense grids, is presented by Bickley [21]. The surface Laplacian can also be computed on an irregular grid; methods for this purpose were discussed by Huiskamp [109].

3.4.4 Measurements of the transmembrane current

Several methods have been proposed to estimate the transmembrane current using multiple closely separated electrodes [116, 165, 277]. The transmembrane current is used to study the electrical behaviour of the tissue, such as the occurrence of "injury currents" [116], in which case the value of the transmembrane current is of interest. In addition, a signal that is proportional to the transmembrane current can be used as an indicator for local activation (section 3.5).

Janse et al. [116] used the Laplacian to compute transmembrane currents of ischaemic cells. They applied equation (3.9) with an experimentally derived value of $4\,\Omega\,m$ for the tissue resistance ρ_e. For the Laplacian, they used equation (3.10). The study suggested that the DC "injury current" generated by ischaemic cells at the border zone of an area of acute infarction could be responsible for focal arrhythmias.

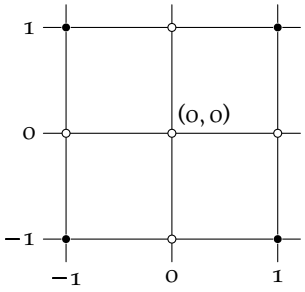

Figure 3.4: *Grid points involved in surface Laplacian computation. The central electrode is labelled* $(0,0)$*. The other electrodes used in* S_+ *(equation 3.11) are indicated with open circles. These electrodes are known as the "4-connected neigbours" of the central electrode. The electrodes used in* $S_\times$ *(equation 3.12) are indicated with solid dots. Together with the 4-connected neigbours these electrodes constitute the "8-connected neigbours" of the central electrode.*

3.4.5 The surface ECG

The surface ECG can be considered as an extracellular electrogram recorded at a relatively large distance. The large distance between the current sources in the heart and the surface electrodes has two consequences: first, the maximum potential difference between electrodes is much smaller (typically a few mV on the body surface and about 20 mV in the heart) and second, there is no electrode available that may be considered "infinitely far away" with respect to surface electrodes. Therefore, the average signal of three electrodes attached to the arms and the left leg, known as "Wilson's central terminal" (WCT), is commonly used as a reference. The surface ECG is discussed in chapters 5–8.

3.5 Activation Mapping

In section 3.4.1, the two major types of electrograms, the unipolar and the bipolar, were introduced. A disadvantage of bipolar electrograms is that they need two electrodes and thus two wires for each measuring position. This can be especially important if electrograms are recorded simultaneously from many positions. Such simultaneous multilead recordings are commonly used for activation mapping: the assessment of cardiac activation patterns. This section discusses methods of activation detection that can be used with unipolar electrograms, especially those from large, dense electrode arrays as used in activation-mapping procedures.

A moving activation front in the heart results in a deflection in an extracellular electrogram [246]. When the front moves towards the recording electrode it records a positive potential, and when the front moves away a negative potential ensues. This results in a biphasic deflection. When a front passes at a distance, roughly the same waveform is recorded, but the deflection is less steep. Since the steepness also depends on the front's size, on the depth below the surface, and on tissue properties, it can not always be decided from the steepness of a single electrogram whether local activation occurs. A deflection can only be known to be local in one place if it is known that it is not local in a different place. This can be established by recording simultaneously from many sites. The activation front at a certain instant is determined by the recording sites where electrograms show the steepest negative deflection at that instant. This is the classical method of activation mapping.

3.5.1 Single-lead criteria

Additional criteria that may be used to identify local activation are that the deflection should be steeper than a limit value, that the peak-peak amplitude of a local bipolar lead should exceed a limit value, and that they should fit in a propagating activation front [4, 6, 14].

As pointed out by Anderson et al. [4], these methods can bias the results because they use preconceptions such as the idea that a single propagating activation front should be present. These authors combine three such criteria to assign a rank to deflections in order to obtain a performance test for activation-detection algorithms. This test is applied to several candidate algorithms, using epicardial recordings obtained from humans (8×8 electrode array, 2 mm interelectrode distance, 500 Hz sampling frequency). The first derivative turned out to perform very well, if an appropriate limit value was chosen. The best separation between high-ranking and low-ranking deflections was provided by the function

$$\psi = \frac{\ddot{\phi}_3}{\phi_{40}} + c\phi_{40} \tag{3.13}$$

where c was a constant (depending on the units employed), $\phi_{40}(t = t_1)$ was the potential difference between the peak and nadir voltages within a time window $(t_1 - 40\,\text{ms}, t_1 + 40\,\text{ms})$, and $\ddot{\phi}_3$ was the peak-to-peak voltage in a ± 3 ms window of the second derivative, computed with a 5-point formula.

A drawback of locally operating functions like these is that a limit value must be chosen, and the optimal limit value depends on the recording circumstances: there are differences between the intact and the open chest,

between atrial and ventricular tissue, species, subjects, etc. Probably the constant c in (3.13) also depends on the recording circumstances.

Not only the constants, but even the selection of functions for a linear combination such as (3.13), like $\dot{\phi}$ and $\ddot{\phi}_3$, may depend on the recording circumstances. This became clear in another study by the same group [5] where epicardial recordings from human atria and ventricles were obtained simultaneously; it turned out that $\dot{\phi}$ provides the best separation between local ventricular and remote ventricular deflections, but the function

$$\nu_{40} = \frac{\dot{\phi}_{min}}{\phi_{40}} \tag{3.14}$$

performed best for local atrial and remote ventricular deflections. The authors explained the relatively poor performance of ν_{40} for ventricular locations with the relatively large contribution of remote activity to the amplitude of ventricular deflections, compared to atrial deflections, due to the thicker ventricular wall. This results in a large ϕ_{40} for ventricular deflections, and thus a smaller ν_{40}.

3.5.2 The Laplacian and the transmembrane current

In two studies, Witkowski et al. established the transmembrane current as a measure of local activation [277, 278]. Both were based on electrode grids with interelectrode spacing of about 200 µm, which approximates the length of cardiac cells.

The first study aimed at estimating the transmembrane current itself. Five-element electrode arrays on the in situ epicardium in dogs were used, and sampled at a frequency of 16 kHz. Because the electrodes were contained in an insulating plaque, and the heart was exposed, no current could flow perpendicular to the epicardium. The peak negative $d\phi/dt$ was used to find local activations; for sinus rhythm, the limit for local activation was set at $-10\,V/s$. The transmembrane current I_m was computed as proportional to the time derivative of the surface electric field magnitude $E = (E_x{}^2 + E_y{}^2)^{1/2}$, which was in turn computed from the potential differences between the electrodes; $E_x = -\partial\phi/\partial x$ and $E_y = -\partial\phi/\partial y$.

Several schemes to compute E can be used, differing in the number of electrodes required, and the position where E is computed. Three methods are illustrated in figure 3.5. The third method combines the advantages of symmetry and a small neighbourhood, and may therefore be considered optimal. A disadvantage of this method is that values of E are defined at positions between the positions where ϕ is defined, i.e. on a different grid. This can be inconvenient for software implementations.

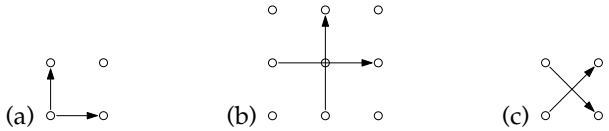

Figure 3.5: *Three schemes to compute the electric field $\vec{E}$ in a square rectangular electrode array. Dots indicate electrodes, arrows indicate which electrodes are used to compute a component of $\vec{E}$.* **(a)** *Using two neighbours; this is highly local, but the formula is asymmetric, i.e., it is not clear for which position $\vec{E}$ is computed.* **(b)** *Using four neighbours; it is now clear that $\vec{E}$ is computed at the central electrode, but the neighbourhood is much larger. This means that the data are more smoothed, and that the area where the electric field can be computed is smaller, since neighbours on all four sides are required.* **(c)** *The electric field is computed at a position between the electrodes; four neighbours are used, but the neighbourhood is as small as in panel a.*

Although theoretically the activation time derived from I_m is best predicted by the negative zero crossing of the signal, Witkowski et al. used the peak negative dI_m/dt. It is likely that these instants differ but little, especially in normal propagation. There was good agreement between activation detection by $\max(-dI_m/dt)$ and by $\max(-d\phi/dt)$. It was noted that the areas of I_m above and below zero are approximately equal for normal propagating activations.

The second study by Witkowski et al. [278] explored the possibilities of using the transmembrane current thus estimated for activation detection during ventricular fibrillation (VF). In particular the authors tested the hypothesis that the presence of a balanced inward and outward transmembrane charge could differentiate between deflections originating at sites with normal propagation, sites of origin, sites of activation block, and sites without local activity. The presence of propagating activation was tested optically, using a voltage-sensitive dye.

Maglaveras et al. used the transmembrane current I_m, which is proportional to the surface Laplacian by equation (3.9), in a model study [165]. A relatively small, two-dimensional sheet of tissue was simulated using cells with Beeler–Reuter kinetics. The purpose of the study was to investigate methods for measuring activation times at discontinuities during propagation delay in bifurcating bundles. Activation times were estimated using several methods; among these, the instant of maximum negative slope of the ion-current signal served as a gold standard. It was shown that activation times computed from the zero crossing of I_m were more accurate than

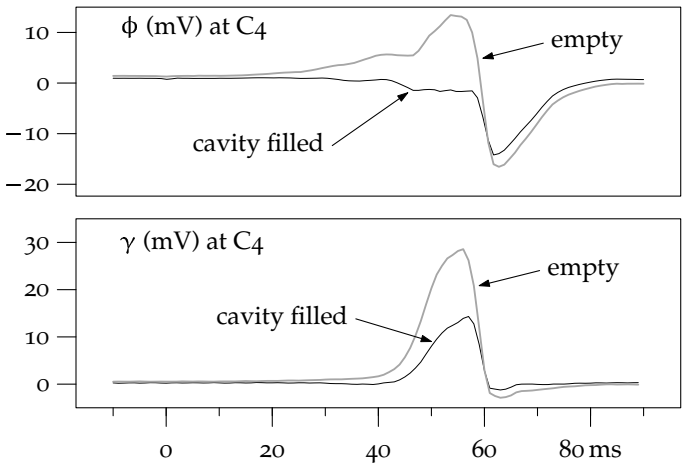

Figure 3.6: *Upper panel: two electrograms recorded during pacing at the same position in an isolated porcine heart; the black electrogram was recorded while the cavity was filled with perfusion fluid, the grey electrogram while the cavity was empty. It is hypothesized that the increased influence of remote activation caused by the high conductivity of the perfusion fluid causes the different morphologies in these leads. The Laplacian signal should be able to reduce this influence. Lower panel: the corresponding Laplacian signals. Their amplitudes are different, but the shape of the two signals and the instant of downward zero crossing, which is used to estimate the activation time, are similar.*

those generated with the maximum negative $d\phi/dt$. More specifically, the activation times estimated using I_m indicated an extended zone of slow conduction, rather than an abrupt conduction block. In addition, at some sites the activation time estimated from min $d\phi/dt$ was clearly wrong because a large remote component resulted in a steeper deflection than a small local component. This problem did not occur with the I_m-based method.

Influence of remote activity is a major problem in the analysis of unipolar electrograms from endocardial basket catheters, as discussed in chapter 4. Although not firmly established for the relatively large interelectrode distances in basket catheters, the surface Laplacian appears to be useful for the recognition of local activation in these signals [47]. An example is shown in figure 3.6.

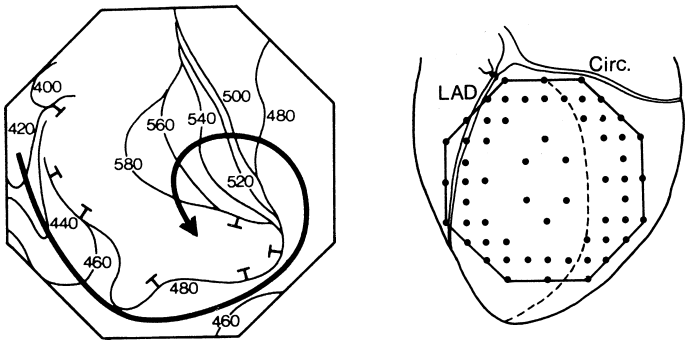

Figure 3.7: *Example of a hand-crafted isochronal map (left), reproduced from Van Capelle et al. [31], and the electrode configuration with which the activation times were measured. The line with 'T' symbols attached to it indicates a line of conduction block.*

3.6 Isochrones

Activation isochrones, commonly referred to as "isochrones," are lines that connect points of equal activation time. These maps are the common means of depicting an activation pattern. Because an isochronal map can depict only one activation time for each location, a time interval must be chosen to which the map will apply. In this interval, each signal should contain at most one local activation. Isochronal maps are sometimes annotated with arrows to indicate the major propagation paths. An example of an isochronal map is shown in figure 3.7. Isochrone mapping is a complicated process, and isochronal maps must be created with care [114]. Spatial and temporal undersampling can easily lead to incorrect conclusions. Investigators therefore sometimes decided to draw isochrones by hand, based on computer-generated tables of activation times [14]. An investigator who manually draws an isochronal map may use the drawn isochrones to change activation times that were used to create the map. This can be an advantage; for example, it may help in deciding which deflection corresponds to a local activation front. On the other hand, it allows for complicated methodology that is hard to reproduce, and allows preconceptions to have an influence on the results.

If large quantities of data have to be analyzed, and the activation pattern itself is not a subject of investigation, alternative methods can be applied. For example, to compute statistics on wave duration, a computer program may decide which activations in neighbouring electrodes correspond to the same wave and automatically identify independent waves [23]. If statistics

on conduction velocity are desired, conduction vectors can be used; this method is discussed in section 3.8.

Colour maps can also be used to display the activation pattern. They have the advantage that early and late activated sites are visible at a glance, but as it is hard to see small colour differences, only the major features of the activation pattern can be perceived. Also, colour printing is relatively expensive and cannot always be used. Therefore this method is primarily useful on computer screens and to complement isochrones, for example during interactive creation of an isochronal map. Colours alone do not allow sufficiently accurate perception of activation times.

3.7 Automatic Isochrone Drawing

When it is necessary to display an activation pattern accurately, isochrones are preferred. For efficiency and objectivity it may be desirable to have a computer program draw isochrones. In a series of three papers, Barr et al. [15–17] described a system for contour drawing of potential maps on an irregular, triangulated mesh. Contour drawing on a square grid for body surface maps was discussed by Linnenbank [154]. Contour drawing routines are a standard part of most data analysis and visualization software, such as MATLAB.

However, isochrone drawing is more difficult than ordinary contour drawing of, e.g., potential maps because zones of conduction block have to be treated in a special way. Two situations that need special care are:

- Activation times in adjacent electrodes differ to the extent that the apparent conduction velocity is lower than considered possible [10,126], which implies that they cannot be part of the same activation front. This can happen if conduction block is present and if a reentrant activation returns at the point where it started. In both cases, a standard contour algorithm would draw a set of crowding isochrones. This would inadvertently suggest the presence of very slow conduction. Instead, a line with a special style should be plotted; either a block line to indicate a total stop (the line with 'T' marks in figure 3.7), or a line that indicates the beginning and end of an interval of reentrant activation. This cannot be accomplished with standard contouring programs.

- In some electrodes, no activation occurs within the given interval. When a standard contouring program is used, such situations can be handled by treating the region of this electrode as if it was not included in the grid, i.e. making a "hole" in the grid before feeding

it to the contouring algorithm. No contours will then be drawn in this region. In case of an isochronal map, such regions would look similar to regions of very high conduction velocity, where isochrones are also at large distances from each other; the observer would have to discriminate these phenomena from the context of the entire map. Ideally, a block line or a patch with a different shade should be drawn for regions of conduction block.

Additional problems with isochrone drawing are:

- When the data from a measuring point cannot be used, for example due to broken wiring, standard contouring methods either insert a value interpolated from the neighbours (for a regular grid) or remove the point from the grid (for irregular, triangulated grids). However, in isochrone mapping, when a bad signal occurs adjacent to a zone of conduction block, it is not clear which neighbours can be used to interpolate the activation time. A choice must be made whether to interpolate from values on one side of the zone of block, or from the other side, or to consider the point as part of the zone of block.
- A conduction path may be only a single electrode wide; in this case, standard contouring programs may create contours of zero length.
- More than one activation detected at the same electrode in the predetermined time interval cannot be displayed using isochrones.

A specialized program is thus necessary; however, to a large extent it can use existing algorithms. An experimental program for this purpose, called "isomap," was developed as part of the MATLAB software [207,208] (chapter 10). This program can handle lines of conduction block (figures 3.8 and 3.9) and reentrant activation (figure 3.10) correctly. It can work on surfaces in 3-D as well as in 2-D, and with both triangulated and rectangular grids. In its current implementation it decomposes rectangles into triangles, so that only an algorithm for contour drawing on a triangulated grid is needed. Output of this program is shown in figures 3.8, 3.9, and 3.10.

An important feature of the isomap program is that it can automatically indicate lines of conduction block: if the activation-time difference between neigbouring electrodes is so large that the apparent conduction velocity is below a user-specified limit, the program assumes conduction block between these electrodes, and will indicate this with a special line style. Ordinary isochrones are not drawn in such regions. Since isomap can handle a typical activation map in a few milliseconds, the software operates fast enough to allow experimentation with limit values (figure 3.8) in an interactive way.

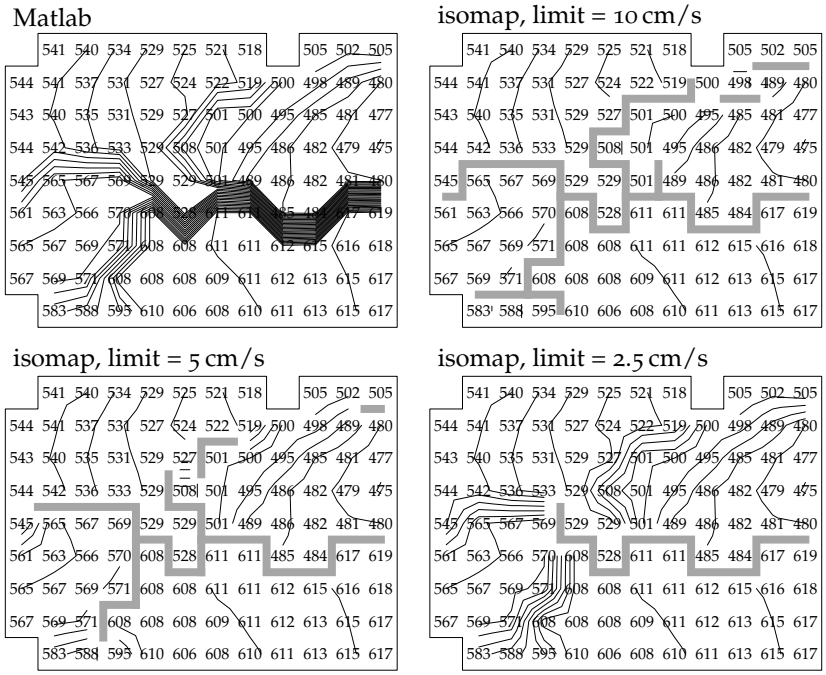

Figure 3.8: *Activation maps featuring a line of block [80] drawn with isochrones using the general contour function from Matlab (top left), and using the specialized isomap program. The latter can automatically indicate conduction block based on a minimal conduction velocity as discussed in the text, and will not draw normal isochrones between electrodes where conduction block is thus detected. In this figure, block lines are rendered thick and grey. By varying the limit value, an operator can easily see the effect of different assumptions on the isochronal map. In most circumstances, conduction cannot be slower than 10 cm/s [10, 126]. Using this as a limit value, the map in the upper right panel results. If so-called "very slow conduction" is expected, conduction can be as slow as 5 cm/s [126]. The map based on this assumption is shown in the lower left panel. If even slower conduction would be deemed possible, for example 2.5 cm/s, the map in the lower right panel would result. In all maps, activation times are indicated in milliseconds and isochrones are drawn at 5 ms intervals. Timings are relative to a pacing spike that occurs earlier in the recording. Inter-electrode spacing was 0.1 cm [80].*

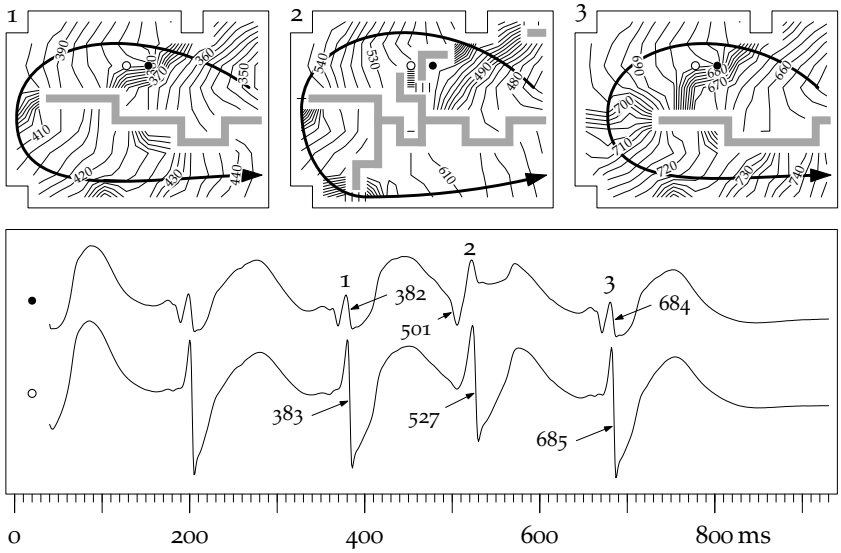

Figure 3.9: *Three subsequent beats from the same recording; the middle one is also shown in figure 3.8. The activation patterns of these beats are different due to lines of functional block or "extremely slow conduction." The conduction-velocity limit was set at 5 cm/s, which is equivalent to 20 ms delay between electrodes (interelectrode distance 1 mm) [80]. Isochrones are drawn at 2 ms intervals. In the lower panel, electrograms are shown that were recorded at two electrode positions, which are indicated in the maps (an open circle and a dot, respectively). The deflections corresponding to the three maps are labelled 1, 2, and 3. The instants of peak negative* dV/dt *which were used for the maps are indicated with arrows in the electrograms. The second deflection is very slow in the upper trace; it corresponds to transient block (additional block line between the two indicated recording sites in the second map) or to extremely slow conduction.*

Provided with adequate software, computers are highly useful for the creation and inspection of large numbers of activation maps. It should be noted, however, that the clarity of hand-crafted maps (figure 3.7) is unsurpassed by computer programs—at least by the programs presented here. On the other hand, the process by which this clarity is obtained involves assumptions on the activation process that are not made explicit. It is therefore subjective, and the resulting maps are sometimes debatable.

A good compromise between efficiency and reliability is presented by computer programs that incorporate all possible clarifications that are not

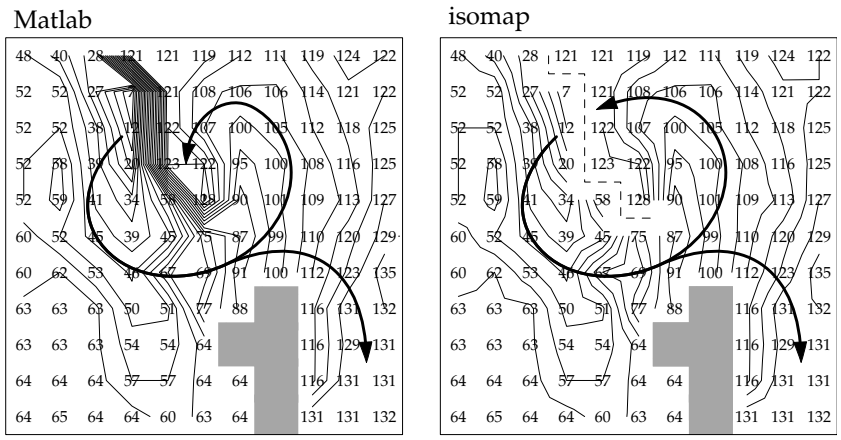

Figure 3.10: *Handling of reentry by the isomap program. These maps represent a circulating activation pattern [82]. The operator has chosen the time window where activations are detected such that all electrodes show one activation. If an ordinary contour algorithm is used, isochrone crowding occurs in the area where the activation front is at the begin and end of this window. This looks very similar to activation block, as in figure 3.8. Using the isomap program it is possible to draw a single contour in a special style instead, such as the dashed line used here. The grey area indicates a zone of activation block. Isochrones are drawn at 5 ms intervals.*

debatable. Isomap was created for this purpose. By letting the user specify isochrone levels, it allows the right number of isochrones for a given situation to be drawn. By letting the user state explicitly which delay signifies conduction block, it allows the creation of block lines in an objective and reproducible way.

One reason for the poorer esthetic quality of computer-generated maps, with respect to hand-crafted maps, are the limitations of software packages used. Limitations in MATLAB, for example, make it desirable to edit graphical output from the MAPLAB package (which is implemented in MATLAB; see chapter 10) with specialized graphics software when it is to be used for publication. The isochronal maps presented here (figures 3.8, 3.9, 3.10, and 3.11) were rendered by a script written in the MetaPost graphics language [91], using data generated by MAPLAB routines.

Another reason for the poorer esthetic quality of computer-generated maps is that hand-drawn isochrones are often drawn smoothly, which gives a clear impression, while programmers of contour algorithms are reluct-

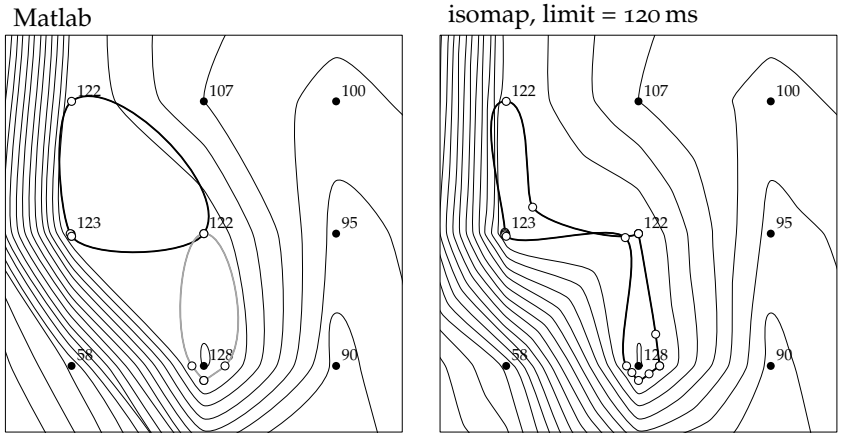

Figure 3.11: *Illustration of problems due to smooth contour drawing with splines. A magnified part of the activation map shown in figure 3.10, with isochrones drawn as B-splines [91]. Results are shown here for the Matlab contour algorithm, and for the isomap program. For the 122 ms isochrone in this region, both algorithms return control points that, when rendered with splines, yield curves that intersect other isochrones. The Matlab routine returns two contours, drawn (left panel) with a thick black and a thick grey line. Control points are shown with small circles. In order to show isomap's solution (right panel), the block-limit value was set at a very high value; otherwise the problematic region would have been crossed by a block line, as in figure 3.10. Isomap returns one contour for the 122 ms level instead of two, and more control points.*

ant to implement smoothing, for several reasons: First, smoothing implies interpolation, which is not always valid in activation maps, and requires the choice of an interpolation method, which in turn implies assumptions about the data. Second, smooth lines suggest a higher resolution than is actually available. Third, it is difficult if not impossible to guarantee that no artifacts like crossing isochrones occur. Control points generated by standard contour algorithms are usually intended for straight-line drawing; rendering them with splines instead may give reasonable results in many cases, but errors may result if the splines are not tense enough, as shown in figure 3.11.

3.8 Conduction Vectors

Isochronal maps give a good indication of the pattern of activation, but it is difficult to determine the conduction velocity from them. As an alternative, conduction vectors may be computed. If the activation time is considered as a scalar field T, the conduction vector (CV) $\vec{v}$ can be defined as the vector with the direction of the gradient of T, and as magnitude the estimated local velocity of the activation front:

$$\vec{v} = v \cdot \hat{n} = \begin{pmatrix} (\partial T/\partial x)/s^2 \\ (\partial T/\partial y)/s^2 \end{pmatrix} = \begin{pmatrix} dx/dT \\ dy/dT \end{pmatrix} \tag{3.15}$$

with s the inverse velocity, or *slowness*,

$$s^2 = (\partial T/\partial x)^2 + (\partial T/\partial y)^2 \tag{3.16}$$

The partial derivatives of T may be estimated using finite differences [227], or by fitting a first-order or second-order polynomial surface [18, 177, 267]. The choice for either method, and the order of the surface, depends on the number of neighbouring electrodes that are sufficiently close and take part in the same activation wave.

An example of a conduction-vector map and the corresponding isochronal map are shown in figure 3.12.

The conduction velocities in this map were computed at positions in the middle of four grid points, as in figure 3.5, panel c (page 58). A problem with conduction vectors is that they are sensitive to temporal undersampling: discretization of activation-time differences may then lead to very long conduction vectors in areas of fast conduction. This problem occurs at several positions in figure 3.12. A solution would be to average over several beats with the same pattern or to compute velocities using more grid points.

Provided that the temporal resolution is high enough, a conduction-vector map can be used to depict the local conduction velocities for a specific activation pattern. Also, velocities can be averaged over an area to obtain an indication of overall conduction velocity, which is useful for assessment of the effects of drugs or genetic disorders [177, 220].

3.9 Conclusion

Computer programs are useful for the analysis of activation maps, primarily for three reasons. First, they can perform tasks that are dull and/or time consuming for human investigators, such as the detection of the steepest deflection in an electrogram and the creation of large series of activation

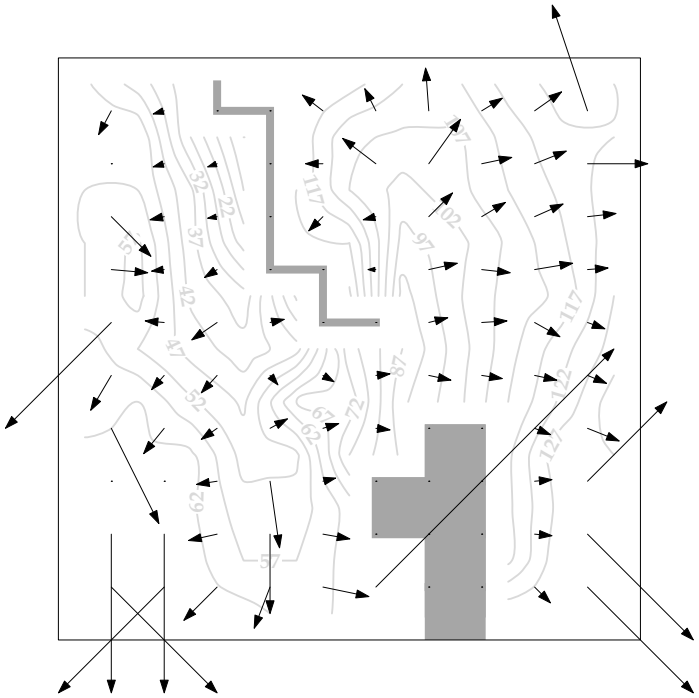

Figure 3.12: *Conduction-vector map, superposed on the isochronal map of the same activation-time data (the same as in figure 3.10; in this case drawn with splines). The spatial derivatives of the* T *field were computed at each point in the middle of four electrode positions using symmetric first-order derivatives (figure 3.5c). The vector was not drawn if the time difference between two electrodes in a set of four exceeded 40 ms. Artifacts, i.e. very long arrows, occur in regions where the measured activation times are the same at several electrodes; this may happen in regions with very high conduction velocity, at colliding wave fronts, near lines of block, and if activation moves in the vertical direction, i.e. perpendicular to the electrode plane.*

maps. Second, they can perform mathematically defined signal processing tasks, such as the computation of Laplacian signals, in order to assist investigators in the analysis of electrograms. Finally, implementation in a computer program of analysis tasks that can also be performed by humans can help to make assumptions, which are necessary in the analysis of activation maps, more explicit. The isomap program fulfills the latter goal, as it can show quickly what the results of different values of the minimal conduction velocity are for the interpretation of an activation map.

Chapter 4

Properties of Unipolar Electrograms Recorded With a Basket Catheter

Unipolar electrograms obtained from a basket catheter in the blood-filled cavity differ from those obtained by endocardial balloons during antiarrhythmic surgery. We investigated these differences using basket catheter recordings obtained from isolated porcine and canine hearts which could be filled with perfusion fluid and evacuated at will. The results indicated that the differences between basket and balloon recordings are largely attributable to the presence and absence of blood. Activation maps obtained in the presence and absence of blood were usually similar and only differed in a minority of cases at sites where electrograms revealed multiple deflections. — Submitted for publication [204].

4.1 Introduction

Multielectrode "basket" catheters allow the simultaneous recording of up to 64 unipolar endocardial electrograms. Basket catheters have been used in animals [63, 78, 117], human atria [221], and the human left ventricle [229], and are applied in patients to analyze a tachycardia circuit prior to ablation [78]. Our group has used the Constellation™ Basket catheter (Boston Scientific Inc., Natick, MA, USA) with 64 unipolar leads in combination with body surface mapping, e.g. to study the arrhythmogenic substrate and exit-site localization of postinfarction ventricular tachycardia (VT) [48]. The study revealed that electrograms obtained with the basket catheter

differed from those obtained with other recording techniques, most notably by showing relatively slow deflections and a low incidence of R waves. These differences were not apparent in earlier reports on basket catheter applications, where bipolar recordings were used [63, 78, 117, 221, 229].

A modality that lends itself for comparison is the endocardial balloon, which has been used during antiarrhythmic surgery [7, 8]. Basket and balloon recordings made by our group are comparable in the sense that they both have 64 unipolar leads and a similar interelectrode distance.

This study was aimed at characterizing the quantitative differences between electrograms recorded with basket catheters, with endocardial balloons, and with conventional catheters, in order to detect possible sources of error when using the basket catheter for diagnosis.

It was expected that the presence of blood would be a major cause of differences between electrograms recorded with the endocardial balloon and the basket catheter. Therefore, we recorded electrograms with the basket in the left ventricle of isolated canine and porcine hearts, where the ventricle could be filled with perfusion fluid and evacuated at will. This allowed us to record electrograms in both absence and presence of fluid in otherwise comparable circumstances.

The differences between the empty and filled cavity found in these experiments are compared to differences between balloon recordings and basket recordings in patients, in order to estimate the applicability of the results to human electrograms.

4.2 Methods

Endocardial electrograms were recorded in unipolar mode in patients and in isolated animal hearts, using a total of three modalities: the endocardial balloon [7, 8], the basket catheter, and conventional mapping catheters. The endocardial balloon was only used in patients, because the available balloons were too large for the animal hearts. Measurements with the basket catheter were made in both patients and isolated canine and porcine hearts. Since the recording system used for standard mapping catheter recordings in patients did not allow digital export of data, we could not use these data for quantitative analysis. Therefore, only mapping catheter data obtained from isolated animal hearts were analysed.

It was shown previously that activation times correspond with the instant of maximum negative dV/dt in the local unipolar electrogram [5, 248]. Since activation detection is an important application of endocardial mapping, we studied $\max(-dV/dt)$ values in the electrograms. Using the notation $D \equiv dV/dt$ we denote $\max(-dV/dt)$ as D_{min}. In addition, R-wave

peak amplitudes and total QRS amplitudes were studied. Analysis was performed using our own MAP_LAB software [207, 208] (chapter 10) and custom software written in MATLAB (The MathWorks Inc., Natick MA, USA).

4.2.1 Patient data

In five patients, both endocardial balloon and basket catheter recordings were obtained (not simultaneously).

Balloon recordings were made during antiarrhythmic surgery [9]. Signals were band-pass filtered (3 dB points 0.16 and 400 Hz), and digitized at a frequency of 1 kHz with 2 µV resolution and a range of 16 bits. Sixty-four channel recordings of 1.5 s duration were made during endocardial pacing. A total of 316 paced complexes was analyzed. We limited the study to paced beats because we wanted to assess the influence of the activation order, particularly in the animal data, which requires pacing, and paced beats cannot easily be compared with spontaneous beats.

Recordings with the basket catheter were made during preoperative electrophysiologic study. Pacing was attempted at all basket electrodes; paced beats were recorded while pacing with a current strength just above threshold. Simultaneous recordings from 61 basket leads and 64 body surface leads were made continuously during the procedure. The surface leads were used in this study for QRS detection, and were used in other studies. Signals were band-pass filtered (3 dB points 0.16 and 400 Hz) and digitized at a frequency of 2 kHz with 2 µV resolution and a range of 16 bits. For each pacing electrode where capture was obtained, at most nine complexes were analyzed (eight complexes on average).

Automated analysis of basket data The basket recordings obtained from patients were analyzed automatically. Techniques for automatic QRS detection and baseline correction described in chapter 6 were used for this purpose. This approach made it possible to analyze vast amounts of data with relatively little effort. Typically nine beats were analyzed for each of the 64 pacing electrodes while these paced beats had to be located first within a number of recordings, each of several minutes length—a task that would have been rather tedious to perform manually.

4.2.2 Animal data

Endocardial electrograms were recorded with the basket in one canine heart and two porcine hearts in Langendorff setups [171]. Because the aorta was cannulated, the basket catheter was inserted into the left ventricle through the mitral valve ring, after removal of the left atrium. The ventricle was

filled with perfusion fluid (50 % blood 50 % Tyrode's mixture), allowing the recording of electrograms in the presence and absence of blood but otherwise equal conditions. The filled cavity was emptied by opening a canula which was located in the LV apex. Recordings were made while the heart was paced either at the right atrium, at the LV apex, or at the LV base. In the porcine hearts, a standard 7 F endocardial catheter was inserted between the splines of the basket.

Signals were band-pass filtered (3 dB points 0.16 and 800 Hz) and digitized at a frequency of 1 kHz with 2 µV resolution and a range of 16 bits.

4.2.3 Analysis

Values of D_{min}, peak-to-peak amplitudes of the QRS complex, and R-peak amplitudes were compared between balloon and basket recordings in patients. In animal hearts, additionally values of D_{min}, peak-to-peak amplitudes of the QRS complex, R-peak amplitudes, and activation times were compared between the empty and filled cavity.

The S-peak amplitude V_S was defined as the most negative potential occurring in the QRS complex. The R-peak amplitude V_R was defined as the highest potential occurring between QRS onset and the S-peak. In leads with a relatively early and initially negative deflection, V_R could be slightly negative. Total (peak-to-peak) QRS amplitude was defined as $V_R - V_S$.

4.3 Results

4.3.1 Maximum slope values and slope ratio

Values of D_{min} for the three different recording techniques are shown in figure 4.1. The values recorded in isolated animal hearts were larger than those recorded in in-situ patient hearts. However, there was a consistent difference between values obtained in the filled and empty cavity in all subjects, and for all pacing positions in isolated hearts.

There was considerable variability in values between electrodes, and between pacing positions. Therefore, the ratio of values in filled and empty cavities should in principle be compared on a per-electrode basis. We computed this ratio for each electrode in the porcine heart and determined the median, R_1 (table 4.1).

This ratio can not be used to compare animal data with patient data and to compare balloon with basket recordings because there are no corresponding electrode positions. Therefore, we also computed a ratio R_2, defined as the ratio of the median D_{min} value over all electrodes in the filled cavity and the median D_{min} value over all electrodes in the empty

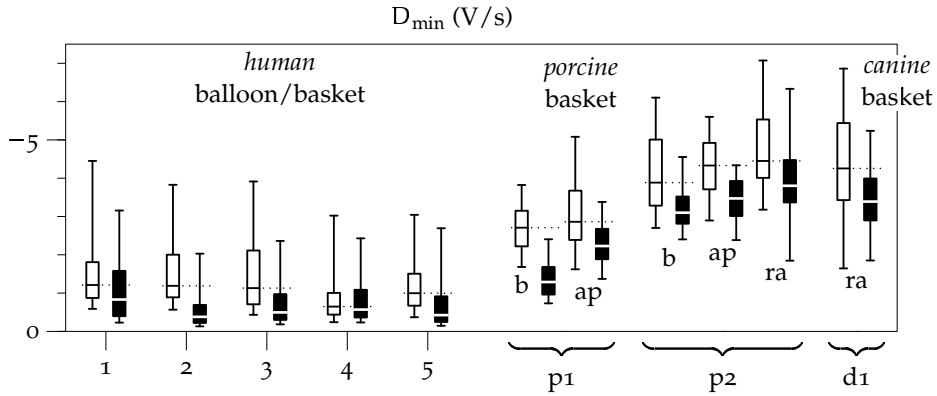

Figure 4.1: *Percentile graphs of* dV/dt *values, specified in V/s. The vertical axis is reversed because the values are negative. The central horizontal line in each box represents the median value, i.e. the 50th percentile; the ends of each box indicate the 30th and 70th percentiles. The T-shaped lines indicate the 10th and 90th percentiles. To facilitate comparison, the median levels of all 'empty' sets are indicated with dotted lines. Patients are labelled 1–5, porcine hearts p1 and p2, the canine heart d1. For animal hearts, data are presented separately for apical (ap), basal (b), and right atrial (ra) pacing; comparing basket recordings in the empty and filled cavity. For patients, basket and balloon data are compared. In all data sets, black boxes indicate a filled cavity and open boxes indicate an empty cavity.*

cavity (table 4.1). Because the animal experiments showed that both ratios are similar, we used ratio R_2 to compute slope attenuation in patients (comparing balloon and basket recordings), and to compare it with slope attenuation in isolated animal hearts (computed by comparing basket recordings in an empty and filled cavity).

4.3.2 R-peak and total QRS amplitude

In figure 4.2, R-peak amplitudes and total (peak-to-peak) QRS amplitudes are shown for all recordings in both patients and isolated animal hearts. In patients, the median R-peak amplitude was 3.6–5.8 mV in balloon recordings and 0.0–1.4 mV in basket recordings. In the isolated animal hearts, mostly low-amplitude R waves were present even when the cavity was empty. Filling of the cavity yielded either disappearance or attenuation of the R waves by 0–3 mV.

Median total QRS amplitude was 7–15 mV (mean 11.4 mV) in balloon recordings and 4–7 mV (mean 5.0 mV) in basket recordings in patients. In isolated animal hearts, median total QRS amplitude depended on the pacing site; the mean reduction factor (R_1) was 0.71 on average.

Table 4.1: *Ratios R_1 and R_2 (see section 4.3.1), for D_{min}, R-peak amplitude, and total QRS amplitude. In isolated animal hearts, ratios were computed from comparable measurements in the empty and filled cavity. In patients, R_2 was computed from the averages of the medians of all balloon and basket recordings.*

subject	D_{min}		*R-peak ampl.*		*QRS ampl.*	
	R_1	R_2	R_1	R_2	R_1	R_2
1	n.a.	0.69	n.a.	0.26	n.a.	0.56
2	n.a.	0.32	n.a.	0.01	n.a.	0.35
3	n.a.	0.44	n.a.	0.02	n.a.	0.49
4	n.a.	0.88	n.a.	0.00	n.a.	0.79
5	n.a.	0.43	n.a.	0.04	n.a.	0.44
pig 1	0.67 ± 0.19	0.66	0.43 ± 0.29	0.34	0.71 ± 0.07	0.71
pig 2	0.75 ± 0.14	0.75	0.72 ± 0.22	0.70	0.83 ± 0.07	0.83

For a quantitative comparison of patient data and animal data, the ratios R_1 and R_2 for the R-peak amplitude and QRS amplitude are given in table 4.1.

The activation order, which was varied by changing the pacing site (figure 4.3), had an influence on both R-peak amplitude and total QRS amplitude, as shown for a subset of leads in figure 4.4. The magnitude of these differences was comparable to that resulting from the presence or absence of perfusion fluid in the cavity.

4.3.3 QRS morphology in isolated hearts

In the isolated porcine hearts, pacing was performed at three positions: apical, basal, and right atrial. For each of the three pacing positions, recordings were made with empty and filled cavities. Electrograms were compared between pacing positions and the presence or absence of perfusion fluid; time alignment was based on the pacing spike. Complexes recorded with an identical pacing position and cavity filling resembled each other well in morphology, dV/dt, and amplitudes. These features were all reproducible after repeated cavity filling and draining. Clear differences were present between complexes recorded in different situations: both the activation order and the filling of the cavity yielded changes in the shape of the electrograms. Results for a subset of leads are shown in figure 4.4.

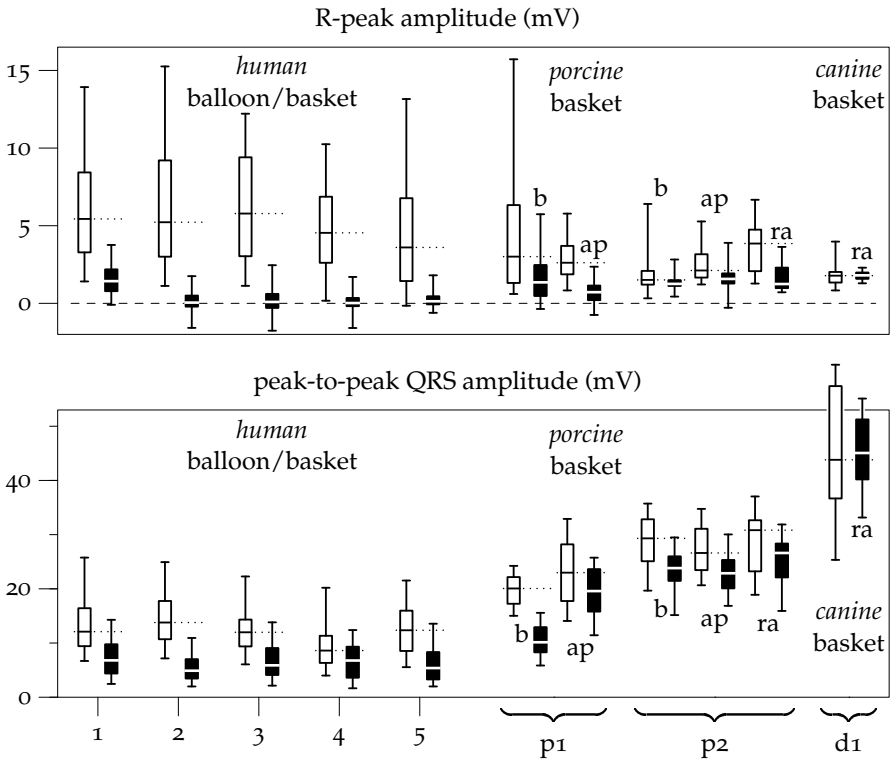

Figure 4.2: *R-peak and total QRS amplitude, both in mV. Labels are the same as in figure 4.1. In all data sets, black boxes indicate a filled cavity while open boxes indicate an empty cavity. In the animal hearts, R peaks are always smaller in the filled cavity, as compared to the same pacing position in the empty cavity. Relatively large R peaks are observed in p1 for basal pacing (especially at late activated sites, as can be seen in figure 4.4); these peaks are attenuated when the cavity is filled. Slightly negative R peak values are sometimes observed (see section 4.2.3). Total QRS amplitude is also consistently reduced by cavity filling. It is larger in isolated porcine hearts than in in-situ human hearts, and even larger in the canine heart.*

Electrograms recorded with a conventional mapping catheter, which was inserted between the splines of the basket, did not differ substantially from those recorded at the surrounding basket electrodes. An example is shown in figure 4.5.

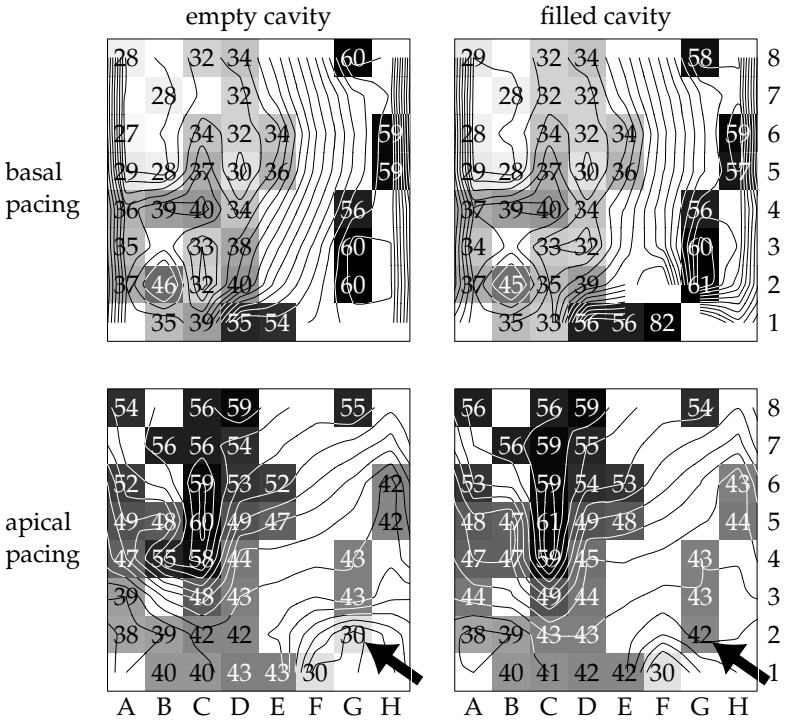

Figure 4.3: *Examples of activation maps obtained from a porcine heart (p1) with basal (upper panels) and apical pacing (lower panels), in the empty cavity (left panels) and in the blood-filled cavity (right panels). The base of the ventricle is located just above the mapped region, near row 8; the apex is located below row 1. Each basket spline is represented by a column of the map, labelled A–H. Splines A and H are adjacent and located at the septal wall. Splines B and C are located anteriorly; D and E laterally; F and G posteriorly. Basal pacing was performed near spline A and apical pacing near spline G. Activation times are given in milliseconds with respect to the pacing spike. No activation time is printed at sites where it could not be determined due to broken wiring of the basket catheter. Isochrones are drawn at 2 ms intervals. The electrode naming scheme is indicated at the sides of the activation maps. Most activation times differ little between recordings obtained either in an emtpy or filled cavity. An exception is electrode G2 (arrows); this is explained in figure 4.7.*

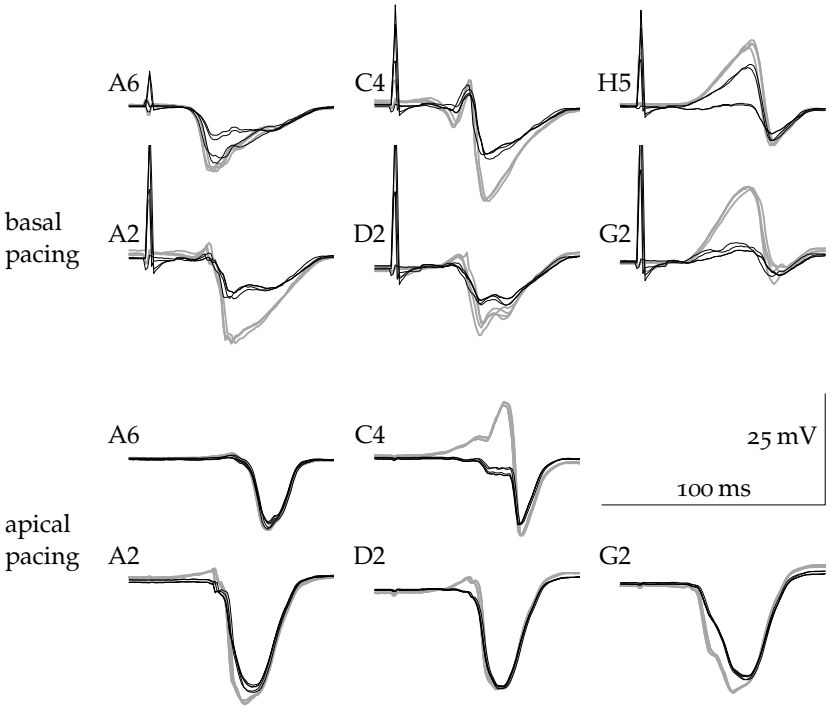

Figure 4.4: *Selected electrograms obtained from a porcine heart (p1) with basal (upper panel) and apical pacing (lower panel). The corresponding activation maps are shown in figure 4.3. To show both the differences between the empty and filled cavity and the variability in each situation, electrograms of several complexes are superimposed, using the pacing spike for alignment. Grey lines represent complexes recorded in the empty ventricle; black lines complexes recorded in the filled ventricle. Unusual variability is observed in the electrograms recorded in the filled cavity in leads A6 and H5 with basal pacing. This is probably due to incomplete filling, as it is only observed in basal leads. During basal pacing, large R peaks (up to 15 mV) are observed at sites with the latest activation times in the empty cavity (G2, H5); in the presence of perfusion fluid these R peaks almost disappear. During apical pacing, R peaks are much smaller in most leads; a notable exception is lead C4. Complete statistics are given in table 4.1.*

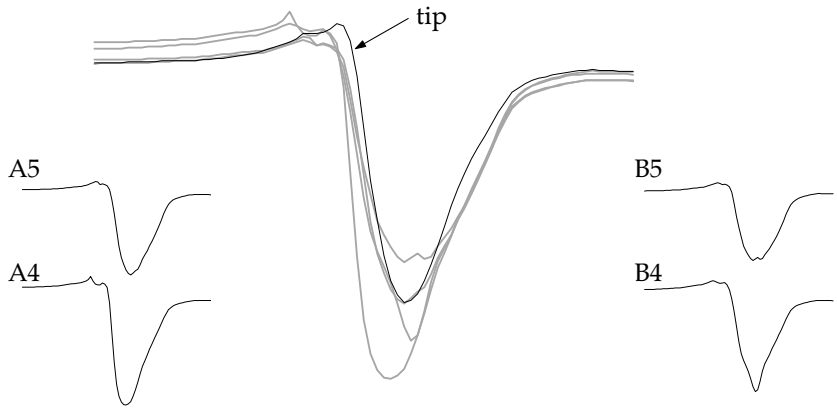

Figure 4.5: *Example electrogram recorded from the tip electrode of a standard 7 F mapping catheter (tip), inserted between the splines of the basket in an isolated porcine heart (p1). Electrograms from surrounding basket electrodes (A4,A5,B4,B5) are plotted for comparison; with grey lines and superimposed on the tip lead signal, and in scaled-down versions adjacent to it. The electrograms were recorded at mid-wall positions (see for example the activation map in figure 4.4) during apical pacing in the filled cavity.*

4.3.4 Activation times in isolated hearts

In the recordings made during apical stimulation in one of the isolated porcine hearts (p1), activation times were compared between empty and filled cavity. Statistically significant ($p < 0.05$) differences in estimated activation times were found in 8 of 40 leads (figure 4.6 (a)). The most pronounced difference, 12 ms, occurred in lead G2 (arrows in figure 4.3; figure 4.7). This was caused by a double deflection where the presence of blood decreased the slope of the first deflection, which was the steeper in the empty cavity. Filling of the cavity did not influence the slope of the second deflection, so that the second deflection became slightly steeper than the first. A similar effect yielded an activation-time difference of 8 ms in lead B4 in the same recordings (see the activation maps in figure 4.3). Other differences in activation times were in the order of 2–4 ms, and appeared to be due to a continuous shift in the timing of the deflection (figure 4.6 (a)).

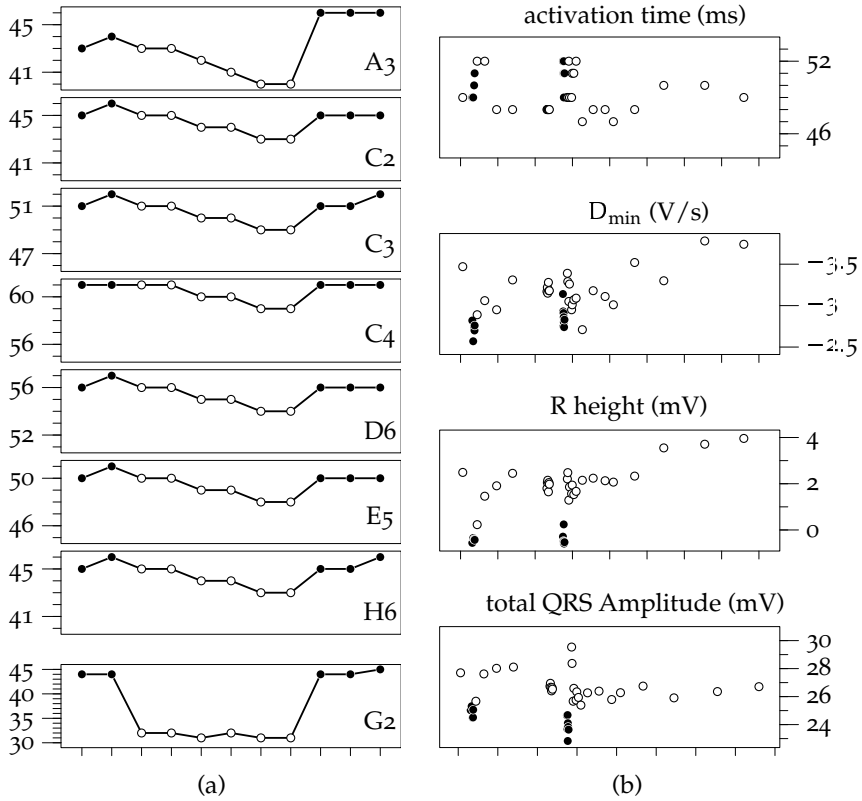

Figure 4.6: *Time dependence of the effects of cavity filling on electrograms.* **(a)** *Activation times of selected leads, obtained by a basket catheter in an isolated porcine heart (p1; see also the lower panel of figure 4.4) are shown. Tick marks on the horizontal scale of each plot indicate the recording number; approximately 30 seconds elapsed between recordings. The lead names shown in the bottom right corner of the plots are the same as in figures 4.3 and 4.4. The recording sequence begins with two recordings in the filled cavity (solid circles), followed by 6 recordings in the empty cavity (open circles), and another three recordings in the filled cavity. For most leads, a linear trend is visible when the cavity is drying. In lead G2 (figure 4.7), the change in the estimated activation time is due to a discontinuous effect, and occurs immediately when the blood is removed.* **(b)** *Effect of presence of fluid on activation time, D_{min}, R-wave amplitude, and total QRS amplitude, in lead E2 in a porcine heart (p2), while pacing apically. Each complex is represented with a solid dot (filled cavity) or an open circle (empty cavity). Tick marks on the horizontal axis represent intervals of 100 seconds. The cavity was filled for two periods of approximately three seconds each. In this lead, effects of presence of fluid lasted over 100 s in D_{min} and R-wave amplitude.*

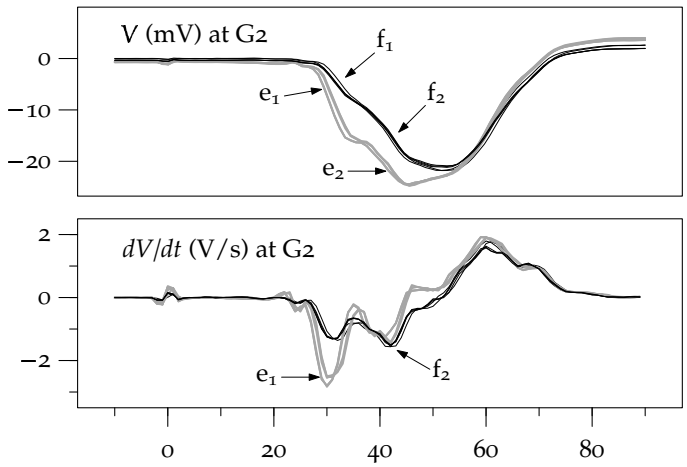

Figure 4.7: *Electrogram from lead G2 (upper panel) and its first derivative (lower panel) in a porcine heart (p1, the same as in the lower panel of figure 4.4). A total of 11 complexes is superimposed. Five complexes were recorded in the blood-filled ventricle (black lines) and six in the empty ventricle (grey lines), all during apical pacing. In the electrograms recorded in the empty cavity, the first deflection (labelled e_1) was steeper than the second (e_2). In the filled cavity, the first deflection was attenuated more than the second. Therefore, in the filled cavity, the second deflection (f_2) was steeper than the first (f_1). Consequently, in the filled cavity the local activation time was estimated 12 ms later than in the empty cavity. The corresponding activation maps are shown in figure 4.3.*

4.4 Discussion

4.4.1 QRS morphology and amplitude

Unipolar endocardial electrograms obtained during activation of healthy myocardial tissue consist of either a positive and a negative deflection (a "RS wave"), or a single positive deflection ("R wave"), or a single negative deflection (a "QS wave"). Particularly in diseased tissue, more complex configurations may occur ("fractionation"). Initial positive deflections are associated with an approaching wavefront. QS waves are associated with sites from which the activation only moves away, i.e. mainly early activation sites.

In a set of recordings made in unipolar mode with a 64-channel basket catheter in patients, we observed almost exclusively QS waves even at sites far from the pacing site.

Initial negativity in the electrogram was shown by Zimmerman and Hellerstein to be a characteristic of the cavity potential, which is entirely negative in the left ventricle [284]. Durrer and Van der Tweel, who recorded electrograms with multi-electrode needles in the intact in-situ heart, reported that R waves occur only in epicardial and subepicardial layers; cavity leads (recorded from the distal electrodes of the epicardially inserted needles) featured slow symmetric QS complexes [58, 59]. In a computer model study, Geselowitz et al. reported large differences in both R-wave and S-wave amplitude between endocardially and intramurally obtained electrograms, even at a very small depth (50 µm) [73]. In a study with an intracavitary probe, Liu et al. presented examples of cavity potentials in an isolated blood-filled canine heart [156]. These recordings also featured small or absent R waves.

In this study, we observed a profound difference in R-wave amplitude between electrograms recorded with the balloon (empty cavity) and the basket (filled cavity) in patients, and hypothesized that this is due to the greater influence of remote tissue through the cavity potential when blood is present in the cavity.

To test this hypothesis we made recordings in isolated animal hearts which could be filled with perfusion fluid and evacuated at will. Few R waves were present in any of the basket recordings in the isolated hearts, in both empty and filled cavity. Filling of the cavity yielded disappearance of the R wave in some cases, and attenuation of the R wave in other cases. In many leads, attenuation of the S wave was observed after filling of the cavity.

We observed in individual leads that the presence of blood in isolated animal hearts caused attenuation of the electrograms and decrease of D_{min}, with approximately a factor 0.7 (median over all leads; R_1 in table 4.1). Using a ratio of median values in the empty and filled cavity, these data can be compared to the patient data (R_2, table 4.1). The average ratio found after comparison of balloon and basket recordings in patients, which ranged from 0.32 to 0.88, was comparable to that found in animals (0.66 and 0.75, respectively).

We conclude that the differences between balloon and basket recordings are largely due to the presence of blood in the cavity during basket recordings. Another possible source of differences is the electrode geometry and wall contact. The basket splines are thin and are not pressed against the wall as adequately as the balloon electrodes or the tip electrode of a conventional catheter. In addition, wall contact is reduced because the basket electrodes do not project from the basket splines like the electrodes of the endocardial balloon do. Lastly, trabeculae may prevent splines from making proper contact with the endocardium at all electrode positions. We in-

serted a conventional catheter between the basket leads for a limited number of measurements. An example is shown in figure 4.5. In all cases, the signal from the catheter was similar to the signals from surrounding basket leads, although the negative wave in the catheter tip signal in figure 4.5 is slightly narrower than that in the surrounding basket leads.

The differences in amplitude of QRS complexes between the empty and the filled cavity are similar to the results of Geselowitz et al. [73], who observed profound differences between dry tissue and tissue in a layer of fluid using computer model studies. Interestingly, these authors reported that even a very thin layer of fluid (50 µm) can have the effect of diminishing the amplitude by approximately a factor 2. This could explain the slow effect of draining the cavity in our experiments (figure 4.6 (b)), because the withdrawing of most of the perfusion fluid may take a few minutes.

4.4.2 Differences in estimated activation times

Activation times estimated as the instant of D_{min} in a unipolar electrogram were mildly affected by the presence of blood. In our experiments, no significant difference was observed in the majority of leads. Usually, differences were in the order of a few milliseconds, but values up to 12 ms were observed in fractionated electrograms (figure 4.7).

4.4.3 Implications

Mapping catheters usually have a ring-shaped electrode proximal to the tip electrode, making it possible to record both unipolar and bipolar electrograms. Ambiguities in the unipolar electrogram can therefore be resolved by the bipolar electrogram, which due to the ring shape of the second electrode is not orientation-dependent if the angle between the wall and the catheter is large. The endocardial balloon and basket electrodes do not have this option. Particularly the basket electrode has a limited number of leads due to the limitation in the number of wires that can be contained in the catheter shaft. Currently, at most 32 bipolar positions or 64 unipolar positions can be used. Bipolar positions consist of two electrodes separated by a shorter distance than the distance between the pairs, or between the electrodes of the unipolar version of the basket catheter. Unipolar positions, in contrast, are equally spaced. Since the resolution of unipolar mapping is twice the resolution of bipolar mapping with the same (limited) number of leads, unipolar mapping may be preferable. In addition, bipolar basket electrode pairs have an orientation parallel to the wall, making them highly dependent on the direction of an activation front, and thus weakening the advantages of bipolar leads.

Given the double resolution of the unipolar basket and the limited use of bipolar pairs parallel to the tissue it is worthwile to attempt unipolar mapping with either the balloon or the basket catheter. We showed that in the presence of blood, activation times can still be estimated using the D_{min} instant. However, the presence of blood may influence the decision in double activations or fractionated electrograms, like leads G2 and B4 in figure 4.7. Fractionation is rare in our data of isolated animal hearts, but is frequently observed in electrograms recorded with the basket catheter in patients, since the basket is usually applied in patients who suffered from previous myocardial infarction and considerable scarring of the left ventricle. For improved accuracy and robustness, activation times may be estimated using the Laplacian of the potential as a measure of the transmembrane current I_m [143, 165, 277]. For accurate I_m estimation, interelectrode distances should be very small, that is, in the order of 0.1 mm. Coronel et al. showed that the Laplacian decreases with interelectrode distance 0.3, 0.6, ... 1.8 mm, but that the instant of zero crossing, which is used to estimate the activation time, does not change [37]. Additional work is needed to establish the applicability of this technique to grids with interelectrode distances in the order of 1 cm, which were used in our studies.

The D_{min} value in an electrogram is sometimes used to estimate the position of infarct scars. When selecting a threshold value for this purpose, the attenuation caused by the presence of blood should be taken into account.

In conclusion, we have shown that unipolar electrograms recorded with a basket catheter are affected by the presence of blood, but can still be used for activation mapping if appropriate care is taken in the analysis of fractionated electrograms.

Chapter 5

Characterization of Body Surface Maps

Characterization and comparison of body surface maps is necessary for the localization of cardiac arrhythmias, diagnosis of ischaemia, dysplasia, hypertrophy, and conduction abnormalities. Various methods for comparison have been used, the choice of a method depending on the application. An overview of these methods is given in this chapter. An improvement for one of these methods, the "nondipolar content," is also presented. — Presented in part at the *World Congress on Med. Phys. and Biom. Eng.*, 1997 [211].

5.1 Introduction

Multichannel ECG data are generally to be processed by a computer in some way to obtain a useful diagnostic parameter. Generally, we may speak of "characterization of body surface maps." Often characterization is based on comparison of a map with another map that corresponds to a known diagnosis. An overview of methods for comparison and other diagnostic tools is given in this chapter. Since the term "body surface map" has been used with different meanings, this treatment starts with a definition of terms.

A surface ECG recording with many leads will be called a multichannel ECG (MECG). The term "total body surface map" (TBSM) has been used with the same meaning. A set of MECGs recorded with the same lead system can be considered as a set of matrices with each matrix having a fixed number of rows (representing leads) and a variable number of columns (representing samples), as depicted in figure 5.1.

The term "body surface map" (BSM) will be used to denote one sample

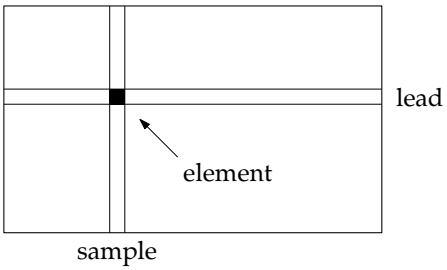

Figure 5.1: *A multichannel electrocardiogram recording is represented by a matrix: each row is an ECG signal (lead) and each column is a sample. The number of signals is usually 64–256, common numbers of samples range from a few hundreds to many thousands. An "element" is the cross section of a sample and a lead, and is represented by a single number.*

from a multichannel ECG, i.e. a vector or array with one element for each recording lead. It represents the distribution of voltages over (a part of) the body surface. The term BSM will also be used to denote the visualization of this vector, as in figure 1.2 on page 16. The term "body surface potential map" has been used to denote a BSM as well.

In addition, the abbreviations QRSI and QRSTI will be used for "QRS integral map" and "QRST integral map," respectively. These objects are introduced below.

The term "map" is used for brevity to refer to a BSM, QRSI, or QRSTI, if it is clear from the context what is meant.

5.1.1 Comparing maps

Direct comparison of MECGs is only possible if they were recorded with the same system or were converted to the same system, an operation that can only be performed if a certain error is allowed [97, 98].

Two different MECG matrices recorded with the same lead system will have the same number of rows (representing leads) but generally a different number of columns (representing samples). A general measure of difference between matrices with unequal dimensions is not known. In order to give a useful answer to the question how MECGs should be compared one must know the purpose of the comparison: this allows summarization of the MECG information in such a way that a comparison can be made. Well-known purposes are identification of the site of origin of arrhythmias, identification of pacing sites, and diagnosis of depolarization and repolarization disorders. Examples of summarizations that are applied, are the QRS

integral map (for localization of arrhythmias) and the nondipolar content (to quantify dispersion of repolarization), which are both discussed below.

Multichannel ECGs are determined by several factors. The nature of the cardiac rhythm, the anatomy and condition of the subject, respiratory effects, noise, and movements of the subject all have their influence. As could be expected, the influences of the different parameters overlap. For example, algorithms as discussed in chapters 6 and 7 can compute the site of origin of an arrhythmia from ECG characteristics but these results are influenced by respiratory effects and body posture.

A method often used to determine the effect of one parameter is to attempt to keep other parameters at stable values, average over parameters that cannot be stabilized, and then to find the features of a MECG that are specific for the parameter of interest. For example, QRS integral maps may be compared to find the origin of a VT. Respiratory effects are reduced by recording the maps in a similar respiratory phase. The QRS interval is determined by predefined criteria. The effect of noise may be made sufficiently small by using high-quality recording equipment, integrating over time, and averaging over several beats. The effect of the patient's condition on the ECG may be reduced by comparing the ECG to those of a patient in a similar condition (e.g. same infarct location). When the influence of other variables has thus been sufficiently reduced it becomes clear that, for example, the pattern of a QRS integral map is very specific for the site of origin, and mathematical analysis teaches that the QRS integral map can, with a small error, be parameterized with only 2 parameters. This is discussed in section 5.6.

5.2 Potential Maps

A BSM ("potential map") is one sample (i.e. one column) from a MECG (see figure 5.1). It represents the potential distribution on the body surface at a certain instant. There are several measures of similarity between potential maps in use, such as the summed difference, the RMS error, and the correlation coefficient.

If a potential map x, being represented by a set of numbers, is viewed as a set of variates x_i where i is the lead number, the most straightforward way to compare two maps x and y is to compute the *correlation coefficient*, also known as the *parametric correlation coefficient*, *Pearson's* r, or *Pearson's coefficient*

$$r = \frac{\sum (x_i - \bar{x})(y_i - \bar{y})}{\sqrt{(\sum x_i - \bar{x})^2 (\sum y_i - \bar{y})^2}} \tag{5.1}$$

where the summations are over all leads i, $\bar{x}$ is the mean of all x_i and $\bar{y}$ is

the mean of all y_i. Because the mean value of a lead over a time interval is meaningful in electrocardiography, it is customary not to subtract the mean values $\bar{x}$ and $\bar{y}$ in (5.1) [100,263]. The *electrocardiographic correlation coefficient* is thus defined as

$$\rho = \frac{\sum x_i y_i}{\sqrt{\sum {x_i}^2 \sum {y_i}^2}} \tag{5.2}$$

where the summations are over all leads i. If each map is geometrically interpreted as a vector in a multidimensional space, two maps can be compared by the *normalized inner product* of the vectors, which is computationally equivalent to the "electrocardiographic" correlation coefficient, ρ in (5.2). Examples of maps and their mutual correlation coefficients are shown in figure 5.2.

The electrocardiographic correlation coefficient is insensitive to the amplitudes (vector norms) of the maps it compares. This property renders it useful for comparison of maps between subjects because the amplitude of an ECG is highly variable between subjects and is assumed to provide little information about the activation order.

5.3 Temporal Integration: Integral Maps

For the comparison of MECGs of different lengths it is first necessary to represent each of them in a way that makes the representations directly comparable. One method to achieve this is to integrate over the time interval considered. This results in an array containing one element for each lead, called an *integral map*. Integration is of course only useful if no relevant information is lost by lumping together of several potential maps. This is the case for QRS and P-wave integral maps, which proved to be highly specific for the site of origin or exit site of arrhythmias and paced beats because they are more stable than the underlying potential maps [236].

Localization of arrhythmias is an important application of QRS and P-wave integral maps (see section 6.5.1); QRST integral maps are used in the diagnosis of repolarization disorders [1, 42, 44, 192, 193] (section 5.7).

Integral maps can be compared by the same methods as potential maps. Measures such as the summed difference, RMS error, and correlation coefficient, can be computed for pairs of integral maps. Examples of QRS integral maps and their correlations are shown in figure 5.2.

5.4 Comparing Intervals

For two MECGs of equal length, the correlation coefficient can be computed for each pair of instantaneous maps, and the resulting set of correlation

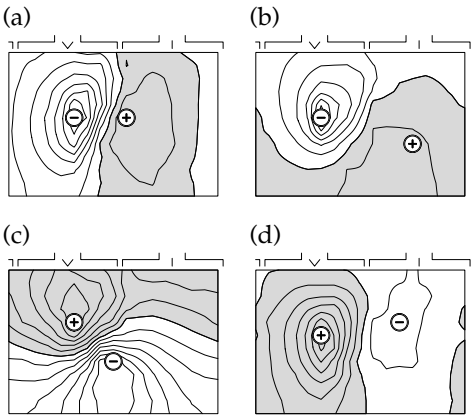

	a	b	c	d
a	1	0.86	−0.29	−0.96
b	0.86	1	−0.68	−0.74
c	−0.29	−0.68	1	0.15
d	−0.96	−0.74	0.15	1

Figure 5.2: *Four QRS integral maps and a table of their mutual correlations. The correlation between similar patterns is near 1; visually opposite patterns have correlation near −1.*

coefficients may be plotted as a *correlation curve*, which gives an impression of the development of the similarity of two recordings over time. Correlation curves have been applied for the localization of anterogradely conducting atrioventricular pathways in patients with WPW syndrome [54,176], and to determine the accuracy of body surface mapping by observing the differences between MECGs generated by pacing at closely separated sites [76,176]. Examples are shown in chapter 6 (page 115).

Another method to compare two MECGs of equal length is the "TBSM correlation:" Each MECG is considered as a vector and the normalized dot product of the two vectors is computed. This method is illustrated together with the correlation curve in section 6.5.3.

5.5 Spatial Integration

Pure integration of MECGs over space, analogous to the temporal integration discussed in section 5.3, is not a common operation in electrocardiography. Weighted linear and nonlinear combinations of leads are, however, quite common. Examples are 1) the "augmented" Einthoven leads, 2) the orthogonal Frank leads [69] (see section 1.2), 3) the SA signal (the sum of the absolute values of all channels, section 6.2), 4) the *vector amplitude*, consisting of the root-summed-square value of all channels, and 5) signals corresponding to "*eigenmaps*" resulting from a KL transformation of a MECG (section 5.6). The rationale for making combined leads varies. In case of the

augmented Einthoven leads, the original motivation was to obtain larger potentials, while the SA signal and *vector amplitude* are used to summarize information from a large number of leads.

5.6 KL Transformation

Multichannel ECG data are *redundant*: each lead or sample of a MECG can be predicted to a certain degree from other leads or other samples, and the accuracy of the prediction increases when the spatial or temporal resolution of the electrode grid increases.

For presentation of body surface maps, this redundancy is not a problem. In fact, display software often increases the redundancy by interpolating the data between grid points to provide a smooth image, which is more agreeable than an image of the raw data. In case of the surface ECG, smoothing can be done by minimizing the surface Laplacian, since the Laplacian of the potential distribution is small (zero on the surface of a homogeneous torso that does not contain current sources or sinks). This kind of interpolation is used by our group for the display of body surface maps.

For other purposes, redundancy reduction can be useful. A well-known example is data compression for storage of large amounts of data. In addition, complicated analysis programs can be made more efficient by letting them operate on a more compact version of the data. For data compression, any compression algorithm can be used, whether it is designed specifically for ECG data or not. However, general compression algorithms represent the packed data in such a way that it cannot be easily used for any other purpose than unpacking. They are therefore not suitable for efficiency improvement of analysis algorithms. Data compression as a purpose was discussed in chapter 2.

A data reduction method that is useful for various analysis purposes is Karhunen-Loève (KL) transformation. This technique can be used for sets of signals that are linearly dependent. We consider a MECG M as a set of S signals with T samples. A sample of the MECG can be considered as a vector $\vec{x}$, that is, a weighted sum of a set of basis vectors $\vec{n}_i$ ($1 \leq i \leq S$):

$$\vec{x} = \sum_{i=1}^{S} e_i \vec{n}_i \tag{5.3}$$

where $e_i = \vec{x} \cdot \vec{n}_i$ are the weight coefficients. If the basis vectors $\vec{n}_i$ constitute the canonical basis

$$(1, 0, \ldots, 0), (0, 1, 0, \ldots, 0), \ldots, (0, \ldots, 0, 1)$$

the weight coefficients e_i are simply the elements of the vector $\vec{x}$. Other choices can also be made for the basis vectors. It can be shown that if the basis vectors are the eigenvectors $\vec{\psi}_i$ of the covariance matrix of the signal set, in order of decreasing eigenvalue, the expectation value of the representation error $\|\vec{x} - \vec{x}_m\|^2$, where

$$\vec{x}_m = \sum_{i=1}^{m} c_i \vec{\psi}_i \qquad c_i = \vec{x} \cdot \vec{\psi}_i \tag{5.4}$$

is, for any m ($1 \leq m \leq S$), smaller than for any other choice of basis vectors. Transformation by the matrix $\Psi = [\psi_1, \ldots \psi_S]$ is called Karhunen-Loève (KL) transformation. Determination of Ψ is also known as *principal component analysis*. If, analogous to the electrocardiographic correlation coefficient ρ (5.2), an "electrocardiographic covariance"

$$C_{ij} = \frac{1}{T} \sum_{t=1}^{T} M_{it} M_{jt} \tag{5.5}$$

is used, principal component analysis is equivalent to *singular value decomposition*, a technique that is frequently used for the solution of possibly overdetermined or underdetermined sets of linear equations [215].

If the S signals are all linear combinations of N linearly independent signals, where $N \leq S$, the representation error $\|\vec{x} - \vec{x}_m\|^2$ is zero for $N \leq m \leq S$. In physiological measurements, this situation usually does not occur. Even if the measured phenomenon were simple enough, measurement noise and artifacts would make all signals slightly independent. In other words, all eigenvalues of the covariance matrix C would be nonzero. However, in case of a MECG, the eigenvalues do become very small (figure 5.3). For many purposes, a representation with only about ten signals suffices. In chapter 7, a representation with only three elements is used for characterization of QRS integral maps.

5.7 Nondipolar Content

The basis vectors ψ_i that result from principal components analysis have the same dimensions as potential maps, i.e. samples from a MECG. They can therefore be represented in the same way and are casually referred to as "eigenmaps." In figure 5.4, eigenmaps are presented that were derived from the covariance of a large set of recordings from different subjects. Note that the first three eigenmaps have smooth dipolar patterns, whereas the others show increasing complexity. This phenomenon is observed for all sets of eigenmaps derived from large patient data sets [161,211]. Abildskov

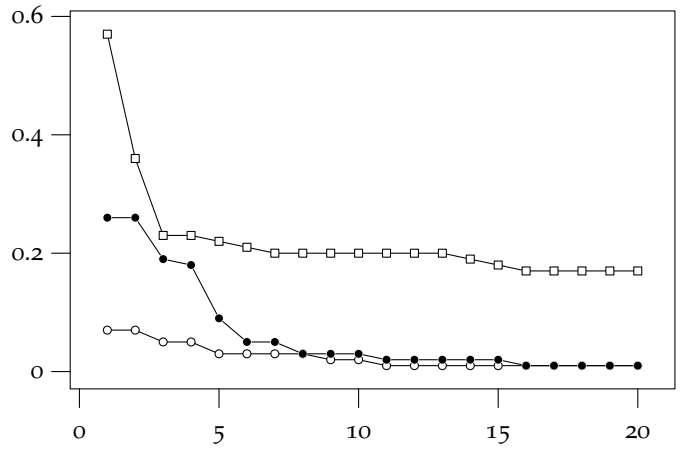

Figure 5.3: *Representation error for three different maps as a function of the number of KL coefficients used for the representation. With open circles, the representation error for a simple "dipolar" map pattern is indicated. Such patterns occur as QRST integral maps in normal subjects and as QRS integral maps. The solid dots indicate the error for a more complex pattern, while the squares are for a very complex map, typically found in patients with some type of heart disease. The corresponding map patterns are shown in figure 5.5 on page 93. For the first two maps, about 10 coefficients suffice to represent the pattern accurately. The third map cannot be represented accurately even with 20 coefficients.*

proposed to use this feature to quantify the "nondipolarity" of body surface maps [1, 161].

If a normalized map $\vec{x}$ is expressed in terms of these basis vectors

$$\vec{x} = \sum_{i=1}^{S} c_i \vec{\psi}_i \qquad c_i = \vec{x} \cdot \vec{\psi}_i \tag{5.6}$$

then we call the contribution of the first three vectors the "dipolar content," and the contribution of the others the "nondipolar content." Mathematically, the nondipolar content $\mathcal{N}(\vec{x})$ can be defined as

$$\mathcal{N}(\vec{x}) = 1 - \sum_{i=1}^{3} (c_i)^2 \tag{5.7}$$

Nondipolar content correlates with the visual impression of nondipolarity and with other diagnostic parameters [1, 42, 193, 211]. This is illustrated in figure 5.5.

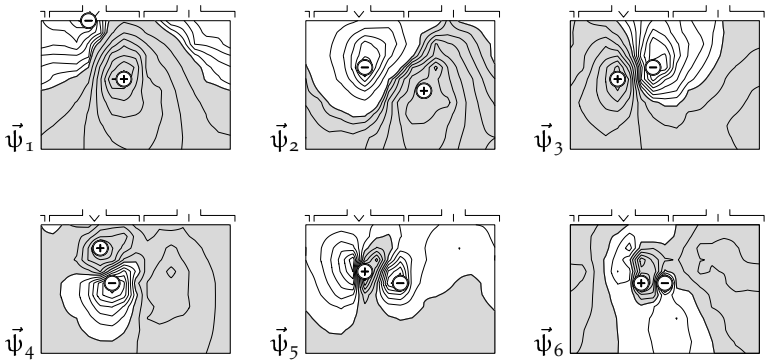

Figure 5.4: *The first six eigenvectors of the covariance of a large set of pooled MECG data, shown as maps. The first three "eigenmaps" ψ_i have dipolar patterns. The other maps, including the remaining 186 maps that are not shown, have nondipolar patterns of increasing complexity.*

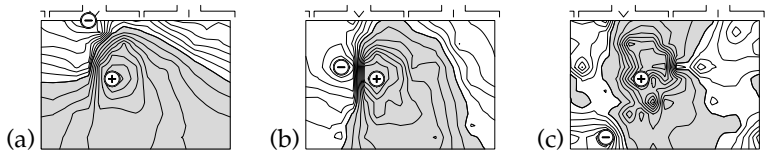

Figure 5.5: *Three QRST integral maps.* **(a)** *A dipolar map with nondipolar content $\mathcal{N} = 0.05$.* **(b)** *A map that is nondipolar according to the traditional method ($\mathcal{N} = 0.19$) and only slightly nondipolar ($\mathcal{N}_s = 0.09$) according to the shifting method.* **(c)** *A map that is clearly nondipolar with $\mathcal{N} = \mathcal{N}_s = 0.23$.*

In figure 5.6 (a), values of nondipolar content are given for maps that were also classified visually as dipolar or nondipolar. Five groups of subjects were considered: 1) 27 normal controls, all with visually dipolar map patterns, 2) 9 patients suffering from primary electrical disease (PED) having visually dipolar patterns, 3) 8 PED patients with visually multipolar map patterns, 4) 53 patients with chronic infarction and visually dipolar map patterns, and 5) 25 infarct patients with visually multipolar map patterns.

Although the mathematical nondipolar content relates well with the visual nondipolarity, there is some overlap in values in figure 5.6 (a). One cause of this overlap is the fact that nondipolar content is sensitive to shifts in the map pattern while a human observer is not.

For better compatibility, nondipolar content was computed for left- and

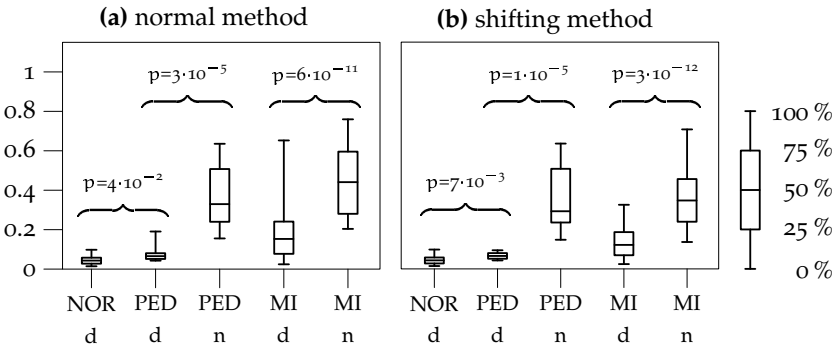

Figure 5.6: (a) *Percentile graphs of nondipolar content for five groups of subjects: normal controls (NOR) with dipolar map patterns; patients suffering from primary electrical disease (PED), i.e. arrhythmia occurring without structural abnormalities of the heart with visually dipolar (d) or nondipolar (n) map patterns; and patients with chronic myocardial infarction (MI), also subdivided in visually dipolar and nondipolar map patterns.* **(b)** *Values of nondipolar content for the same five groups as in panel (a) determined with the "shifting method." With this method, there is no overlap between visually dipolar and nondipolar patterns in the PED group, and a reduced overlap in the MI group.*

right-shifted maps as well, and the minimum value $\mathcal{N}_s$ was reported. The results of this analysis are shown in figure 5.6 (b). It appears that $\mathcal{N}_s$ can separate patterns that were classified visually as dipolar or nondipolar completely in patients with structurally normal hearts (PED). However, complete separation is not obtained for patients with previous myocardial infarction (MI), although the shifting method does reduce the overlap in this group considerably.

The nondipolar content is used to estimate repolarization abnormalities [42] and for risk stratification in patients with primary electrical disease [193].

5.8 A Two-Dimensional Representation of Body Surface Maps

If a map pattern has a low nondipolar content, it can be represented in terms of the first three eigenmaps ψ_i (figure 5.4) with only a small error. When this error is allowed, the map can thus be described with three coefficients c_i according to equation (5.6). It is usually assumed that the amp-

litude of the map provides little or no information on some issues, such as the location of the exit site of an arrhythmia. Thus only the pattern of the map needs to be described, for example by specifying only c_2/c_1 and c_3/c_1. Alternatively, the set (c_1, c_2, c_3) may be considered as a vector in a 3-D space, and its direction may be specified by two angles, ignoring the length of the vector. In either way, a 2-D representation of a map is obtained.

Two-dimensional representations of maps are useful for various purposes. They give a quick overview of the major characteristics of a set of maps and allow a subdivision of the set. Another application is discussed in chapters 6 and 7: QRS integral maps of ventricular paced beats and ventricular tachycardia are assumed to be determined by the endocardial pacing site or the exit site. This is a 2-D parameter space. It proves to be possible to devise a continuous and bijective mapping from this parameter space to the 2-D truncated QRSI space. This mapping allows to predict the exit site or pacing site accurately from the QRSI pattern. This method is possible due to the low nondipolar content of QRS integral maps, which allows to represent them in 2 dimensions with only a small error.

Chapter 6

Detection, Classification, and Localization of Ectopic Ventricular Beats

This chapter discusses (literature on) automatic detection and classification of QRS complexes, and localization of VT and VES by body surface mapping. The idea of an integrated automatic guidance system for catheter ablation of ventricular arrhythmias is introduced. — Presented in part at the *NFSI* symposium, September 2001 [199].

6.1 Introduction

6.1.1 Automated ECG analysis

The surface ECG can be used for localization of the exit site of cardiac arrhythmias. In case of ventricular arrhythmias, such as VT or ventricular extrasystoles (VES), this is done by inspection of the part of the ECG that represents ventricular activation, the QRS complex (figure 6.1). For cardiologists, it is in most cases a trivial matter to recognize a QRS complex in a single ECG tracing, and it is a simple task to find its onset and offset (begin and end) with moderate accuracy. Classification of the QRS complex is performed by inspecting the sequence and relative amplitudes of positive and negative peaks in the different leads.

For a computer algorithm, the tasks of QRS detection and especially delineation are surprisingly difficult. Although a simple thresholding algorithm is able to detect most QRS complexes in sinus rhythm in a recording with a good signal-to-noise ratio (SNR), the construction of a robust

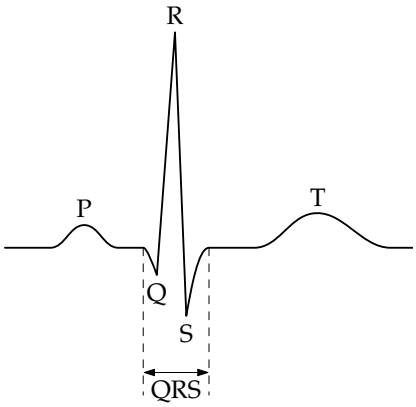

Figure 6.1: *Part of the nomenclature for electrocardiograms. Indicated are the P wave, Q, R, and S peaks as well as the QRS complex and the T wave. The P wave represents atrial depolarization, the QRS complex ventricular depolarization, and the T wave ventricular repolarization. Atrial repolarization results in a very small signal that is obscured by the QRS complex.*

algorithm that detects and delineates *all* QRS complexes, either normal or ectopic, is much more involved. On the other hand, computers can be helpful in cases where humans encounter problems. In rapid ventricular tachycardia (VT), it is often difficult to see the difference between QRS and T wave in a single lead, while different leads seem to give contradictory results. The problem can be solved by combining many leads, e.g. all leads from a body surface map, and quantitatively analyzing the slope of the leads [123]. Computers are much better equipped for these tasks than humans, and are capable of producing a signal that has different values in QRS complexes and T waves of a rapid VT. For the final decision, however, contextual information can be helpful, making human supervision preferable. Therefore such arrhythmias can be most successfully analyzed if a computer processes the data from many leads into one or a few signals that can be interpreted by a human expert. An example is presented below in section 6.2 on page 100.

Localization of exit sites by computer programs is done by entirely different criteria than those used by human experts. This is partly due to the fact that some properties that are easily perceived by humans are hard to express formally, a prerequisite for implementation in a computer program. On the other hand, computers can accurately inspect relations between signals, such as the relative timing of peaks and relative amplitudes; this type

of analysis is hard to perform for a human observer making use of ECG tracings. Another reason for the different criteria is that computers are often applied for the analysis of multilead ECGs, which, due to the size and redundancy of the data, are characterized in a way different from standard 12-lead ECGs.

Detection of ectopic ventricular beats requires not only detection of QRS complexes, i.e., recognizing the part of the signal that results from ventricular depolarization, but also classification as corresponding to an abnormal activation sequence. These are partially related subjects because classification can, in most cases, only be performed after detection and because they are sometimes implemented in the same algorithm [55]. Implementation in a single algorithm is theoretically advantageous because normal and arrhythmic QRS complexes are characterized by different, possibly disjunct, feature sets, which makes the tasks of detecting them all and subsequently discriminating them relatively inefficient.

6.1.2 Automated arrhythmia monitoring in the catheterization laboratory

Detection and classification of QRS complexes are important in automatic patient monitoring, for example in the coronary care unit (CCU) [33, 168, 189, 283], during surgery [87], in automatic (implantable) defibrillators [33, 174], and for analysis of very long recordings, such as Holter recordings [189, 231, 232] and continuous recordings made during electrophysiologic study as described in chapter 4. This chapter focuses on a fifth application, which is less covered in the existent literature: automatic analysis of recordings made during electrophysiologic study, especially during endocardial catheter-mapping procedures for localization and radiofrequency ablation of VT.

Body surface mapping (BSM) systems are used during catheter mapping for accurate localization of VT exit sites and pacing sites [194]. Currently, BSM systems used in this setting make a recording on demand, after which the operator has to identify a QRS complex of interest as well as isoelectric instants that can be used for removal of baseline drift and DC offset. A computer algorithm then delineates the QRS complex [123], but the result sometimes needs to be corrected by the operator. Provided with an accurate QRS delineation, the computer can estimate the exit site of the complex [212, 236, 237].

6.1.3 Outline of this chapter

Ideally, an automatic arrhythmia monitoring system should record continuously, and detect, delineate, and localize QRS complexes of VT and paced beats without any operator intervention. In section 6.2 to 6.5, an overview is given of methods that can be used for these purposes. Section 6.2 is a review of the literature on complex detection and delineation. The next step, classification of complexes, is discussed in section 6.3. The overview ends with sections 6.4 and 6.5, which provide a general discussion of arrhythmia-localization methods.

Section 6.5 introduces the methods of localization that are used in this thesis. Localization of VT using pacemap databases, the method that is used by our research group, is introduced in sections 6.6 and 6.7. Specific problems of the traditional method of comparing maps using correlation coefficients are also discussed. Section 6.8 introduces an improved method for the estimation of distances between pacing sites, and the concept of relative localization. Finally, sections 6.9 and 6.10 introduce the new continuous localization method, which is discussed more comprehensively in chapters 7 and 8.

6.2 QRS Detection and Delineation

6.2.1 Literature overview

QRS detection is a popular and long-lasting topic in the signal-processing and biomedical engineering literature. Several trends in signal-processing methods can be recognized. For example, syntactic algorithms, popular in the 1960s and 1970s, and wavelet transforms, popular in the 1990s, were applied to the problem of QRS detection and delineation [2, 39, 120, 145, 259, 283]. Most published algorithms are aimed at long records, often to be analyzed in real-time, of single lead electrocardiograms.

The success of a QRS detection or delineation algorithm depends on the quality of the recording and the selected lead(s). When comparing algorithms, it is therefore necessary to use the same data to evaluate their performance. For this purpose, annotated ECG databases were developed. They consist of several long recordings, annotated by experienced cardiologists with wave or complex types (P, QRS, T), classes (normal, VT, etc.) and sometimes onsets and offsets of waves or complexes. Unfortunately, different authors tested their algorithms on different databases; therefore there is still some uncertainty in the comparison. Some well-known databases are:

- The CSE database, produced by the Common Standards for Quantitative Electrocardiography project (CSE). This database contains re-

cordings with relatively good SNR [273, 274]. These 250 recordings contain a total of approximately $1.6 \cdot 10^4$ beats, sampled at 500 Hz.

- The MIT-BIH database, which contains approximately 10^5 beats, sampled at 360 Hz [87, 105].

- The American Heart Association (AHA) ECG database, which contains approximately $1.5 \cdot 10^5$ beats sampled at 250 Hz [255].

In contrast to the CSE database, the latter two databases contain "real-life" data, including very noisy records, which makes them more suitable for robustness tests. All databases are annotated by expert reviewers.

syntactic algorithms Perhaps the oldest class of QRS-detection algorithms is the class of *syntactic algorithms*. In the 1960s, computers had become powerful enough to allow programming in *high-level languages*, i.e., programming languages with abstraction levels higher than single machine instructions. In contrast to human language, programming languages, being completely and formally specified, can be interpreted by computer programs [66]. Algorithms to perform this task are termed *syntactic algorithms*, or *parsers*. There has been much interest in this topic, perhaps due to the prospect of interpreting human language by computer, and consequently attempts have been made to use parsers also for some kinds of signal processing, notably speech recognition and ECG analysis.

An important characteristic of parsers is that they have to be fed with a limited set of elementary language parts, which are known as *tokens* [144]. In ECG analysis, tokens might be signal samples. However, in a typical signal recorded with 12-bits accuracy there would be 4096 tokens, presented to the parser in long sequences, and thus a great number of parsing rules would be needed to reduce them to the level of "P wave" or "QRS complex." A reduction of both the token set and the sequence length was obtained by the AZTEC algorithm, which encodes a single-channel ECG in terms of straight line segments [38]. This and similar algorithms were used with some success for QRS detection and classification [39, 262, 283]. Another reduction of the token set was reported by Belforte et al. [20] who used variable-width peaks characterized by height classes as tokens; only three tokens were needed for QRS detection. Recent syntactic methods use attribute grammars, i.e., grammars for tokens with one or more properties ("attributes") whose values are taken into account by the parser [71]. This reduces the required number of tokens and parsing rules. Syntactic methods have been shown to be capable also of accurately determining onset and offset of QRS, P wave, and T wave [259] in CSE database records.

Syntactic algorithms may be considered promising, but more work is needed to obtain the same accuracy as some simpler algorithms [273]. A rationale for using syntactic algorithms is that syntactic reasoning is also used by human experts analyzing an ECG [20]. Rules like "a sinus beat consists of a P wave followed in about 150 ms by a normal QRS complex" are useful to obtain a macroscopic understanding of an ECG, and may also be used to infer the type of an ambiguous wave. However, most syntactic algorithms reported in the literature apply rules at a lower level, in order to assemble waves from short lines or mere samples [39, 259, 262, 283]. Macroscopic rules are generally applied in a more recent method: the hidden Markov model (HMM).

hidden Markov models A method related to syntactic algorithms is the *hidden Markov model* (HMM) [36, 137, 216, 257]. With this approach, the ECG is assumed to be the *output* of a hidden point process. The qualification "hidden" implies that the process is not observed directly, but through a probabilistic relationship. The hidden process is at any time in one of a finite set of *states*. States might correspond to features like a QRS complex or P wave. For each state, there is a probability function defined which specifies the likelihood of all possible outputs if the system is in this state. In addition, for each state there are probabilities defined for moving to other states or remaining in the current state. The process is called a *Markov process* if the transition probabilities depend only on the current state and the new state, i.e., not on previous states. Commonly, the transition probabilities have fixed values.

Decomposition of an ECG signal is done by determining the state sequence that is most likely to underly the signal, given a set of transition probabilities and output functions. The characterization and delineation of the ECG parts follow from the state sequence found to be the most probable. The Markov property makes it possible to do this in a number of steps that is linearly, rather than exponentially, dependent on the number of states and length of the signal.

Evaluation of detection and delineation accuracy of these methods with a public ECG database has not yet been reported.

thresholding algorithms The most widely applied algorithms are those based on peak searching in a suitably processed ECG signal. These algorithms have several elements in common: 1) a low-pass filter for noise suppression, 2) a high-pass filter for removal of baseline drift, 3) a differentiator for enhancement of the QRS complex (which is characterized by high slope values), 4) computation of an "energy signal" by squaring and moving-

average filtering [147, 255], and 5) simple or adaptive thresholding, including refractory-period blanking and backsearching [87]. Ligtenberg and Kunt describe an algorithm for detection only, of this type [147]. This algorithm also works for abnormal beats and is not sensitive to baseline offset. It was reported to be highly accurate with an error rate of only 0.2 %. However, the testing data set was limited, consisting of only 1172 complexes from three patients, and no public database was used. Pan and Tompkins [189] described a similar method which differs only in the design of the band-pass filter and the threshold computation. They report an error rate of 0.68 % on the MIT-BIH database. Hamilton and Tompkins [87] improved the algorithm and achieved 0.54 % error (0.23 % false positives and 0.31 % false negatives) on the MIT-BIH database.

The CSE database was used, immediately after its creation, for a comparison of 11 commercial and non-commercial algorithms for delineation of P waves, QRS complexes, and T waves [273]. This study showed that some algorithms estimated QRS onset and offset deviating less than 5 ms from the timings established by a group of reviewers, in relatively "clean" recordings. Falsely detected complexes are not reported.

Especially for analysis of continuous recordings, sensitivity to noise and baseline wander is an important issue. Friesen et al. compared the noise sensitivities of nine algorithms for detection and determination of QRS onset using single-lead ECGs contaminated with artificial noise of several types [70]. Although the ranking depends on the type of noise presented, it may be concluded that "digital-filter" type algorithms (simplified energy-signal type algorithms) perform best, and that 100 % accuracy, i.e. detection of all QRS complexes and no false positives, is attainable with several algorithms for realistic noise levels. Descriptions of the algorithms are included, which makes their paper suitable as a cookbook. These authors did not evaluate delineation accuracy.

Suppappola and Sun [255] compared two earlier algorithms [87, 185] to their own. They tested on the AHA ECG database (see page 101). Of these, the Hamilton–Tompkins algorithm [87] performs best with 1.9 % false positives and 2.0 % false negatives. This performance is less accurate than that reported by Hamilton and Tompkins themselves, who tested on the MIT-BIH database [87]. The results are also less accurate than those reported by Friesen et al. [70]. This is not surprising since the latter authors used only a short recording from a normal subject, contaminated with artificial noise, while most other authors tested on one of the public ECG databases which contain real patient data.

Many thresholding algorithms depend on peak detection. Todd et al. recently developed a formal definition of a peak and an algorithm for peak detection that is somewhat robust to baseline drift and artifacts [258].

other methods Artificial neural networks (ANN) are used for adaptive template matching, noise management, and classification of beats [105,281]. Hu et al. reported testing on the MIT-BIH database (see page 101). The QRS-detection error for a relatively noisy record of the database was only 0.2 %. Two other methods were tested and they showed error rates above 2 % [105]. Hamilton and Tompkins earlier reported 3 % error for this particular record [87].

Recently, more complicated methods were developed that are still ultimately based on the work of Pan, Hamilton and Tompkins [87,189]. Li et al. [145] use wavelet transforms and complicated decision rules for thresholding in combination with the well-known blanking and backsearching strategy [87]. Afonso et al. [2] adapted the Hamilton–Tompkins method [87] by first decomposing the ECG in several frequency bands, combining these to signals, and using these in decision rules for QRS detection. With 0.8 % error on the MIT-BIH database, the results are not as good as those reported earlier by Hamilton and Tompkins [87].

6.2.2 Multilead electrocardiograms

Relatively little has been published on QRS detection in multilead electrocardiograms. The availability of leads on all sides of the thorax may facilitate detection of ectopic beats. On the other hand, multilead algorithms are generally used for more difficult tasks. If QRS delineation is to be used for automatic localization of VT, it has to be able to find QRS complexes in VT, or even polymorphic VT (PVT), which is a difficult task even for a human expert.

Kemmelings et al. described a QRS-detection and delineation algorithm for use with 64-lead surface ECG recordings [123]. It was created primarily to find and delineate QRS complexes in rapid VT. A later implementation by Linnenbank allows the user to select a QRS complex, and does only delineation. This implementation is used in the MA$^{P}_{L}$AB package [207, 208, 210] (chapter 10). These algorithms are based on three signals, derived from a multichannel ECG recording:

SA the sum of the absolute values of all channels. It can be shown that this signal has the same characteristics as the better-known *vector amplitude* (R): the square root of the sum of the squares of all channels. The SA signal, however, is computationally cheaper to an extent that was important at the time Kemmelings and Linnenbank created their algorithms [123, 210]. In addition, the SA signal is less sensitive to large baseline offsets. This property is important since the SA signal is used in Kemmelings' algorithm without prior baseline correction.

Like R, this signal generally has a large peak in the QRS complex, and smaller peaks in the T wave and P wave.

SAD the sum of the absolute values of the first derivatives of all channels. This signal has a number of sharp peaks in the QRS complex. For sinus rhythm these peaks are concentrated in the middle of the QRS complex, while in ectopic beats (ventricularly paced beats and VT) they are more dispersed.

DDSA the second derivative of the sum of the absolute values of all channels. This signal has several peaks in the QRS complex, some of which coincide with the onset and offset of the QRS complex. This signal is very sensitive to noise. However, the implicit low-pass filtering due to the definition employed by Kemmelings [123],

$$\mathrm{DDSA}(t) = \mathrm{SA}(t+8) - 2\mathrm{SA}(t) + \mathrm{SA}(t-8)$$

where t is in milliseconds, works very well even in relatively noisy recordings.

In the MAP$_{\text{LAB}}$ package [207–209], these leads are not only used in the QRS-detection algorithm but can also be visualized directly, together with the original signals, as "special channels" (chapter 10). Examples of the signals SA, SAD, DDSA, R, and the Ligtenberg-Kunt "energy signal" E_{LK} for a VES, a sinus beat, and VT are shown together with precordial lead V_3 in figure 6.2.

In sinus rhythm, as well as in relatively slow arrhythmias, the QRS onset and offset are often determined as the first/last instants where the signal exceeds a given limit, such as 0.2 mV. When body surface mapping is used, the first and last instants where *any* signal exceeds the limit may be used instead [236].

In VT, however, it can happen that the signal exceeds the limit during the entire QRST interval. A simple solution is to determine the lowest point between the assumed QRS complex and T wave. A more elaborate and perhaps more accurate approach, created specifically for body surface map data, was presented by Sun et al. [254]. This algorithm finds the instants where the global extrema of the map, whose positions change only gradually during the QRS interval, appear and disappear. The algorithm needs prior QRS detection and baseline correction. Results on (presumably) sinus rhythm show SD errors of 2 and 4 ms in the QRS onset and offset detection, respectively. Although results on VT were not reported, this is a potentially very accurate technique for the analysis of VT recordings.

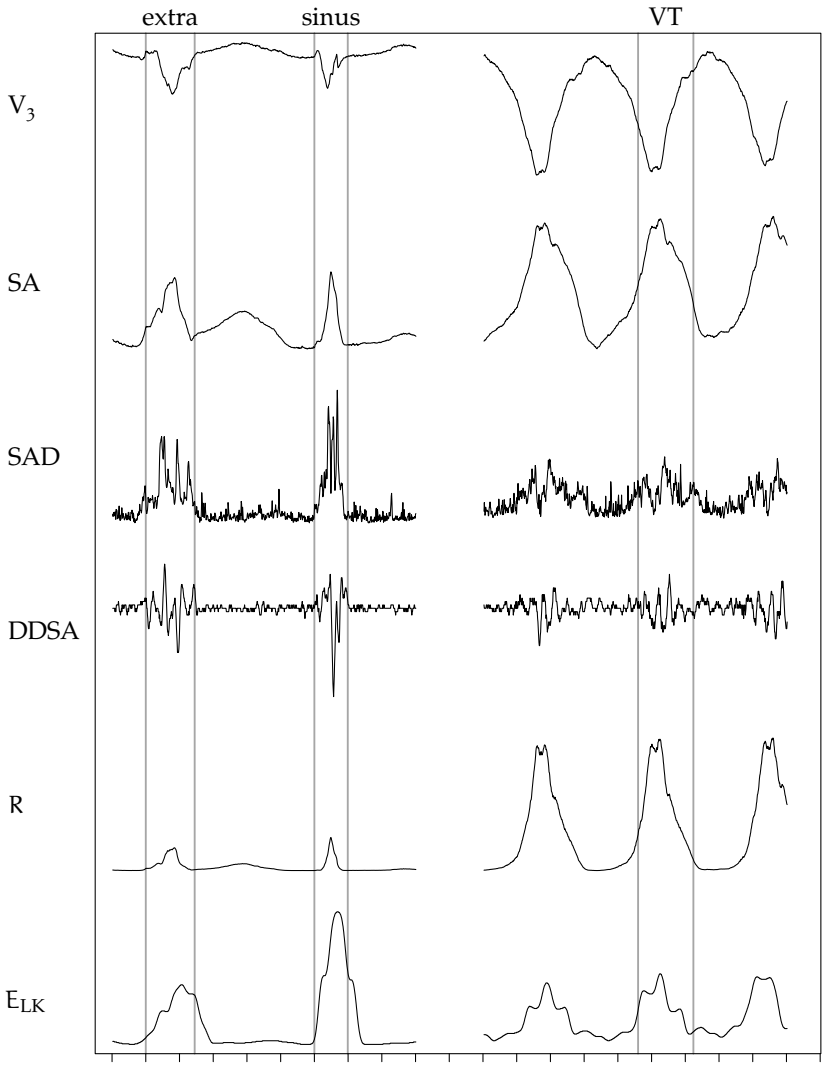

Figure 6.2: *Lead V_3, SumAbs (SA) signal, SumAbsDiff (SAD) signal, second derivative of SumAbs (DDSA) signal, vector amplitude* R*, and the Ligtenberg–Kunt energy signal* E_{LK} *[147], of three different heart beats. On the left, the first complex is a ventricular extrasystole, immediately followed by a normal "sinus" beat. A separate interval of ventricular tachycardia (VT), from a different patient, is shown on the right. Operator-determined QRS onsets and offsets are indicated.*

6.2.3 Interaction with baseline correction

Many QRS-detection algorithms depend on some kind of *baseline correction* for removal of non-physiologic DC offset and drift in the signal. Robust detection algorithms usually include a simple baseline correction such as subtraction of the mean value over some interval. For very accurate QRS detection, a more accurate baseline correction is also necessary.

One method for accurate baseline correction is to indicate one or more instants where the physiological signal is expected to be nearly zero, and then to adapt the signal in such a way that it becomes zero at these instants. Depending on the number of indicated zero points, this may be done by zero-order (offset correction), first-order (linear trend correction), or higher-order methods.

Instants where the signal should be zero can be found relative to the QRS complex. Obviously, this method cannot be employed to correct the signal before QRS detection. A solution for fully automatic systems is first to apply a robust method for coarse QRS detection, then to correct the baseline, and finally to delineate the QRS complex accurately.

6.2.4 Conclusions

Reported accuracies for the detection of normal QRS complexes in single-channel electrocardiograms vary from 0.54 % to 4 % [87, 255]. An overview paper using the CSE database suggests that a zero error rate is attainable, but this is not stated explicitly [273].

A detection system in the catheterization laboratory has two advantages over most systems reported in the literature: it can make use of more leads and the ECG quality is controlled by the medical personnel. We may therefore expect the error rate in this situation to be relatively low. Detection of VT QRS complexes, our main target, is less certain since most authors do not report on detection of arrhythmic complexes.

Onset and offset of the QRS complex during VT can be determined using Kemmelings' algorithm with about 20 ms standard deviation when comparing algorithm results with those of a human observer. The algorithm results are therefore not always accurate enough for VT localization. In its current implementation in online BSM software and in the MAP$_{\text{L}}^{\text{P}}$AB package the algorithm can be used for convenience: when an operator points at a QRS complex, the algorithm gives initial estimates of the onset and offset, which the operator operator may subsequently correct [154, 208]. Higher accuracies were reported by Sun et al. for normal beats using multilead ECG data [254], but their method has not yet been tested on VT recordings.

In conclusion, results reported in the literature show that automatic de-

tection and delineation of VT QRS complexes are possible and can be used either under human supervision, or for tasks that allow a certain error rate, such as the detection of many paced complexes reported in chapter 4. In addition, results suggest that the creation of an unsupervised system for QRS detection and delineation, accurate enough for VT localization and subsequent catheter guidance, is also possible. However, to date such a system has not been reported.

6.3 QRS Classification

Automated ECG-based classification of heart beats has been investigated for several decades, but the problem has still not been solved well enough for most purposes. Although a gold standard is usually not available, it is believed that computer algorithms for this purpose perform considerably less accurate than human experts. An overview of the literature on this subject is presented here.

template matching QRS complexes can be classified by comparing them to a set of examples representing the classes. In the time domain, *template matching* is used. This entails selection of ECG fragments of limited length, and estimating the correlation with a given template signal. When the correlation exceeds a limit, the template is said to match, and a complex of the template's class is found. If onset and offset values were assigned to the template, which can be done manually by a cardiologist, this process performs implicit QRS onset and offset determination.

Template matching with a single template is done for the purpose of *signal alignment*. Alignment of complexes is a prerequisite for *signal averaging* where normal beats are be extracted from a record of several minutes length [25, 169], and for other analyses where many complexes of the same kind are to be located or extracted for analysis of subtle differences, such as heart-rate variability and "alternans" [223, 243].

Template matching with multiple templates can be done to recognize normal and arrhythmic beats, for example to summarize Holter recordings. This kind of template matching was performed with nonlinear, rather than linear, methods of comparison [65].

neural networks A promising range of techniques for classification is formed by artificial neural networks (ANN) [34, 35, 43, 55, 65, 105, 152, 153, 174, 268]. Several network architectures and variants have been applied to several classification problems.

Linnenbank et al. applied neural networks for localization of ectopic ventricular beats by the classification of VT QRS integral maps [152, 153]. The vast majority of papers deals with single-channel or few-channel recordings and pattern recognition in the time domain, rather than the spatial domain.

The most obvious way to apply an ANN to a single lead is first to detect the QRS complex, and then to feed the values of N samples around the onset or the peak of the complex to the N inputs of a perceptron (see figure 6.3). For a complete discussion, see a textbook on neural networks such as Rumelhart and Zipser [226] or the original work by Rosenblatt [224]. The outputs of the perceptron correspond to the classes to be distinguished. The optimal parameters of the network (such as the number of layers and the number of neurons in each layer) depend on the problem involved, and can be determined experimentally. Hu et al. [105] reported QRS detection and classification of normal heart beats and 12 arrhythmia types using two-layer perceptrons. With a separate network for normal/abnormal discrimination, 84.5 % correct classifications was obtained. If normal beats were to be identified by the same network as all classes of abnormal beats, the classification rate was only 65 %. The networks used 51 samples, centred on the database fiducial points, as input; the sampling rate (MIT-BIH database, see page 101) was 360 Hz.

As with the syntactic methods and hidden Markov models discussed above, there is again a similarity between ECG analysis and speech recognition in the field of neural networks. Particularly several kinds of delay-based neural networks have been reported as methods for both kinds of signal analysis [35, 43, 55, 65, 268].

Several papers deal with the identification of arrhythmias, usually VT and VF, in continuous recordings. Clayton and coworkers applied two neural networks to the problem of discriminating VF from VF-like signals, such as resulting from bad electrode contact [34]. These authors compared the performance of the two networks to those of 4 other algorithms. Among these, the neural network had the best sensitivity (84 %), but not the best specificity: 59 %, versus 93 % for the most specific algorithm, which on the other hand had a poor sensitivity of 53 %.

general nonlinear mapping An overview of nonlinear mapping and classification methods, including neural networks, that may be applicable to several ECG-related problems is given by Maglaveras et al. [167]. The same authors report classification of ST-segment abnormalities using nonlinear mapping and neural-networks based shrinking classification, as well as discrimination between normal and premature ventricular beats using bidirectional associative memories (BAM) [164]. Another study by the same group

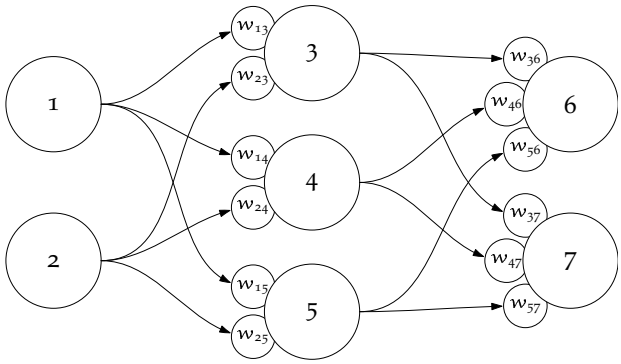

Figure 6.3: *An artificial neural network consisting of seven neurons. An artificial neuron computes a weighted sum of its inputs and "fires" if the sum exceeds a threshold. The network learns by adapting the weights w_{ij}. A network is called a "perceptron" if it is subdivided into layers, where neurons only connect to neurons in the next layer. Generally, there are $n(n-1)$ connections possible between n neurons. The subdivision into layers reduces the number of allowed connections, and more importantly, it enables (supervised) learning by backpropagation. The depicted network is a three-layer perceptron. The input layer consists of neurons 1 and 2, the hidden layer of neurons 3–5, and the output layer of neurons 6 and 7. Due to the subdivision into layers, the depicted network has only 12 of the 42 possible connections; in other words, only 12 of the weights w_{ij} can be nonzero.*

describes ischaemia detection using an adaptive backpropagation neural network [168]. A method that may be applicable to many purposes, nonlinear principal components analysis (NLPCA), is employed by Stamkopoulos et al. [253] for ischaemia detection.

6.3.1 Conclusions

A system for unsupervised detection and localization of ventricular beats during electrophysiologic study prior to catheter ablation of VT requires accurate classification of ventricular versus non-ventricular beats. The system should not annoy the operators with many "false alarms," which means that detection of ventricular beats should be specific. On the other hand, high sensitivity may be necessary if arrhythmias must be analyzed that are hard to induce, or are badly tolerated by the patient. The results obtained with single-lead electrocardiograms [174], and the general observation that multilead ECGs increase accuracy of analysis, suggest that detection with 99 to 100 % sensitivity and specificity is attainable. However, a system that performs this specific task has not yet been reported.

6.4 Localization of Arrhythmias: An Overview

Once a P wave or QRS complex has been selected, identified as arrhythmic, and accurately delineated, the site of origin can be determined from the morphology of the signal. There are many methods by which a computer can determine the site of origin of a complex from the surface ECG. These methods may be globally categorized as follows:

solutions of the inverse problem The so-called "inverse problem of electrocardiography" is the computation of epicardial or even endocardial potentials from the body surface potentials. By applying these methods to the QRS potentials one can observe the spreading of the activation front, which is characterized by a large gradient, and thus find the site of origin of a heart beat. It is now possible to compute the epicardial potential distribution with satisfactory accuracy if the cardiac and torso geometry of the subject are known, e.g. from an MRI scan [77, 108, 113, 187]. Even without accurate knowledge of the individual geometry, activation patterns can be determined [218]. However, the problem is in principle ill-posed: there is always an infinite number of solutions from which the most likely one must be selected. This requires assumptions about the solution, such as the assumption of a single activation wave. Notwithstanding its importance, this category will not be discussed here in further detail. Reviews on this subject were published, for example, by Van Oosterom [186], Gulrajani [83, 84], and Smith [244].

simulation Using a model of the heart that simulates the intracardial activation, embedded in a volume-conductor model of the thorax, it is possible to estimate the body surface potentials corresponding to a given activation sequence [142, 158, 173, 217]. This is known as the "forward problem of electrocardiography." If activation propagation is also modelled, it is possible to compute the surface potentials that result from activation originating from a given focus. By repeating this procedure for several foci, one can estimate the location of the focus corresponding to a given set of body surface potential maps [104]. It is then important to know how these body surface maps should be compared, that is, what features of the multichannel ECG (MECG) are characteristic of the focus. For example, the 40-ms map [90], the initial minimum position [121], and the QRS integral map [236, 237] are used for localization of VT exit sites, delta-wave maps for localization of accessory pathways in Wolff–Parkinson–White (WPW) syndrome [54, 180], and P-wave integral maps for localization of atrial arrhythmias [234, 238, 240].

empirical methods A relatively simple and clinically practical method for localization is to link the MECG pattern directly to the site of origin. By recording the body surface potentials corresponding to a known focus, one may set up a database that maps the MECG to a location [54, 236, 237]. A known focus is created by pacing with an endocardial catheter at a known location. As with simulation methods, it is important to know what features of a given MECG are to be compared with the MECG patterns listed in the database. Because the number of locations in a database is typically limited, it is also necessary to use some kind of interpolation algorithm to obtain a precise estimate of the location corresponding to a recorded MECG. This can be done by a neural network that is trained with the database [152, 153], or by an approximate functional relationship between MECG and site of origin (chapter 7) [200, 212]. Such a relationship can be verified using the database

In the remainder of this chapter, as well as in chapters 7 and 8, empirical methods for localization of VT exit sites are discussed. These methods are all based on the use of QRS integral maps.

6.5 Empirical Methods of Localization

6.5.1 The QRS integral map

The QRS complex in the ECG (figure 6.1) represents the electrical activation of the ventricles, and is therefore used to find the exit site of VT. For exit-site localization using body surface mapping, the relation between exit site and MECG has to be known. Sippens Groenewegen et al. established this relation by pacing the heart at known locations with an endocardial catheter inserted into the ventricle [235–237, 242]. They showed that the QRS integral map (QRSI), defined as the summation of the MECG over the QRS complex, is highly specific for the pacing site (figure 6.4).

In order to minimize inter-patient variability, they grouped paced QRS integral maps with similar patterns; to each group corresponds an endocardial *segment*, defined by the pacing positions, and a *mean map*, computed as the mean of the contributing QRS integral maps. The set of segments and corresponding mean maps is referred to as a pace-map database. Using a pace-map database, the exit site of a given QRSI is estimated by finding the best-matching mean map in the database.

In these studies, QRS integral maps x and y were compared using the

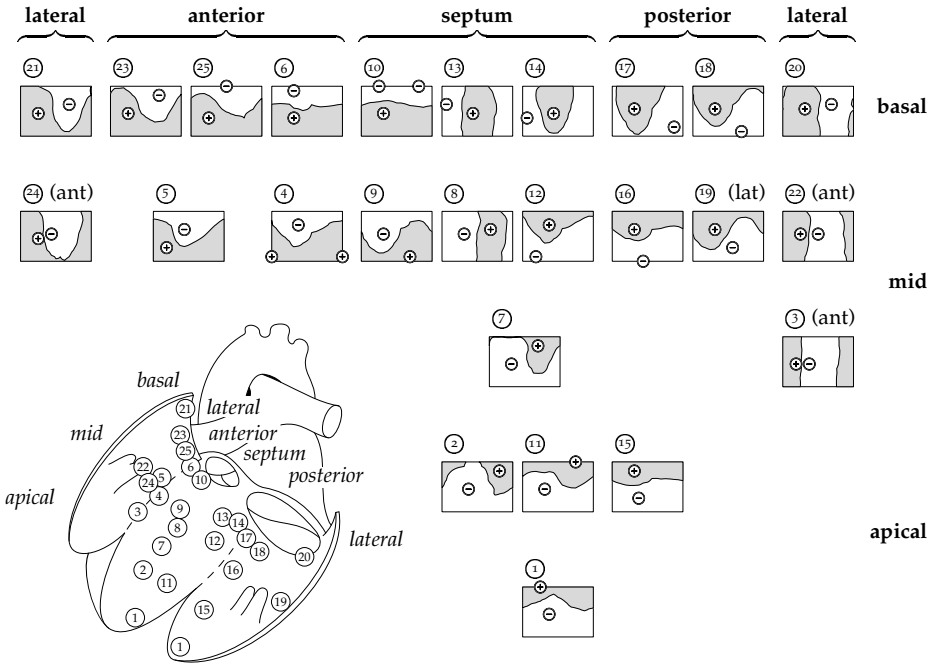

Figure 6.4: *The database of 25 mean paced QRS integral maps obtained from the structurally normal left ventricle [236]. The maps are represented in the format introduced in figure 1.2 on page 16. Each map corresponds to a mean segment position in a schematic diagram of the left ventricle (encircled numbers). The maps are arranged in a way that approximates the corresponding positions in the left ventricle.*

electrocardiographic correlation coefficient (5.2):

$$\rho = \frac{\sum x_i y_i}{\sqrt{\sum {x_i}^2 \sum {y_i}^2}}$$

where the summations are over all leads i. If the maps are considered geometrically as vectors in a multidimensional space, the electrocardiographic correlation coefficient is equivalent to the normalized inner product

$$\rho = \frac{\vec{x} \cdot \vec{y}}{\|\vec{x}\| \, \|\vec{y}\|} \tag{6.1}$$

Instead of using ρ directly, one may compute the angle between the two vectors as the inverse cosine of ρ, which may have a more linear relation

to the distance between ectopic foci than the inner product itself. This is evaluated in section 6.8.

An advantage of the geometrical interpretation is that it permits the formulation of a continuous subspace of the signal space, that contains the QRS integral maps. This leads to the continuous localization methods outlined in section 6.10.

6.5.2 Early QRS patterns

If an exit site is determined with endocardial electrograms, the analysis concentrates on the initial activation. This approach has also been tested with multichannel surface ECGs. Examples are the position of the initial minimum of a MECG [121], and the potential map at 40 ms after QRS onset [90]. SippensGroenewegen and coworkers reported that the QRSI performs better than these measures [236]. The superior performance of the QRSI may be due to the noise reduction inherent with temporal averaging, and to normal non-specific variability in the initial potential patterns observed in the early part of the QRS complex ("initial pattern instability" [236]).

6.5.3 "TBSM correlation" and the correlation curve

For MECGs of equal length, a correlation can be computed between potential maps at each time instant. Plotting the correlations as a function of time yields a *correlation curve* [54]. The information can be summarized in a single number by computing the mean value of the correlation over all time instants

$$\rho_m = \frac{1}{T}\sum_{t=1}^{T} \frac{\vec{x}_t \cdot \vec{y}_t}{\|\vec{x}_t\|\,\|\vec{y}_t\|} \tag{6.2}$$

where T is the number of samples and $\vec{x}_t, \vec{y}_t$ are the samples at time t from two MECGs.

Alternatively, the entire MECG can be interpreted as a vector, and the so-called "total body surface map (TBSM) correlation" between MECGs $\vec{X}$ and $\vec{Y}$ be computed as

$$\rho_t = \frac{\vec{X} \cdot \vec{Y}}{\|\vec{X}\|\,\|\vec{Y}\|} \tag{6.3}$$

Note that ρ_m and ρ_t are generally not equal: using

$$\vec{X} \cdot \vec{Y} = \sum_{i=1}^{TN} X_i Y_i = \sum_{t=1}^{T}\sum_{n=1}^{N} x_{tn}\, y_{tn} = \sum_{t=1}^{T} \vec{x}_t \cdot \vec{y}_t \tag{6.4}$$

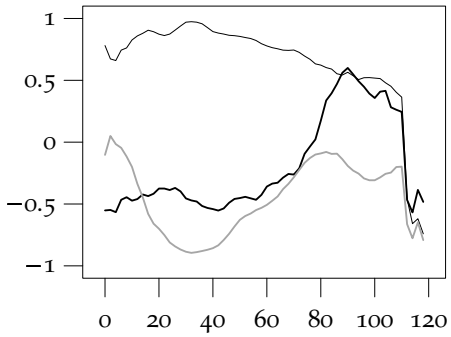

line	*segm.*	*distance*	ρ	ρ_m	ρ_t
thin	2	21 mm	0.86	0.78	0.65
thick	13	47 mm	−0.37	−0.36	−0.19
grey	22	61 mm	−0.51	−0.51	−0.45

Figure 6.5: *Examples of correlation curves between a QRS complex obtained by pacing in left-ventricular (LV) segment 11 (figure 6.4 or figure 6.7) and three other paced QRS complexes, which were all obtained from the same patient, by pacing in LV segments 2, 13, and 22. In the table on the right, the distances between the paired pacing sites as well as the ordinary correlation between QRSIs, ρ, the mean correlation ρ_m, and the TBSM correlation ρ_t are given.*

we have

$$\|\vec{X}\|\,\|\vec{Y}\|\,\rho_t = \sum_{t=1}^{T} \vec{x}_t \cdot \vec{y}_t \tag{6.5}$$

By comparison with (6.2) we see that the right-hand side of (6.5) cannot be expressed in terms of ρ_m. Only if all $\|\vec{x}_t\|$ and $\|\vec{y}_t\|$ are normalized, the two are equal. This can be seen by substituting $\|\vec{x}_t\| = \|\vec{y}_t\| = 1$, and consequently $\|\vec{X}\| = \|\vec{Y}\| = \sqrt{T}$, in (6.5), and dividing by T, which yields

$$\rho_t = \frac{1}{T} \sum_{t=1}^{T} \vec{x}_t \cdot \vec{y}_t = \rho_m$$

Some examples of correlation curves and the corresponding values of ρ_m and ρ_t are shown in figure 6.5. Applications of the TBSM correlation are discussed in section 6.7.

6.6 Correlation in the Left Ventricle

The pace-mapping database created by SippensGroenewegen et al. for the structurally normal left ventricle, the "NLV database," consists of 25 endocardial segments (figure 6.4), created from a total of 99 pace maps obtained from 8 patients [236]. The NLV database has been presented in a polar diagram, illustrated in figures 6.6 and 6.7. The other two databases they cre-

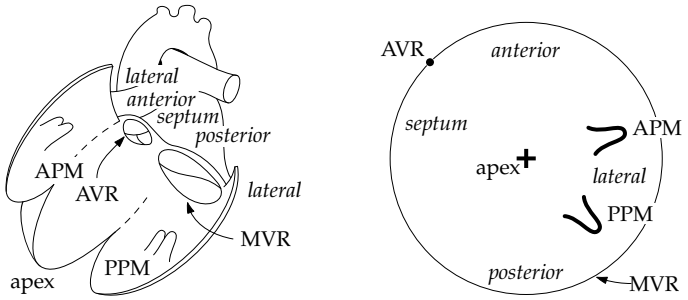

Figure 6.6: *Schematic anatomic diagram (left) [32, 119] and polar projection of the left ventricle (right) [236]. The polar projection can best be understood by imagining that one is looking at the ventricle from apex to base. This corresponds approximately to a left anterior oblique (LAO) view of the left ventricle. The circumference of the diagram represents the mitral valve ring (MVR); the position of the aortic valve ring (AVR) is also indicated. The positions of the anterior and posterior papillary muscles (APM and PPM) and endocardial quadrants (septum, anterior, lateral, and posterior) are indicated in both diagrams.*

ated for the left ventricle, i.e., those for patients with previous infarction, are discussed in the context of continuous localization in chapter 8.

In figure 6.8, correlations between selected mean maps and all other mean maps of the NLV database are shown graphically. To facilitate interpretation, the data in this figure were interpolated over the diagram between the mean segment positions. Extrapolation to the borders of the diagram was achieved by adding data points at the border which were assigned values determined by nearest neighbour interpolation. Data were then interpolated and smoothed by bicubic spline interpolation, and isocorrelation lines were computed from the smoothed data.

Correlations between segment mean maps range from -0.98 to $+0.96$. For each segment, approximately three quarters of the endocardial surface have low correlations, ranging from -0.98 to $+0.50$. The smooth monopolar patterns shown in figure 6.8 are representative for the entire database. Two minor deviations can be discerned, however. They are illustrated in figure 6.9 and figure 6.10.

In figure 6.9 the correlations with segment 25, in the vicinity of segments 6 and 10, are depicted. Segment 10 correlates better with segment 25 than segment 6, although segment 6 is closer to segment 25. This may be due to the elongated shape of segment 10 (figure 6.7) [236]. This segment consists of three pace maps, two of which are located between segments 6 and 25, while the third is situated near the aortic valve ring (AVR). The

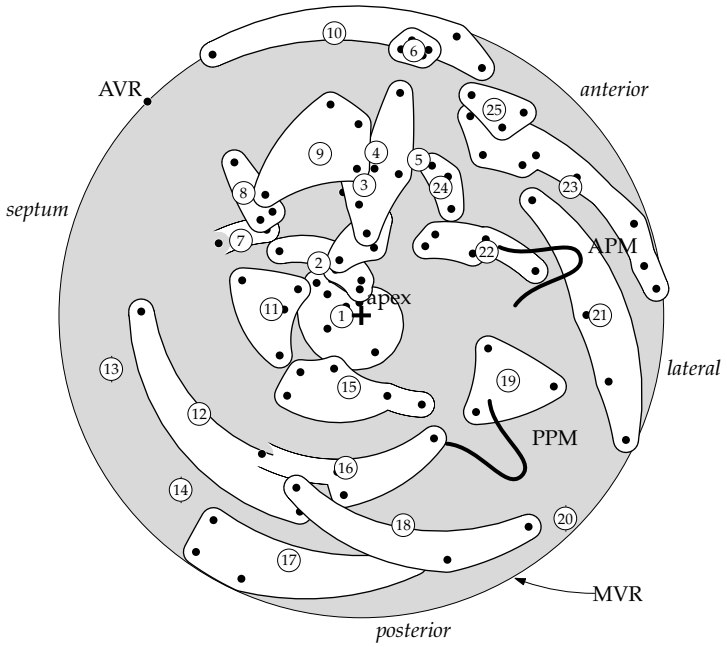

Figure 6.7: *Database segments and pacing positions of the QRSI database for the structurally normal left ventricle [236], indicated in a left-ventricular polar projection as explained in figure 6.6. Individual pacing positions are shown with dots. Segments, created by grouping positions with similar QRSI patterns, are indicated with white patches and labelled with encircled numbers.*

mean position of the segment was estimated as the geometric middle of the three pacing positions. A position more proximal to the first two pacing positions would have agreed better to the data of segments 6 and 25.

Figure 6.10 shows that the high correlation of segment 12 to segments 18 and 19 suggests that its position should be more proximal to the latter two. The explanation is the same as for segment 10 discussed above: segment 12 also consists of three pace maps, two of which are located between segments 16 and 17 (figure 6.7), the third close to segment 13 [236]. The mean position of the segment was again estimated by SippensGroenewegen et al. as the geometric middle of these three pacing positions, while a position near the first two would have been in better agreement with the data from neighbouring segments.

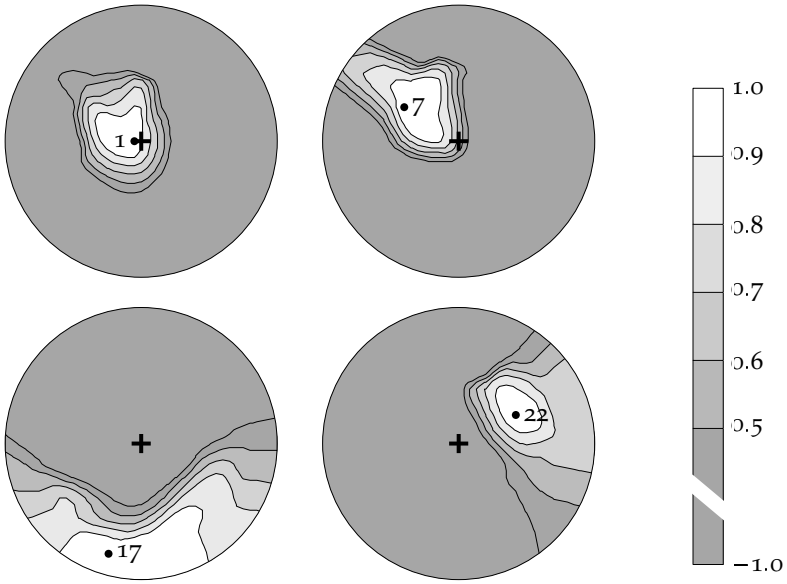

Figure 6.8: *Correlations of selected database mean maps in the normal left ventricle. In each of the 4 diagrams, the correlation of one database mean map* M *with all other mean maps in the database is shown graphically with greyshade coding and iso-correlation lines. The position corresponding to* M *is indicated with a dot and its segment number is indicated. Iso-correlation lines are drawn for correlation values of 0.5, 0.6, . . . , 0.9. All correlations below 0.5 are indicated with a single shade.*

6.7 Correlation in the Right Ventricle

The pace-mapping database created by SippensGroenewegen et al. for the structurally normal right ventricle (NRV), further referred to as "the NRV database," consists of 13 segments and corresponding segment mean maps, as illustrated in figure 6.11. The NRV database was created from a total of 83 pace maps obtained from six patients [236]. The positions of the pace maps and extent of the database segments are shown in figure 6.13 using a right-ventricular polar diagram, as illustrated in figure 6.12.

Correlations between segment mean maps of the NRV database range from −0.40 to +0.97, a smaller interval than in the NLV database (−0.98 to 0.96) [236]. In figure 6.14, correlations between selected mean maps and all other mean maps of the right-ventricular database are shown graphically. When comparing these results to the data shown in figure 6.8, it is also clear

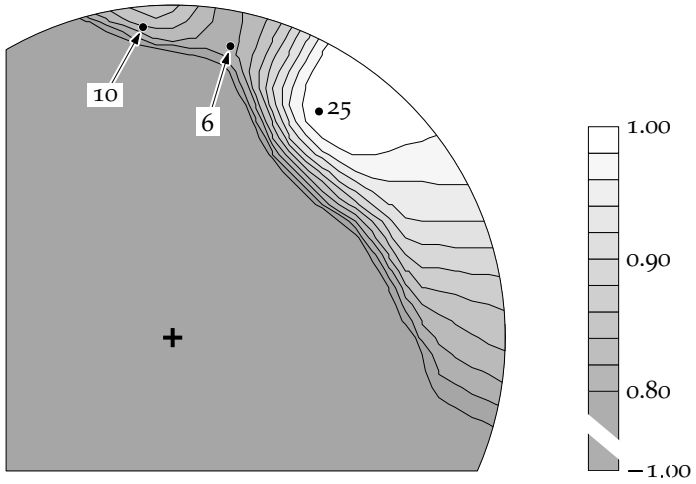

Figure 6.9: *Correlation with segment 25 in the normal left ventricle. The positions of segments 6 and 10 appear to be interchanged. The correlation distribution of segment 25 is used to illustrate this. The correlation with segment 6 is 0.83. Although segment 10 is located further away from segment 25, its correlation is higher (0.86). This results in a local maximum in the correlation distribution around segment 10. The positions of segments 6, 10, and 25 are indicated with dots. Iso-correlation lines are drawn for correlation values of 0.80, 0.82, . . . , 0.98. All correlations below 0.8 are indicated with a single shade.*

that the inter-segment correlations occupy a smaller range than for the NLV database. While approximately three quarters of the left-ventricular endocardium are covered by the darkest colour, i.e., have correlations lower than +0.5, this area is only approximately one quarter of the right-ventricular endocardium for the NRV database (figure 6.8). This difference cannot be explained from differences in LV and RV area; on the contrary, the RV endocardium has a larger area than the LV endocardium. Our conclusion is, therefore, that the localizing sensitivity of the QRSI is lower in the RV than in the LV. This may be due to the relatively thin wall of the RV, which, with its small muscular mass, contributes relatively little to the surface ECG.

In addition, figure 6.14 demonstrates that there are two distant areas, the anterior side of the lateral wall (segment 9) and the anterior side of the interventricular septum (segment 13), which have a higher QRSI correlation with each other than with areas in between, such as the apex and the anterior wall [236].

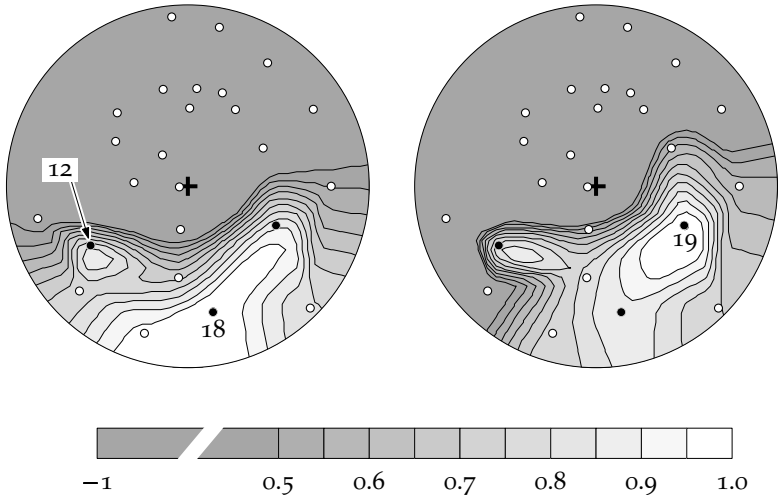

Figure 6.10: *This figure illustrates the non-conformant position of segment 12 in the NLV database. Correlations with segment 18 (left panel) and segment 19 (right panel) are depicted. The higher correlation values around segment 12 suggest that it should lie closer to segments 18 and 19. Note that the (cubic) interpolation algorithm predicts a higher correlation in the area next to the mean position of segment 12, than the correlation of the segment mean map itself. In both diagrams, the positions of segments 12, 18, and 19 are indicated with black dots. The positions of the other segments are indicated with open circles. Iso-correlation lines are drawn for correlation values of 0.50, 0.55, ..., 0.95. All correlations below 0.50 are indicated with a single shade.*

An explanation for this phenomenon is that the thin lateral wall of the right ventricle has a very small contribution to the QRSI pattern. Activation starting in the lateral wall will spread towards the septum and activate the relatively thick left-ventricular wall in approximately the same way as septal activation would. The lateral wall activation itself, in addition to generating less current, may look similar on the body surface to septal activation originating in an opposed position.

Thus, other criteria than the QRSI alone are to be introduced to differentiate between ectopic ventricular beats of septal and lateral origin. It appears that the negative QRSI extreme can be used to discriminate between RV segments 9 and 13. Given the inter-patient differences in ECG amplitudes, it is preferable to use the ratio of the positive and negative QRSI extrema instead. The ratio q of the negative content and positive content of the map

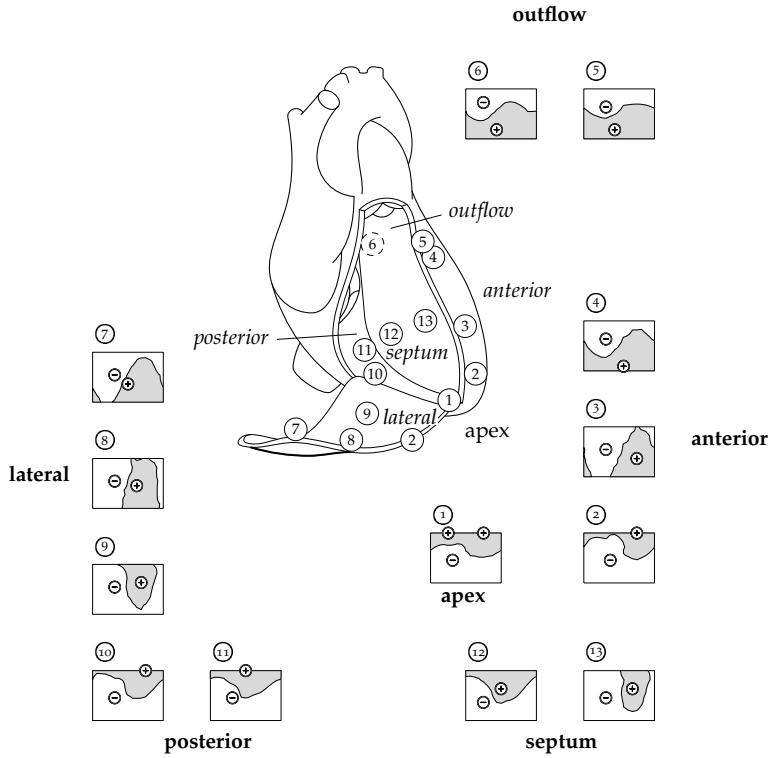

Figure 6.11: *The database of 13 mean paced QRS integral maps obtained from the structurally normal right ventricle [236]. The maps are represented in the format introduced in figure 1.2 on page 16. Each map corresponds to a mean segment position in the right ventricle (encircled numbers), represented in a schematic diagram. The maps are arranged in a way that approximates the corresponding positions in the ventricle.*

was computed as

$$q = \left(\sum_{i \in \{i_n\}} {v_i}^2 \Big/ \sum_{i \in \{i_p\}} {v_i}^2 \right)^{1/2} \tag{6.6}$$

where v_i are the elements of the QRSI, $\{i_n\}$ are the indices of the elements $v_i < 0$ and $\{i_p\}$ are the indices of the elements $v_i > 0$. The distribution of q over the RV, which was estimated from the database maps and interpolated (cubic), is shown in figure 6.15.

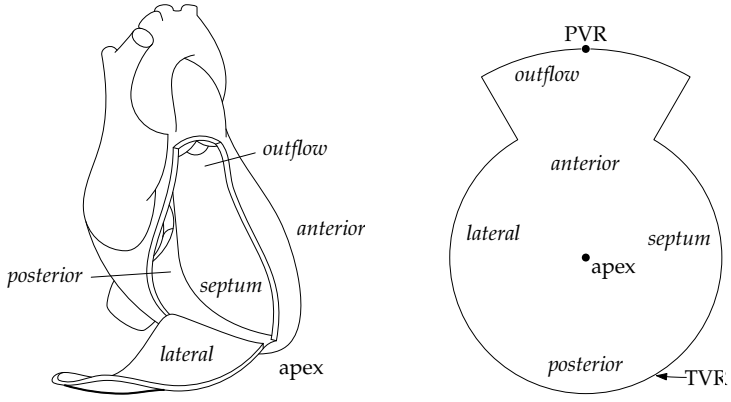

Figure 6.12: *Schematic anatomic diagram of the right ventricle (left) [119, 236] and polar projection of the same (right) [236]. The polar projection can best be understood by imagining that one is looking at the ventricle from apex to base. The circumference of the diagram represents the tricuspid valve ring (TVR); the wedge-shaped part on top is the right-ventricular outflow tract, which is shown in an unwrapped format and ends in the pulmonary valve ring (PVR). The positions of the apex and endocardial quadrants (septum, anterior, lateral, and posterior) are indicated in both diagrams.*

From this figure it appears that high q values are very specific for the anterior septum of the RV; the value of 11.6 in segment 13 is much larger than in the other segments. Intermediate values are found in the anterolateral area, i.e., the area that also resembles segment 13 most in terms of QRSI pattern. However, the difference in q value is large enough to differentiate between the two. The negativity can therefore be used as an adjunct to the correlation coefficient in order to discriminate between the regions around segments 9 and 13.

The performance of q and the map minimum itself are compared in figure 6.16. It is apparent from this figure that there is considerable overlap in minimum value between maps from segment 13 and maps from other segments. There is almost no overlap in q values between maps from segment 13 and maps from other segments, although maps from segment 2 also have high q values.

Also shown in figure 6.16 are

- the correlations between all paced QRSIs underlying the RV database and the mean QRSI of segment 13, as well as
- the "TBSM correlations" (section 6.5.3) between a QRS complex ob-

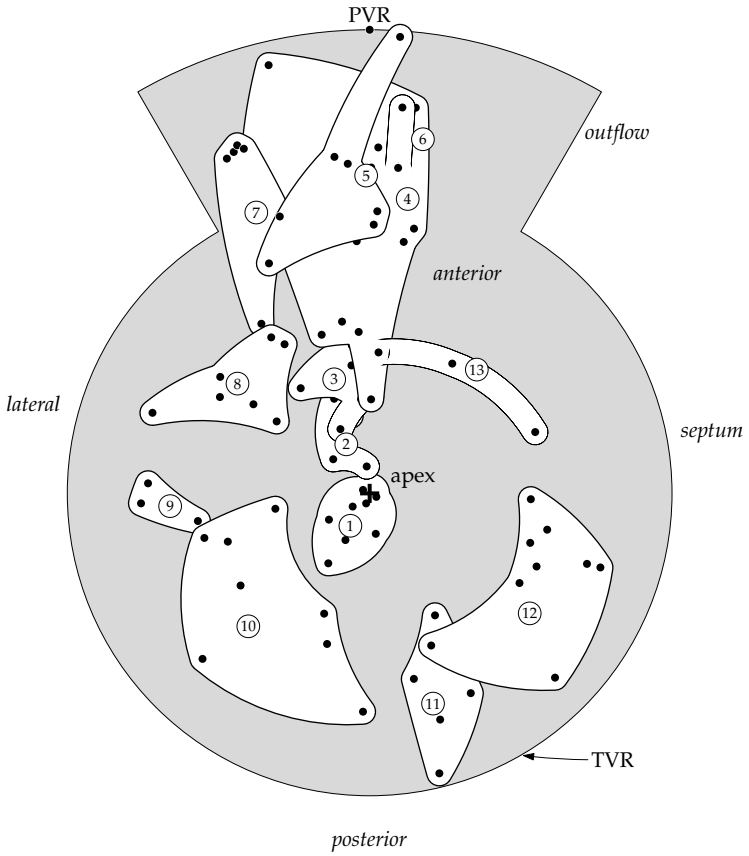

Figure 6.13: *Database segments and pacing positions of the QRSI database for the structurally normal right ventricle [236], indicated in a right-ventricular polar projection as explained in figure 6.12. Individual pacing positions are shown with dots. Segments, created by grouping positions with similar QRSI patterns, are indicated with white patches and labelled with encircled numbers.*

tained by pacing in segment 13 and all other paced QRS complexes belonging to the database.

Instead of the correlation itself, its inverse cosine is shown; the rationale for this conversion will be discussed in section 6.8. It appears that the QRSI correlation can separate segment 13 completely, while the TBSM correlation cannot.

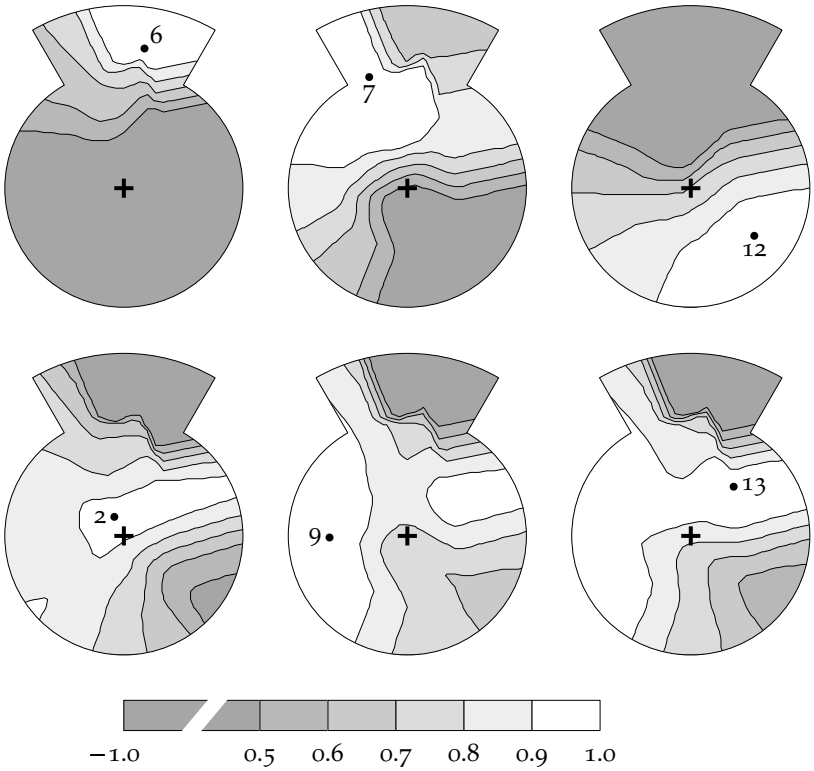

Figure 6.14: *Correlations of selected database mean maps in the right ventricle. In each of the 6 diagrams, the correlation of one database mean map M with all other mean maps in the database is shown graphically, with greyshade coding and iso-correlation lines. The position corresponding to M is shown with a dot, and its segment number is indicated. Iso-correlation lines are drawn for correlation values of 0.5, 0.6, . . . , 0.9. All correlations below 0.5 are represented with a single shade. The upper three diagrams are examples of 'normal' cases, where the correlation decreases with increasing distance from the map. The lower three diagrams show problematic cases, where distant areas show larger correlations than more proximal areas. The two most notable areas with high mutual correlations are the anterior side of the lateral wall (segment 9) and the anterior side of the interventricular septum (segment 13).*

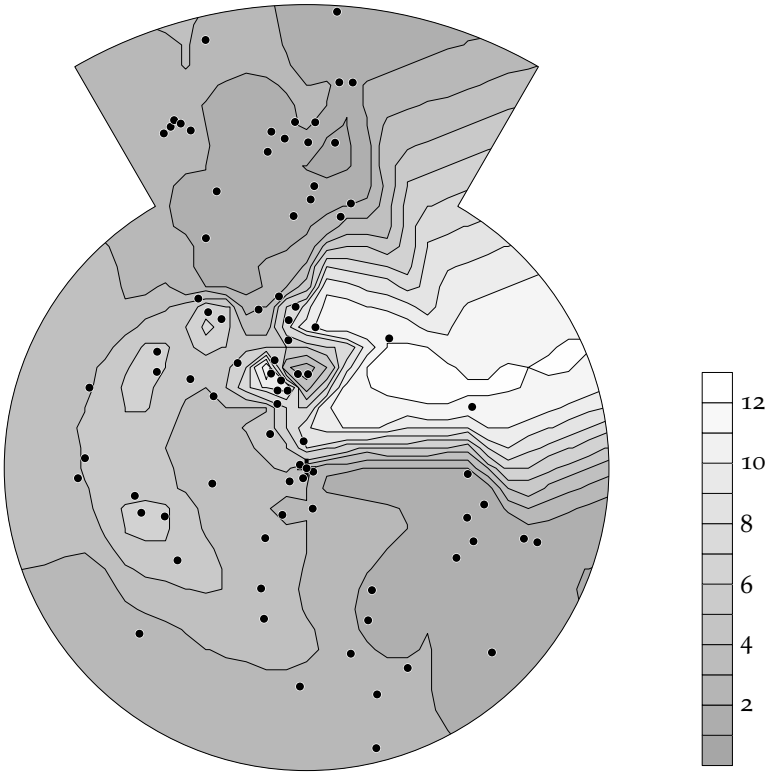

Figure 6.15: *Distribution of the QRSI negativity* q *(equation 6.6) over the right ventricle, computed from the values of the individual pace maps. The dimensionless quantity* q *ranges from 1.1 to 11.6 for mean segment positions, and from 1.0 to 11.8 for individual pace maps. Contours are drawn at unit intervals; in addition, values are indicated with shades of grey. The positions of the data points (pacing positions) are indicated with dots. The cross sign indicates the right-ventricular apex.*

6.8 Relative Localization: Distance Between Exit Sites

The relation between (normalized) QRS integral map and location is a continuous one; that is, an infinitesimal change to a map always corresponds to an infinitesimal change in location. Knowledge of this relation is useful for diagnosis and pace mapping procedures, as it allows the estimation of

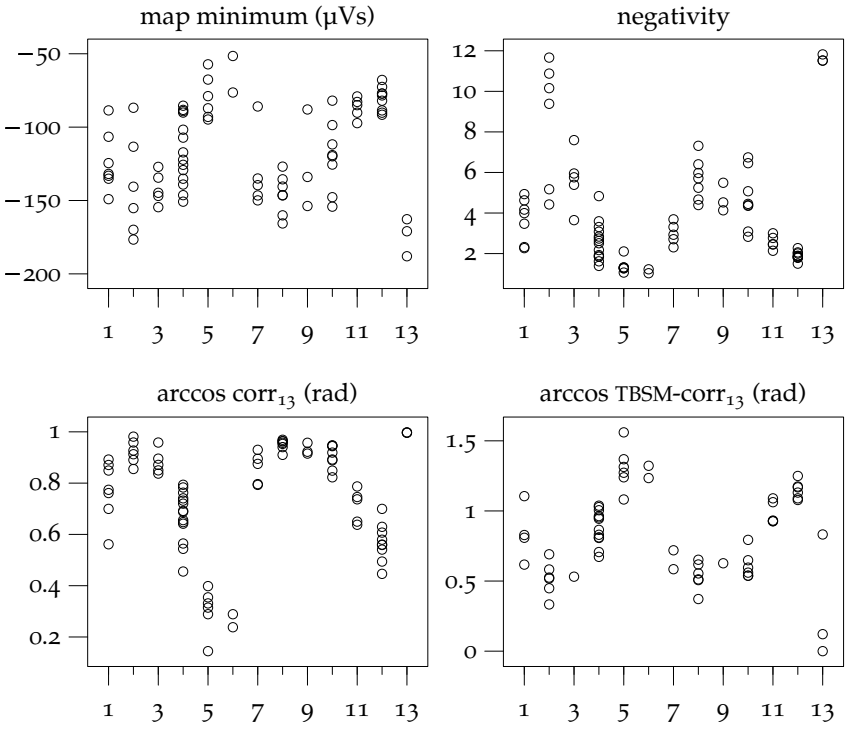

Figure 6.16: *Four measures to compare maps in segment 13 with segments in the lateral wall: the minimum of the map, negativity* q*, correlation to the mean map of segment 13, and TBSM correlation to a MECG from segment 13, respectively. Each dot indicates the value for one pace map. A total of 80 pace maps was analyzed. The negativity index separates segment 13 better from the free-wall segments 8 and 9 than the minimum value itself and the two correlations, but segment 2 also has a remarkably large negativity. Segments 3, 8, 9, and 10 also have a high negativity, but not so high as to make them indistinguishable from segment 13. Large negativity is not a characteristic of the entire septum: all maps in segment 12 have a very small negativity, so that the boundary runs through the middle of the septum as can be seen in figure 6.15. QRSI correlation and TBSM correlation give comparable results, except that one of the maps from segment 13 has a relatively low TBSM correlation with the other maps in this segment. The QRSIs of segment 13, in contrast, correlate very well. Instead of the correlation itself, the inverse cosine of the correlation was shown, in order to make differences at high correlation values more clear.*

distances between different exit sites of an arrhythmia, or between the exit site of the target arrhythmia and a pacing position. In the following sections, the term "distance between exit sites" is sometimes used to denote all such distances; also if pacing sites are involved.

6.8.1 A linear distance estimator

The traditional statistic to compare QRS integral maps is the electrocardiographic correlation coefficient ρ (5.2). However, it is known that the relation between distance and ρ is not linear. In particular, for short distances, highly similar ρ values are found (0.98–0.99) while values near -1 are found for the most distant sites. Sometimes correlation coefficients for pairs of near sites has to be compared using tenths of percents, while large distances are compared in terms of *tens* of percents. This means that the software used for pace-mapping procedures must display correlation coefficients with 3 or 4 digits of which the last one or two should often be ignored. The nonlinearity between distance and ρ is also inconvenient because it is difficult to estimate the distance between exit sites from ρ values.

We assessed the relation between distance and correlation coefficient for the pace maps in the NLV database. For each patient, on average 13 pace maps are available (range 8–21) [236]. With n pace maps, $\frac{1}{2}n(n-1)$ distances and correlation coefficients can be computed. Obviously these are not all independent. A total of 669 map pairs was analyzed. Distances are straight-line distances in 3-D (for larger distances, these may differ considerably from the distance along the wall). The correlations ρ between the maps are plotted against the distance between the pacing positions in figure 6.17. It is evident from this figure that there is a large spread in distances found for approximately the same correlation coefficient. This may be expected, since it was shown before that the "electrocardiographic sensitivity" is not the same in all regions of the heart. In addition, each pacing position is subject to a measurement error of up to 7 mm [88].

Mean and standard deviation of ρ were estimated as functions of the distance by dividing data in intervals of 20 mm. Fisher's z was computed for the ρ values to obtain more normally distributed data. Mean μ_z and standard deviation σ_z were estimated from the z values. Values of $\mu_z - \sigma_z$, μ_z, and $\mu_z + \sigma_z$ were transformed back to the ρ domain in order to make appreciation of confidence intervals possible. This analysis was performed for bins centred at 2, 4, ..., 80 mm; the results are shown with lines in figure 6.17. The back-transformed value of σ_z itself was approximately constant at a level of 0.55.

It is also evident from figure 6.17 that the relation between distance and correlation is nonlinear. For distances up to 20 mm, the correlation coef-

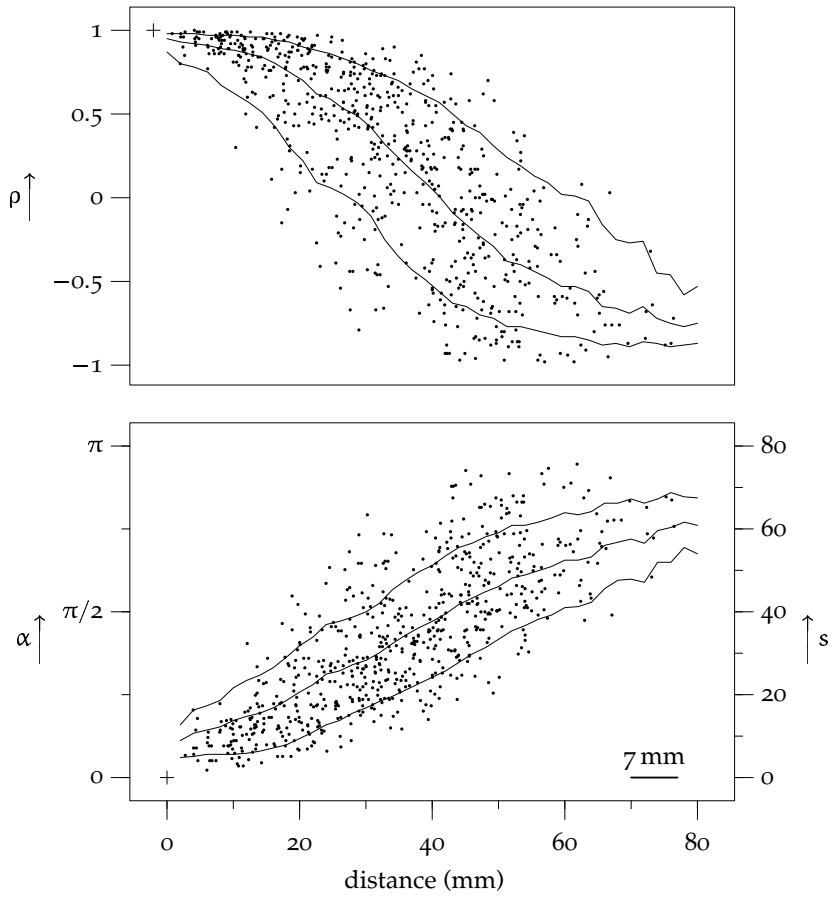

Figure 6.17: *Correlation coefficient* ρ *of pairs of paced QRS integral maps (upper panel) and inverse cosine* $\alpha = \arccos \rho$ *(lower panel), each plotted as a function of the distance* d *between the measured pacing positions. The distance was normalized by dividing 3-D distances by the individual ventricular length and multiplying them by a typical ventricular length of 80 mm. Data were taken from the 99 pace maps and corresponding pacing positions of the NLV database. Estimates of mean* ρ *and mean* α *as well as their standard deviations, are indicated with curves in the diagrams. One observes that the relation* $\rho(d)$ *is a nonlinear function, resembling a cosine on the interval* $[0, \pi]$*. Accordingly, the relation* $\alpha(d) = \arccos \rho(d)$ *is more linear. In both graphs, the value for identical maps (*$d = 0, \rho = 1, \alpha = 0$*) is indicated with a cross. On the right side of the lower plot, a scale for the quantity* s *(equation (6.9) on page 130) is plotted.*

ficient decreases very slowly, while it decreases rapidly and with a larger spread for distances of about 40 mm. The relation between distance and correlation resembles an inverse cosine rather than a straight line. This is not surprising: the pace-mapping studies by SippensGroenewegen et al. showed that QRS integral maps paced at opposite sides of the left ventricle had opposite patterns [236, 237]. In the geometrical interpretation of QRS integral maps, this means that the map vectors from such sites have opposite directions. Given the continuous relation between map pattern and exit site, it may be expected that the angle between QRSI vectors (in the multidimensional signal space) is linearly related to the spatial angle defined by a central point somewhere in the LV cavity and the positions on the LV endocardium, which is in turn, by a crude approximation, linearly related to the distance. In that case, a linear relation exists between the distance and the inverse cosine of the correlation coefficient,

$$\alpha = \arccos \rho \tag{6.7}$$

The relation of α to the distance is depicted in the lower panel of figure 6.17. Despite the large variation between patients and endocardial areas, it is discernible from this plot that the relation between α and distance is approximately linear. Mean and standard deviation of α are shown with lines in the same plot. The standard deviation is constant for distances above 20 mm and decreases for distances close to zero.

When the mean line in figure 6.17 is extrapolated to distance zero, it crosses the vertical axis at a nonzero level. This offset can also be assessed by fitting a straight line to the data. Using a least-squares fit, we find

$$\alpha = 0.087 + 0.035\,(\mathrm{rad/mm})\ d \tag{6.8}$$

where d is the distance between pacing sites, in millimeters. The offset of 0.087 radians suggests that two QRSIs paced at exactly the same location in the same respiratory phase are not exactly the same. In order to exclude all other variability, this was verified using series of beats paced at the same site while the patient was holding his breath. Values of α were computed for all possible pairs of maps from this series, yielding $\bar{\alpha} = 0.07 \pm 0.04$ (mean $\pm$ standard deviation), which is well in agreement with the offset value of 0.087 obtained above. The origin of this dissimilarity in maps is not clear. If we assume that it results from white noise (random errors) in the integral maps, adding noise to measured maps allows us to estimate that the amplitude of the noise would have to be approximately 5 % of the norm of the map, i.e., approximately 6 µVs. For the data used here, the total noise level of a QRSI due to 3 µV measurement noise, and additional noise due to baseline correction [154] is approximately 1 µVs. Physiological

variability may therefore provide the largest contribution to the difference although errors in QRS onset and offset detection may also play a role.

Due to its approximately linear relation with the distance between exit sites, α is useful for presentation of map differences during catheterization procedures. For convenience, α can be scaled; for example, the quantity

$$s = \frac{\alpha}{\pi} \cdot 80\,\mathrm{mm} \tag{6.9}$$

is be approximately equal to, and linear with, the distance between exit sites in the left ventricle. Therefore it would be a highly intuitive estimate for the distance. Since $0 \leq s \leq 80$, and sub-millimeter accuracy is neither needed nor attainable, s can always be represented with two digits. The constant $80\,\mathrm{mm}/\pi$ was obtained from equation (6.8), ignoring the small offset.

6.8.2 Correlation between maps paced at short distances

The data presented in figure 6.17 have a broad distribution. This has at least two causes: 1) errors of up to 7 mm are made in the determination of individual pacing positions, leading to even larger errors for the distances between pairs of positions, and 2) the relation between distance and correlation varies in different regions of the heart. Both causes can be excluded when pacing is performed with a single multi-electrode catheter, placed in a stable position. Results from a pilot experiment of this kind are shown in figure 6.18.

The data in figure 6.18 were obtained by unipolar pacing via all electrodes of a decapolar catheter which was kept at a stable position in the right ventricle. The interelectrode distance of this particular catheter was 2 mm. Since only one patient was involved and the pacing positions are relatively close, there is less variability in these data than in those shown in figure 6.17.

Using these data it is possible to demonstrate that ρ is not a linear function of the distance, while the linearity of α cannot be disproved. For each distance between pairs of pacing positions, a mean value (referred to as y_i) and standard deviation (referred to as σ_i) were computed. A straight line was fitted through the data points by minimizing

$$\chi^2 = \sum_{i=1}^{N} \left(\frac{y_i - (ax_i + b)}{\sigma_i} \right)^2 \tag{6.10}$$

where x_i is the distance, y_i stands for either ρ or α, and the constants a and b specify the line $y = ax + b$. For a "good" fit, χ^2 should be smaller

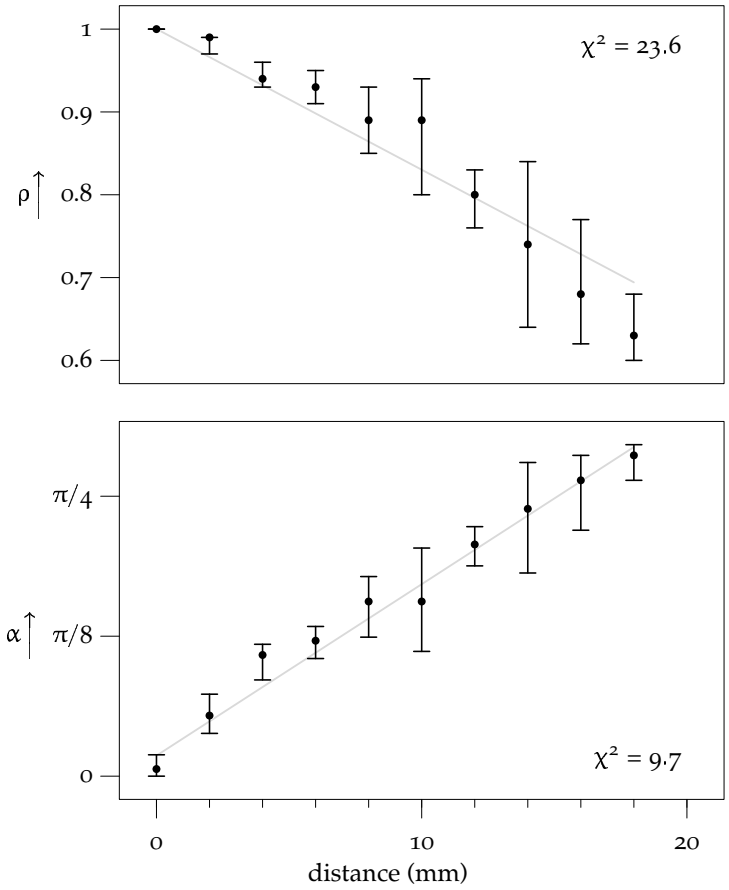

Figure 6.18: *Correlation coefficient* ρ *of pairs of paced QRS integral maps (upper panel) and inverse cosine* $\alpha = \arccos\rho$ *(lower panel), each plotted as a function of the known distance* d *between the measured pacing positions. Pacing was performed via all electrodes of a single decapolar catheter with 2 mm interelectrode spacing, which was kept in a stable position. Correlation with a map paced at the first electrode was computed for each paced map. For every pacing electrode, the mean correlation is shown with a dot; minimum and maximum are indicated with T-shaped lines. Note that the relation* $\rho(d)$ *is a nonlinear function. A straight-line fit of these data has* $\chi^2 = 23.6$*, which can be considered as a bad fit given that there are 10 data points and 2 fitting parameters. In addition, the deviations of the data points with respect to the line are systematic: the first six points are located above the line and the last three points below it. The relation* $\alpha(d)$ *is more linear with* $\chi^2 = 9.7$ *and without systematic deviations.*

than the number of data points N minus the number of parameters [215], i.e. $\chi^2 \approx 8$. As shown in the figure, $\chi^2 = 23.6$ for ρ, indicating a bad fit; while $\chi^2 = 9.7$ for α, indicating a reasonably good fit. The variability in the data is caused primarily by respiration, and to a lesser extent by noise. This effect can be reduced either by using only maps paced in a similar respiratory phase, or by averaging over at least one complete respiratory cycle. For the data shown in figure 6.18, the respiratory phase was unknown and there were not always enough paced complexes available for averaging over a complete cycle. This may have led to an underestimation of some of the σ_i and bias in the averages y_i.

For α, the line parameters were $a = 0.058$ and $b = 0.048$. Thus, comparing to equation (6.8), it seems that the offset was somewhat smaller and the line steeper. However, the offset value lies in the range of 0.07 ± 0.04 obtained for pacing at a single site. The difference is probably not significant. Otherwise, the smaller offset may be due to the shorter interval over which the maps were obtained (a few minutes in total, compared to a pace-mapping session which may have taken several hours). The larger slope b may be explained by the position of the catheter, which had its distal electrode in the RV outflow tract and its proximal electrode in the RV lateral wall, thereby covering an area with relatively high electrocardiographic sensitivity (figure 6.14 on page 124).

6.9 Interpolation

The pace-mapping databases created by SippensGroenewegen et al. [236, 237] and the data presented in section 6.8 suggest that there is a unique relation between exit site and QRS integral map pattern. Since this relation should also be continuous, i.e., any infinitesimal change in map results in an infinitesimal change in pattern, it follows that localization is in principle possible with unlimited resolution—albeit not with unlimited accuracy, due to measurement errors and biological variability. This continuous relationship can be exploited essentially in two ways: by "continuous localization," introduced in section 6.10, and by interpolation.

Interpolation of maps was investigated by Latour et al. [139, 140]. If two or more QRS integral maps have been created by pacing at known positions, any QRSI M can be approximated by a weighted sum of these maps. The approximation is better if more maps are used. Since QRSIs have a low nondipolar content (chapter 5) a good representation is possible with only three maps. The position corresponding to M is then predicted as the same weighted sum of the positions.

This method is primarily useful for pacing positions that are not far

apart. It is applicable in the final phase of a pace-mapping procedure [194] when several paced maps have been created in the vicinity of the exit site in order to predict the position of the exit site itself.

6.10 Continuous Localization

If we consider a QRS integral map as a vector in a multidimensional space where each dimension corresponds to a lead, there must be a continuous 2-D subspace in which all QRS integral maps with left-ventricular endocardial exit sites lie. If the continuous relation between QRSI and exit-site location, discussed in section 6.8, holds in all directions, then not only the distance between exit sites can be estimated in a continuous way, but also the direction of their difference. If that is true, the location corresponding to a map that does not perfectly match any of the database maps, can be estimated by interpolating between several maps that correlate well.

Alternatively a well-behaved surface S could be fitted to the database maps and a mapping could be created from S to the endocardial location. What "well-behaved" means, is not clear in advance. It can be determined by observing the difference in maps originating from relatively close positions. An advantage of this approach is that it reduces the effect of errors in the database locations and maps because many database entries contribute to each single point of S. A surface with a simple description also enables fast computation of location estimates with arbitrary precision (but not arbitrary accuracy, because the accuracy is limited by the accuracy of the database). A precise estimate can prove useful when an advice on catheter positioning must be generated.

A method to obtain a description of a surface is a self-organizing map (SOM). A well-known implementation of a SOM is the Kohonen network [133, 134]: a set of interconnected points that are attracted by a set of training points, and where each point also tries to stay close to its pre-specified neighbours, so that a continuous mapping can develop.

A more simple method is described in chapters 7 and 8 [212]. This method makes use of the fact that QRS integral maps can, by normalization and Karhunen–Loève (KL) transformation, be described to a large extent with only two parameters. In this case, the surface S is a sphere in the first three dimensions determined by the KL transformation.

In chapter 7, the continuous localization method is developed and evaluated with the data underlying the NLV database. Adaptation to infarction-specific databases, which allows the method to be used more efficiently in patients with chronic infarction, is discussed in chapter 8. In addition, chapter 8 presents an application of the method for the estimation of devi-

ation in body surface map patterns due to chronic infarction.

6.11 Discussion

The creation of an automatic system for complete arrhythmia monitoring, i.e., detection, delineation, classification, and localization of arrhythmias, for use in the catheterization laboratory, is technically feasible. A review of the literature on detection, delineation and classification (sections 6.2 and 6.3) indicates that these problems can be solved, especially BSM data are available. Localization of VT using databases of paced body surface maps (section 6.4) provides improved accuracy for initial catheter positioning.

Using the correlation between a VT map and paced maps, or preferably the distance estimate presented in section 6.8, the catheter can be directed quickly to the exit site of the VT. The continuous localization method, further discussed in chapters 7 and 8, can additionally estimate the direction in which the catheter should be moved, thereby possibly reducing the number of pace maps that must be made before the exit site is found.

A remaining problem is how to present the catheter positioning advice. Currently, polar diagrams as described in this chapter are used for clinical tests, but they are difficult to interpret and to relate to the other imaging modalities that are used during catheterization. An improved method, which can display localization results obtained with the methods described here in a friendlier way, is described in chapter 9.

Chapter 7

Continuous Localization of Cardiac Activation Sites Using a Database of Multichannel ECG Recordings

Monomorphic ventricular tachycardia and ventricular extrasystoles often have a specific exit site which can be localized using the multichannel surface ECG and a database of paced ECG recordings. An algorithm is presented that improves on previous methods by providing a continuous estimate of the coordinates of the exit site instead of selecting one out of 25 predetermined segments. The accuracy improvement of the proposed method is greatest, and most useful, when adjacent pacing sites in individual patients are localized relative to each other. Important advantages of the new method are the objectivity and reproducibility of the localization results. — *IEEE Trans. Biomed. Eng.* 47(5) pp. 682–689, May 2000 [212];

7.1 Introduction

Electrocardiographic body surface mapping is used in the catheterization laboratory to perform high-resolution localization of endocardial exit sites of ectopic ventricular beats and monomorphic ventricular tachycardia (VT) [235–237, 242]. For this purpose, the surface potentials during such an arrhythmia are summed over the QRS complex of the electrocardiogram (ECG).

Using the resulting QRS integral map (QRSI), the exit site can be attributed to one of 25 different segments of origin in the structurally normal human left ventricle [236]. The latter result is obtained using a database consisting of 25 mean paced QRSIs [236] (see figure 7.1 (c)). Each mean QRSI in the database corresponds to a known endocardial segment of activation onset. The exit site of a VT can be predicted by comparing its QRSI with the paced QRSIs in the database.

A three-phase mapping procedure is currently used by our group to guide the catheter to the optimal site for curative ablation [194]. First, a QRSI is obtained from the target arrhythmia. This QRSI is displayed and compared to the database of 25 mean maps to select the best matching database map. The segment that corresponds to this database map is the initial estimate for the exit site of the arrhythmia. Maps are compared using the correlation coefficient [151].

Second, an endocardial catheter is positioned at the identified ventricular segment. By electrical stimulation with the distal electrode pair of the catheter, ectopic ventricular beats are electrically induced (paced) while the position of the catheter tip is monitored using biplane fluoroscopy. The surface ECG corresponding to the paced beats is recorded and the QRSI of a paced beat is computed. This paced QRSI is displayed and compared to the QRSI of the arrhythmia and to the database maps, to estimate the exit site of the arrhythmia relative to the catheter position. The catheter is subsequently moved to the estimated exit site. The ventricle is paced again at this site and a new QRSI is made. These steps are repeated until the site is found where the paced QRSI matches best with the QRSI of the arrhythmia.

In the third phase of the mapping procedure, local activation sequence mapping [119] is performed, starting at the site identified in the second phase. This procedure is aimed at finding the site where the earliest endocardial activation (premature depolarization) can be recorded, i.e., the site of origin of the arrhythmia. This is the target site for ablation, which may differ from the exit site which is found in the second phase of the procedure. Ablation is performed by applying radiofrequency current from the tip electrode of the catheter.

A limitation of the database-lookup method is that it provides discrete results; the localization result of the first phase is a selection of one out of 25 possible segments of origin. This means that the estimated position cannot be more precise than the size of a segment. The segment size in this database is $3.3 \pm 1.4\,\mathrm{cm}^2$ [236]. In contrast, the resolution of stimulus site separation using body surface potentials has been estimated at 2–5 mm [76, 176], i.e., identification of a circular area smaller than 0.1–0.8 cm^2. The large difference between this accuracy and the mean database segment size suggests that the current method does not take optimal advantage of

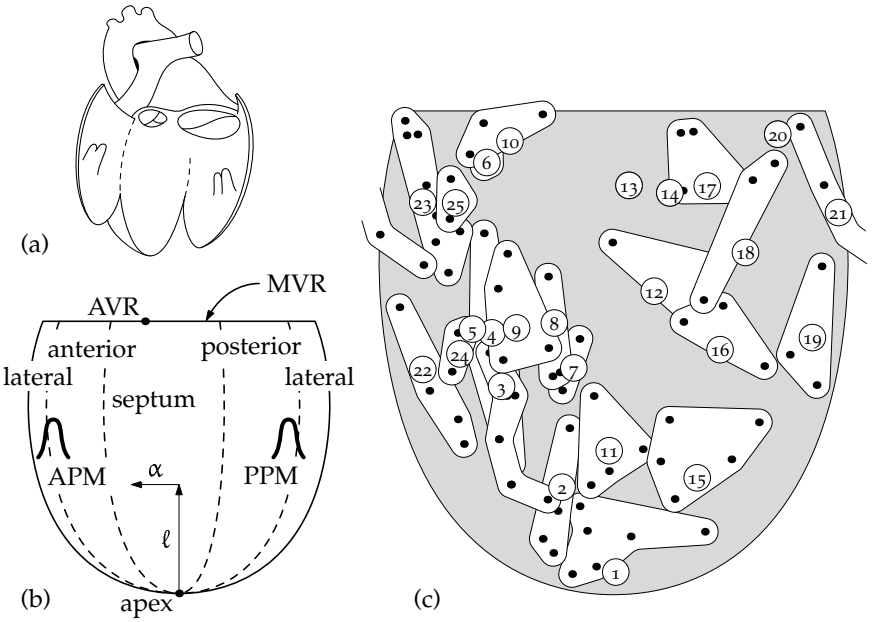

Figure 7.1: (a) *Cut-open view of the left ventricle and* **(b)** *illustration of the left ventricular diagram. This diagram displays the endocardium, opened at the lateral wall; it resembles the cut-open view shown in panel a. The top edge represents the mitral valve ring (MVR), the apex is indicated at the bottom. The width mimics the circumference of the ventricle as a function of the ventricular length. Also indicated are the four longitudinal quadrants (anterior, septum, posterior, and lateral) separated by dashed lines, the anterior and posterior papillary muscles (APM and PPM), and the aortic valve ring (AVR). This diagram can be generated directly from left ventricular cylinder coordinates (discussed in text): ventricular length ℓ translates to the vertical distance to the apex and the horizontal position is a fraction $\alpha/2\pi$ of the diagram width at the given length ($-\pi < \alpha \leq \pi$), where α represents the ventricular angle.* **(c)** *Pacing sites, indicated with dots, and pacing segments, indicated with white patches, of the database of 25 mean pace-maps for the structurally normal left ventricle, previously created by SippensGroenewegen et al. [236]. Mean positions of segments are labelled with encircled numbers. Segment 21 crosses the border of the diagram.*

the attainable resolution. Another limitation of the current method is that, in the second phase, physicians have to interpolate mentally between a pace-map and at least three database maps to determine the optimal site for subsequent catheter placement. This is a task for which a computer program might be more adequate. A computer program would be able to make full use of the precision of body surface mapping and would provide objective and reproducible results.

The method that will be described here serves to remove the limitations that the discreteness of the database imposes and provides objective results by giving a continuous estimate of the location corresponding to a given QRSI using the full information content of the database. The accuracy of this estimate remains of course limited by the accuracy of the database locations and their corresponding QRSIS. However, the better resolution, and the use that is made of all the information that is contained in the database—instead of just the single map that correlates best—may improve the localization accuracy considerably. More importantly, if two or more paced QRSIS are obtained from the same patient in a single session, as is the case in the second phase of the mapping procedure, a precise estimate of their relative positions is provided which can be used to guide the catheter quickly to the exit site.

Our method, which is described fully in section 7.2, is based on the following considerations. Paced QRSI patterns originating from the left ventricle are mainly determined by the pacing position on the endocardial surface of the left ventricle [104,236]. If we assume that the activation sequence is uniquely determined by the pacing site and does not vary significantly from patient to patient, and if we assume that the QRSI varies continuously with the endocardial position of origin, then there exists a subspace S in the multidimensional QRSI space with the same topology as the left ventricular (LV) endocardial wall, that is, a surface. Each point on S then corresponds to an endocardial position. By identifying S, we can compute the position on a two-dimensional approximation of the endocardium from a given QRSI by projecting the QRSI on S and applying an $\mathbb{R}^2 \rightarrow \mathbb{R}^2$ function ($\mathbb{R}$ is the set of real numbers).

Because it was observed that the amplitude of a QRSI does not contain information on the site of origin [236], we assume that S is star-like with respect to the origin of map space (i.e., a straight line from any point on S to the origin does not intersect S), and project it on a unit sphere in the first three dimensions after application of a Karhunen–Loève (KL) transform, previously determined from a large set of paced QRS integral maps. S can then be parameterized using spherical coordinates. The mapping to the endocardial surface is obtained by fitting a continuous mapping function to a set of pace-maps and their measured pacing positions.

7.2 Methods

The endocardial wall is described using "left ventricular cylinder coordinates" [236]. These coordinates are based on the line from the LV apex to the geometric middle of the mitral valve ring (MVR). The *ventricular length* ℓ is the distance of a position, projected on this axis, to the apex, and normalized to the axis length; the *ventricular angle* α is the angle of a position relative to the angle of the aortic valve ring. Figure 7.1(b) illustrates these concepts.

Pace-mapping data from the studies of SippensGroenewegen et al. were used to train and test our method [236]. To create the database of 25 mean pace-maps for the structurally normal left ventricle, they recorded 62-lead body surface ECGs during LV pace-mapping in a group of eight patients with normal cardiac anatomy. The three-dimensional (3-D) position of the catheter tip was determined quantitatively using digitized biplane fluoroscopic images with a localization error $\leq$7 mm [88, 89, 236] (circular area of 1.5 cm^2). A total of 99 pace-maps was used to create the database; these pace-maps are used here to fit and test our algorithm.

The 62 unipolar ECGs were recorded with equipment that was previously described by Grimbergen and MettingVanRijn [79, 172]. The electrode positions, which included the standard precordial leads, were chosen from the 192 vertices of a regular 12×16 grid covering the chest and back of the patient [160, 241]. Onset and offset of the QRS complex and suitable time instants for baseline correction were selected manually according to previously defined criteria [236]. A linear correction for baseline drift was applied. The QRS integral map was computed by summing each lead over the QRS complex, and then interpolating the irregularly spaced sites to a regular 12×16 matrix by iterative discrete Laplacian minimization [154]. In the interpolation process, data values from failing leads were replaced by values obtained by interpolation from neighbouring leads in the same way as the non-measured grid points. For further analysis, we used the 192-element maps. This was done to work with a more universal electrode array; we could also have used the 62 leads with interpolated rejected leads.

7.2.1 Localization algorithm

A QRSI is regarded as a 192-element vector containing an element corresponding to each of the 12×16 grid points. A fixed KL transform, previously determined from the 99 QRSIS, was applied to each QRSI [161]. The covariance between the 192 "channels" of the maps was computed, and the eigenvectors $\vec{\psi}_i$ of the covariance matrix were determined using MATLAB software. Then each QRSI $\vec{m}$ was expressed in terms of these (orthonormal)

eigenvectors, as

$$\vec{m} = \sum_{i=1}^{192} w_i \vec{\psi}_i \tag{7.1}$$

where

$$w_i = \vec{m} \cdot \vec{\psi}_i \tag{7.2}$$

We found that the first three coefficients w_i, which correspond to the three $\vec{\psi}_i$ with the largest eigenvalues, describe at least 90 % (97 ± 2 %) of the energy content of $\vec{m}$, that is, $({w_1}^2 + {w_2}^2 + {w_3}^2)/|\vec{m}|^2 > 0.9$ for each $\vec{m}$ (see results).

The coefficients w_1, w_2, and w_3 of each map $\vec{m}$ were treated as Cartesian coordinates in a 3-D space and expressed in spherical coordinates r, θ, and ϕ, and the other 189 coefficients were discarded. The axis of the spherical coordinate system was chosen such that the database QRSI corresponding to the LV apex had $\theta = 0$. The radius r is an estimate of the total energy content of the map, and was also discarded, because the assumption that S is star-like with respect to the origin of map space is equivalent to the assumption that only the *pattern* of the QRSI contains information about the site of origin. If correlation coefficients are used to compare maps, the effect is also that the total energy content is discarded. The surface S, described by the θ and ϕ coordinates must now be mapped to the LV endocardial surface.

A position on the LV wall is denoted with a pair (ℓ, α), where ℓ stands for the ventricular length and α represents the ventricular angle [236] (see panel b in figure 7.1). Estimated coordinates are indicated as $\hat{\ell}$ and $\hat{\alpha}$.

We observed that parameter θ of a QRSI corresponded approximately to the ventricular length ℓ of the site of origin and ϕ corresponded approximately to the ventricular angle α. This is partly a result of our definition that $\theta = 0$ in the apex. The relationship between the pairs (θ, ϕ) and (ℓ, α) is illustrated in figures 7.2 and 7.3.

Figure 7.2 shows that the relation between α and ϕ is almost linear and is approximated by superposing a small sine wave on a straight line. Figure 7.3 shows that ℓ depends primarily on θ, with a small contribution of ϕ, which can be approximated by adding a sine-wave contribution that is slightly larger for higher values of θ. We devised the following functions to relate ℓ and α to θ and ϕ:

$$\hat{\alpha} = \phi + c_1 + c_2 \sin(\phi - c_3) \tag{7.3}$$

$$\hat{\ell} = \theta \left(d_1 + d_2 \sin(\phi - d_3) \right) / \pi \tag{7.4}$$

The parameters c_i and d_i of functions (7.3) and (7.4) are obtained by fitting these functions to the database maps. The resulting functions $\hat{\alpha}$ and $\hat{\ell}$ are shown by solid lines in figures 7.2 and 7.3, respectively.

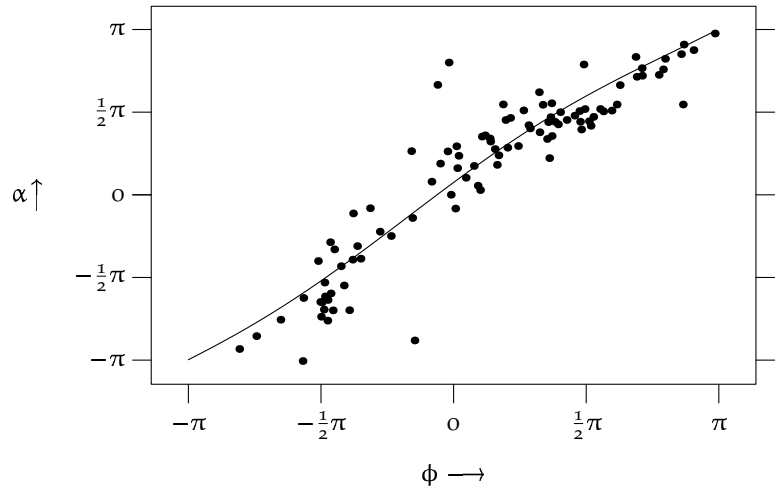

Figure 7.2: *Measured coordinate α of the database of 99 pace-maps shown with dots versus the map coordinate ϕ. The solid line represents the estimate $\hat{\alpha}$ computed with equation 7.3.*

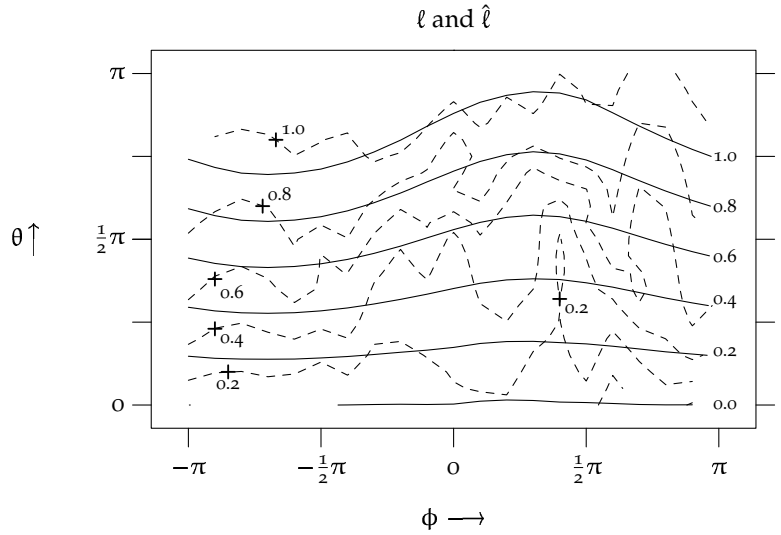

Figure 7.3: *Measured coordinate ℓ of the 99 pace-maps, interpolated in the θ–ϕ plane, shown with dashed contour lines; these contour lines are labelled with "plus" signs. Also shown, with solid contour lines which are labelled on the right side of the plot, is the estimate $\hat{\ell}$ computed with equation 7.4 (see text for details).*

7.2.2 Relative localization

The primary purpose of the algorithm is to provide catheter positioning advice. For that purpose it must estimate the positions of pacing sites relative to each other, rather than relative to the endocardium. This kind of localization is referred to as "relative localization." The computation of the position itself will be referred to as "absolute localization." We estimate the accuracy of relative localization by computing the difference between pairs of measured pacing sites and comparing it to the difference between the pacing sites predicted by the algorithm.

7.2.3 Error measures

Errors in absolute and relative localization were computed by projecting the localization result, which is given in LV cylinder coordinates, on a triangulated model of the ventricular wall. The model was scaled such that the length of the axis from the apex to the geometric middle of the MVR was 85 mm. Localization differences can then be expressed as 3-D distances in millimeters in order to provide an indication of the resolution of the algorithm.

Training and testing were performed using the same set of 99 pace-maps. In order to obtain a representative and unbiased estimate of the error that the algorithm will make if applied to new maps, we used cross-validation on the 99 pace-maps: the fitting procedure for c_i and d_i was applied to all but one of the database maps, the localization error of the omitted map was computed, and this procedure was repeated leaving out every map in turn. Because the error estimate is continuous, cross-validation is permissible in this situation [62].

Also, the number of maps used in the fitting procedure was decreased to see whether this influenced the localization accuracy: for $N = 2 \cdots 98$ we created a test set of N maps by random selection without replacement, and used the remaining maps to fit the algorithm. This was repeated 200 times for each N, and mean, minimum, and maximum localization errors for each N were computed.

Endocardial positions are displayed in a schematic diagram of the left ventricle (figure 7.1). This diagram can easily be related to a cut-open view of the left ventricle. Compared to the LV polar projection presented previously by SippensGroenewegen et al. [236], this diagram has the advantages that differences in α at different values of ℓ are easier to compare mentally and that the physicians involved consider it easier to translate to the cardiac image that they have in mind during a catheterization procedure. A drawback is that this diagram, contrary to the polar projection, is discontinuous

Table 7.1: *Localization Errors*

L_g (mm)	abs. err. (mm)	rel. err (mm)	p	N_g
5	12.0±6.6	6.7±5.0	$2.4 \cdot 10^{-2}$	14
10	13.2±6.2	8.9±6.7	$3.9 \cdot 10^{-3}$	40
15	14.4±6.7	10.2±6.0	$6.8 \cdot 10^{-5}$	77
20	13.5±6.8	11.7±6.9	$3.5 \cdot 10^{-2}$	130
25	13.2±7.0	12.3±7.0	$2.3 \cdot 10^{-1}$	172
30	13.6±7.2	13.6±7.7	1.00	226

along a line from the apex to the MVR.

7.3 Results

The first step in the localization algorithm is to represent each map $\vec{m}$ with a triple of coefficients (w_1, w_2, w_3) as $\vec{m}' = w_1\vec{\psi}_1 + w_2\vec{\psi}_2 + w_3\vec{\psi}_3$. The associated representation accuracy is expressed as

$$\sum_{i=1}^{3} {w_i}^2 \Big/ \sum_{i=1}^{192} {m_i}^2 \tag{7.5}$$

with w_i as defined in equation 7.2. For the 99 pace-maps, this value ranged from 90 to 99 %.

The differences between the measured and computed locations of the 99 pace-maps are shown in figure 7.4, in a schematic representation of the left ventricle. Also shown are the positions of the 25 database mean maps [236] which correspond to the 25 segments shown in figure 7.1 (c).

The distance between the measured and computed positions of the 99 pace-maps was 14.6 ± 8.2 mm and the distance between the 25 mean segment positions and the segment positions computed from the corresponding mean maps [236] was 9.2 ± 3.0 mm. In figure 7.5 (a), the localization results for a subset of five pace-maps, obtained from four patients, are shown. It is clear that the localization differences of maps originating from the same region were diverse in size and direction, but, as illustrated in figure 7.5 (b), were similar if only maps of a single patient were considered.

If pairs of pace-maps are considered from the same patient, with closely separated measured positions, the error for relative localization can be estimated. The mean value of this error depends on what we consider "closely

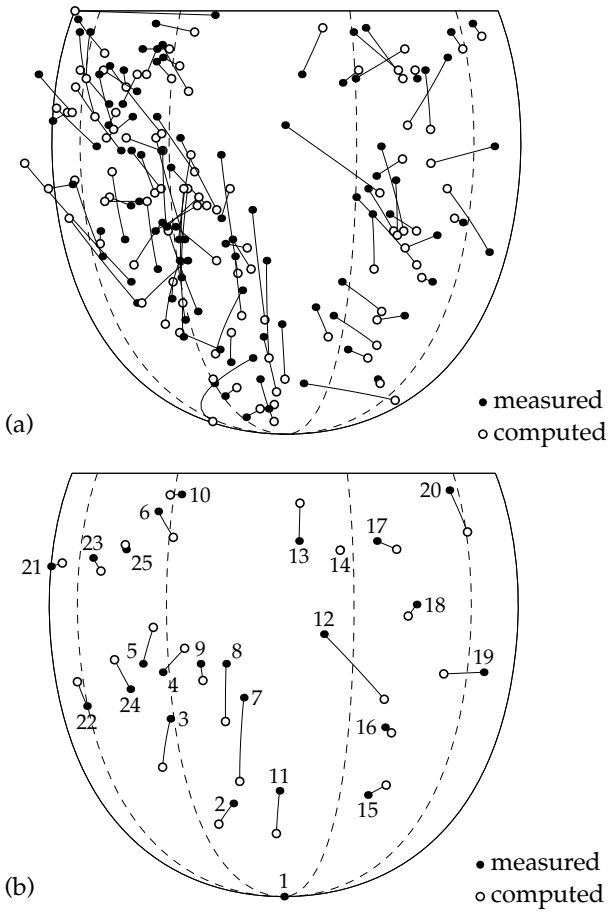

Figure 7.4: (a) *Differences between positions computed from the θ and ϕ coordinates of the 99 pace-maps by the functions (7.3) and (7.4), and corresponding measured positions where pacing was performed. The computed positions are indicated by open circles, the measured positions by black dots.* **(b)** *Differences between the positions of the 25 database mean maps as determined by SippensGroenewegen et al. [236] and the corresponding computed positions of the database QRSI's.*

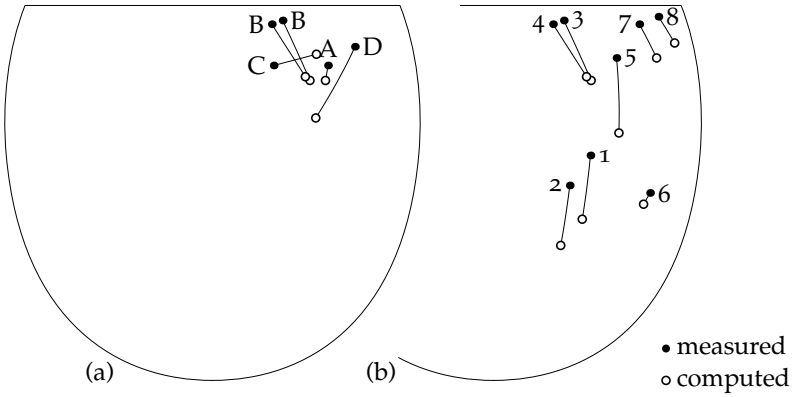

Figure 7.5: (a) *Computed and measured positions corresponding to five pace-maps obtained at a similar location (the basal posterolateral wall of the left ventricle) from four different patients, labelled A, B, C, and D. Black dots indicate measured positions, open circles indicate computed positions. The computed positions of all maps are close together but the deviations from the measured positions are different in size and direction. The two maps of patient B have approximately the same error.* **(b)** *Computed and measured positions corresponding to eight pace-maps obtained at a similar location (the middle and basal posterolateral wall of the left ventricle) from a single patient. Considerable errors exist, but they are closely related, and the relative positions of measured and computed locations are approximately the same. Similar systematic shifts were observed in all patients.*

separated." Therefore, we constructed several groups of pace-map pairs, each group with a maximum measured distance L_g between the members of each pair. We refer to the number of maps in each group as N_g; for larger L_g, more pairs can be found. Errors in relative localization were then computed for each group. Results are given in table 7.1. Each row of the table shows errors of relative and absolute localization for all pairs in a group as well as the p-value for the difference between errors for absolute and relative localization in the group, and the number of pairs in the group, N_g. The p-value was computed using Student's t-test. We found that for pairs of pace-maps whose measured positions were closer than 20 mm, the errors for relative localization were evidently smaller than the errors for absolute localization.

Localization accuracy obtained using reduced sets of maps for the fitting procedure and using the remaining maps for testing, are shown in figure 7.6. This figure shows that the mean error was constant for 98 down to 20 maps and that the maximum error increased only slightly when redu-

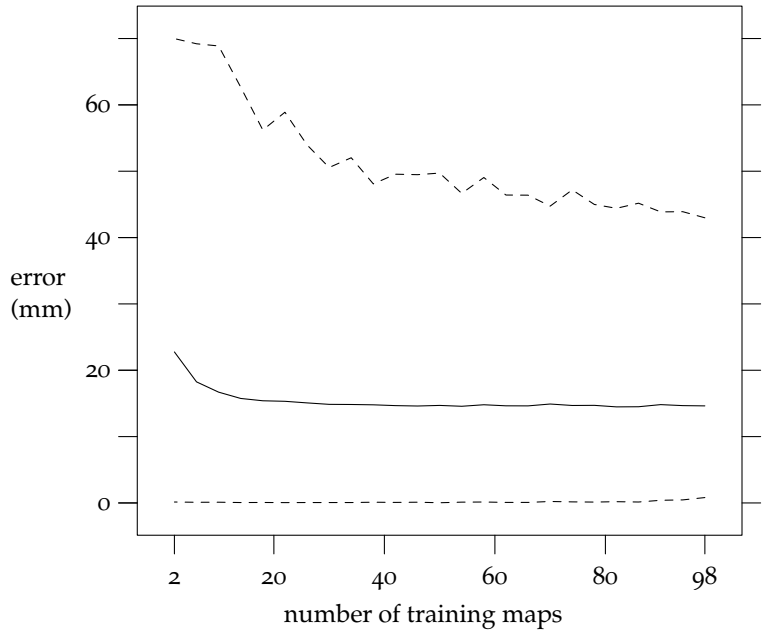

Figure 7.6: *Localization error for database mean maps as a function of the number of maps used for the training procedure, computed for 2 up to 98 training maps. The mean error is shown with a solid line, minimum and maximum errors are shown with dashed lines.*

cing the fitting set to approximately 40 maps.

7.4 Discussion

An algorithm is proposed that can provide a continuous estimate of the site of origin of a paced QRSI. It can be applied for relative localization, i.e. the assesment of *differences* in catheter positions, using pace-maps obtained from a specific patient.

For the purpose of relative localization, the algorithm depends on two assumptions: 1) The QRSI must vary continuously with the site of origin and 2) the set of all possible QRSIS that result from LV pacing must be star-like. The first assumption is corroborated by the observation of gradually changing patterns both in measured and computed QRSIS [104,236]. The extent to which the second assumption can be tested depends directly on the accuracy of the position measurements. For absolute localization using this

algorithm, we also have to assume that the relation between QRSI and site of origin is the same in all subjects. This is known to be true only in a very loose sense; this is one possible source of the large error for absolute localization of 14.6 ± 8.2 mm (section 7.3). Interpatient differences in thoracic anatomy, position and orientation of the heart, electrical conduction, and perhaps small differences in wavefront propagation due to varying underlying anisotropy may all contribute in causing different mappings between QRSI pattern and exit site. From the work of Hren et al. [103] it may be deduced that differences in torso boundary alone may account for approximately 10 mm localization difference. These differences will be less prominent in relative localization than in absolute localization. A tailor-made database, using only pace-maps from a single patient, would reduce the latter error. However, with our current data, featuring eight patients with 6–23 pacing positions each, we did not obtain better results when applying the fitting and testing procedure to only the maps of a single patient. With this data, only relative localization could be shown to work as a means to adapt the method to individual patients (table 7.1).

Apart from nonapplicability of the assumptions, there are several possible explanations for differences between computed and measured positions:

- Errors in the fluoroscopic localization can cause errors in the database as well as errors in the positions that are used for evaluation. These errors can be as large as 7 mm [88, 89].
- Interpatient differences in the local geometry of the ventricular wall can cause different mappings from endocard to cylinder coordinates; these differences may be expected to be less prominent in relative localization.
- Inaccuracies in the two mapping functions increase the difference between measured and computed locations. These functions are simple and somewhat arbitrary. The localization accuracy might be improved by using a better mapping function, such as a self-organizing map (SOM) [134]. These differences may also be expected to be less prominent in relative localization.
- Changes in QRSI pattern with the respiratory phase may influence the localization accuracy. Amoore et al. [3] reported that the patterns of body surface potential maps shifted inferiorly by about 2 cm at deep inspiration. The localization algorithm is sensitive to pattern shifting. However, pace-maps were recorded in a similar respiratory phase [236], so the respiratory disturbance may be considered to play only a minor role.

- Noise and distortion of the ECG may increase the localization error.
- Data loss due to the selection of only three parameters to describe a QRSI (accuracy 90 % to 99 %) may influence the localization accuracy. However, the representation error was related to the localization error in only one of eight patients ($r = 0.63$ for 13 pace-maps). Moreover, it is likely that the selection of three KL coefficients reduces noise and removes some patient-specific features of the QRSI. We observed that the KL transformation matrix, which was created from the 99 QRSIS themselves, could be replaced by others transform matrices, created from potential maps of other patient groups, yielding a much larger average representation error (over 15 %), with only a minor change in localization error.

Taking the most important sources of errors into account, we expect our data not to be more accurate than about 10 mm. In this respect, we believe that the 14.6 mm absolute and 10.2 mm relative accuracy (table 7.1, $L_g = 15$ mm) indicate that the approach is sound and that more accurate techniques for catheter localization are necessary to establish the accuracy of our method.

For pairs of pace-maps whose measured distances L_g are below 15 mm, an average relative localization error of 10.2 mm was obtained; for L_g under 5 mm, the average error was only 6.7 mm. Although this is a very small error, it is on average larger than the measured distance.

By reducing the number of maps used for the fitting procedure, we have shown that the number of pace-maps used is large enough. The number of maps can be reduced to 20 without any impact on the average localization error; only the maximum error increases slightly. Perhaps a small decrease in maximum error may be expected if the number of pace-maps would be increased beyond the current 99.

In a previous study, Muilwijk [179] compared the results of arrhythmia localization by body surface mapping, using the database-lookup method, with the results of intra-operative mapping in 62 VT morphologies obtained from 42 patients with previous anterior or inferior myocardial infarction. She reported a distance of 18 ± 14 mm between the exit site localized by body surface mapping and the intra-operatively determined site of origin (which may not coincide with the exit site of the VT). The resolution reported in the present study is better, which is to be expected since we compared the computed pacing site directly to the measured pacing site.

Because there are no data available of intra-operatively determined VT *exit sites* in combination with body surface maps of the same arrhythmia, there is no gold standard to test localization algorithms other than comparing them to the position of the catheter tip. However, catheter-tip localiza-

tion by biplane fluoroscopy may not be accurate enough for this purpose. Magnetic localization (using ultralow magnetic fields and a special catheter containing a miniature magnetic field sensor) [230] or electrical localization (by measuring, with the catheter electrodes, the local potential induced by small currents applied at the body surface) [279] are promising alternatives. However, the most important advantage of the described algorithm is not the improved accuracy, but rather the increased objectivity of the results, the less time it takes as compared to "manual" localization, and the ability to display localizations and their differences automatically. Because database interpolation is performed by a computer instead of a human observer, the results are instantly available to the computer for further processing such as automatic display of localization results in 3-D or in the standard biplane fluoroscopic projections used in the catheterization laboratory.

The algorithm can employ different databases, for example the infarct-specific databases created by SippensGroenewegen et al. [237]. We expect that it can also work with delta-wave maps, used by Nadeau et al. [180] for localization of the atrioventricular pathway in patients with the Wolff–Parkinson–White (WPW) syndrome [54, 176], and to atrial databases, which contain P-wave integral maps [240].

Preliminary results indicated that the method does not work for the right ventricle. Although the technique was able to differentiate between some RV pace-maps, it could not differentiate between maps paced in the RV side of the septum and maps paced at the RV free wall. Such differentiation may require consideration of individual potential maps in the QRS complex, or information on the amplitude of the QRSI [236] which is ignored in our current approach (i.e., for the right ventricle S is not star-like).

An alternative for our database interpolation algorithm could be the creation of a database of any desired precision using a computer heart model, after quantitative verification of the results of this model with an empirical database. The advantage of such model studies is that they can be used with very closely separated "pacing sites," including intramural and epicardial pacing sites, and that accurate analysis of the effects of individual geometry and constitution is possible. Several groups created models that can be used for this purpose [141, 158]. Xu [280] and Hren [104] compared the results of such models to the database of SippensGroenewegen et al. [236] which was also used in the present study. These simulation results resembled the database well, but these authors did not yet provide a quantitative evaluation of the simulation results.

The most desirable localization procedure may be provided by a computational solution of the inverse problem of electrocardiography [84], because it would, like the forward methods discussed above, provide a true understanding of the underlying electrical phenomena, and in contrast to

forward solutions, may be applied directly to the measured data. For example, single moving-dipole solutions for the early QRS [102, 228] or activation sequence models [111, 112] may be employed. However, these methods require excellent signal quality and accurate geometrical modelling of the subject [113], and to date no clinically practical method with sufficient accuracy has been reported. We believe that, until this kind of solution becomes available, our algorithm will provide a reasonable alternative in clinical applications.

7.5 Conclusion

A quantitative method is described to compute accurately the location of the endocardial site of origin of a paced body surface QRS integral map, in terms of coordinates, instead of a limited number of segments corresponding to a fixed reference set of mean paced QRSIS. Moreover, this algorithm uses information of all pace-maps in the database for the localization of a single site and leads to a continuous and regular conversion of QRSI data to LV coordinates. This is likely to improve the localization accuracy.

The most important advantages of the new method are the continuity, quantitative nature, objectivity, and reproducibility of the localization results. Also, it can be used to compute *differences* between exit sites or pacing sites (relative localization), thus using data measured in an individual patient to increase the accuracy.

The localization errors that were found can be attributed to a large extent to the uncertainty in the pacing position measurements. More accurate measurements may provide a better estimate of these errors.

The algorithm can be used clinically during pace-mapping of LV arrhythmias to guide the catheter to the site of origin prior to ablation and may be particularly useful due to the possibility of displaying catheter positioning advice in 3-D or in the standard fluoroscopic projections used in the catheterization laboratory. It may also prove useful in research, for example on polymorphic ventricular tachycardia (PVT), to compute the relative positions of exit sites of consecutive beats.

Chapter 8

Continuous Localization in the Infarcted Left Ventricle

The continuous localization method for the normal left ventricle, described in chapter 7, can be adapted for infarcted left ventricles, and yield a comparable performance. In addition, it can be used to quantify the differences in the relation between site of origin and surface ECG pattern between normal and infarcted hearts. — Presented in part at the *NFSI* symposium, September 2001 [201]; *World Congress on Medical Physics and Biomedical Engineering*, July 2000 [214]; *20th Annu. Int. Conf. IEEE EMBS*, October 1998 [206].

8.1 Continuous Localization in Infarcted Hearts

Cardiac activation that results from ventricular pacing consists of a wave front spreading from the pacing site toward the opposite ventricle [245]. In infarcted hearts, electrically inactive and slowly conducting regions exist, which can alter this activation sequence [11, 56, 271]. It is expected that these alterations cause differences in the surface ECG waveforms resulting from pacing at the same site in infarcted and non-infarcted hearts. Indeed such differences were found in the 12-lead ECG [99, 270]. Despite the summation over time provided by integral mapping, body surface QRSI patterns also reflect these changes [237]. Hence, for accurate localization of VT in infarcted hearts, specific pace-map databases have been created for patients with inferior (IMI) or anterior myocardial infarction (AMI) [236, 237].

For the database of paced QRS integral maps for the structurally normal left ventricle created by SippensGroenewegen et al. (figure 6.4) [236], an interpolation method was developed in chapter 7 [212]. The algorithm is

trained using a pace-map database, in this case the database for the normal left ventricle (NLV). In principle, the algorithm can be trained with the AMI and IMI databases as well.

8.1.1 Methods

Tests indicated that the relation between map pattern and exit site is more complex in the AMI and IMI databases as compared to the NLV database. A slight adaptation of the algorithm was therefore necessary to make an accurate fit to the AMI and IMI databases possible. Equations (7.3) and (7.4)

$$\begin{aligned} \hat{\alpha} &= \phi + c_1 + c_2 \sin(\phi - c_3) \\ \hat{\ell} &= \theta \left[d_1 + d_2 \sin(\phi - d_3) \right] / \pi \end{aligned}$$

which related the estimated exit-site coordinates $(\hat{\ell}, \hat{\alpha})$ to the QRSI parameters (θ, ϕ), are replaced by the expression

$$\hat{\ell} = \left[d_4 + \theta \right] \left[d_1 + d_2 \sin(\phi - d_3) \right] / \pi \tag{8.1}$$

and, for $\hat{\alpha}$, a spline with N_c control points having evenly distributed ϕ coordinates and $\hat{\alpha}$ coordinates c_i. It turned out that $N_c = 11$ was the smallest value that could be chosen for the number of control points without increasing the average localization error. The coordinates c_i were constrained to be monotonically increasing.

8.1.2 Results

Fitted functions for the AMI and IMI databases are presented in figures 8.1, 8.2, 8.3, and 8.4. In figure 8.4 a region without contours is present in the upper left corner, approximately for $-\pi < \phi < 0$ and $\pi/2 < \theta < \pi$. This means that maps with a pattern characterized by these values of θ and ϕ do not occur in the IMI patients (figure 8.5). In NLV patients, these map patterns corresponded to pacing sites near the MVR in the posteroseptal region, e.g. segments 12 and 14 in the NLV database (chapter 7). In IMI patients, maps paced in this region have a pattern similar to those paced at more posterior positions in NLV patients, as discussed in section 8.3 and section 8.4.

The algorithm, adapted according to section 8.1.1, was trained with each database in turn, and then tested with all databases. Estimated localization errors are given in table 8.1.

8.1.3 Discussion

It was demonstrated that, as expected, an algorithm specifically trained for a database performed best for that particular database. In addition, the NLV

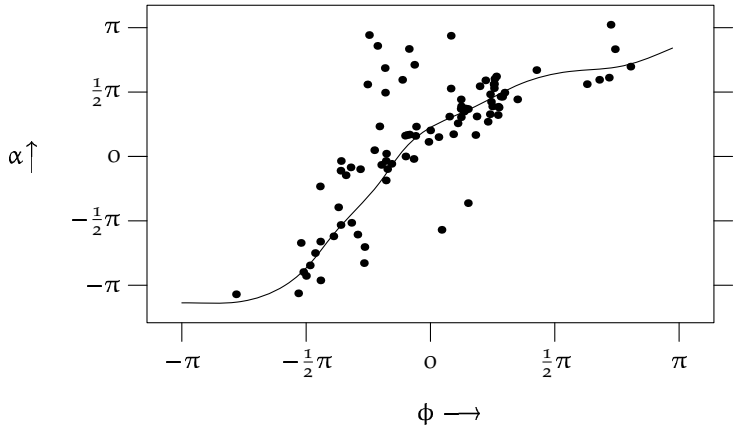

Figure 8.1: *Measured coordinates α of the AMI database of 92 pace-maps shown with dots versus the map coordinate ϕ. The solid line represents the spline estimate for $\hat{\alpha}$, fitted to the AMI database.*

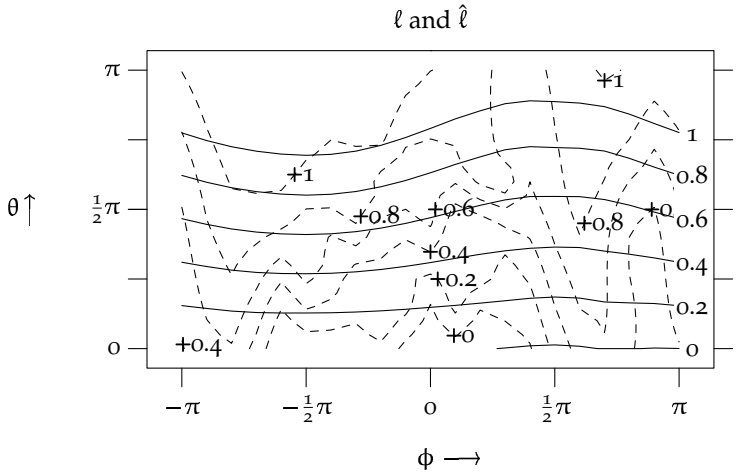

Figure 8.2: *Measured coordinates ℓ of the AMI database of 92 pace-maps, interpolated in the θ–ϕ plane and shown with dashed contour lines; these contour lines are labelled with "plus" signs. Also shown, with solid contour lines labelled on the right side of the plot, is the estimate $\hat{\ell}$ computed with equation (8.1) and fitted to the AMI database.*

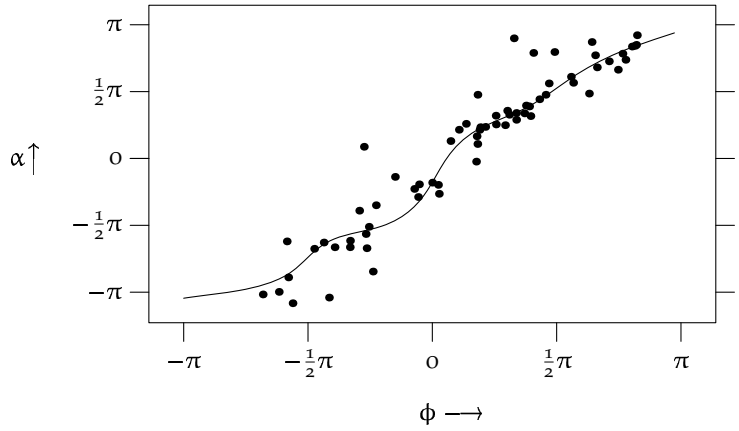

Figure 8.3: *Measured coordinates α of the IMI database of 66 pace-maps shown with dots versus the map coordinate ϕ. The solid line represents the spline estimate for $\hat{\alpha}$, fitted to the IMI database.*

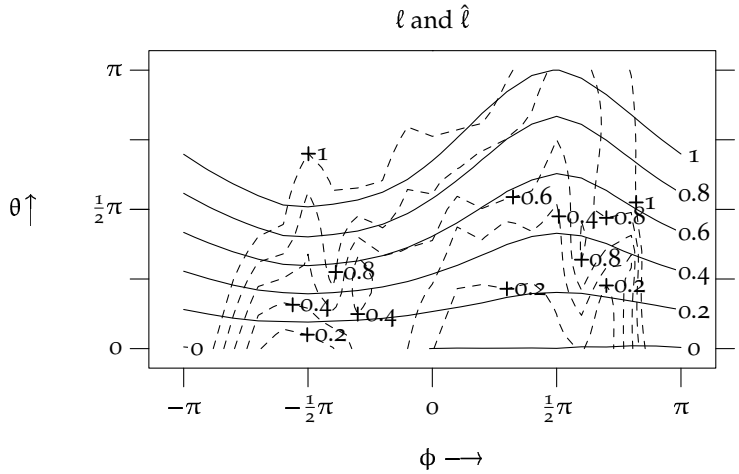

Figure 8.4: *Measured coordinates ℓ of the IMI database of 66 pace-maps, interpolated in the θ–ϕ plane and shown with dashed contour lines; these contour lines are labelled with "plus" signs. Also shown, with solid contour lines labelled on the right side of the plot, is the estimate $\hat{\ell}$ computed with equation (8.1) and fitted to the IMI database.*

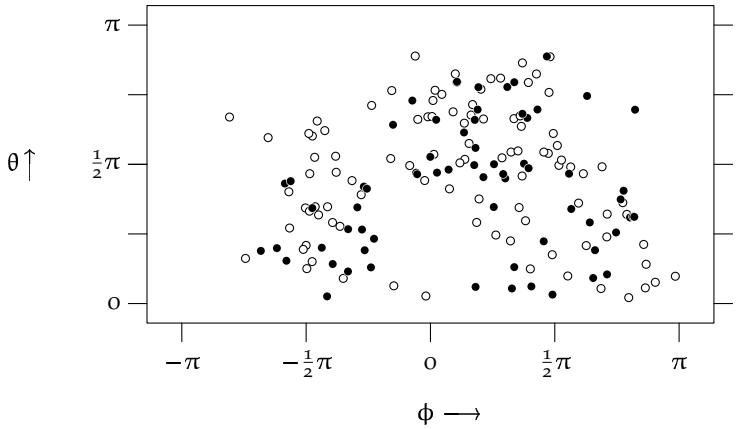

Figure 8.5: *Map coordinates θ and ϕ of pace-maps obtained in NLV patients (open circles) and IMI patients (solid circles). A small area in the upper left part of the plot contains no IMI maps, but it does contain NLV maps. Since this gap does not correspond to an uncovered area of the endocardial wall, it may be concluded that this region represents a map pattern that does not occur in IMI patients.*

algorithm performed reasonably well for all three databases, and clearly better than the IMI algorithm performed for the AMI test set and the AMI algorithm for the IMI test set.

The results indicate that: (1) The algorithm works well for all three databases, with localization errors in the order of 15 mm. These errors may be largely attributable to uncertainty in the catheter-position data (max. 7 mm [88]) and inter-patient variability. (2) Specific training of the algorithm was more useful for the IMI database than for the AMI database. When using the NLV algorithm, the average error was 16 mm for AMI and 17 mm for IMI. With database-specific algorithms this error reduced to 15 mm for AMI and 12 mm for IMI. The difference between these improvements, 5 mm for IMI and only 1 mm for AMI, may be due to a larger inter-patient variability in the AMI group. (3) An algorithm fitted to AMI and applied to localize an exit site in an IMI patient or vice versa has a larger error than an algorithm fitted to NLV. This suggests that the effects of AMI and IMI on the relation between exit site and QRSI pattern are in part opposite.

Continuous localization in patients with infarct scars, as described here, is important since these patients constitute the majority of all ventricular arrhythmia patients. Moreover, these patients often suffer from poor left

		no. of patients	*no. of pace-maps*	*mean (s.d.) error in mm for testing set*		
				NLV	AMI	IMI
training set	NLV	8	99	**13 (8)**	16 (10)	17 (12)
	AMI	8	92	15 (8)	**15 (10)**	19 (11)
	IMI	4	66	18 (13)	21 (12)	**12 (11)**

Table 8.1: *Localization errors of the adapted continuous localization algorithm, trained and tested on all three left-ventricular databases. Values for localization with the correct database are printed in boldface.*

ventricular (LV) function and are therefore more likely to become haemodynamically compromised during prolonged ventricular arrhythmia occurrences in the electrophysiology laboratory, so it is clear that a rapid pace-mapping procedure increases the likelihood of obtaining a successful catheter-ablation result in these patients.

Applicability to patients with other types of infarction, such as lateral myocardial infarction (LMI), has not been tested since there were currently not enough data available from patients with such types of infarction [237].

8.2 Database Segment Mean Maps

When creating their pace-mapping databases, SippensGroenewegen et al. divided the QRSIS they obtained after pacing into groups with similar patterns [236,237]. It turned out that these groups corresponded with compact segments of the endocardium. Subsequently, a *mean map* was created for each segment. Localization of VT could then be performed by correlating the VT QRSI with the mean maps and expressing the localization result as the corresponding segment.

In chapter 7, the performance of the continuous localization algorithm was illustrated by applying it both to the individual pace-maps and to the database mean maps. In section 8.1, the performance of the algorithms for the AMI and IMI groups was expressed as the average localization error for the individual pace-maps in each group.

In this section, an overview is presented of estimated positions of the mean maps of all three databases (figure 8.6).

As may be expected from the results for individual pace-maps (section 8.1, table 8.1), the localization errors are of comparable magnitude in the three databases. The errors appear to be randomly distributed. This indicates that there are no major systematic errors in the algorithms.

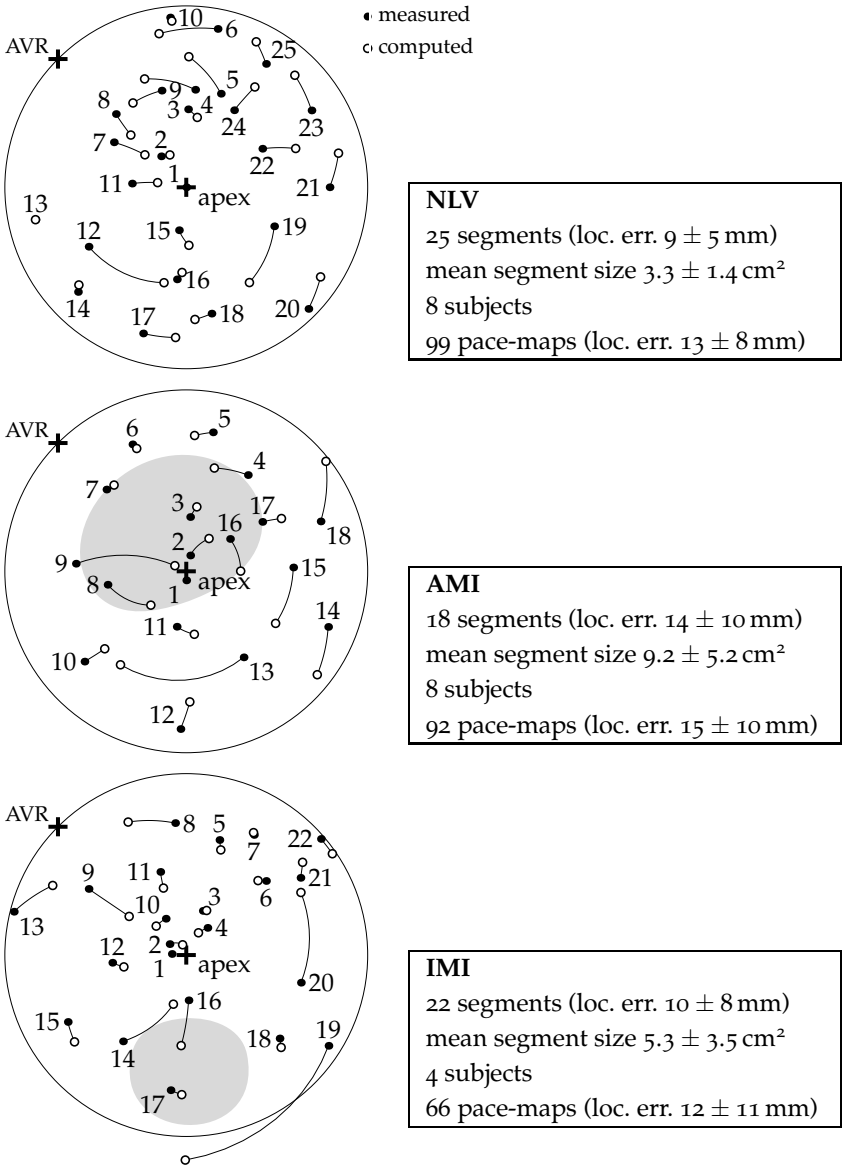

Figure 8.6: *Overview of the three databases of mean maps. Measured, i.e. visually established, mean segment positions are indicated with black dots. Estimated positions, computed from the mean maps corresponding to these segments, are indicated with open circles. For each group (NLV, AMI, IMI), the specific algorithm (section 8.1) was used. In the lower two diagrams, the approximate location of a typical AMI or IMI infarction is indicated with a grey patch.*

In each group, there were one or two relatively large deviations. Although it cannot be excluded that they were due to errors in the algorithm, it is more likely that they were the result of errors in the visual determination of the mean segment positions. Notably, segments NLV 12, AMI 9 and 13, and IMI 19 showed much larger deviations than their neighbours. In addition, the position of NLV 6 was located on the opposite side of NLV 10. This may be understood from the fact that segment NLV 10 was estimated from three pacing positions, one of which was located relatively far from the other two, and the position of the entire segment was estimated to be the centre-of-mass of the segment, rather than the centre-of-mass of the three positions [236]. The estimated position of segment IMI 19 was located on the other side of the approximate infarct position. This may be a a coincidence, but it can also be due to pacing in the infarct scar, causing activation to proceed slowly through a narrow path of surviving tissue in the scar [6] and to reach viable tissue at a site remote from the actual pacing position.

8.3 Effect of Infarct Scars on Exit-Site Localization (Mean Maps)

In section 8.1, three pace-mapping databases were discussed which can be used for localization of VT. The three databases have been obtained from three different patient groups: patients with a left ventricle without structural heart disease (NLV), with previous AMI and with previous IMI. The NLV database consists of 25 mean QRSIS, the AMI database of 18, and the IMI database of 22 mean QRSIS [236, 237]. The varying numbers of segments in the databases are the result of the varying resolution that was found in the three patient groups.

It is useful to integrate the knowledge contained in the three databases and combine it with the information on a specific patient in order to create a customized localization algorithm. A first prerequisite would be to quantify the differences between the three databases. Information on infarct size and location is often incomplete. From the results in table 8.1 we can infer that the absolute value of the localization error increases on average by a few millimetres if the wrong database is used. In this section, an estimate of the direction and distribution of these additional errors is presented.

In addition, observing the differences between the three databases may give us insight in the changes in wavefront propagation and the resulting changes in QRS pattern caused by different types of infarction.

Because the three databases have different segments, the assessment of differences between the three patient groups could up to now only be per-

formed in a qualitative fashion [237]. Using the continuous localization algorithm for the NLV described in chapter 7 [212], a quantitative assessment based on measured data has now become feasible. We will use this algorithm to estimate the differences between the structurally normal left ventricle on the one hand, and the ventricle with anterior or inferior infarct scars on the other hand.

8.3.1 Methods

The continuous localization algorithm for the NLV was applied to all mean QRSIS in each database (NLV, AMI, IMI) and then used to compute the mean segment positions. Application to the NLV database (figure 8.6) shows that this approach has an error of approximately 1 cm [212].

Since the algorithm was created specifically for the NLV database, we do not expect it to work just as well for infarcted hearts (section 8.1). However, by applying it to the AMI and IMI database of paced QRS integral maps, and observing the differences between computed positions of the mean maps and the measured mean segment positions, one obtains an estimate of the differences between the NLV and the AMI and IMI databases.

8.3.2 Results

The results of the comparison between the NLV database and the infarct-specific databases are shown in figure 8.7. These deviations should be compared to the errors that remain if the algorithm is applied to the NLV mean maps (figure 8.6). In this figure and subsequent figures, a polar representation of the left ventricle has been employed. This type of presentation was chosen, rather than the more intuitive diagram used in chapter 7, because the discontinuity in the latter diagram is more difficult to deal with in the current chapter.

For the AMI group, significant localization differences were found only in the posteroseptal region. Deviations in the anterior quadrant were not significant. Deviations in the lateral quadrant were larger but of the same order of magnitude as the localization errors for the NLV group in the same region (figure 8.6).

Deviations in the IMI group were larger than in the AMI group. In the anterior, lateral, and posterior quadrants, there is a consistent rotation in the counterclockwise direction. An additional deviation in the direction of the apex is observed in the posterior quadrant.

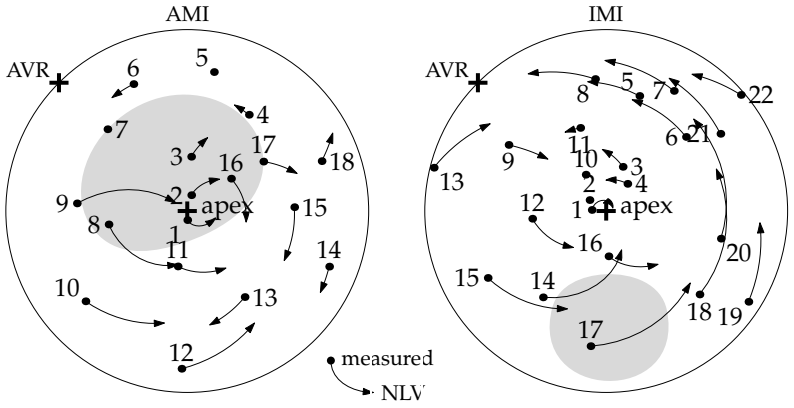

Figure 8.7: *A comparison of measured mean segment positions in the AMI (left panel) and IMI (right panel) databases and computed positions based on the mean QRS integral maps of the database, using an algorithm that was fitted to the NLV database. This provides an estimate of the differences between the NLV and AMI or IMI databases. The measured mean segment positions in the AMI or IMI databases are indicated with black dots; arrows point to the positions where, according to the algorithm, the same QRSI pattern would be obtained in the NLV. The deviations should be compared to the errors in localizing the NLV mean segment positions (figure 8.6). In both diagrams, the approximate location of a typical AMI or IMI infarction is indicated with a grey patch. Since the arrows point from the location of a map in the infarcted heart to the location in the NLV, they can be read as "the map looks like it is coming from here (in a normal heart)."*

8.3.3 Discussion

In several regions, considerable differences in estimated positions exist between the NLV and the AMI and IMI databases. This is in agreement with the increased error found when applying the NLV algorithm to the individual pace-maps underlying the AMI and IMI databases in section 8.1. However, the deviations are well-behaved, so that the errors resulting from the selection of a wrong database will be similar for multiple closely separated pacing sites in a single patient. This means that the effect on the estimation of pacing site positions relative to each other is comparatively small, which has important implications for pace-mapping procedures [194].

We found slightly larger deviations than SippensGroenewegen et al. did by their visual analysis of the same data [237]. In addition, we found a consistent rotation in the anterior, lateral, and posterior quadrants for the IMI database. Otherwise, their results are comparable to ours.

The deviations in the IMI group are relatively simple to describe. It may be possible to parameterize them in order to interpolate between the NLV and IMI databases, to optimally adapt the localization algorithm to an individual patient when the infarct size and precise location are known.

A limitation of the database lookup method is that it provides discrete results; the localization result is expressed as just one out of 18 to 25 segments of origin. This limitation was taken away by the introduction of a continuous localization algorithm [212] (chapter 7), which can be used to give directional catheter-positioning advice with any desired resolution and sub-centimetre accuracy.

Another limitation is that an infarct-specific database must be chosen from a limited set: NLV, AMI, or IMI. Knowledge about the size and precise location of infarct scars cannot be used. On the other hand, such knowledge is often very incomplete. This study shows that the differences between the databases are such that it is likely that a continuous localization algorithm can be tailored to a specific patient, and, on the other hand, that the effect of choosing an incorrect database will be limited, especially if relative localization is used.

Computer models were previously applied to simulate body surface QRS integral maps from complexes originating at various locations in the normal heart [104,280]. Such models can also be applied to infarcted hearts. It will then be possible to study the effect of infarct scars more accurately and to compute the relation between exit site and body surface pattern for a specific patient using information on the patient's anatomy—including scars if their location is known with sufficient accuracy.

8.4 Effect of Infarct Scars on Exit-Site Localization (Difference Vectors)

Using the specific localization algorithms for NLV, AMI, and IMI groups developed in section 8.1, differences between the databases can be illustrated in a more pleasing way, as illustrated in figure 8.8 (a).

These diagrams may be easier to interpret than those in figure 8.7. Their disadvantage is that the results are computed using two localization algorithms instead of one, with their errors combined. On the other hand, the somewhat subjective determination of the middle of a segment and the division of the database into segments itself play no role here.

The effects present in figure 8.7, such as the counterclockwise rotation in the lateral quadrant in the IMI diagram, are also manifested in figure 8.8 (a). In addition, this figure shows that the estimated exit site, not corrected for infarct position, generally moves away from the infarct location.

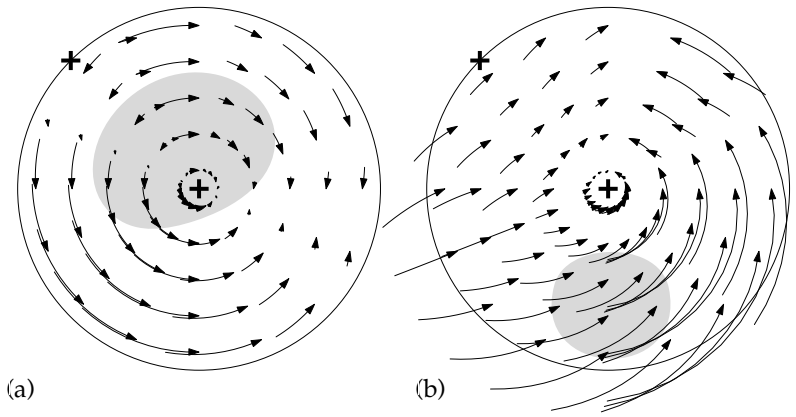

Figure 8.8: (a) *AMI database compared to NLV database. For a regular grid of NLV exit-site coordinates, the corresponding map coordinates* θ *and* ϕ *were computed by the inverse of the NLV-specific algorithm and from* θ *and* ϕ *the* $\hat{\alpha}$ *and* $\hat{\ell}$ *coordinates were computed using the AMI-specific algorithm. For each* (θ, ϕ) *pair an arrow is drawn, which points from the computed AMI location to the computed NLV location.* **(b)** *IMI database compared to NLV database, in the same way as in panel (a). The arrows point from the IMI locations to the NLV locations with the same map coordinates.*

The latter effect can be explained by the presence of conduction block or slow conduction in or near the infarct scar, i.e. near the grey areas in figure 8.8 (a). This block causes an activation front that starts near the scar to proceed away from it and activate the ventricle along the opposite wall. When summed over the QRS interval, the resulting body surface potentials may well look as if the pattern originated from a site somewhat further from the presumed zone of block than the actual pacing site. The strength of this effect decreases with increasing distance between the site of origin and the infarct location. Zero rotation is observed in the region most distal to the infarct.

In panel b of figure 8.8 several arrows are located partially outside the ventricle. These were computed from map coordinates that do not correspond to ventricular positions, that is, map coordinates that are not expected to be observed in patients. The range of non-physiological map coordinates is larger in the IMI group than in the NLV and AMI groups, as can be seen from the several arrows pointing inward from the posterior side in figure 8.8 (b).

8.5 Discussion

Infarct scars alter the relation between the site of origin of an arrhythmia and the resulting QRSI pattern. Due to the variety in scar location and size, it is to be expected that this disturbed relation may be somewhat unpredictable. Indeed, average localization errors obtained using the continuous localization method are larger in the AMI and IMI groups than in the NLV group (section 8.1). In addition, the maximum error was 37 mm in the NLV group, 48 mm in the AMI group, and 55 mm in the IMI group.

Comparing BSM database localization results, i.e., ECG-based results obtained without subsequent pace-mapping, with endocardial measurements obtained with a basket catheter, Van Dessel et al. reported that BSM localization fails to predict the correct segment or an adjacent segment in 30 % of pace-maps and 40 % of VT maps in infarcted ventricles [47]. In order to compare these values with the continuous localization results, "failure" must be defined for the continuous error estimates. Defining failure, somewhat arbitrarily, as a localization error larger than 20 mm, we obtained a 15 % error rate in the IMI group and a 28 % error rate in the AMI group. The latter figure is comparable to the error percentage for pace-maps reported by Van Dessel et al. The smaller error rate in the IMI group may be due to the usually smaller amount of ventricular myocardium that is destroyed with IMI, as compared to AMI [237].

Van Dessel et al. also investigated the mechanisms responsible for localization errors. Three mechanisms could be identified: extensive lines of conduction block, multiple exit sites, and endocardial areas with low electrogram amplitudes [47]. Since the presence and effect of these mechanisms are not predictable with surface ECGs endocardial catheter mapping and intra-operative mapping are required to find the site of origin in these 30–40 % of VT morphologies in patients with infarct scars. In these cases, the role of body surface mapping is confined to guiding the catheter quickly to a region of interest. In the remaining 60–70 % of VT morphologies, exit-site localization using body surface map data can be considered to be correct, and in many cases sufficiently accurate for exit-site localization.

Chapter 9

Conversion From Endocardial Coordinates Into Biplane Fluoroscopic Projections

The BSM-based localization methods described in previous chapters provide their results in a coordinate system relative to the heart. It is preferable to present these results in the biplane fluoroscopic views that are routinely used to monitor catheter positioning. We investigated how well cardiac coordinates can be converted into fluoroscopic projections with the limited anatomical data available in clinical practice. Endocardial surfaces from MRI scans of 24 healthy volunteers were used to create an appropriate model of the left ventricular endocardium. Methods for estimation of model parameters from biplane fluoroscopic images were evaluated using simulated biplane data created from these surfaces. In addition, the conversion method was evaluated using 107 catheter positions obtained from 8 patients. The median distance between reconstructed positions and measured positions was 4.3 mm. — *Med. & Biol. Eng. & Comput.*, 2001 (in press) [197];

9.1 Introduction

Electrocardiographic body surface mapping provides noninvasive localization of supraventricular and ventricular arrhythmias, which may be used to direct catheter mapping prior to radiofrequency (RF) ablation [54, 194]. Methods for electrocardiographic localization of exit sites in the left vent-

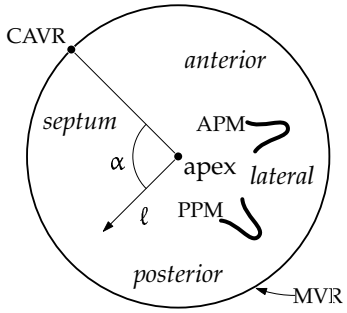

Figure 9.1: *Left-ventricular polar projection, illustrating left-ventricular cylinder coordinates. The apex of the left ventricle is indicated in the middle of the diagram; the circumference represents the mitral valve ring (MVR). The centre of the aortic valve ring (CAVR) is indicated. Left-ventricular cylinder coordinates consist of a relative length ℓ, indicating the distance along the apex–CMVR axis relative to the length of this axis, and an azimuth α, defined with respect to the position of the CAVR.*

ricle, based on the use of the QRS integral map (QRSI) of a single beat of a ventricular arrhythmia, were discussed in chapters 6, 7, and 8. These methods provide their results in a coordinate system relative to the heart, called "left ventricular cylinder coordinates" (LVCC). These coordinates can be presented in a schematic diagram, such as the polar plot presented in figure 9.1 and the more intuitive diagram presented in chapter 7 (page 137).

While these methods can predict the positions of VT exit sites and pacing sites with respect to each other, they do not provide information on the location of the catheter at intermittent times when no pace map is created. Such information is necessary when the catheter is being inserted into the heart, and when it is maneuvered to a new position. The traditional method of catheter-position monitoring is (biplane) fluoroscopy. Because the radiation involved in this method is harmful for both patient and medical personnel, alternative methods have been developed, such as magnetic localization [125, 230] and electrical localization [279]. These methods provide only information on the 3-D catheter position and not on the surrounding anatomy. Therefore they are commonly applied together with fluoroscopy in order to reduce fluoroscopy time but not to replace fluoroscopy completely.

During a catheter-ablation procedure, the physician observes the position of the catheter relative to the heart using either fluoroscopy or one of the alternative methods. He has to interpret this information as well as the

localization result in the schematic LV diagram, and to translate these to the anatomical picture he has in mind, before he can move the catheter to the estimated site of origin of an arrhythmia in the left ventricle. For more accurate operation and shorter time it is expedient to combine these two kinds of information in a single mode of presentation. For example, with biplane fluoroscopy the physician's task is facilitated if the estimated exit site appears on the biplane monitors, together with the most recent catheter-tip position. This would provide actual *catheter guidance*, rather than separate exit-site localization and catheter-tip localization. Such catheter guidance can only be provided by combining catheter localization methods, either fluoroscopic, magnetic, or electric, with arrhythmia localization methods, viz. electrocardiography.

In this chapter, the feasibility of a catheter guidance system is investigated. Since our group has used mainly biplane fluoroscopy for catheter-position monitoring, the discussion will concentrate on this method. However, the method that is presented is applicable to electric and magnetic localization techniques as well.

9.2 Overview

In order to present localization results on the monitors of the fluoroscopy system, LVCC have to be converted into fluoroscopic projections. If the positions of the X-ray sources and detectors are known, fluoroscopic projections of points in space can be created from their three-dimensional (3-D) coordinates. The 3-D coordinates of points on the left-ventricular (LV) endocardial wall in turn can be computed from LVCC by projection on the wall if the wall geometry is accurately known, and if each cross section of the wall perpendicular to the apex–mitral valve ring axis is star-like with respect to the intersection point with the axis, i.e., any half-line that lies in a cross section and intersects the axis, intersects the endocardium exactly once, as illustrated in figure 9.2. We assume that in the ventricle the deviations from a star-like shape are small enough to ignore for our purposes.

The LV wall geometry of a particular patient is usually not accurately known. In most cases, at best endocardial contours obtained by contrast ventriculography are available during a catheter ablation procedure. Therefore, we investigated construction of fluoroscopic projections from LVCC with a simple model for which all the required parameters can be obtained from the biplane images.

Based on visual inspection of magnetic resonance imaging (MRI) data of the hearts of 24 healthy subjects, we created two models to describe the left-ventricular wall: 1) a full ellipsoid of revolution of which only a part is used,

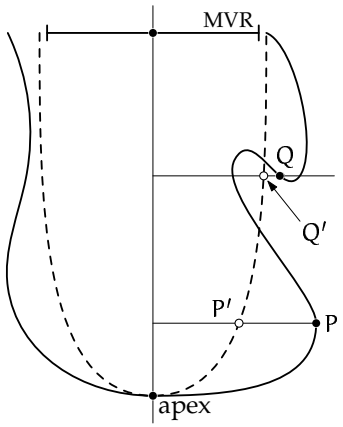

Figure 9.2: *Cross section of an imaginary left-ventricular wall, parallel to the apex–CMVR axis, illustrating the conversion from wall position to left-ventricular cylinder coordinates (LVCC) and its reverse. The wall is indicated with a solid line, while a model of the wall is shown with a dashed line. Point* P *is represented in LVCC in a unique way. Perfect conversion from LVCC to a wall position is possible for point* P *if the wall is perfectly known. For the model in this illustration the computed position is* P′*, and a considerable representation error is made, but the computed position will be unique. In contrast, if point* Q *is represented in LVCC, the reverse mapping cannot be performed in a unique way, because the projection line from* Q *to the axis crosses the wall several times. In this case, if the reverse mapping is carried out using the model, yielding point* Q′*, the error will be small because the model happens to cross the projection line very near to* Q*. The resulting position is unique with respect to the LVCC provided that the cross section of the model model perpendicular to the axis, is star-like with respect to the intersection point of the axis and this cross section. However, it is not unique with respect to the original positions. In this example, the cross section of the ventricle perpendicular to the axis is star-like at the level of* P *but not at the level of* Q*. We assume that, in practice, such deviations are small enough to be ignored.*

and 2) a half ellipsoid of revolution. We studied how well these two models describe the LV wall geometry by fitting them to the MRI data. Second, we studied whether their parameters can be estimated from biplane fluoroscopic projections of the heart. These projections were simulated from the MRI data. Finally, we tested the application of the second model for conversion from LVCC into fluoroscopic projections using both the MRI data and actual biplane images obtained during cardiac catheterization.

9.3 Materials

Geometric data of the LV endocardial wall were obtained from MR images of 24 healthy subjects (14 male and 10 female). Their age ranged from 22 to 64 years. The MRI scanner used was a 1.5 T Siemens Magnetom SP. The scanned MR images were perpendicular to the so-called "long axis of the heart," based on standard echocardiographic imaging views [28]. This axis runs approximately parallel to the line from the LV apex to the middle of the mitral valve ring (MVR). The long axis of the heart is indicated schematically in figure 9.3. Images perpendicular to this axis are called "short-axis images." For each subject, the long axis of the heart was selected using the procedure described by Burbank et al. [28,95] and the heart was imaged using about 12 short-axis images at 10 mm distances (Turbo-flash sequence). An example is shown in figure 9.3. To minimize movement artifacts, these images were produced during end-diastole by triggering on the peak of the R wave of the ECG, with the subject holding his breath. The contours of the LV endocardium (the inner surface of the left ventricle) were discretized from the MR images using dedicated segmentation software. A triangulated representation of the endocardium was constructed from these contours. The resulting triangulations consisted of 85 ± 17 vertices (range 55–120, depending on the size of the ventricle).

To test clinical applicability, we also used 107 catheter positions measured with biplane fluoroscopy in eight patients (eight to 21 positions per patient). These data were taken from the pace-mapping study in patients with normal cardiac anatomy, previously performed by SippensGroenewegen et al. [236]. For each patient, contrast ventriculograms in the right (RAO) and left anterior oblique (LAO) projections were available. Three anatomical landmarks were derived from these ventriculograms by an expert cardiac electrophysiologist: the apex and the circumferences of the MVR and the aortic valve ring (AVR). From the circumferences of these valves, their centers (CMVR and CAVR) were estimated. In addition, several catheter positions were determined from ventriculograms acquired during the subsequent catheter mapping procedure. The endocardial contours were also determined, but were only used for visualization purposes. The biplane image coordinates of landmarks and catheter positions, determined from the ventriculograms, were converted into 3-D coordinates by taking cross-bearings. First, a point was identified in both images. Then, the two projection lines from the X-ray sources to the detectors were specified and their intersection point was determined. Due to measurement errors, these lines may fail to cross. Therefore, the intersection point was approximated by taking the midpoint of the shortest line segment $P_1'P_2'$ that connects the two projection lines. This is illustrated in figure 9.4. The length of $P_1'P_2'$ was

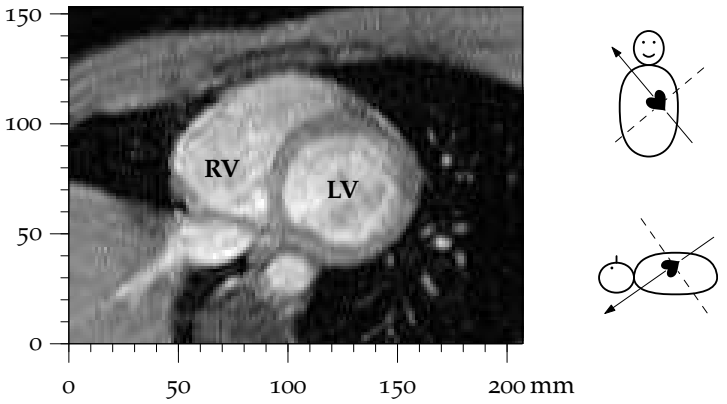

Figure 9.3: *A short-axis MR image from one of the 24 healthy subjects (male, age 37 years). The slice was taken perpendicular to the long axis of the heart and is indicated with a dashed line in the two schematic torso diagrams on the right. The long axis itself is indicated with an arrow. The image was taken during end-diastole. A 151 × 112-pixel area is shown. Since the pixel diameters are 1.37 mm, this area comprises 207 × 153 mm. The bright areas are blood masses. The bright circular area in the middle of the image is the left ventricle (LV). The LV wall and interventricular septum are well discernible, but the thin right-ventricular (RV) free wall cannot be recognized.*

used to estimate the accuracy of the measurements. Median values were 3 mm for catheter positions and 4 mm for the anatomical landmarks (CMVR, CAVR, and apex).

9.4 Methods

9.4.1 Fitting ellipsoids

The first model of the LV endocardium, a full ellipsoid of revolution, was fitted to each MRI data set by minimizing the RMS distance between the vertices of the triangulated endocardium and the model surface. This ellipsoid was constrained to have one aphelion located at a vertex designated as the LV apex. The part of the ellipse that would cover the data points could be freely chosen by the fitting algorithm. The model parameters were the semi-major axis a and the semi-minor axis r. These parameters determine an ellipsoid obtained by rotating an ellipse around the apex–CMVR axis. The semi-minor axis of the ellipse is referred to as the "radius" of this model.

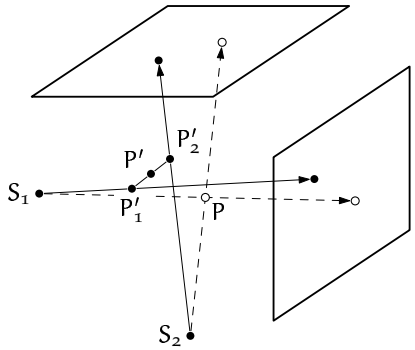

Figure 9.4: *Reconstruction of a point from biplane ventriculograms. The actual point* P *is indicated; the dashed lines indicate its correct projection from the two X-ray sources* S_1 *and* S_2 *on the detectors. Due to measurement errors, the drawn lines are measured instead. Since these lines do not cross in 3-D space, the shortest segment* $P'_1P'_2$ *that connects them is computed. The midpoint of this segment,* P′*, is used as an estimate for* P*.*

The second model of the LV endocardium consisted of one half of an ellipsoid of revolution also with its aphelion located at the apex. In contrast to the first one, this model had its centre at a fixed position, coincident with the CMVR (figure 9.5). It follows that the semi-major axis a of this model is equal to the CMVR–apex distance. With a thus fixed, the radius r was obtained by fitting the model to the vertices of the triangulated endocardium. Fitting was performed by minimization of the RMS distance between the vertices and the model. The optimal radius is referred to as r_f.

9.4.2 Testing

Because the results of the fitting procedures (section 9.5) indicated that model 2 did not perform worse than model 1, and is more convenient because its semi-major axis a can be easily determined from the fluoroscopic data, we selected model 2 for further testing. It was tested for clinical applicability using actual biplane ventriculograms (see Materials). The semi-major axis a was made equal to the CMVR–apex distance. The radius was determined in two ways: 1) as the estimated radius of the MVR, r_m; and 2) as the CMVR–CAVR distance, r_a. The results for these two methods were subsequently compared. From the 3-D coordinates of the catheter positions obtained from biplane ventriculograms, LVCC were computed [236]. The LVCC (length ℓ and azimuth α) were projected on the model surface and

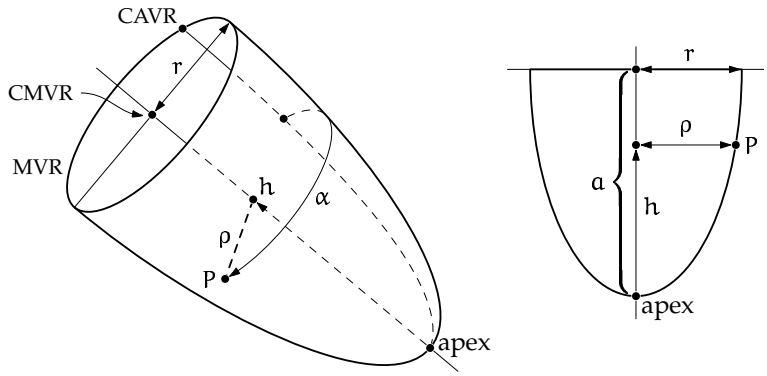

Figure 9.5: *The half-ellipsoid model of the left-ventricular endocardium, consisting of one half of a surface of revolution with an elliptical cross section. The apex, mitral valve ring (MVR), center of the MVR (CMVR), center of the aortic valve ring (CAVR), parameters* a *and* r *of the ellipse, and the coordinates* α, h, *and* ρ *of an arbitrary point* P *are indicated. The* h *coordinate is defined as* $h = \ell a$, *where* $0 \leq \ell \leq 1$. *Endocardial cylinder coordinates specify* h *and* α. *The* ρ *coordinate can only be obtained with the help of a wall model, as presented here. The right panel shows a cross section of the model through the axis and point* P.

the localization errors, defined as the distances between the positions thus estimated and the measured positions, were computed. For visualization purposes the LAO and RAO projections were computed from the reconstructed 3-D coordinates. Since the fluoroscopic data were not calibrated, we expressed the error in the 3-D coordinates as a fraction of the individual ventricular length (the distance between apex and CMVR), multiplied by 80 mm, which is a typical ventricular length, to obtain error estimates in millimetres. For visualization purposes the LAO and RAO projections were computed from the reconstructed 3-D coordinates by simulating X-ray projections.

The model was tested in a similar way on the MRI data, using the vertices of the triangulation as a substitute for catheter positions.

9.5 Results

9.5.1 Fitting the full-ellipsoid model

A full ellipsoid was fitted to each of the 24 MRI data sets. Since there was no penalty for model parts that were far from the data points, the fitting

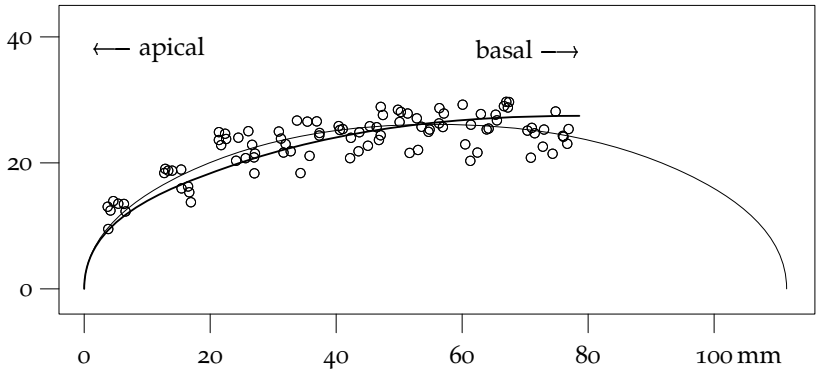

Figure 9.6: *Ventricular radius plotted against ventricular-length coordinate for a set of vertices of the triangulated left-ventricular (LV) endocardium obtained from MRI data of one of the 24 healthy subjects (male, age 27 years). A full ellipse (model 1, thin line) and a half ellipse (model 2, thick line) are fitted to these data. Since the azimuthal angle plays no role here, the ellipsoids were "collapsed" to one angle in this figure. Thus, only a half cross section is shown. About 70 % of the full ellipse is used in this case. The full ellipse has a slightly smaller radius* r *than the half ellipse.*

algorithm was free to choose the optimal section of the ellipsoid to use; only the aphelion and major-axis direction were fixed. This optimal part of the ellipsoid was expressed as the projection of the most basal data point on the axis, normalized by the semi-major axis a. This value had mean and standard deviations of 0.5 ± 0.2 (range 0.1–0.8), indicating that the data sets resembled a half ellipsoid rather than a full ellipsoid. The median distance from the data points to this model, pooled over all MRI data sets, was 2.1 mm (range 0.0–13.5 mm). An example of a fitted ellipsoid is shown in figure 9.6.

9.5.2 Fitting the half-ellipsoid model

The half-ellipsoid model was also fitted to all MRI data sets. Fitting of the model comprised fixation of the semi-major axis a to the apex–CMVR distance and fitting the radius $r = r_f$. An example of a fitted half ellipsoid is shown in figure 9.6. The median distance from the data points to the model, pooled for all subjects, was 2.2 mm (range 0.0–14.1 mm). These values are similar to those for fitting full ellipsoids. Since the semi-major axis of the half-ellipsoid model can be more easily determined from the data

than that of the full-ellipsoid model, we concentrated on this model in the subsequent experiments.

9.5.3 Estimates for the model radius

In the catheterization laboratory, the model radius r has to be obtained from the biplane ventriculograms since there are generally no 3-D data available to fit the model. Therefore, we studied the relation between r_f, obtained from the fitting procedure, and the two estimates r_m (the MVR radius) and r_a (the CMVR–CAVR distance). As an estimate of the MVR radius, we used the average radius of the most basal short-axis cross section in each MRI data set. Estimate r_m performed well: the difference $r_m - r_f$ was 0.0 ± 0.9 mm (range -1.6 to $+2.2$ mm). The distance between CAVR and CMVR proved to be a less accurate estimate for r_f: $r_a - r_f$ was 0.6 ± 5.0 mm (range -7.1 to $+10.5$ mm).

9.5.4 Testing the half-ellipsoid model

The method was evaluated using 107 catheter positions obtained with biplane fluoroscopy from eight patients. The model parameters were obtained from the ventriculograms, a being the distance from CMVR to apex and r being estimated using r_a and r_m. Cylinder coordinates were computed for the catheter positions and projected on the model. Localization errors, i.e., distances between the positions estimated by the model and the positions measured with biplane fluoroscopy, are listed in table 9.1. In addition, the mean values of all patients and the pooled values for all positions together, are given. With $r = r_a$, the pooled reconstruction error for all fluoroscopic data had median 4.3 and range 0.3–17.1 mm. When r_m was used as an estimate for the radius, the errors were somewhat larger with a median of 4.7 mm and a range of 0.0–26.0 mm. In figure 9.7, RAO and LAO projections of the measured and estimated catheter positions of a single patient are shown in relation to the cardiac anatomy.

For testing the model on the MRI data, the r parameter was again estimated using r_m (MVR radius) and r_a (CAVR–CMVR distance). With r_m, we obtained a median reconstruction error of 2.2 mm (range 0.0–14.7 mm) for all MRI data sets; with $r = r_a$, the median reconstruction error was 3.5 mm (range 0.0–18.0 mm).

9.6 Discussion

Two simple models of the LV endocardium, a full ellipsoid of revolution and a half ellipsoid of revolution, were used to reconstruct catheter positions

Table 9.1: *Localization errors in millimetres for eight patients. For each patient, the number* N *of catheter positions, median error, minimum error, and maximum error are given, for both methods of estimating parameter* r*, i.e., using 1) the distance between CMVR and CAVR,* r_a*, and 2) the MVR radius,* r_m.

		localization error with $r = r_a$			localization error with $r = r_m$		
patient	N	median	min	max	median	min	max
1	8	2.0	0.8	10.2	2.3	0.4	11.7
2	12	7.6	3.1	13.5	3.6	0.0	17.9
3	14	3.2	0.3	13.5	4.7	0.5	14.3
4	10	3.8	1.1	10.1	3.5	0.1	12.0
5	10	2.1	0.7	5.1	5.6	1.7	10.7
6	21	5.3	0.4	17.1	12.2	1.4	26.0
7	16	3.1	0.7	13.4	3.5	0.3	11.6
8	16	5.8	0.8	12.4	3.8	0.0	10.2
mean	13.4	4.1	1.0	11.9	4.9	0.6	14.3
pooled	107	4.3	0.3	17.1	4.7	0.0	26.0

from LVCC. When these models were fitted to the 3-D MRI data, median fitting errors were 2 mm for both. We conclude that a half ellipsoid performs just as well as a full ellipsoid (where the used part of the ellipsoid is selected by the fitting algorithm). Since the half ellipsoid can be parametrized more easily, we chose to use this model for further testing with clinical data.

An median representation error of 4.3 mm was obtained over the pooled positions of all patients when testing the half-ellipsoid model on fluoroscopic data. The maximum error in a single patient, taken over all patients, ranged from 5 to 17 mm. These errors can be attributed in part to inaccuracies in measuring the actual catheter positions in the fluoroscopic data; these inaccuracies can be as large as 7 mm [88]. Inaccuracy in the catheter-position measurement may be an important contribution to the error obtained for position 1 in patient 7 (figure 9.7). In the LAO view, the measured position lies outside the ventricular contour which was determined earlier by contrast ventriculography. Movement of the patient during the procedure and deformations of the endocardial wall caused by catheter pressure may also contribute to errors of this kind.

Since we could not infer absolute distances from our fluoroscopic data, we had to assume a ventricular length of 80 mm for all hearts in order to

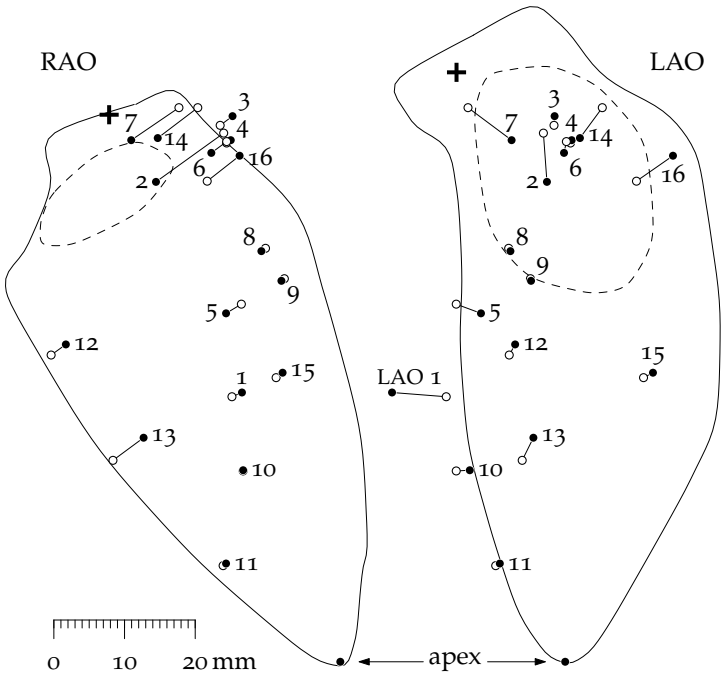

Figure 9.7: *Right (RAO) and left anterior oblique (LAO) projections of the left ventricle of patient 7 (male, age 25 years). Black dots indicate measured catheter positions; open circles indicate the corresponding positions reconstructed from lleft-ventricular cylinder coordinates using the half-ellipsoid model. The catheter positions are labelled with numbers from 1 to 16, to facilitate comparison of RAO and LAO data. The mitral valve ring is indicated with a dashed line. A plus sign indicates the position of the centre of the aortic valve ring. The contours of the left ventricle, determined with contrast cineangiography, are shown for convenience; these contours were not used in our conversion method.*

estimate absolute reconstruction errors. For a clinical application, it would be preferable if absolute sizes could be computed. This would be feasible if the X-ray source and detector positions are known. However, absolute dimensions are not crucial for our method. Provided that the landmark positions are measured with the same system as catheterization is performed, it is possible to present catheter positions on the fluoroscopy monitors even if only relative dimensions are known.

By extracting the positions of apex, CMVR, and CAVR, as well as the circumference of the MVR, from the MRI data sets and using the vertices

of the triangulated endocardium as a substitute for catheter positions, we could also perform the testing procedure on the MRI data. Using the estimated MVR radius r_m, the median reconstruction error was 2.2 mm, which is comparable to the residual error of the fitted half-ellipsoid model (median 2.2 mm). Using r_a to estimate the radius, we obtained a less accurate model with a median reconstruction error of 3.5 mm, and a larger maximum error. For the fluoroscopic data, the reverse was true: 4.3 mm median representation error with r_a and 4.7 mm with r_m as an estimate for r (table 9.1). In addition, the maximum error was much larger with the latter method: 26 mm instead of 17 mm. These differences between fluoroscopic data and MRI data can be attributed to the difficulty of detecting the mitral valve contour in the ventriculograms and recognizing the AVR in the MR images. However, the overall reconstruction errors of fluoroscopic data and MRI data were remarkably similar.

A VT exit site that is localized by BSM-guided pace mapping is generally used as a starting point for an activation mapping procedure aimed at identification of a suitable site for radiofrequency ablation [194]. Precise accuracy requirements for this purpose are not known. However, occasionally the exit site itself is a target for ablation. For conventional radiofrequency ablation, positioning of the ablation catheter within 5 mm from the target site is required to secure a successful outcome [233]. Although the average reconstruction errors are below this limit, 12 % of the errors in the MRI data and 45 % of the errors in the fluoroscopic data are larger. Application of the recently introduced cooled radiofrequency technique for VT ablation is likely not to require such a high level of reconstruction accuracy because the cooled-tip catheters produce significantly larger lesions [29, 182].

For a better understanding of the limitations of the model employed here, we fitted ellipses to the short-axis cross sections of the triangulated endocardia obtained from the MRI data. These ellipses (x, y) had a free origin (x_o, y_o), semi-major/minor axes a, b, and orientation θ

$$\begin{pmatrix} x \\ y \end{pmatrix} = \begin{pmatrix} x_o \\ y_o \end{pmatrix} + \begin{pmatrix} \cos\theta & \sin\theta \\ -\sin\theta & \cos\theta \end{pmatrix} \begin{pmatrix} a\cos\phi \\ b\sin\phi \end{pmatrix}.$$

Subsequently, we analysed the parameters a, b, and d, where the "centre offset" $d = [(x_o - x_a)^2 + (y_o - y_a)^2]^{1/2}$ is the distance between the centre of the fitted ellipse and the intersection point of the cross section with the apex–MVR axis, (x_a, y_a). Results for all subjects are shown in figure 9.8. The excentricity of the fitted ellipses was small, as can be judged from figure 9.8. The distance d was small compared to a and b in most cases except for several cross sections in subjects 3, 10, and 22. The largest fitting error found was 3.7 mm. When circles with fixed origin $(x_o, y_o) = (x_a, y_a)$ were fitted, the maximum error was 13 mm. This suggests that a more complicated

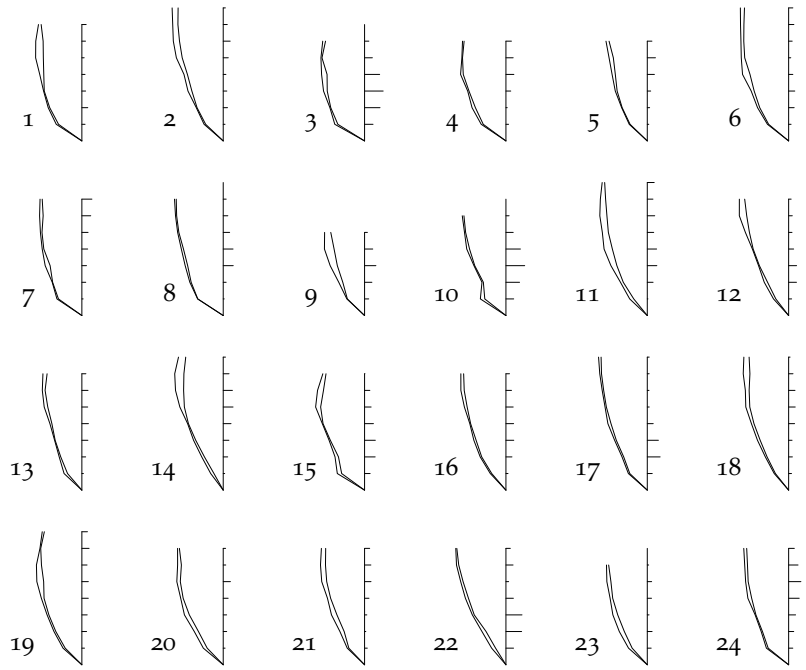

Figure 9.8: *Major axis* a*, minor axis* b*, and centre offset* d *resulting from fitting ellipses to short-axis cross sections of 24 subjects. Cross sections were made at 10-mm intervals. For each subject, the two lines on the left of the diagram indicate the semi-major and semi-minor axes as a function of the ventricular length coordinate. The bars that extend on the right of the axis indicate the centre offset. Note that the direction of the major axis and the direction of the offset are not indicated in these diagrams. In four subjects (3, 8, 10, and 23), the most basal cross section could not be fitted because there were not enough data points (fits were automatically rejected if the gap between successive points was more than a quarter circle).*

model consisting of non-aligned ellipses, as depicted in figure 9.9, could represent the ventricle better in subjects like numbers 3, 10, and 22 (figure 9.8). Of course, more information than just the apex and valve positions is needed to set up such a model.

Several other models were used previously to represent the LV endocardium; an exhaustive list was given in a recent review by Frangi et al. [68]. Simple models of the entire LV wall were used for simulation of cardiac excitation and recovery [142, 184] but may be too inaccurate for our purpose. A bullet model was applied for LV-volume computation using echo-

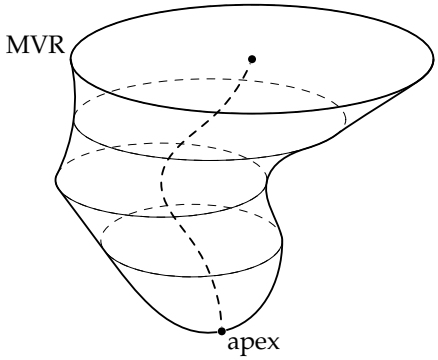

Figure 9.9: *A model of the left ventricle consisting of non-aligned ellipses. The apex and mitral valve ring (MVR) are indicated. The axes and centre of each ellipse can be determined from the points of intersection of the contrast fluoroscopic outlines with the plane of that ellipse.*

cardiography [181]. A full ellipsoid is commonly used for contrast fluoroscopic LV-volume computations [49]. A half ellipsoid was previously used by Gustavsson et al. [85] as an initial approximation of the LV shape, which was meant to be refined with data from 2-D echocardiograms. One could also use a triangulated model of a "standard" heart or a heart properly selected, using simple patient information, from a database like the currently applied MRI data sets. Finally, one could fit a spline surface in three dimensions to the cardiac contours if these are available. This would require 3-D echocardiography, MRI, or CT imaging prior to an ablation procedure. Electron beam computed tomography (EBCT) may be able to provide even more accurate images of the heart [50]. However, in current clinical practice, usually only low-intensity biplane ventriculograms and perhaps previously created contrast cineangiograms, are available. Therefore, for our model we opted to use only the positions of the apex, CMVR, and CAVR, and optionally the radius of the MVR. Still, it may be of interest to develop a method that can use MRI or CT scans if they happen to be available.

In an on-line clinical application for guidance during catheter mapping and ablation of ventricular arrhythmias it may be possible to obtain catheter positions at any time from the biplane images or from other catheter localization modalities [230,279]. If it is also known at which times the catheter tip touches the endocardial wall, this 3-D position information can be used to adapt the model instantly.

We chose the fluoroscopic projections as a presentation mode because they play a key role in the electrophysiology laboratory. Perhaps it seems

more straightforward to present the heart geometry and catheter positions as a 3-D image. However, presentation of quantitative 3-D information is difficult. The use of a stereoscope, red-green glasses, or LCD glasses may be too distracting as the physician also has to observe the real world of the laboratory. Presentation on a normal video display would require depth cues, which would make the scene rather busy in the presence of many anatomic landmarks and catheter positions. A solution might be to use 2-D projections of a 3-D image that is maintained by the computer. If projections are used, it is preferable to choose projections that are familiar to the physician, i.e., either RAO and LAO or frontal and lateral projections. This approach would allow for easy comparison of catheter positions and electrocardiographic localization results, particularly if the data can be combined with the biplane fluoroscopic images on a single monitor.

Since presentation of data on monitors in the catheterization laboratory can only be performed by the manufacturer of the equipment, prototype systems will have to use their own monitors. However, in our experience, a standard video output is often provided with fluoroscopic equipment. This makes it possible to superimpose catheter guidance information on fluoroscopic images on an additional video monitor. Such a prototype will obviously not reduce the number of monitors, but does improve the presentation of the data to the physician by superimposing the image and displacement advice. It will thus reduce the number of monitors that the physician has to observe while maneuvering the catheter in the cavity. The original monitors, which have a much higher resolution than the standard video signal provided for external systems, may be needed in other phases of the procedure.

Although the standard RAO and LAO projections are almost always used for fluoroscopy during electrocardiographic catheterization procedures, the physician sometimes chooses different directions for a specific patient. For example, a 60° LAO projection with 25° cranial angulation may be used to obtain a better view of the LV outflow tract [222]. An implementation of our method should therefore be able to produce any desired projection.

A direct advantage of our method is that it provides a quantitative and objective alternative for a procedure that the physician now has to carry out by visually relating the LVCC provided by our electrocardiographic localization methods to the fluoroscopic projections. In conclusion, presentation of ECG mapping data directly in biplane fluoroscopic projections provides a novel, accurate, and intuitive method to guide catheter positioning and mapping prior to ablation of cardiac arrhythmias.

Chapter 10

The MAPLAB Software for Integrated Mapping

Analysis of multichannel ECG recordings requires special software. We created a software package and a user interface on top of a commercial data analysis package (Matlab) by a combination of high-level and low-level programming. Our software was created to satisfy the needs of a diverse group of researchers. It can handle a large variety of recording configurations. It allows for interactive usage through a fast and robust user interface and batch processing for the analysis of large amounts of data. The package is user-extensible, includes routines for both common and experimental data processing tasks, and works on several computer platforms. The source code is made intelligible using software for structured documentation and is available to the users. — *Comp. Meth. Prog. Biomed.* (in press) [208].

10.1 Introduction

Electrocardiographic body surface maps and high-resolution intracardial maps typically consist of many signals sampled simultaneously. Recordings with over 500 leads have been reported [18]. Our group records mapping data with 64 up to 247 leads which are sampled with frequencies ranging from 0.5 to 4 kHz and 8, 14, and 16-bit resolution at bit steps of 0.73 up to 40 µV [172]. Datafile sizes range from 48 kB to circa 300 MB. A variety of recording situations is employed, resulting in intracardial electrograms, surface electrograms, electrograms recorded in cell cultures, and combined multichannel endocardial and body surface map (BSM) recordings [48].

The methods that are used for the analysis of multichannel ECG recordings differ strongly from those for single-lead or standard 12-lead ECGs. The

large number of channels makes visual inspection of all waveforms almost impossible: even if an experienced investigator were to inspect one electrogram per second, it would take more than eight minutes to evaluate a 500-lead recording. On the other hand, the availability of data sampled at many sites does enable spatial representation of parameters such as potential or activation time using, for example, pseudocolour maps. In addition, computer algorithms of varying complexity are employed to convert the large amounts of data into concise diagnostics. Standard ECG-analysis tools are therefore inadequate for multichannel ECG (MECG) analysis.

10.2 Background

Analysis of multichannel ECG data requires specialized software. Due to the variety in research purposes and available hardware, many custom software packages were created in laboratories involved in electrocardiographic research. However, it is advantageous to make such software as general as possible, making it applicable at many different laboratories. This could prevent repetition of effort and make implementation of difficult algorithms and a sophisticated user interface more worthwile. We shall analyse some requirements for such software and present a software package that is aimed to fulfill these requirements and to be general enough to be useful for several research groups.

10.3 Design Considerations

Interactive processing is required in various situations. For example, if analysis of BSM recordings is used on-line to guide catheter ablation of an arrhythmia, a computer program can perform all computations, but the physician has to select the QRS complex of interest [194, 212]. An interactive system is also expedient if data are processed off-line but with input from a human expert. Such a system should, for example, be able to apply baseline corrections, integrate over time, and produce maps of potentials and integral values in several different styles (figure 10.1). It has to detect activations in intracardial recordings and QRS complexes in BSMS, and allow the user to correct detection results interactively. For research purposes, it is necessary that new algorithms can be incorporated with little effort in a user-interface package so that they can be tested interactively. Such incorporation of new program parts should preferably not break the existing software, even if there are errors in the experimental parts, since such errors are very likely to be present, and would otherwise necessitate many re-starts of the sofware, which may consume much time.

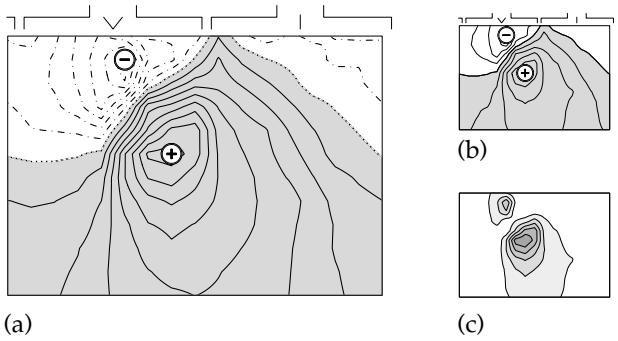

Figure 10.1: *Examples of body surface maps.* **(a)** *Large format, used to show details clearly. Potential values are indicated with isopotential lines; solid lines are used for the positive area, dash-dotted lines for the negative area, and a dotted line for the zero level. The area with positive potentials is shaded. Maximum and minimum are indicated. Above the map, the positions of shoulders, sternum, and spine are indicated schematically.* **(b)** *Economy-size map. All contour lines are drawn in a solid style because their curvature is too high for display in a dashed or dotted style.* **(c)** *Special format for unsigned data, such as squared potentials. Both contour lines and grey values are used to display the values. In this map, the schematic torso anatomy was omitted as is often done when many maps are shown in a single display.*

There are also circumstances where batch processing of data is more appropriate. For example, to create and test a new algorithm it is often necessary to go through the cycle of changing and testing a program several times, while testing a large number of recordings. The creation of programs for such jobs is easier if separate routines are available for basic tasks such as loading of recordings from file, baseline correction, and activation detection. Note that these are tasks that are also performed in an interactive analysis program.

Interactive and noninteractive software thus have many requirements in common. Creating them in the same programming environment has the advantage that basic routines can be shared, and that interchange of data between interactive and noninteractive software is more easily achieved than when both are completely separate programs. It is expedient if basic routines for tasks like sorting, differentiation, principal components analysis, and notably graphics presentation are already present in the programming environment. The same applies to user-interface routines; for the creation of interactive software, the need of an easily programmable user

interface is obvious. Batch programs can also benefit from user-interface facilities, particularly in the testing stage. For example, when inspecting outliers in a scatter plot, it is desirable to just click on a data point with a pointer device to view the corresponding ECG data. A convenient way to achieve this is by making calls to an existing user-interface package in the same programming environment. The common environment is a clear advantage in such cases.

Software documentation and source control are indispensable, particularly for experimental software. Good documentation facilitates maintenance of software. Source control, by which we mean the automated logging of changes to software, provides crucial information to the programmer who wants to change an existing program. Such a system can also provide file locking services, which prohibit multiple programmers overwriting each other's changes by accident, thus facilitating the work of a team of scientists and programmers cooperating on a project.

In conclusion, research in the field of multichannel electrocardiography can strongly benefit from a software package that has both a user interface and a programmer interface, provides basic as well as sophisticated ECG analysis routines, has access to existing graphical, mathematical, and user-interface programming libraries, and is well documented and organized. We describe how we created and worked with a software package that fulfills all these requirements. We shall not discuss the algorithms that are used, since the purpose of our software is to provide a framework for the implementation of algorithms, and not to make a selection from them. In fact, several alternative methods were implemented for particular tasks, so that users can make their own choices.

We chose to create our software under an interactive programming environment (IPE). By IPE we mean an interactive program that can execute typed commands and programs or "script files." An IPE can include libraries of mathematical, graphical, user interface, and other functions. It can be platform-independent in the sense that the same commands have equivalent results on different platforms. It is an advantage if an IPE can communicate with external programs or call functions written in a system programming language to allow efficient handling of bottleneck operations. It is also advantageous if the IPE programs are plain-text files, because this facilitates documentation and source control (section 10.4.2). "Visual" programming languages and IPEs with a graphic programming interface are therefore less suitable for our purposes. An IPE can also be an extremely versatile debugging program because it allows access to internal data at any time, can use its graphical capabilities for display of debugging output, and may permit substitution of program parts without restarting the whole program.

10.4 System Description

10.4.1 Choice of platform

The IPE we used was MATLAB (The MathWorks Inc., Natick, MA, USA), a program that can apply mathematical operations to matrices, has functions for graphics and user interfaces built-in, and includes libraries of mathematical routines. Apart from platform-specific bugs, MATLAB programs run without modification on several operating systems and computer architectures. This allowed us to develop the software and do our experimental work on a UNIX system while also providing code for MS-windows and Apple Macintosh systems.

Interpreted programs run slower than system programs. Modern computers are capable of running an interpreter fast enough for a user interface or small computations, but for bottleneck operations such as baseline correction of a multilead ECG it could be necessary to write a function in a compiled language and use this function in the IPE. The IPE we use, supports dynamic linking of functions programmed in the C language. We used this feature selectively for often-used routines that caused significant delay when programmed in the IPE language.

The C functions are a limitation to platform-independence because they must be compiled specifically for each platform. We made our C sources compilable for all platforms used, by programming strictly conforming to the ANSI standard, without using compiler-specific or platform-specific libraries, whenever possible. We had to resort to platform-specific code at two occasions: when implementing directory reading and for TCP/IP communication (section 10.5.1).

10.4.2 Documentation and source control

We chose the "literate programming" technique [129, 130] (Appendix A) to document our software. A "literate" program is written in the style of a monograph and consists of small pieces of code which are written in the programming language(s) of choice—in our case MATLAB and C. These code fragments are called "refinements" and can be partially or completely defined in terms of each other. Each refinement comes with a documentation part, written in a document formatting language—in our case LaTeX. This means that the program documentation can include mathematical formulae, graphics, references, indexes, etc. The refinements can be presented in any order the author wishes. By application of refinements in other refinements the code is ordered for the compilers's purposes. Because the documentation parts can be large compared to the code parts, without ob-

scuring the program structure, it is possible to give a thorough description of the code, explaining not only *what* it does, but also *why* it does so. The latter is often neglected in traditional software documentation, but highly important for scientific and experimental software. Literate programming systems allow the definition of multiple program files in a single document. This facilitates comprehensive documentation of interrelated program files. A small program, illustrating some of these aspects, is shown in Appendix A.

Our C-language functions were created and documented with the CWEB system [132]. For the MATLAB programs we created a literate programming system, called MWEB [203]. We also made provisions to include CWEB and MWEB programs in LaTeX documents [202] and to implement a uniform layout of the circa 90 program documents. The documentation could be printed and was also made available on our internal web server as hypertext in PDF format.

Additional tools were the Revision Control System (RCS) [22], which provided for automated revision archiving, the standard UNIX `make` program and a few small programs written in a scripting language (Perl [269]) to control the compilation process.

10.4.3 Structure

To accommodate both interactive use and batch processing we created two packages: a low-level toolbox, called MAPLIB, and a user interface, called MAPLAB, which was created using MAPLIB routines. The toolbox contains all routines that interactive and noninteractive programs can share; it can also be used independently for batch jobs and for user-created additions. Communication of data between MAPLAB and batch jobs is done with IPE variables, and with files if the data have to be passed between invocations of the IPE.

The user-interface package consists of several tens of functions, whose syntax is documented in the source files. This allows experienced programmers to make calls to the user interface from experimental programs, for example to inspect internal data of these programs with existing tools. It is also possible to let user-created programs be called from MAPLAB. This is done by a general hook mechanism. Programs that run in the IPE can add a code fragment to one of MAPLAB's hooks. This code fragment is then executed whenever the hook is activated, e.g., every time a new file is loaded, an activation marker is moved, or baseline adjustment is performed. Some of MAPLAB's programs are activated by this hook mechanism as well.

Two new file formats are used by our software: a datafile format for storage of ECG data and a metafile format for descriptions of data (we con-

sider it undesirable to store such descriptions in the datafile itself because the integrity of the datafiles, which may contain clinical data, must be guaranteed, and because datafiles are often stored on a read-only medium such as CD-ROM).

A metafile contains the name of a datafile and a set of time instants such as begin and end of a QRS complex and activation times which refer to the datafile. The aim of the metafile format was to store descriptions of datafiles on disk. Metafiles can be loaded in the MATLAB package in the same way as datafiles. The software will then load the corresponding datafile and place the time markers at the positions indicated in the metafile. This makes it convenient to load, for example, previously determined time instants for baseline correction together with the datafile. Our metafiles are often used to postprocess hand-made analyses in a batch job. In addition to the datafile reference and time instants, a metafile can contain a checksum to allow verification of the identity of the datafile, a time-stamp, and an identification of the researcher and the analysis software. The software finds a datafile by the name and location recorded in the metafile. If the file is not found at the specified location, for example because metafile and datafile were transported to a computer with a different directory structure, the software will search for it by means of a configurable search path.

The datafile format is discussed in section 2.5.4. The two file formats are designed according to the IFF metaformat [178], which also underlies, e.g., Amiga's ILBM format. This design allows extensions (such as new compression types [149], or additional parameters) with backward and forward compatibility.

10.4.4 Generality

The MATLAB package was designed to cope with every possible electrode configuration, including body surface map configurations [98] and various grids for intracardial recordings (figure 10.2). Regular and irregular one-, two-, and three-dimensional shapes [155] can be handled. For each configuration, an *electrode definition file* was created, which specified the positions of the electrodes, the corresponding lead numbers, and the type of lead (surface, endocardial, epicardial, etc.). Users can create such files when they employ new grids or need to make ad hoc changes to compensate for wiring errors. The software uses this configuration information to display maps taking into account the differences between types of leads. For example, it does not automatically perform activation detection in surface leads, which would be meaningless.

Potential maps, integral maps, activation time maps, and maps of other data can be displayed in several different formats. It is possible to indicate

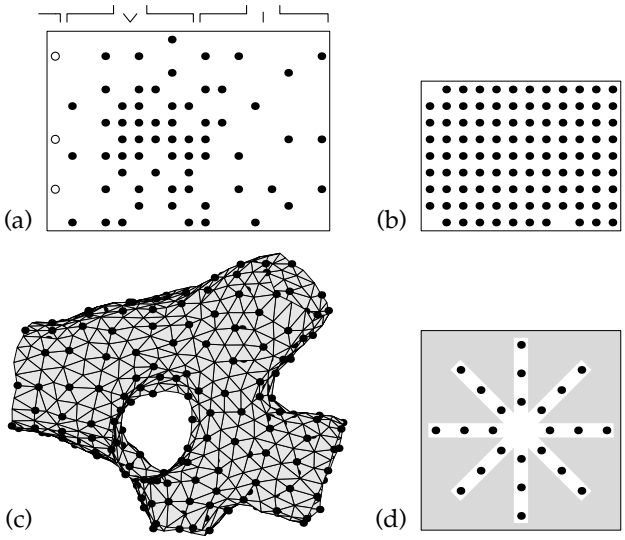

Figure 10.2: *Examples of electrode configurations. Dots indicate electrode positions.* **(a)** *Sixty-four-channel body surface map configuration. This configuration was used for the maps in figure 10.1. This is a cyclic grid; the rightmost column of electrodes is repeated on the left, indicated by open circles. The vertical interelectrode distance* s *is approximately 3 cm; the electrode diameter* d *is 1 cm.* **(b)** *A 105-channel configuration for intracardial maps,* $s = 0.8\,mm$, $d = 0.1\,mm$. **(c)** *A 3-D multielectrode with 197 terminals fitting in the left atrium of a dog,* $s \approx 1\,mm$, $d = 0.1\,mm$ *[155].* **(d)** *A star-shaped grid used for cell cultures of cardiac myocytes;* $s = 300\,\mu m$, $d = 24\,\mu m$ *[12]. Cells grow only in the white area.*

data values for electrodes with an interpolated or non-interpolated pseudocolour map. In addition, data values can be printed at the electrode positions, and several contour algorithms are available to draw, for example, activation isochrones (figures 10.4, 3.8, 3.9, 3.10). One of these is the "isomap" algorithm presented in section 3.7. Data for pseudocolour maps, texts, and contours can be chosen independently; this facilitates comparison of e.g. potential maps to an activation (isochrone) map.

10.4.5 Features

The MAPLAB package is intended as a basis for development and implementation of algorithms. It includes basic, established, and experimental algorithms. Among the implemented routines are various filters, zeroth- and first-order baseline correction, QRS detection [123], arrhythmia localization

by body surface mapping using either databases [194, 236] or a continuous algorithm [212], a configurable activation-detection algorithm, computation of nondipolar content [1, 211], signal alignment and signal averaging, and various display methods discussed above. As mentioned in section 10.3, we shall not go into details about the algorithms.

Important features are the possibility to edit results of automatic analyses, such as activation detection, by hand quickly and easily, and the provisions for storing such edited results for later review or processing by batch jobs.

The software package creates several windows on the screen; each window displays the data or a part of the data in a different way, and contains user-interface controls for tasks relevant to the kind of display. For example, the Channel window (figure 10.3) shows one or more ECG tracings and contains a user interface for selection of time instants, baseline correction, filtering, etc. In contrast to this temporal display, the Map windows show data in the spatial domain, such as potential maps and activation maps. Examples are shown in figure 10.4. Time instants for maps are selected in the Channel window, and working channels can be selected conversely from Map windows by clicking at electrode positions.

We chose to have multiple instances of some windows, while other windows could be one-of-a-kind. For example, multiple Map windows can show potential maps and activation maps simultaneously. In contrast, only one Channel window was needed, because it can show as many simultaneous ECG tracings as the user wishes and because it is usually preferred to display all ECG tracings in a single frame.

Another window that can have multiple instances is the Localizer window, which shows results of arrhythmia localization obtained with body surface maps. Multiple instances of this window were desirable because it is useful to see results for different cavities or by different algorithms at the same time (figure 10.5). Localization is performed either by comparing QRS integral maps to database maps [236] or by a continuous algorithm [212]. Databases exist for human ventricles and atria [236, 239, 240]. The Localizer windows can present localization results in several different diagrams for both ventricles and atria.

For each window there are one or more programs to create and maintain that particular window. We tried to make the programs corresponding to different windows as independent as possible, but some interrelations were inevitable, for example to keep track of a "current channel," rejected channels, and marker values in different windows. Most relations, however, are hierarchical; for example, a button in one window can make a call to a function that creates another window.

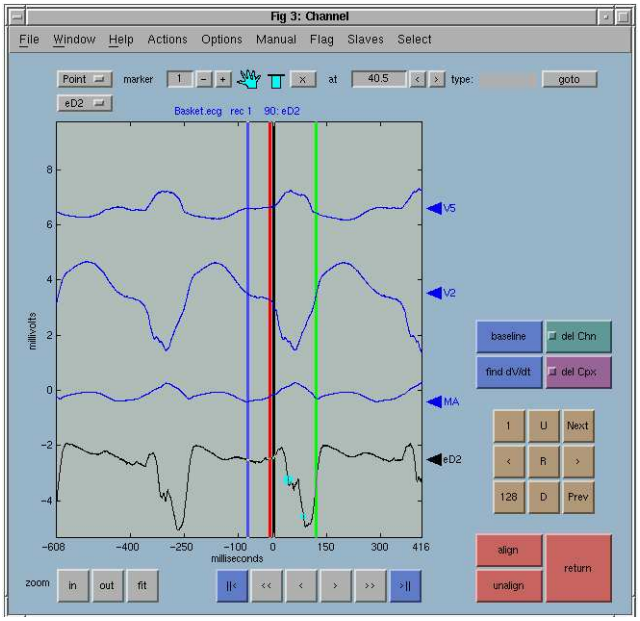

Figure 10.3: *Channel window. The vertical lines between the ECG tracings and the two dots on the lowest tracing are called "markers" and are used to indicate time instants. Dot-shaped markers indicate instants that are applicable to a single lead, e.g. activation times, while line-shaped markers are used for instants that apply to all leads, such as onset and offset of the QRS complex. The markers can be placed automatically by the software, for example by the activation-detection routine, as well as by the user, by dragging them with a pointer device.*

10.5 Discussion

Software for MECG analysis should be fast, flexible, extensible, easy to program, and easy to use. These requirements are partly at cross-purposes. The software we created is flexible, but not as fast as would be possible if it were implemented entirely in a system programming language such as C. This is a trade-off between programming efficiency and usage efficiency. User responses are fast enough if a modern computer is used. For example, on a Pentium-II PC at 233 MHz, drawing an annotated isochrone and pseudocolour map (as in figure 10.4) with 121 electrodes takes approximately 0.3 s, activation detection on 121 channels and 130 samples takes about one second, and dragging of markers happens with no noticeable delay.

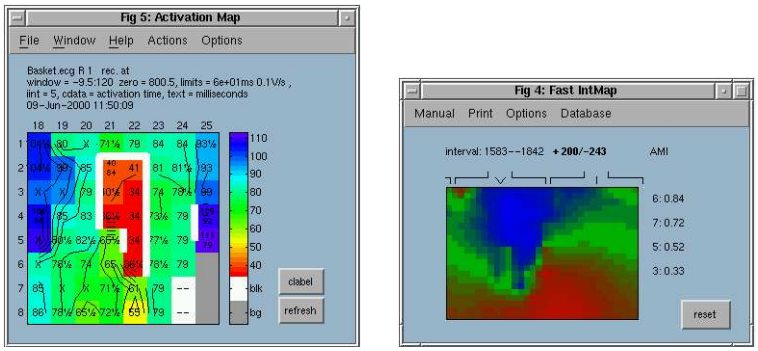

Figure 10.4: *Activation Map window (left) and body surface map (BSM) window (right). The activation map is shown with isochrones, pseudocolours, and texts. The white lines in the activation map represent lines of block, as determined by the activation time difference between adjacent electrodes. A white area represents electrodes where no activation was detected within the current complex. The BSM window shows the body surface QRS integral map corresponding to this activation map. The format of this map is quite different from that shown in figure 10.1; the pseudocolour map used here can be generated faster and is useful for display on a computer monitor. A contour plot as in figure 10.1 is more suitable for hardcopy.*

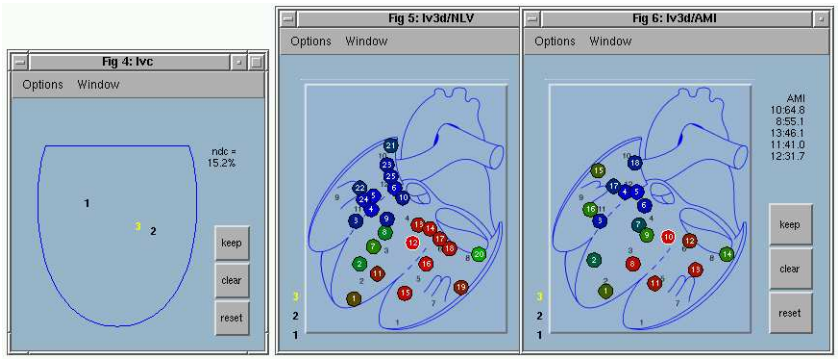

Figure 10.5: *Examples of Localizer windows. Several of these windows can be active in a single* MAPLAB *session while each of them displays localization results in a different format. The middle and right windows show database localization results [236], indicated in a left-ventricular pseudo 3-D plot using different databases. The title of the right window indicates that this is a (psuedo) 3-D left-ventricular diagram (lv3d) featuring the anterior myocardial infarction (AMI) database. At the righ side of this window, the 5 best-correlating segment numbers are indicated with the correlation values in percents. The left window shows continuous localization results [212], given in a schematic diagram of the left ventricle. Numbers (in this case 1, 2, and 3) are used to indicate localized positions; these numbers can be clicked with the mouse to reload the corresponding ECG data.*

One requirement for the package was that it would be extensible. Several extensions have been written and subsequently incorporated in the package. One such extension constitutes the interactive display of a three-dimensional (3-D) multielectrode for the left atrium of a dog heart [155] (panel c in figure 10.2). The left atrium is a complex 3-D structure that cannot be mapped on a flat surface without losing important geometrical information. To overcome this problem, the 3-D shape of this 197-electrode device was obtained from CT scans and stored as a triangulated surface, which was visualized on the computer. Measured potentials and activation times were displayed on this surface, and electrode positions were indicated. The object could be rotated with the mouse to allow inspection of all sides. This software was written in the same IPE as MAPLAB so that it could easily interface with the latter. For example, analysis of ECG leads was performed with MAPLAB and results are presented directly on the surface. Electrode markers on the surface could be clicked with the mouse to show the corresponding ECG tracing in MAPLAB's Channel window (figure 10.3). The special window thus operated in the same way as MAPLAB's own Activation Map window.

On several occasions, we implemented new methods first as small MATLAB scripts, then improved them, and finally re-implemented them in C for better performance.

A minor drawback of an IPE is that—in principle—it allows the user to corrupt internal data. Therefore, we used variable names that are unlikely to be used by accident and while doing so we experienced no problems in this respect.

As it stands, our software is less suitable for real-time clinical applications, such as BSM-guided catheter ablation [194]. Although it can serve as a prototype in the hands of an experienced operator during clinical evaluation of a new procedure, it is too complicated and perhaps not sufficiently robust for routine clinical use. For such purposes, dedicated software and hardware, such as created previously for BSM procedures [154], remains a better choice.

The software is used by several medical and biomedical researchers in both clinical and fundamental research groups [12, 42, 48, 81, 82, 92, 93, 118, 122, 157, 193, 194, 220, 240, 275]. The software has been used for the creation of graphics for several years [42, 193, 194, 240]. Examples of MAPLAB's graphical output are shown in figure 10.1 and in the maps shown elsewhere in this thesis. It has become the primary tool for several research groups and has played a part in many clinical and experimental studies [12, 48, 81, 82, 92, 93, 118, 122, 157, 220]. The MAPLIB toolbox and the MAPLAB interface were used in all ECG-related studies performed by its authors [206, 211, 212, 275]. The resulting experience and the frequent contact with other users have

accelerated the development of the system.

Platform-independence turned out to be important. We programmed most comfortably on a Linux system. Linux, a UNIX implementation for the IBM-compatible PC and other architectures, is a robust operating system for which all programmer's tools, such as a powerful text editor, text processing tools, C compiler, TEX system, `make`, and RCS are readily available, stable, free, and working seamlessly together. The system's robustness is even more important for programmers than for other users: segmentation faults are common during development and a UNIX system handles them gracefully without consequences for other processes or the operating system itself, even after hundreds of segmentation faults have occurred. On the other hand, two or three segmentation faults of our software or problems in other applications sufficed to crash any version of the MS-windows system. However, most users prefer systems such as MS-windows or the Apple Macintosh. Therefore, we wanted to generate code for these platforms but develop it on a UNIX system.

We found that literate programming (Appendix A) makes our programs more readable for ourselves and for others. It allows the authors of MAPLAB to understand, comment, and change each other's programs. Our experience confirms the observation that literate programming encourages the programmer to scrutinize the code [130]; many a misconception was brought to light by trying to explain the code.

Source control using the RCS system [22] and software building using the `make` program (which is standard software on UNIX systems) allowed different programmers to work on the same set of source files without the risk of overwriting each other's changes and to create consistent distributions of the package at any time.

10.5.1 Submitting diagnostic information through Internet

One feature of the MAPLAB software that has not been discussed yet is its ability to submit error reports through the Internet. All software, and especially software that is continuously under development like MAPLAB, can emit several kinds of error messages. These include reports of relatively harmless user errors as well as possibly fatal errors that occur due to bugs in the software. The latter are important for the development team. Even if the developers use the software themselves and may encounter the error message in practice, it is very likely that they use the software in such a way that some problems never occur, while they do occur with other users. It is therefore important that such errors are reported.

Our experience has shown that users cannot be relied upon to pass such reports to the authors of the software. Therefore, we developed routines

that submit such reports automatically over the Internet. Several problems in the software have since been solved due to reports received in this way, to the surprise and satisfaction of the users who encountered the error before.

Several problems had to be solved for the implementation of Internet logging. The first problem was that although network communication protocols are standardized (TCP/IP), the software libraries that can be used for this purpose are system dependent. On UNIX systems, a standard implementation, called the "sockets" interface, can be used. A similar interface is available for MS-Windows, but it differs enough from the UNIX interface to require a few tens of exceptions in our code (using "`#ifdef`" in the C language). We have made no attempt to implement Internet logging on Macintosh computers.

The next problem was presented by company firewalls. The MATLAB software is typically used on computers connected to hospital or university intranets that are connected to the Internet through gateways known as "firewalls" because they run software that prevents unauthorized connections. It depends on company policy what is authorized; in many cases this policy prevents the creation of a direct TCP/IP link between a computer inside, and another outside the hospital. In our case, the computer that receives the reports is connected to a hospital intranet as well, and its firewall prevents connections to be made from outside the hospital.

We circumvented problems with firewalls by using the Internet mail protocol (SMTP) to submit the error reports. This protocol does not require a direct link between the submitting and the receiving computer. Mail is sent to a dedicated "mail server" and from there submitted to the mail server at the receiving end, from where it can be picked up by the receiving computer. An example diagnostic message is presented in figure 10.6.

Obviously, Internet logging does not work on computers that are not connected to the Internet. In addition, it is problematic on computers that are connected by a non-persistent link, such as a telephone line, where an automatic logging mechanism may cause a connection to be made at inconvenient times. Therefore, it must be made easy for the user to switch off the automatic submission of log reports—in such a way that the user is not tempted to do so in situations where internet logging does no harm.

Another application of Internet logging is the acquisition of usage statistics. Every invocation of a user-interface element in MATLAB (buttons, menus, etc.) is counted, and at the end of a session these statistics are submitted together with the error reports. This allows the authors of MATLAB to find out which functions are used most, and it can help them to decide which user-interface elements should have the most prominent positions. For example, if a menu item appears to be used very often, it may be replaced by a button that can be clicked directly. Conversely, buttons that are rarely used may

```
1  BS_LOG_MESSAGE $Revision 1.19 $
2  MyName = <980600079>
3  MyFullName = <980600079.amc.uva.nl>
4  MyIPAddr = <145.117.46.205>
5  MyRealName = <amcip0787.amc.uva.nl>
6  MaplabVersion = 1.43.85
7  found a log file:
8  > bs_log: found host <barlaeus.ic.uva.nl>
9  > bs_log: connected to <145.18.68.50>
10 > bs_log: R: 220 barlaeus.ic.uva.nl ESMTP Sendmail 8.9.3/8.9.3;
11 > bs_log: S: helo 980600079
12 > bs_log: R: 250 barlaeus.ic.uva.nl Hello amcip0787.amc.uva.nl
13 > bs_log: S: mail from:<maplab%gnu@amc.uva.nl>
14 > bs_log: R: 250 <maplab%gnu@amc.uva.nl>... Sender ok
15 > bs_log: S: rcpt to:<mlog%gnu@amc.uva.nl>
16 > bs_log: R: 250 <mlog%gnu@amc.uva.nl>... Recipient ok
17 > bs_log: S: BS_LOG_MESSAGE $Revision 1.19 $
18 > bs_log: RealTime = <4> seconds
19 > msg = <load file 131*1792 'unknown'>
20 > msg = <load rec 2 from 131*1792 'unknown'>
21 > msg = <load file 241*7168 'tdp'>
22 > BEGIN ERROR
23 >   Reading header failed. RecNr too high?
24 > END ERROR
25 > msg = <load rec 1 from 241*7168 'tdp'>
26 > msg = <load file 241*7168 'tdp'>
27 > BEGIN ERROR
28 >   Unforeseen error in MapLab
29 >   please inform the authors about this
30 >   line 1814 of bs_chn.m in channel.web,v 1.260, ID = 102
31 >   lasterr = Index exceeds matrix dimensions.
32 > END ERROR
```

Figure 10.6: *Example* MAPLAB *log message. It starts with the revision number of the sending program, which identifies the format of the message. Lines 2–5 identify the sending machine and line 6 the software version. The program then reports that it found a log file, which contains a report of the previous session. Lines 8–32 show this report. The report starts with a transcript of the communication between the previous invocation of the sending program and the mail server. On line 19, the actual diagnostic report begins. Lines 19–21 show that datafiles were loaded. The file type is indicated but the file name is not, in order to protect privacy. Line 22 displays a "user error:" the user attempted to load the next recording from the file while there was none (the software cannot currently test for this circumstance in advance). Lines 27–32 display an "unforeseen error" which means that a part of* MAPLAB *was interrupted by* MATLAB*. This usually indicates a bug in the* MAPLAB *code. This error triggered an immediate submission of the log file.*

be removed to save space.

10.5.2 Conclusion

The MAPLAB software is available free of charge for research purposes. Our work has several other aspects that may be of interest to other researchers either in the field of electrocardiology or other disciplines. Our approach to interaction between a user interface and batch-job programming, as well as the combination of documented and revision-controlled software with a commercial data-processing package, may be of general interest.

Our work may also be helpful to researchers who have to choose new data analysis software either in ECG analysis or in other areas. Options range from home-grown programs in a low-level programming language, via higher level or visual programming languages, IPEs, to off-the-shelf data analysis packages. The latter are not suitable when experimentation with new algorithms is needed. Visual programming languages have the disadvantage that they cannot be combined with general tools for literate programming and source control, which require plain-text program files. We chose an IPE because it allows a combination of high-level and low-level programming and interactive development, and—in our case—is largely platform-independent. Because our IPE uses plain-text program files, we could apply literate programming and source control. We thus obtained a compromise between program speed, programming speed, ease of use, flexibility, extensibility, and readability that serves us well.

10.5.3 Future plans

The software described here facilitates the implementation of data processing methods for multichannel ECGs and allows biomedical researchers to use them interactively. Researchers with some programming skills have already written extensions and also use the software for batch processing. Availability of a graphical user interface during batch-job programming was found to be very useful. These properties make the software suitable for continuing development. We expect that a growing user community will create custom extensions and that we shall be involved in several projects where extensions of the software are desired that are more difficult to program. In addition, we shall continue to improve the software, particularly in those places where weaknesses exist or develop. In our experience, addition of features to software often implies the addition of bugs as well as new manifestations of existing bugs in other parts of the software. Handling these will be a continuing effort while MAPLAB is further developed.

Chapter 11

Summary and Discussion

In this chapter, an overview is given of the research presented in this thesis, and its position in the field of cardiac arrhythmia localization. In addition, possible extensions of this research are presented.

11.1 Introduction

The surface electrocardiogram (ECG) is used to obtain information on the electrical activity of the heart in a non-invasive manner. The research on multichannel surface ECGs (MECGs) described in this thesis deals with the diagnosis of dysfunctions in the activity of the heart. A major part of the work was dedicated to localization of exit sites of ventricular tachycardia (VT).

Cardiac electrical activity can also be measured inside the heart. In a clinical setting, this is done during endocardial catheterization and during antiarrhythmic surgery, for the study and treatment of tachyarrhythmias. In addition, various techniques are used for endocardial, epicardial, and intramural measurements in experiments on isolated hearts or tissue specimens. Such experiments are used to gain insight into the physiological or pathophysiological electrical properties of the heart.

Endocardial catheters are used, e.g., to localize the site of origin of arrhythmia such as VT, in order to provide a cure by ablation of arrhythmogenic tissue. For catheter position monitoring during cardiac catheterization, fluoroscopy or biplane fluoroscopy is most commonly applied. Recently, instrumentation for catheter localization using electric or magnetic fields has become available [230, 279]. These techniques are preferred to fluoroscopy because they are harmless and provide a better accuracy. However, they cannot completely replace fluoroscopy, since they can only

provide position information when the catheter tip is inside the heart. Even when electric or magnetic localization is applied, fluoroscopy is used to monitor the position of the catheter while it is guided to the heart. Together with other disadvantages of the newer methods, such as the cost and the need for placement of extra electrodes, this may cause cardiologists to prefer the use of fluoroscopy despite its lower accuracy.

Analysis of endocardial electrograms and analysis of surface ECGs have traditionally been treated as separate subjects. A few surface leads are usually recorded during catheterization or surgery, in order to compare the timing of subsequently obtained endocardial signals, and to identify different arrhythmias. On the other hand, some endocardial catheter leads are recorded during paced body surface mapping. In current clinical practice, these endocardial leads and surface leads are recorded with different systems. Simultaneous multichannel recordings from the endocardium and from the body surface have only recently become possible [46]. This thesis describes results of the first such *integrated mapping* recordings obtained from patients.

11.2 Electrocardiographic Mapping

In both the fields of surface ECG recording and endocardial recording of electrograms, employment of many recording leads simultaneously has distinct advantages. In surface ECG mapping, application of 30–60 leads ensures that all relevant information that can be obtained from the body surface is captured. The extra information, compared to the standard 12-lead ECG, can be used for more accurate localization of VT exit sites, and more sensitive testing for various pathological conditions, such as late potentials and repolarization abnormalities.

In endocardial mapping, application of many recording electrodes allows to measure the activation pattern of each single beat. Presently, this allows us to obtain information about the mechanism of a specific arrhythmia. For example, macro-reentry can be discriminated from micro-reentry and focal tachyarrhythmia. Such knowledge is helpful in the selection of a treatment. If the density of the electrode grid is high enough, endocardial mapping would allow the selection of a suitable site for catheter ablation. To date the number of simultaneous endocardial leads that is technically feasible has been too small to allow such dense mapping in the entire heart. Regionalized dense endocardial mapping might overcome these technical limitations, but would be less efficient, and has not yet been attempted by noninvasive means. Currently, a roving catheter has still to be used for the final phase of an arrhythmia mapping procedure.

Endocardial mapping can be performed during antiarrhythmic surgery with multiterminal balloon electrodes or during catheterization with multipolar catheters, such as the basket catheter. The signals obtained during these two types of procedures have different characteristics; in particular, their amplitudes and maximum slopes differ. In chapter 4, it was shown that the absence of blood during antiarrhythmic surgery largely accounts for these differences. However, the mechanical properties of the basket catheter may also be in part responsible for these differences.

11.3 Software

Due to the size and redundancy of multilead recordings, specialized analysis methods are needed. Examples of these are creation of endocardial activation maps (chapter 3), computation of nondipolar content of body surface maps (BSMS) (chapter 5), and KL transformation for data reduction as part of an algorithm for localization of VT exit sites (chapter 7). With this kind of data, application of computers for recording, presentation, and analysis of results is inevitable. It is useful to make the software that is created for such analysis suitable for use by many research groups. Time that would otherwise be spent on duplication of effort can be invested in better software if this software is used by more groups. Such software has to be extensible and allow adaptation to a wide range of experimental setups, especially a variety of electrode grids. The MAP$_{\text{L}}$AB software described in chapter 10 achieves such a level of flexibility. It was intended as a foundation for the development of new algorithms. In addition to many specialized functions, it provides a user interface and basic functionality that underlies many of the more sophisticated algorithms. Because the software uses external electrode-grid definitions, which can be easily created by users, it can be used to analyze recordings made with virtually every electrode grid, thus allowing application in many laboratories. Furthermore, the software is well-documented and extensible. This facilitates the incorporation of new methods by anyone who uses the software.

The software allows determination of standard electrophysiological parameters such as activation times and onset and offset of the QRS complex. It provides an efficient user interface, which for example allows the user to adjust computed activation times in a convenient way. In order to assist the user with such tasks, the software can display derived signals such as the signal slope, the surface Laplacian, or an energy signal. The software includes several methods of data display, such as pseudocolour maps and isochronal maps. Activation isochrones are a popular mode of display of endocardial activation patterns. One of MAP$_{\text{L}}$AB's algorithms for the com-

putation of activation isochrones is described in chapter 3. This algorithm improves upon standard algorithms by correct handling of lines and zones of activation block, and it can work with rectangular as well as triangulated grids. Other components, such as baseline correction, QRS detection, and VT exit site localization, were published previously [123, 149, 151, 154, 155, 212].

Future work on MAP$_{L}$AB may include an improved handling of irregular 2-D and 3-D electrode grids. Presently, the creation of MAP$_{L}$AB grid definitions for such grids is a difficult task which can only be performed by software experts. In order to handle a wider variety of grids, creation of grid definitions should be made easier.

11.4 Integrated Mapping

The research described in this thesis was concerned with the first integrated mapping studies performed in patients. As discussed in chapter 2, the requirements for recording instruments for surface and endocardial electrograms differ considerably. Recording hardware for integrated mapping has to accommodate these differences, by using either specialized acquisition modules for both types of data or modules that can handle both data types well. The recordings used in this research were obtained with the latter kind of hardware (chapter 2).

Integrated mapping data obtained from patients provides unique opportunities to study the mechanisms of arrhythmogenesis and to develop techniques for localization of arrhythmogenic sites from surface data alone. The analysis of these data also introduces new challenges. Integrated mapping has been performed only in patients with extensive infarct scars. This makes the analysis of the data especially difficult. On the other hand, it makes the data useful for detailed study of the relation between arrhythmogenic site and surface ECG pattern. This was the topic of research performed in collaboration with Van Dessel et al. [47, 48, 206].

An important clinical outcome of this work concerns the mismatch between BSM-based localization and catheter activation mapping of VT. Van Dessel et al. concluded that zones of conduction block, regional differences in endocardial signal amplitude, and the occurrence of multiple endocardial breakthrough sites are frequent causes for this mismatch [47]. In another study, Van Dessel et al. demonstrated that BSM localization of VT can be used as an alternative for preoperative catheter activation sequence mapping [46].

The work on integrated mapping data described in this thesis supports these pathophysiological studies by examining the properties of the measured endocardial signals (chapter 4). In addition, the MAP$_{L}$AB software de-

scribed in chapter 10 played a major role in the analysis of the clinical data.

11.5 Localization of Cardiac Arrhythmias

The research presented in this thesis was performed as part of a longer-term effort towards an automated system for detection and localization of cardiac arrhythmias. Therefore, the majority of chapters is dedicated to the subjects of detection and localization of arrhythmias, and the presentation of localization results.

In current clinical practice, the classical "standard 12-lead ECG" is most commonly applied for the localization of arrhythmias. It is assumed that the ECG pattern originating at a particular exit site can be reproduced by applying electrical stimuli ("pacing") with an endocardial catheter at the same location. Using this method, the relation between exit site and 12-lead ECG pattern was previously assessed [270]. The same method is applied with multichannel BSM data, resulting in a more accurate localization of the arrhythmia exit site [236, 237].

In chapters 6 and 7, the *continuous localization* method was introduced to further improve the localization accuracy of MECG data by interpolating the ECG patterns corresponding to known pacing locations. This method allows an accuracy improvement of approximately an order of magnitude, solely by improved processing of existing data. The continuous localization method was initially created only for the structurally normal left ventricle. In chapter 8, it was shown that it can also be applied, with similar performance, in infarcted ventricles.

In chapter 9, a method was described for presentation of localization results on the fluoroscopic monitors that are used during a catheterization procedure to monitor the catheter position. This provides an efficient translation between functional and anatomical information, and should help the physician to position the catheter quickly at the exit site of the arrhythmia. Thereby, the procedure of localization and ablation of arrhythmias as a whole can be accelerated.

11.6 Future Developments

By combining automatic VT detection (chapter 6), continuous localization (chapter 7), and conversion into biplane fluoroscopic projections (chapter 9), an *automated system for detection and localization of cardiac arrhythmias* can be created. The next step in this research is building a prototype clinical system, which should automatically and in real-time perform the detection

and localization of VT, as well as the presentation of localization results on the fluoroscopic monitors, so as to provide optimal catheter guidance.

The localization and presentation methods described in chapters 6–9 were developed solely for the left ventricle of the heart. Extension to the right ventricle and the atria is very important for clinical application of these methods. Due to the more complex anatomical structure and smaller muscular mass of the right ventricle and the atria, as compared to the left ventricle, this will require more complicated methods. The development of such methods is a challenging subject for future research.

A catheter guidance system as described above could be combined with catheter localization techniques that are more accurate than fluoroscopic localization [230, 279]. This would improve the procedure by providing more accurate results, and allow a better assessment of this accuracy.

Electrocardiogram analysis is an evolving field. New recording techniques and new research questions such as the detection of changes in cardiac activation resulting from genetic disorders call for the continuous development of new diagnostic algorithms. The MAP LAB software, described in chapter 10, provides an excellent infrastructure for such development. The widespread application of this software makes it possible to share new algorithms with several research groups, while still maintaining the flexibility needed to accommodate a wide range of experimental setups.

The differences between electrograms obtained during antiarrhythmic surgery and those obtained with endocardial (basket) catheters are not yet explained completely, although it was shown in chapter 4 that the difference is largely caused by the absence of blood during antiarrhythmic surgery. In order to improve the analysis of the signals obtained with endocardial catheters, a better understanding of these signals is necessary. Since the physics and physiology of the phenomena underlying these signals are well known, such knowledge can be obtained with computer models. Therefore, computer modelling of endocardial electrograms is an interesting topic for future research, which has the capacity of substantially improving the analysis of clinically obtained signals.

In contrast to the modelling of endocardial electrograms, modelling of surface electrocardiograms has already been extensively reported [83, 84, 103, 104, 280]. Provided with approximate anatomical information, computer models have the capability to predict the surface ECG pattern corresponding to a given activation sequence. It is also possible to let the activation sequence in turn be computed, given only a "pacing site." Such models improve our understanding of the relation between endocardial electrograms and BSM patterns. In addition, they can be used to create high-precision pace-mapping databases, adapted to the specific anatomy of a patient. For example, by including infarct scars in the model, the rela-

tion between BSM and site of arrhythmia origin can be assessed more accurately for a specific patient with infarction scars, if the location of such scars is known. It is important that such models are validated using measured data, such as can be obtained using integrated mapping techniques.

Both the empirical methods of arrhythmia localization and the modelling approach have the disadvantage that they can only assess the relation between cardiac electrical events and BSM for a predetermined set of pathologies. In contrast, by estimating the intracardial voltage distribution or activation pattern directly from the BSM data, one may investigate any given pathological or nonpathological condition. This estimation procedure is called solution of the *inverse problem of electrocardiology*. The main difficulty of this approach is that the inverse problem is *ill-posed:* there is an infinite number of voltage distributions and or activation patterns that is physically compatible with any given BSM pattern. Fortunately, not all physical solutions are *physiologically* possible, and those that are physiologically possible can be assigned a varying likelyhood based on physiological considerations. Thus, by combining the laws of physics with physiological knowledge, it is possible to determine the most likely solution. Clinical experience is also needed, in order to specify how the solution should be presented, e.g. as an activation sequence for the localization of arrhythmia, or as a voltage distribution for the localization of ischaemia. Collaboration of clinicians, experimentalists, and physicists is needed to develop this method further in order to make it clinically useful.

Three classes of methods are thus available for BSM-based diagnosis: empirical methods such as described in this thesis (chapters 5–8), forward modelling, and inverse solutions. Of these three, the empirical methods are currently the most practical, and inverse solutions are the most promising, while the forward modelling approach holds a second position in both respects. For all three approaches, cooperation between physicists and cardiac electrophysiologists is indispensable.

Appendix A

Literate Programming

> As an introduction to the concept of Literate Programming, which is mentioned in several places in this thesis, a concise literate program is presented. This example program displays most of the features provided by a literate programming system that is used in this work. — submitted in part for publication [205, 208].

For programs to be understood by humans, and not only by compilers, documentation is indispensable. The computer programs that were used for the work described in this thesis were almost exclusively created and documented using the "literate programming" technique [129, 130].

A "literate" program consists of small pieces of code, which are written in the programming language(s) of choice—for example MATLAB or C [132, 203]. These code fragments are called "refinements" and can be partially or completely defined in terms of each other. Each refinement comes with a documentation part written in a document formatting language—in our case LaTeX. This means that the program documentation can include mathematical formulae, graphics, references, indexes, etc. and can be typesetted professionally. The refinements can be presented in any order the programmer wishes. By application of refinements in other refinements the code is ordered for the compilers purposes. Because the documentation parts can be large compared to the code parts without obscuring the program structure it is possible to give a thorough description of the code, explaining not only *what* it does but also *why* it does so.

A well-known example of literate programming is the source code of TeX, which was published as a book as part of a series on computer typesetting [128]. A collection of routines for graph handling was also published as literate programs [131].

A small program written in the MATLAB language using the MWEB sys-

tem for literate programming [203] is described in the following sections.

A.1 The Source Code

The following program, which is written in the MATLAB language using the MWEB system, shows some of the possibilities of a literate programming system. The "web file," which is written by the programmer using a text editor, is discussed first. Subsequent sections will present the typeset documentation and the compilable program.

The web file starts with a comment line containing version information that is automatically updated by the Revision Control System (RCS) [22]. Then follow some LaTeX macro definitions (`\def`...), which make the documentation easier to write and determine some aspects of the appearance of the typeset output. The actual program consists of three sections. A section (at level 2) starts with the control code "`@*2`." The first section defines the file `rot3d.m`. This file begins with four comment lines. These are displayed by MATLAB when a user requests help on the `rot3d` function. The fourth comment line contains a source-file identification that is automatically updated by RCS. The next section describes the algorithm and defines a refinement "`@<compute $R(\a,\phi)$@>`" containing the implementation of the algorithm. The last section defines a refinement "`@<check arguments@>`." These refinements are used in the first section.

```
% $Id: rot.web,v 5.17 2001/10/14 18:35:12 potse Exp $
\def\eref#1{(\ref{#1})}
\def\xwebContentsTop{}  \def\xwebContentsBot{}
\def\eye{\underline{1}}
\def\x{\vec{x}} \def\a{\vec{a}} \def\xp{\vec{x}\,'}
\begingroup\catcode`\_=11 \gdef\xweb_IndexTop{} \endgroup

@*2 Introduction. A transform matrix\index{transform matrix} for
rotating three-dimensional
vectors can be specified by a rotation axis and an angle.  This
function takes a 3-element vector $\a$ and an angle $\phi$, and
returns the transformation matrix~$R$.

@f phi TeX    % \rm makes \textit{phi} show up as $\phi$

@(rot3d.m@>=
@% ROT3D(vec,phi)  3d rotation  R(vec,phi)
@% returns a 3-D rotation matrix to rotate by angle phi about
@% the axis defined by vec.
@% $Id: rot.web,v 5.17 2001/10/14 18:35:12 potse Exp $
function R = rot3d(vec, phi)
   @<check arguments@>
   @<compute $R(\a,\phi)$@>

@*2 Algorithm. Suppose we are rotating a vector $\x$ around a unit
```

```
vector $\a$ by an angle $\phi$. Let point $N$ be the projection of
$\x$ on $\a$ and define point $P$ by $\vec{NP}=\a\times\x$:
\begin{center}
  \mbox{\epsffile{rotfig.1.eps}}
\end{center}
Then the rotated vector $\xp$ can be expressed in terms of $\x$, $\a$
and $\phi$ as
\begin{eqnarray}
  \xp & = & \vec{ON} + \vec{NX}\cos\phi + \vec{NP}\sin\phi \label{eq:x}\\[2pt]
      & = & \left[\a\a^T + (\eye-\a\a^T)\cos\phi\right]\x
            + (\a\times\x)\sin\phi  \nonumber
\end{eqnarray}
by application of the identities shown in the figure above.
Using, after Faux and Pratt \cite{faux79}, the matrix
\begin{equation}
  A = a_i\varepsilon_{ijk} =
    \left(\begin{array}{ccc}
       0   & -a_3 & a_2 \\
       a_3 &  0   & -a_1 \\
      -a_2 &  a_1 & 0 \end{array}\right)
\end{equation}
the cross product\index{cross product} $\a\times\x$ can be turned into
a matrix multiplication so that we can express (\ref{eq:x}) in the
form $\xp=R\x$ with
\begin{equation}
  R  = \a\a^T + (\eye-\a\a^T) \cos\phi +  A \sin\phi
\end{equation}
Note that $\a\a^T$ is a  $3\times 3$ matrix if $\a$ is a 3-element
column vector.
@<compute $R(\a,\phi)$@>=
   A=[0,-a(3),a(2);a(3),0,-a(1);-a(2),a(1),0];
   aat=a*a';   % $3\times 3$ matrix
   R=aat + (eye(3,3)-aat)*cos(phi) + A*sin(phi);

@*2 Checking arguments. We expect a 3-vector and a scalar as input
arguments. The axis vector is normalized to make sure that $R$ is
orthonormal, and reshaped into a column vector, so that |a*a'@;| is a
matrix.
@<check arguments@>=
   if nargin~=2
     error('two arguments needed');
   end
   if length(vec(:))~=3
     error('first argument must be 3d vector');
   end
   if length(phi)~=1
     error('second argument must be a scalar');
   end
   a=reshape(vec/norm(vec), 3,1); % column vector

@*2 Index. This index lists the section numbers where identifiers are used.
```

Note that several features of the document processing system were used to improve the documentation, such as a graphic ("`\epsffile`..."), mathematics, and a reference ("`\cite`...").

A.2 The Typeset Documentation

A literate programming system consists of two filter programs. One of these programs, which is called `weave`, translates the source into document formatting instructions, taking care of prettyprinting (syntax highlighting and standard indentation), and copies the documentation parts which are already written in the document formatting language. The output of `weave` is subsequently typesetted by a document processor, in our case by LaTeX. The formatted output of the program shown in the previous section follows now.

1. Introduction. A transform matrix for rotating three-dimensional vectors can be specified by a rotation axis and an angle. This function takes a 3-element vector $\vec{a}$ and an angle ϕ, and returns the transformation matrix R.

format *phi TeX* % makes *phi* show up as ϕ

⟨ `rot3d.m` 1 ⟩ ≡

```
% ROT3D(vec,phi)  3d rotation  R(vec,phi)
% returns a 3-D rotation matrix to rotate by angle phi about
% the axis defined by vec.
% $Id: rot.web,v 5.17 2001/10/14 18:35:12 potse Exp $
function R = rot3d(vec, phi)
    ⟨ check arguments 3 ⟩
    ⟨ compute R(a, phi) 2 ⟩
```

2. Algorithm. Suppose we are rotating a vector $\vec{x}$ around a unit vector $\vec{a}$ by an angle ϕ. Let point N be the projection of $\vec{x}$ on $\vec{a}$ and define point P by $\vec{NP} = \vec{a} \times \vec{x}$:

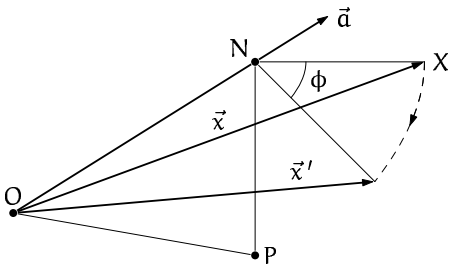

$$\vec{NP} = \vec{a} \times \vec{x}$$

$$\vec{ON} = \vec{a}(\vec{a} \cdot \vec{x}) = \vec{a}\vec{a}^{\mathsf{T}}\vec{x}$$

$$\vec{NX} = \vec{x} - \vec{ON} = (\underline{1} - \vec{a}\vec{a}^{\mathsf{T}})\vec{x}$$

Then the rotated vector $\vec{x}\,'$ can be expressed in terms of $\vec{x}$, $\vec{a}$ and ϕ as

$$\begin{aligned} \vec{x}\,' &= \vec{ON} + \vec{NX}\cos\phi + \vec{NP}\sin\phi \\ &= \left[\vec{a}\vec{a}^{\mathsf{T}} + (\underline{1} - \vec{a}\vec{a}^{\mathsf{T}})\cos\phi\right]\vec{x} + (\vec{a}\times\vec{x})\sin\phi \end{aligned} \tag{A.1}$$

by application of the identities shown in the figure above. Using, after Faux and Pratt [64], the matrix

$$A = a_i \varepsilon_{ijk} = \begin{pmatrix} 0 & -a_3 & a_2 \\ a_3 & 0 & -a_1 \\ -a_2 & a_1 & 0 \end{pmatrix} \tag{A.2}$$

the cross product $\vec{a}\times\vec{x}$ can be turned into a matrix multiplication so that we can express (A.1) in the form $\vec{x}\,' = R\vec{x}$ with

$$R = \vec{a}\vec{a}^{\mathsf{T}} + (\underline{1} - \vec{a}\vec{a}^{\mathsf{T}})\cos\phi + A\sin\phi \tag{A.3}$$

Note that $\vec{a}\vec{a}^{\mathsf{T}}$ is a 3×3 matrix if $\vec{a}$ is a 3-element column vector.

⟨ compute $R(\vec{a},\phi)$ 2 ⟩ ≡

```
A = [0, -a(3), a(2);  a(3), 0, -a(1);  -a(2), a(1), 0];
aat = a*a';          % 3 × 3 matrix
R = aat + (eye(3, 3) - aat)*cos(φ) + A*sin(φ);
```

This code is used in section 1.

3. Checking arguments. We expect a 3-vector and a scalar as input arguments. The axis vector is normalized to make sure that R is orthonormal, and reshaped into a column vector, so that $a*a'$ is a matrix.

⟨ check arguments 3 ⟩ ≡

```
if nargin ≠ 2
  error('two␣arguments␣needed');
end
if length(vec(:)) ≠ 3
  error('first␣argument␣must␣be␣3d␣vector');
end
if length(φ) ≠ 1
  error('second␣argument␣must␣be␣a␣scalar');
end
a = reshape(vec/norm(vec), 3, 1);          % column vector
```

This code is used in section 1.

4. Index. This index lists the section numbers where identifiers are used.

The program consists of three sections. Section 1 defines the file `rot3d.m`. This file begins with four comment lines, the fourth line contains a source-file identification that is automatically updated by the revision control system. Section 2 describes the algorithm and defines a refinement named "⟨compute $R(\vec{a}, \phi)$ 2⟩," which contains the actual computation. Section 3 defines a refinement named "⟨check arguments 3⟩." Sections 2 and 3 are used in section 1. The literate programming system typesets keywords like **function** in bold and identifiers in italics, and ensures correct indentation. In addition, it creates an identifier index, a table of contents, and a list of refinements. The latter is not shown in this example.

A.3 The Tangled Code

The `tangle` program extracts the program parts and puts them in the specified order for the compiler. These are the contents of the file `rot3d.m` created from the MWEB source shown above.

```
% ROT3D(vec,phi)  3d rotation  R(vec,phi)
% returns a 3-D rotation matrix to rotate by angle phi about
% the axis defined by vec.
% $Id: rot.web,v 5.17 2001/10/14 18:35:12 potse Exp $
function R  =  rot3d(vec, phi)
   if nargin~=2
     error('two arguments needed');
   end
   if length(vec(:))~=3
     error('first argument must be 3d vector');
   end
   if length(phi)~=1
     error('second argument must be a scalar');
   end
   a = reshape(vec/norm(vec), 3,1); % column vector
   A = [0,-a(3),a(2);a(3),0,-a(1);-a(2),a(1),0];
   aat = a * a';    % $3\times 3$ matrix
   R = aat + (eye(3,3)-aat) * cos(phi) + A * sin(phi);
```

One can observe that the program parts have been tangled together. Comments, which start with a percent sign, are copied literally from the web

file; the LaTeX code for the comment in the pre-last line is visible. The documentation parts are omitted.

A.4 Formatted Strings in Matlab Code

Programmers often use *preprocessors* to facilitate the creation of code. A preprocessor is a program that modifies the code before it is fed to the compiler or interpreter. A preprocessor can be standard, such as the "C preprocessor," which is built into any C compiler, or it can be home-grown for highly specific purposes. A literate programming system can itself be considered as a preprocessor, and it can also be used to implement other preprocessing tasks. Such combinations are particularly convenient for tasks that interact with the literate programming system.

An example of such a facility is the "formatted string" mechanism in Matlab WEB (MWEB) [203]. Programming languages generally have a mechanism for representing text known as the "character string." For example, in the C language one can write

```
printf("Hello, world.");
```

where the double quotes start and end the string. The MATLAB equivalent is

```
disp('Hello, world.');
```

where single quotes are used as string delimiters. In MATLAB programs, character strings often contain code instead of ordinary text. Such "code strings" are used to specify code that is to be executed when a specific user-interface event occurs. These code strings can become several lines long, and they can contain embedded (code) strings. This embedding can be several layers deep. In MATLAB, embedded strings are created by doubling the number of quotes: a single quote for the outermost string, two quotes for an embedded string, four quotes for a string embedded in an embedded string, etc. This can become quite inconvenient. For example, the code fragment

```
set(gcf,'WindowButtonDownFcn', ['b = get(gca,''CurrentPoint'');', ...
'  L = line([b(1,1),b(1,1)],[b(1,2),b(1,2)],''EraseMode'', ''xor'');', ...
'  set(gcf,''WindowButtonMotionFcn'', ''         ', ...
'    e  =  get(gca,''''CurrentPoint'''');        ', ...
'    set(L,''''XData'''',[b(1,1),e(1,1)],''''YData'''',[b(1,2),e(1,2)]);''); ',...
'  set(gcf,''WindowButtonUpFcn'', ''             ', ...
'        set(L, ''''Color'''', ''''r'''');       ', ...
'        set(gcf, ''''WindowButtonMotionFcn'''','''' '''''); ''); ']);
```

is very hard to write and read, requiring four subsequent quote characters in several places. The MWEB system has a facility that allows the programmer instead to write

```
@ @(drawline.m@>=
   set(gcf,'WindowButtonDownFcn', ‘
      b = get(gca,"CurrentPoint");
      L = line([b(1,1),b(1,1)],[b(1,2),b(1,2)], "EraseMode", "xor");
      set(gcf,"WindowButtonMotionFcn", ‘@<reset the line@>’);
      set(gcf,"WindowButtonUpFcn", ‘
          set(L, "Color", "r");
          set(gcf, "WindowButtonMotionFcn", ‘ ’); ’); ’);

@ @<reset the line@>=
  e = get(gca,"CurrentPoint");
  set(L,"XData",[b(1,1),e(1,1)], "YData", [b(1,2),e(1,2)]);
```

In this code, the single left quote character opens a new level of code string; the single right quote character closes a level, and the double quote character opens and closes ordinary character strings. In addition, refinements were used in this example to make the code more readable. Refinements can be used in formatted strings regardless of the string nesting level. This means that the same code can be used at different levels at the same time. The documentation was omitted here for brevity. The `tangle` processor converts this into something similar to the code fragment shown above. The typeset output of the `weave` processor is as follows

1. ⟨ drawline.m 1 ⟩ ≡

```
set(gcf, 'WindowButtonDownFcn', ‹
    b = get(gca, 'CurrentPoint');
    L = line([b(1, 1), b(1, 1)], [b(1, 2), b(1, 2)], 'EraseMode', 'xor');
    set(gcf, 'WindowButtonMotionFcn', «⟨ reset the line 2 ⟩»);
    set(gcf, 'WindowButtonUpFcn', «
        set(L, 'Color', 'r');
        set(gcf, 'WindowButtonMotionFcn', «»); »); ›);
```

2. ⟨ reset the line 2 ⟩ ≡

```
e = get(gca, 'CurrentPoint');
set(L, 'XData', [b(1, 1), e(1, 1)], 'YData', [b(1, 2), e(1, 2)]);
```

This code is used in section 1.

Note that the single quotes are replaced by one or more *guillemets*; their number indicates the nesting level of the code strings.

The formatted string facility of the MWEB system has been extensively used in the implementation of the MATLAB software described in chapter 10.

Bibliography

This bibliography is sorted alphabetically according to mother tongue rules, which means that, for example, "Van Capelle" is found under C rather than V. In addition to cited references, this bibliography lists the names of all co-authors of all cited works. For each co-author, a list of cited works is included.

1] J. A. **Abildskov**, Larry S. Green, and Robert L. Lux. Detection of disparate ventricular repolarization by means of the body surface electrocardiogram. In *Cardiac Electrophysiology and Arrhythmias*, pages 495–499. Grune & Stratton, 1985. Cited on pages 18, 88, 92, and 189.

J. A. **Abildskov**, see also Lux [160–162] and Moe [175]. Alexandre **Ackaoui**, see Savard [228].

2] Valtino X. **Afonso**, Willis J. Tompkins, Truong Q. Nguyen, and Shen Luo. ECG beat detection using filter banks. *IEEE Trans. Biomed. Eng.*, 46(2):192–202, February 1999. Cited on pages 100 and 104.

Valtino X. **Afonso**, see also Hu [105]. Naohiko **Aihara**, see Kamakura [121]. Maurits A. **Allessie**, see Maglaveras [166].

3] John N. **Amoore**, Yoram Rudy, and Jerome Liebman. Respiration and the ECG: A study using body surface potential maps. *J. Electrocardiol.*, 21(3):263–271, 1988. Cited on page 147.

4] Kelley P. **Anderson**, Richard Walker, Philip R. Ershler, Mark Fuller, Ted Dustman, Ronald Menlove, Shreekant V. Karwandee, and Robert L. Lux. Determination of local myocardial electrical activation for activation sequence mapping; a statistical approach. *Circ. Res.*, 69:898–917, 1991. Cited on pages 50 and 56.

5] Kelley P. **Anderson**, Richard Walker, Mark Fuller, Ted Dustman, Philip R. Ershler, and Robert L. Lux. Criteria for local myocardial electrical activation: Effects of electrogram characteristics. *IEEE Trans. Biomed. Eng.*, 40:169–181, February 1993. Cited on pages 51, 57, and 70.

Kelley P. **Anderson**, see also Shusterman [231]. David C. **Andrews**, see Todd [258]. Pierre **Arnaud**, see Willems [273, 274]. Amalia M. **Arria**, see Calkins [29]. Mauricio **Arruda**, see Nakagawa [182]. R. C. **Arzbaecher**, see Durrer [60].

6] J. M. T. **de Bakker**, R. Coronel, S. Tasseron, A. A. M. Wilde, T. Opthof, M. J. Janse, F. J. L. van Capelle, A. E. Becker, and G. Jambroes. Ventricular tachycardia in the infarcted, Langendorff-perfused human heart: role of the arrangement of surviving cardiac fibers. *J. Am. Coll. Cardiol.*, 15:1594–607, 1990. Cited on pages 56 and 158.

7] J. M. T. **de Bakker**, M. J. Janse, F. J. L. van Capelle, and D. Durrer. Endocardial mapping by simultaneous recording of endocardial electrograms during cardiac surgery for ventricular aneurysm. *J. Am. Coll. Cardiol.*, 2:847–853, 1983. Cited on page 70.

8] J. M. T. **de Bakker**, M. J. Janse, F. J. L. van Capelle, and D. Durrer. An interactive computer system for guiding the surgical treatment of life-threatening ventricular tachycardias. *IEEE Trans. Biomed. Eng.*, 31:362–368, 1984. Cited on page 70.

9] Jacques M. T. **de Bakker**, Frans J. L. van Capelle, Michiel J. Janse, Norbert M. van Hemel, Richard N. W. Hauer, Jo J. A. M. Defauw, Freddy E. E. Vermeulen, and Patricia F. A. Bakker-de Wekker. Macroreentry in the infarcted human heart: The mechanism of ventricular tachycardia with a "focal" activation pattern. *J. Am. Coll. Cardiol.*, 18:1005–1014, 1991. Cited on page 71.

10] Jacques M. T. **de Bakker**, Frans J. L. van Capelle, Michiel J. Janse, Sara Tasseron, Jessica T. Vermeulen, Nicolaas de Jonge, and Jaap R. Lahpor. Fractionated electrograms in dilated cardiomyopathy: Origin and relation to abnormal conduction. *J. Am. Coll. Cardiol.*, 27(5):1071–1078, 1996. Cited on pages 61 and 63.

11] Jacques M. T. **de Bakker**, Frans J. L. van Capelle, Michiel J. Janse, Arthur A. M. Wilde, Ruben Coronel, Anton E. Becker, Koert P. Dingemans, Norbert M. van Hemel, and Richard N. W. Hauer. Reentry as a cause of ventricular tachycardia in patients with chronic heart disease: electrophysiologic and anatomic correlation. *Circulation*, 77:589–606, 1988. Cited on page 151.

12] Jacques M. T. **de Bakker**, Richard Derksen, Tokuhiro Kawara, Sara Tasseron, André C. Linnenbank, Mark Potse, and Michiel J. Janse. Load mismatch as a cause of decremental conduction in diseased myocardium. *Circulation*, 100 Suppl. I(18):836, November 1999. (abstract). Cited on pages 188 and 192.

13] Jacques M. T. **de Bakker**, Richard N. W. Hauer, and Timothy A. Simmers. Activation mapping: Unipolar versus bipolar recording. In Douglas D. **Zipes** and José Jalife, editors, *Cardiac Electrophysiology: From Cell to Bedside*, chapter 94, pages 1068–1078. Saunders, second edition, 1994. Cited on pages 50 and 52.

14] Jacques M. T. **de Bakker**, Michiel J. Janse, Frans J. L. van Capelle, and Dirk Durrer. An interactive computer system for guiding the surgical treatment of life-threatening ventricular tachycardias. *IEEE Trans. Biomed. Eng.*, 31(4):362–8, April 1984. Cited on pages 18, 52, 56, and 60.

Jacques M. T. **de Bakker**, see also Coronel [37], Derksen [45], Van Dessel [47, 48], Hauer [89], Hocini [92, 93], Jessurun [118], Kawara [122], Linnenbank [148, 150, 155], Loh [157], Maglaveras [163, 165], McGuire [171], Potse [197, 204], Van Rijen [220], and SippensGroenewegen [235, 242]. Patricia F. A. **Bakker-de Wekker**, see De Bakker [9]. Donald **Ballew**, see Dodge [49].

15] Roger C. **Barr**, Thomas M. Gallie, and Madison S. Spach. Automated production of contour maps for electrophysiology; I. problem definition, solution strategy, and specification of geometric model. *Comp. & Biom. Res.*, 13:142–153, 1980. Cited on page 61.

16] Roger C. **Barr**, Thomas M. Gallie, and Madison S. Spach. Automated production of contour maps for electrophysiology; II. triangulation, verification, and organization of the geometric model. *Comp. & Biom. Res.*, 13:154–170, 1980. Cited on page 61.

17] Roger C. **Barr**, Thomas M. Gallie, and Madison S. Spach. Automated production of contour maps for electrophysiology; III. construction of contour maps. *Comp. & Biom. Res.*, 13:171–191, 1980. Cited on page 61.

Roger C. **Barr**, see also Geselowitz [73], Smith [244], and Spach [245,246,250]. Senén **Barro Ameneiro**, see Fernández-Delgado [65]. William T. **Baxter**, see Gray [75].

18] Philip V. **Bayly**, Bruce H. KenKnight, Jack M. Rogers, Russel E. Hillsley, Raymond E. Ideker, and William M. Smith. Estimation of conduction velocity vector fields from epicardial mapping data. *IEEE Trans. Biomed. Eng.*, 45(5):563–571, May 1998. Cited on pages 25, 67, and 181.

Anton E. **Becker**, see De Bakker [6, 11] and McGuire [171]. Karen J. **Beckman**, see Nakagawa [182].

19] G. W. **Beeler** and H. Reuter. Reconstruction of the action potential of ventricular myocardial fibres. *J. Physiol.*, 268:177–210, 1977. Cited on page 46.

Salwa **Beheiry**, see Natale [183]. Anna **Beigel**, see Shusterman [231].

20] Gustavo **Belforte**, Renato De Mori, and Franco Ferraris. A contribution to the automatic processing of electrocardiograms using syntactic methods. *IEEE Trans. Biomed. Eng.*, 26(3):125–136, 1979. Cited on pages 101 and 102.

J. J. **Bellanger**, see Thoraval [257]. Jan H. **van Bemmel**, see Willems [273, 274]. Shlomo A. **Ben-Haim**, see Shpun [230]. Dennis M. **Bergau**, see Jenkins [117]. Tito **Bertoni**, see De Ambroggi [44].

21] W. G. **Bickley**. Finite difference formulae for the square lattice. *Q. J. Mechanics and Applied Mathematics*, 1:35–42, 1948. Cited on page 54.

Susan M. **Blanchard**, see Bollacker [23] and Ideker [114]. J. R. **Blickman**, see Durrer [59].

22] Don **Bolinger** and Tan Bronson. *Applying RCS and SCCS*. O' Reilly, August 1995. Cited on pages 186, 193, and 206.

23] Kurt D. **Bollacker**, Edward V. Simpson, Russel E. Hillsley, Susan M. Blanchard, Ronald J. Gerstle, Gregory P. Walcott, Richard L. Callihan, Michael C. King, William M. Smith, and Raymond E. Ideker. An automated technique for identification and analysis of activation fronts in a two-dimensional electrogram array. *Comp. & Biom. Res.*, 27:229–244, 1994. Cited on page 60.

Richard **Borge**, see Greenspon [78]. Martin **Borggrefe**, see Loh [157]. Cornelius **Borst**, see Hauer [88]. G. Faye **Boudreaux-Bartels**, see Kadambe [120]. Derek R. **Boughner**, see Nadkarni [181]. Peter J. **Bourdillon**, see Willems [273, 274].

24] Mary A. B. **Brazier**. *A History of Neurophysiology in the 19th Century*, pages 234–239. Raven Press, New York, 1988. Cited on page 14.

Peter R. **Bream**, see Rogers [222].

25] G. **Breithardt**, M. E. Cain, N. El-Sherif, N. Flowers, V. Hombach, M. Janse, M. B. Simson, and G. Steinbeck. Standards for analysis of ventricular late potentials using high resolution or signal-averaged electrocardiography. A statement by a task force committee between the European Society of Cardiology, the American Heart Association and the American College of Cardiology. *European Heart Journal*, 12:473–480, 1991. simultaneously published in *Circulation*. Cited on page 108.

Stanley A. **Briller**, see Coast [36]. Petro **Broekhuijsen**, see SippensGroenewegen [241] and Spekhorst [252]. Christian **Brohet**, see Willems [273]. Tan **Bronson**, see Bolinger [22]. Doug **Brown**, see Levine [144].

26] Josep **Brugada**, Ramon Brugada, and Pedro Brugada. Asymptomatic patients with a Brugada electrocardiogram: Are they at risk? *J. Cardiovasc. Electrophysiol.*, 12(1):7–8, 2001. Cited on page 46.

Josep **Brugada**, see also Brugada [27].

27] Pedro **Brugada** and Josep Brugada. Right bundle branch block, persistent ST segment elevation and sudden cardiac death: A distinct clinical and electrocardiographic syndrome. *J. Am. Coll. Cardiol.*, 20:1391–1396, 1992. Cited on page 46.

Pedro **Brugada**, see also Brugada [26]. Ramon **Brugada**, see Brugada [26]. Aart **Brutel de la Riviere**, see Jessurun [118]. J. **Büller**, see Durrer [56].

28] Fred **Burbank**, Dave Parish, and Lewis Wexler. Echocardiographic-like angled views of the heart by MR imaging. *J. Computer Assisted Tomography*, 12(2):181–195, 1988. Cited on page 169.

M. J. **Burgess**, see Lux [160, 161]. Alfred E. **Buxton**, see Cassidy [32]. Cándido **Cabo**, see Gray [75]. Kenneth **Caidahl**, see Gustavsson [85]. M. E. **Cain**, see Breithardt [25].

29] Hugh **Calkins**, Andrew Epstein, Douglas Packer, Amalia M. Arria, John Hummel, David M. Gilligan, Janet Trusso, Mark Carlson, Richard Luceri, Harry Kopelman, David Wilber, J. Marcus Wharton, and William Stevenson. Catheter ablation of ventricular tachycardia in patients with structural heart disease using cooled radiofrequency energy: Results of a prospective multicenter study. *J. Am. Coll. Cardiol.*, 35(7):1905–1914, 2000. Cited on pages 18 and 177.

David J. **Callans**, see Rodriguez [221]. Richard L. **Callihan**, see Bollacker [23]. R. W. F. **Campbell**, see Clayton [33, 34]. Gerald G. **Cano**, see Coast [36].

30] Frans J. L. **van Capelle** and Dirk Durrer. Computer simulation of arrhythmias in a network of coupled excitable elements. *Circ. Res.*, 47(3):454–466, September 1980. Cited on pages 47 and 48.

31] Frans J. L. **van Capelle**, Hemmy Morsink, Michiel J. Janse, and Dirk Durrer. Computerized DC epicardial mapping during experimental coronary occlusion. *Comp. in Cardiol.*, pages 99–102, September 1979. Cited on page 60.

Frans J. L. **van Capelle**, see also De Bakker [6–11, 14], Coronel [37], Janse [116], and Maglaveras [163, 165, 166]. René **Cardinal**, see Janse [116] and Nadeau [180]. Mark **Carlson**, see Calkins [29]. G. **Carrault**, see Thoraval [257].

32] Dennis M. **Cassidy**, Joseph A. Vassallo, Alfred E. Buxton, John U. Doherty, Francis E. Marchlinski, and Mark E. Josephson. The value of catheter mapping during sinus rhytm to localize site of origin of ventricular tachycardia. *Circulation*, 69(6):1103–1110, June 1984. Cited on page 116.

Krishnan B. **Chandran**, see Dove [50]. Michael **Chin**, see Eldar [63]. Tom **Christiansen**, see Wall [269]. Edward A. **Clancy**, see Smith [243].

33] R. H. **Clayton**, A. Murray, and R. W. F. Campbell. Comparison of four techniques for recognition of ventricular fibrillation from the surface ECG. *Med. & Biol. Eng. & Comput.*, 31(2):111–117, March 1993. Cited on page 99.

34] R. H. **Clayton**, A. Murray, and R. W. F. Campbell. Recognition of ventricular fibrillation using neural networks. *Med. & Biol. Eng. & Comput.*, 32(2):217–220, March 1994. Cited on pages 108 and 109.

35] Daniel S. **Clouse**, C. Lee Giles, Bill G. Horne, and Garrison W. Cottrell. Time-delay neural networks: Representation and induction of finite-state machines. *IEEE Trans. Neural Networks*, 8(5):1065–1070, September 1997. Cited on pages 108 and 109.

36] Douglas A. **Coast**, Richard M. Stern, Gerald G. Cano, and Stanley A. Briller. An approach to cardiac arrhythmia analysis using hidden markov models. *IEEE Trans. Biomed. Eng.*, 37(9):826–836, 1990. Cited on page 102.

M. **Cohen**, see Liebman [146]. Richard J. **Cohen**, see Rosenbaum [223] and Smith [243]. Steven D. **Colan**, see Jenkins [117]. Thomas **Comer**, see Wiener [271].

37] Ruben **Coronel**, Francien J. G. Wilms-Schopman, Joris R. de Groot, Michiel J. Janse, Frans J. L. van Capelle, and Jacques M. T. de Bakker. Laplacian electrograms and the interpretation of complex ventricular activation patterns during ventricular fibrillation. *J. Cardiovasc. Electrophysiol.*, 11:1119–1128, 2000. Cited on pages 53 and 83.

Ruben **Coronel**, see also De Bakker [6, 11], Derksen [45], De Groot [81, 82], Kawara [122], and Kléber [126]. Garrison W. **Cottrell**, see Clouse [35].

38] J. R. **Cox**, F. M. Nolle, H. A. Fozzard, and G. C. Oliver. AZTEC, a preprocessing program for real-time ECG rhythm analysis. *IEEE Trans. Biomed. Eng.*, 15:128–129, April 1968. Cited on page 101.

39] Jerome R. **Cox**, Harry A. Fozzard, Floyd M. Nolle, and G. Charles Oliver. Some data transformations useful in electrocardiography. In Ralph W. **Stacy** and Bruce D. Waxman, editors, *Computers in Biomedical Research*, volume 3, pages 181–206. Academic Press, 1969. Cited on pages 100–102.

Robert F. **Coyne**, see Rodriguez [221].

40] **CSE Working Party**. Recommendations for measurement standards in quantitative electrocardiography. *Eur Heart J*, 6:815–25, 1985. Cited on page 27.

41] The Comprehensive TEX Archive Network (CTAN). FTP sites: `ftp://ctan.tug.org/tex-archive`, `ftp://ftp.dante.de/tex-archive`, `ftp://ftp.tex.ac.uk/tex-archive`.

P. V. L. **Curry**, see Holt [99]. Sergio **Dalla Volta**, see Willems [273]. R. Th. **van Dam**, see Durrer [60] and Nadeau [180].

42] Jan-Henk E. **Dambrink**, Arne SippensGroenewegen, Wiek H. van Gilst, Katinka H. Peels, Cornelis A. Grimbergen, and J. Herre Kingma. Association of left ventricular remodeling and nonuniform electrical recovery expresssed by nondipolar QRST integral map patterns in survivors of a first anterior myocardial infarction. *Circulation*, 92:300–310, 1995. Cited on pages 18, 88, 92, 94, and 192.

Jens **Damgaard Andersen**, see Willems [273]. Ned D. **Danieley**, see Ideker [114]. Marcel C. G. **Daniëls**, see Peeters [190, 193]. Michael R. **Davenport**, see Day [43]. G. K. **David**, see Spekhorst [252]. Jorge M. **Davidenko**, see Gray [75].

43] Shawn P. **Day** and Michael R. Davenport. Continuous-time temporal backpropagation with adaptable time delays. *IEEE Trans. Neural Networks*, 4(2):348–354, March 1993. Cited on pages 108 and 109.

44] Luigi **De Ambroggi**, Maria S. Negroni, Emanuela Monza, Tito Bertoni, and Peter J. Schwartz. Dispersion of ventricular repolarization in the long QT syndrome. *Am. J. Cardiol.*, 68:614–620, September 1991. Cited on pages 18, 46, and 88.

Renato **De Mori**, see Belforte [20]. Jo J. A. M. **Defauw**, see De Bakker [9], Van Dessel [48], and Jessurun [118]. Rosanna **Degani**, see Willems [273, 274]. Mario **Delmar**, see Morley [177]. Michel **Demeester**, see Willems [273]. Bernard **Denis**, see Willems [273, 274].

45] R. **Derksen**, J. R. de Groot, R. Coronel, J. M. T. de Bakker, A. C. Linnenbank, M. Potse, S. Tasseron, and R. N. W. Hauer. Decremental conduction due to load mismatch in pattern-grown cell cultures. *European Heart J.*, 21 Suppl. S:238, 2000. (abstract).

Richard **Derksen**, see also De Bakker [12], Kawara [122], and Wittkampf [279].

46] Pascal F. H. M. **van Dessel**. *Visualization and functional characterization of the postinfarction arrhythmogenic substrate*. PhD thesis, Utrecht University, Utrecht, The Netherlands, November 2001. Cited on pages 198 and 200.

47] Pascal F. H. M. **van Dessel**, Norbert M. van Hemel, Jacques M. T. de Bakker, André C. Linnenbank, Mark Potse, Emile R. Jessurun, Arne SippensGroenewegen, and Eric F. D. Wever. Relation between body surface mapping and endocardial spread of ventricular activation in postinfarction heart. *J. Cardiovasc. Electrophysiol.*, 12:1232–1241, 2001. Cited on pages 19–21, 59, 163, and 200.

48] Pascal F. **van Dessel**, Norbert M. van Hemel, Jacques M. de Bakker, Mark Potse, Andre C. Linnenbank, Emile R. Jessurun, and Jo A. Defauw. Comparison of simultaneous body surface mapping and 64-electrode endocardial mapping of postinfarction ventricular tachycardia exit. *Circulation*, 100 Suppl. I(18):655–656, November 1999. (abstract). Cited on pages 19, 20, 69, 181, 192, and 200.

Pascal F. H. M. **van Dessel**, see also Linnenbank [148], Potse [199, 204, 206], and Willemsen [275]. P. B. **Deverall**, see Holt [99]. Konstantinos **Diamantaras**, see Maglaveras [167] and Stamkopoulos [253]. Ruud N. **van Dijk**, see Hauer [88]. Koert P. **Dingemans**, see De Bakker [11].

49] Harold T. **Dodge**, Harold Sandler, Donald Ballew, and John D. Lord. The use of biplane angiocardiography for the measurement of left ventricular volume in man. *Am. Heart J.*, 60(5):762–776, 1960. Cited on page 179.

John U. **Doherty**, see Cassidy [32]. Paul C. **Dolber**, see Spach [247, 249].

50] Edwin L. **Dove**, Karun Philip, Nina L. Gotteiner, Michael J. Vonesh, John A. Rumberger, Judd E. Reed, William Stanford, David D. McPherson, and Krishnan B. Chandran. A method for automatic edge detection and volume computation of the left ventricle from ultrafast computed tomographic images. *Investigative Radiology*, 29(11):945–954, November 1994. Cited on page 179.

Maria **Drangova**, see Nadkarni [181].

51] Jean-Pierre **Drouhard** and Fernand A. Roberge. The simulation of repolarization events of the cardiac purkinje fiber action potential. *IEEE Trans. Biomed. Eng.*, 29(7):481–493, jul 1982. Cited on page 46.

52] Jean-Pierre **Drouhard** and Fernand A. Roberge. A simulation study of the ventricular myocardial action potential. *IEEE Trans. Biomed. Eng.*, 29(7):494–502, jul 1982. Cited on page 46.

Bruno **Dubé**, see Savard [228] and Xu [280].

53] Marc **Dubuc**, Paul Khairy, Angel Rodrigues-Santiago, Mario Talajic, Jean-Claude Tardif, Bernard Thibault, and Denis Roy. Catheter cryoablation of the atrioventricular node in patients with atrial fibrillation: A novel technology for ablation of cardiac arrhythmias. *J. Cardiovasc. Electrophysiol.*, 12(4):439–444, 2001. Cited on page 18.

54] Marc **Dubuc**, Réginald Nadeau, Gaétan Tremblay, Teresa Kus, Franck Molin, and Pierre Savard. Pace mapping using body surface potential maps to guide catheter ablation of accessory pathways in patients with Wolff-Parkinson-White syndrome. *Circulation*, 87(1):135–143, January 1993. Cited on pages 89, 111, 112, 114, 149, and 165.

Marc **Dubuc**, see also Molin [176]. Joachim **Dudeck**, see Willems [273]. Arend J. **Dunning**, see SippensGroenewegen [235–237, 241, 242].

55] Richard J. **Duro** and José Santos Reyes. Discrete-time backpropagation for training synaptic delay-based artificial neural networks. *IEEE Trans. Neural Networks*, 10(4):779–789, July 1999. Cited on pages 99, 108, and 109.

56] D. **Durrer**, A. A. W. van Lier, and J. Büller. Epicardial and intramural excitation in chronic myocardial infarction. *Am. Heart. J.*, 68(6):765–776, 1964. Cited on page 151.

57] D. **Durrer** and L. H. van der Tweel. Spread of activation in the left ventricular wall of the dog. I. *Am. Heart J.*, 46:683–691, 1953. Cited on page 32.

58] D. **Durrer** and L. H. van der Tweel. Excitation of the left ventricular wall of the dog and goat. *Ann. N.Y. Acad. Sci.*, 65:779–803, 1957. Cited on pages 25 and 81.

59] D. **Durrer**, L. H. van der Tweel, and J. R. Blickman. Spread of activation in the left ventricular wall of the dog. III. Transmural and intramural analysis. *Am. Heart J.*, 48:13–35, 1954. Cited on pages 25 and 81.

60] Dirk **Durrer**, R. Th. van Dam, G. E. Freud, M. J. Janse, F. L. Meijler, and R. C. Arzbaecher. Total excitation of the isolated human heart. *Circulation*, 41:899–912, June 1970. Cited on pages 25 and 32.

Dirk **Durrer**, see also De Bakker [7, 8, 14], Van Capelle [30, 31], and Janse [115, 116]. Ted **Dustman**, see Anderson [4, 5].

61] Lisa **Ebihara** and Edward A. Johnson. Fast sodium current in cardiac muscle; a quantitative description. *Biophys. J.*, 32:779–790, November 1980. Cited on page 46.

Igor R. **Efimov**, see Salama [227].

62] Bradley **Efron**. Estimating the error rate of a prediction rule: Improvement on cross-validation. *J. Amer. Statistical Assoc.*, 78(38):316–331, June 1983. Cited on page 142.

N. **El-Sherif**, see Breithardt [25].

63] Michael **Eldar**, Adam P. Fitzpatrick, Dan Ohad, Michael F. Smith, Steve Hsu, James G. Whayne, Zvi Vered, Zeev Rotstein, Thomas Kordis, David K. Swanson, Michael Chin, Melvin M. Scheinman, Michael D. Lesh, and Arnold J. Greenspon. Percutaneous multielectrode endocardial mapping during ventricular tachycardia in the swine model. *Circulation*, 94:1125–1130, September 1996. Cited on pages 19, 69, and 70.

Michael **Eldar**, see also Greenspon [78]. Willard S. **Ellis**, see SippensGroenewegen [238]. Andrew **Epstein**, see Calkins [29]. L. **van Erning**, see Hoekema [95]. Philip R. **Ershler**, see Anderson [4, 5], Green [76], and Liu [156]. A. K. **Evans**, see Lux [160, 161]. Raffaele **Fanelli**, see Natale [183]. G. **Faugère**, see Nadeau [180].

64] I. D. **Faux** and M. J. Pratt. *Computational Geometry for Design and Manufacture*. Wiley, 1979. Cited on page 209.

Aaron **Fenster**, see Nadkarni [181].

65] Manuel **Fernández-Delgado** and Senén Barro Ameneiro. MART: A multichannel ART-based neural network. *IEEE Trans. Neural Networks*, 9(1):139–150, January 1998. Cited on pages 108 and 109.

Jason E. **Ferrara**, see Geselowitz [74]. Franco **Ferraris**, see Belforte [20]. Adam P. **Fitzpatrick**, see Eldar [63]. Brian P. **Flannery**, see Press [215]. N. C. **Flowers**, see Breithardt [25] and Horan [100].

66] Robert W. **Floyd**. The syntax of programming languages—A survey. *IEEE Trans. El. Comp.*, 13(4):346–353, 1964. Cited on page 101.

67] Marian **Fournier**. Willem Einthoven – the electrophysiology of the heart. *Medicamundi*, 21(2):65–70, 1976. Cited on page 14.

Harry A. **Fozzard**, see Cox [38, 39] and Yanowitz [283].

68] Alejandro F. **Frangi**, Wiro J. Niessen, and Max A. Viergever. Three-dimensional modeling for functional analysis of cardiac images: A review. *IEEE Trans. Med. Imaging*, 20(1):2–25, jan 2001. Cited on page 178.

69] Ernest **Frank**. An accurate, clinically practical system for spatial vectorcardiography. *Circulation*, 13:737–749, May 1956. Cited on pages 15 and 89.

Roger A. **Freedman**, see Green [76]. G. E. **Freud**, see Durrer [60].

70] Gary M. **Friesen**, Thomas C. Jannett, Manal Afify Jadallah, Stanford L. Yates, Stephen R. Quint, and H. Troy Nagle. A comparison of the noise sensitivity of nine QRS detection algorithms. *IEEE Trans. Biomed. Eng.*, 37(1):85–99, 1990. Cited on page 103.

71] K. S. **Fu**. A step towards unification of syntactic and statistical pattern recognition. *IEEE Trans. Patt. Analysis & Mach. Intell.*, 5(2):200–205, 1983. Cited on page 101.

Mark **Fuller**, see Anderson [4, 5]. John **Gade**, see Kemp [124]. Thomas M. **Gallie**, see Barr [15–17]. Hasan **Garan**, see Rosenbaum [223]. Kathleen **Gear**, see Green [76]. A. S. **Geha**, see Liebman [146]. Lior **Gepstein**, see Shpun [230].

72] Martin **Gerhardt**, Heike Schuster, and John J. Tyson. A cellular automaton model of excitable media including curvature and dispersion. *Science*, 247:1563–1566, 1990. Cited on page 48.

Ronald J. **Gerstle**, see Bollacker [23].

73] D. B. **Geselowitz**, R. C. Barr, M. S. Spach, and W. T. Miller, III. The impact of adjacent isotropic fluids on electrograms from anisotropic cardiac muscle. *Circ. Res.*, 51:602–613, November 1982. Cited on pages 81 and 82.

74] David B. **Geselowitz** and Jason E. Ferrara. Is accurate recording of the ECG surface laplacian feasible? *IEEE Trans. Biomed. Eng.*, 46(4):377–381, April 1999. Cited on page 53.

David B. **Geselowitz**, see also Miller [173]. C. Lee **Giles**, see Clouse [35]. David M. **Gilligan**, see Calkins [29]. Wiek H. **van Gilst**, see Dambrink [42]. M. **Gori**, see Silipo [232]. Nina L. **Gotteiner**, see Dove [50]. Charles D. **Gottlieb**, see Rodriguez [221].

75] Richard A. **Gray**, José Jalife, Alexandre Panfilov, William T. Baxter, Cándido Cabo, Jorge M. Davidenko, and Arkady M. Pertsov. Nonstationary vortexlike reentrant activity as a mechanism of polymorphic ventricular tachycardia in the isolated rabbit heart. *Circulation*, 91(9):2454–2469, May 1995. Cited on pages 26, 47, and 49.

76] Larry S. **Green**, Robert L. Lux, Philip R. Ershler, Roger A. Freedman, Frank I. Marcus, and Kathleen Gear. Resolution of pace mapping stimulus site separation using body surface potentials. *Circulation*, 90(1):462–468, July 1994. Cited on pages 89 and 136.

Larry S. **Green**, see also Abildskov [1].

77] Fred **Greensite** and Geertjan Huiskamp. An improved method for estimating epicardial potentials from the body surface. *IEEE Trans. Biomed. Eng.*, 45(1):98–104, January 1998. Cited on page 111.

Fred **Greensite**, see also Huiskamp [111]. Allan M. **Greenspan**, see Josephson [119].

78] Arnold J. **Greenspon**, Steve S. Hsu, Richard Borge, Michael F. Smith, and Michael Eldar. Insights into the mechanism of sustained ventricular tachycardia after myocardial infarction in a closed chest porcine model using a multielectrode "basket" catheter. *J. Cardiovasc. Electrophysiol.*, 10:1501–1516, November 1999. Cited on pages 19, 69, and 70.

Arnold J. **Greenspon**, see also Eldar [63].

79] C. A. **Grimbergen**, A. C. MettingVanRijn, A. P. Kuiper, A. C. Linnenbank, and A. Peper. Instrumentation for the recording and digital processing of multichannel ECG data. In *Proc. 14th Annu. Int. Conf. IEEE EMBS*, pages 726–727, 1992. Cited on page 139.

Cornelis A. **Grimbergen**, see also Dambrink [42], Hajer [86], Huigen [107], Kemmelings [123], Latour [139], Linnenbank [149–153, 155], MettingVanRijn [172], Peeters [192–194], Potse [197, 199–201, 204, 206–208, 211–214], SippensGroenewegen [235, 242], and Willemsen [275, 276].

80] Joris R. **de Groot**. *Genesis of life-threatening ventricular arrhythmias during the delayed phase of acute myocardial ischemia. Role of cellular electrical coupling and myocardial heterogeneities*. PhD thesis, University of Amsterdam, June 2001. Cited on pages 63 and 64.

81] Joris R. **de Groot**, Ruben Coronel, Francien J. G. Wilms-Schopman, Carol Ann Remme, and Michiel J. Janse. Critical cellular coupling required for 1B ventricular fibrillation in the isolated regionally ischemic porcine heart. *Circulation*, 100 Suppl. I(18):839, November 1999. (abstract). Cited on page 192.

82] Joris R. **de Groot**, Francien J. G. Wilms-Schopman, Tobias Opthof, Carol A. Remme, and Ruben Coronel. Late ventricular arrhythmias during acute regional ischemia in the isolated blood perfused pig heart. Role of electrical cellular coupling. *Cardiovasc. Res.*, 50(2):362–372, 2001. Cited on pages 65 and 192.

Joris R. **de Groot**, see also Coronel [37], Derksen [45], and Kawara [122]. Robert **Guardo**, see Nadeau [180] and Savard [228]. Peter G. **Guerra**, see SippensGroenewegen [239].

83] Ramesh M. **Gulrajani**. Models of the electrical activity of the heart and computer simulation of the electrocardiogram. *CRC Critical Reviews in Biomedical Engineering*, 16(1):1–66, 1988. Cited on pages 111 and 202.

84] Ramesh M. **Gulrajani**. *Bioelectricity and Biomagnetism*. Wiley, September 1998. Cited on pages 45–47, 51, 53, 111, 149, and 202.

Ramesh M. **Gulrajani**, see also Lorange [158], Nadeau [180], Savard [228], and Xu [280].

85] Tomas **Gustavsson**, Ragnar Pascher, and Kenneth Caidahl. Model based dynamic 3D reconstruction and display of the left ventricle from 2D cross-sectional echocardiograms. *Computerized Med. Imag. Graph.*, 17:273–278, 1993. Cited on page 179.

Michel **Haïssaguerre**, see Hocini [92, 93].

86] M. F. **Hajer**, A. C. MettingVanRijn, and C. A. Grimbergen. Design of an optical power supply for biopotential measurement systems. In *Proc. First Joint BMES/EMBS Conf.*, October 1999. Cited on page 26.

87] Patrick S. **Hamilton** and Willis J. Tompkins. Quantitative investigation of QRS detection rules using the MIT/BIH arrhythmia database. *IEEE Trans. Biomed. Eng.*, 33(12):1157–1165, December 1986. Cited on pages 99, 101, 103, 104, and 107.

Toshiyuki **Hanazawa**, see Waibel [268]. Frits M. A. **Harms**, see Willems [273, 274].

88] Richard N. W. **Hauer**, Robert M. Heethaar, Michel T. W. de Zwart, Ruud N. van Dijk, Ingeborg van der Tweel, Cornelius Borst, and Etienne O. Robles de Medina. Endocardial catheter mapping: validation of a cineradiographic method for accurate localization of left ventricular sites. *Circulation*, 74(4):862–868, October 1986. Cited on pages 127, 139, 147, 155, and 175.

89] Richard N. W. **Hauer**, Michel T. de Zwart, Jacques M. T. de Bakker, J. Francois Hitchcock, Olaf C. K. M. Penn, Marianne Nijsen-Karelse, and Etienne O. Robles de Medina. Endocardial catheter mapping: wire skeleton technique for representation of computed arrhythmogenic sites compared with intraoperative mapping. *Circulation*, 74(6):1346–1354, December 1986. Cited on pages 139 and 147.

Richard N. W. **Hauer**, see also De Bakker [9, 11, 13], Derksen [45], Kawara [122], Peeters [190–194], Simmers [233], SippensGroenewegen [235–237,241,242], and Wittkampf [279]. Gal **Hayam**, see Shpun [230].

90] Hiroshi **Hayashi**, Shinji Watabe, Kazuhide Takami, Seitaro Yabe, Haruyoshi Uematsu, Makiko Mizutani, and Hidehiko Saito. Sites of origin of ventricular premature beats in patients with and without cardiovascular disease evaluated by body surface mapping. *J. Electrocardiol.*, 21(2):137–146, 1988. Cited on pages 111 and 114.

Robert M. **Heethaar**, see Hauer [88] and Van der Tweel [261]. Herman K. **Hellerstein**, see Zimmerman [284]. Norbert M. **van Hemel**, see De Bakker [9, 11], Van Dessel [47, 48], Jessurun [118], Linnenbank [148], Peeters [194], Potse [204, 206], SippensGroenewegen [235–237, 240–242], and Willemsen [275]. R. W. **Henthorn**, see Liebman [146]. Russel E. **Hillsley**, see Bayly [18] and Bollacker [23]. Geoffrey **Hinton**, see Waibel [268]. J. Francois **Hitchcock**, see Hauer [89]. Siew Y. **Ho**, see Hocini [92, 93].

91] John D. **Hobby**. *A user's manual for MetaPost. Computing Science Technical Report no. 162*. AT&T Bell Laboratories, Murray Hill, New Jersey, April 1992. Can be obtained by mailing "send 162 from research/cstr" to netlib@research.att.com. Should also be included in any decent TEX distribution. Cited on pages 65 and 66.

92] Mélèze **Hocini**, Jacques M. T. de Bakker, André C. Linnenbank, Yen Ho, Michiel J. Janse, and Michel Haissaguerre. High resolution mapping of the left atrium and the pulmonary veins during pacing and atrial fibrillation in the isolated canine heart. *Circulation*, 99 Suppl. I:208–209, 1998. (abstract). Cited on page 192.

93] Mélèze **Hocini**, Siew Y. Ho, Tokuhiro Kawara, André C. Linnenbank, Mark Potse, Dipen Shah, Pierre Jaïs, Michiel J. Janse, Michel Haïssaguerre, and Jacques M. T. de Bakker. Electrical conduction in canine pulmonary veins: Electrophysiological and anatomic correlation. *Circulation*, 105:2442–2448, 2002. Cited on page 192.

Mélèze **Hocini**, see also Linnenbank [155].

94] A. L. **Hodgkin** and A. F. Huxley. A quantitative description of membrane current and its application to conduction and excitation in nerve. *J. Physiol.*, 117:500–544, 1952. Cited on page 46.

95] R. **Hoekema**, G. J. H. Uijen, L. van Erning, and A. van Oosterom. Interindividual variability of multilead electrocardiographic recordings: Influence of heart position. *J. Electrocardiol.*, 32(2):137–148, 1999. Cited on page 169.

96] R. **Hoekema**, G. J. H. Uijen, and A. van Oosterom. The number of independent signals in body surface maps. *Meth. Inf. Med.*, 38:119–124, 1999. Cited on page 15.

97] R. **Hoekema**, G. J. H. Uijen, and A. van Oosterom. On selecting a body surface mapping procedure. *J. Electrocardiol.*, 32(2):93–101, 1999. Cited on page 86.

98] R. **Hoekema**, G. J. H. Uijen, D. Stilli, and A. van Oosterom. Lead system transformation of body surface map data. *J. Electrocardiol.*, 31(2):71–82, 1998. Cited on pages 17, 86, and 187.

R. **Hoekema**, see also Potse [197]. A. V. **Holden**, see Van Oosterom [186].

99] P. M. **Holt**, C. Smallpeice, P. B. Deverall, A. K. Yates, and P. V. L. Curry. Ventricular arrhythmias; A guide to their localisation. *Br. Heart J.*, 53:417–430, 1985. Cited on page 151.

V. **Hombach**, see Breithardt [25]. B. Milan **Horáček**, see Hren [102–104], Kornreich [135, 136], and Leon [141, 142].

100] L. G. **Horan** and N. C. Flowers. The principle of waveform correlation in electrocardiographic research. *J. Electrocardiol.*, 1:43–50, 1968. Cited on page 88.

Bill G. **Horne**, see Clouse [35]. Leonard N. **Horowitz**, see Josephson [119].

101] Rosalie C. **Hoyt**. Sodium inactivation in nerve fibers. *Biophys. J.*, 8:1074–1097, 1968. Cited on page 47.

102] R. **Hren**, G. Stroink, and B. M. Horáček. Accuracy of single-dipole inverse solution when localising ventricular pre-excitation sites: simulation study. *Med. & Biol. Eng. & Comput.*, 36:323–329, May 1998. Cited on page 150.

103] R. **Hren**, G. Stroink, and B. M. Horáček. Spatial resolution of body surface potential maps and magnetic field maps: a simulation study applied to the identification of ventricular pre-excitation sites. *Med. & Biol. Eng. & Comput.*, 36:145–157, March 1998. Cited on pages 147 and 202.

104] Rok **Hren** and B. Milan Horáček. Value of simulated body surface potential maps as templates in localizing sites of ectopic activation for radiofrequency ablation. *Physiol. Meas.*, 18:373–400, 1997. Cited on pages 111, 138, 146, 149, 161, and 202.

Steve S. **Hsu**, see Eldar [63] and Greenspon [78].

105] Yu Hen **Hu**, Willis J. Tompkins, José L. Urrusti, and Valtino X. Afonso. Applications of artificial neural networks for ECG signal detection and classification. *Journal of Electrocardiology*, 26 Suppl:66–73, 1993. Cited on pages 101, 104, 108, and 109.

Yu Hen **Hu**, see also Xue [281].

106] D. A. **Huffman**. A method for the construction of minimum-redundancy codes. In *Proc IRE*, volume 40, pages 1098–1101, 1952. Cited on pages 37 and 43.

107] E. **Huigen**, A. Peper, and C. A. Grimbergen. Investigation into the origin of the noise of surface electrodes. *Med. & Biol. Eng. & Comput.*, 40:332–338, 2002. Cited on pages 26 and 27.

108] G. J. M. **Huiskamp** and A. van Oosterom. Heart position and orientation in forward and inverse electrocardiography. *Med. & Biol. Eng. & Comput.*, 30:613–620, 1992. Cited on page 111.

109] Geertjan **Huiskamp**. Difference formulas for the surface Laplacian on a triangulated surface. *Journal of Computational Physics*, 95(2):477–496, August 1991. Cited on page 54.

110] Geertjan **Huiskamp**. Simulation of depolarization in a membrane-equations-based model of the anisotropic ventricle. *IEEE Trans. Biomed. Eng.*, 45(7):847–855, July 1998. Cited on page 46.

111] Geertjan **Huiskamp** and Fred Greensite. A new method for myocardial activation imaging. *IEEE Trans. Biomed. Eng.*, 44(6):433–446, June 1997. Cited on page 150.

112] Geertjan **Huiskamp** and Adriaan van Oosterom. The depolarization sequence of the human heart surface computed from measured body surface potentials. *IEEE Trans. Biomed. Eng.*, 35(12):1047–1058, December 1988. Cited on page 150.

113] Geertjan **Huiskamp** and Adriaan van Oosterom. Tailored versus realistic geometry in the inverse problem of electrocardiography. *IEEE Trans. Biomed. Eng.*, 36(8):827–835, August 1989. Cited on pages 111 and 150.

Geertjan **Huiskamp**, see also Greensite [77] and Van Oosterom [187]. John **Hummel**, see Calkins [29]. P. J. **Hunter**, see Nielsen [184]. A. F. **Huxley**, see Hodgkin [94].

114] Raymond E. **Ideker**, William M. Smith, Susan M. Blanchard, Susan L. Reiser, Edward V. Simpson, Patrick D. Wolf, and Ned D. Danieley. The assumptions of isochronal cardiac mapping. *PACE*, 12:456–478, March 1989. Cited on page 60.

Raymond E. **Ideker**, see also Bayly [18] and Bollacker [23]. Mir A. **Imran**, see Ruffy [225]. Warren M. **Jackman**, see Nakagawa [182]. Lance E. **Jackson**, see Rosenbaum [223]. Manal Afify **Jadallah**, see Friesen [70]. Pierre **Jaïs**, see Hocini [93]. José **Jalife**, see De Bakker [13], Gray [75], Morley [177], and Vaidya [267]. G. **Jambroes**, see De Bakker [6]. Thomas C. **Jannett**, see Friesen [70].

115] M. J. **Janse** and D. Durrer. Mechanisme en betekenis van de veranderingen in het ST-segment van het elektrocardiogram tijdens acute ischemie van de hartspier [the mechanism and significance of changes of the ST segment of the ECG in the course of acute myocardial ischaemia]. *Ned. T. Geneesk.*, 122(50):1964–1968, 1978. (Dutch language). Cited on page 50.

116] Michiel J. **Janse**, Frans J. L. van Capelle, Hemmy Morsink, André Kléber, Francien Wilms-Schopman, René Cardinal, Christoph Naumann d'Alnoncourt, and Dirk Durrer. Flow of "injury" current and patterns of excitation during early ventricular arrhythmias in acute regional myocardial ischemia in isolated porcine and canine hearts. *Circ. Res.*, 47(2):151–165, August 1980. Cited on pages 48 and 54.

Michiel J. **Janse**, see also De Bakker [6–12, 14], Breithardt [25], Van Capelle [31], Coronel [37], Durrer [60], De Groot [81], Hocini [92, 93], Kawara [122], Kléber [126], Loh [157], Maglaveras [165], McGuire [171], and SippensGroenewegen [235–237, 242].

117] Kathy J. **Jenkins**, Edward P. Walsh, Steven D. Colan, Dennis M. Bergau, J. Philip Saul, and James E. Lock. Multipolar endocardial mapping of the right atrium during cardiac catheterization: Description of a new technique. *J. Am. Coll. Cardiol.*, 22:1105–1110, October 1993. Cited on pages 19, 69, and 70.

118] Emile R. **Jessurun**, Jacques M. T. de Bakker, Norbert M. van Hemel, Andre C. Linnenbank, Jo J. A. M. Defauw, and Aart Brutel de la Riviere. Surgical modification of the right atrium for the abolishment of atrial fibrillation with maze III does not affect fibrillation intervals. *Circulation*, 100 Suppl. I(18):67, November 1999. (abstract). Cited on page 192.

Emile R. **Jessurun**, see also Van Dessel [47, 48] and SippensGroenewegen [240]. Edward A. **Johnson**, see Ebihara [61] and Spach [246]. Nicolaas **de Jonge**, see De Bakker [10]. Habo J. **Jongsma**, see Van Rijen [220].

119] Mark E. **Josephson**, Leonard N. Horowitz, Scott R. Spielman, Harvey L. Waxman, and Allan M. Greenspan. Role of catheter mapping in the preoperative evaluation

of ventricular tachycardia. *Am. J. Cardiol.*, 49:207–220, January 1982. Cited on pages 116, 122, and 136.

Mark E. **Josephson**, see also Cassidy [32] and Waxman [270].

120] Shubha **Kadambe**, Robin Murray, and G. Faye Boudreaux-Bartels. Wavelet transform-based QRS complex detector. *IEEE Trans. Biomed. Eng.*, 46(7):838–848, July 1999. Cited on page 100.

121] Shiro **Kamakura**, Naohiko Aihara, Mokuo Matsuhisa, Tohru Ohe, Iwao Sato, and Katsuro Shimomura. The role of initial minimum potentials on body surface maps in localizing the earliest endocardial site of ectopic ventricular excitation. *Circulation*, 78 II:138, 1988. (abstract). Cited on pages 111 and 114.

Anthony **Kanai**, see Salama [227]. Shreekant V. **Karwandee**, see Anderson [4]. T. **Katila**, see Mäkijärvi [169]. Mikhail **Kavadias**, see Kornreich [135, 136]. Katherine M. **Kavanagh**, see Witkowski [277, 278].

122] Tokuhiro **Kawara**, Richard Derksen, Joris R. de Groot, Ruben Coronel, Sara Tasseron, André C. Linnenbank, Richard N. W. Hauer, Hans Kirkels, Michiel J. Janse, and Jacques M. T. de Bakker. Activation delay after premature stimulation in chronically diseased human myocardium relates to the architecture of interstitial fibrosis. *Circulation*, 104:3069–3075, 2001. Cited on page 192.

Tokuhiro **Kawara**, see also De Bakker [12] and Hocini [93].

123] J. G. C. **Kemmelings**, A. C. Linnenbank, S. L. C. Muilwijk, A. SippensGroenewegen, A. Peper, and C. A. Grimbergen. Automatic QRS onset and offset detection for body surface QRS integral mapping of ventricular tachycardia. *IEEE Trans. Biomed. Eng.*, 41(9):830–836, 1994. Cited on pages 21, 98, 99, 104, 105, 188, and 200.

J. G. C. **Kemmelings**, see also Linnenbank [149].

124] Bob **Kemp**, Alpo Värri, Agostinho C. Rosa, Kim D. Nielsen, and John Gade. A simple format for exchange of digitized polygraphic recordings. *Electroencephalography and clinical Neurophysiology*, 82:391–393, 1992. Cited on pages 40 and 41.

Marjan J. A. **van Kempen**, see Van Rijen [220]. Bruce H. **KenKnight**, see Bayly [18]. Paul **Khairy**, see Dubuc [53].

125] Apichai **Khongphatthanayothin**, Erol Kosar, and Koonlawee Nademanee. Nonfluoroscopic three-dimensional mapping for arrhythmia ablation: Tool or toy? *J. Cardiovasc. Electrophysiol.*, 11:239–243, March 2000. Cited on page 166.

Dirar S. **Khoury**, see Liu [156]. Michael C. **King**, see Bollacker [23]. J. Herre **Kingma**, see Dambrink [42] and SippensGroenewegen [235–237, 242]. Plato **Kinias**, see Yanowitz [283]. Hans **Kirkels**, see Kawara [122].

126] André **Kléber**, Michiel J. Janse, Francien J. G. Wilms-Schopman, Arthur A. M. Wilde, and Ruben Coronel. Changes in conduction velocity during acute ischemia in ventricular myocardium of the isolated porcine heart. *Circulation*, 73:189–198, 1986. Cited on pages 61 and 63.

André **Kléber**, see also Janse [116].

127] Lawrence S. **Klein** and William M. Miles. Ablative therapy for ventricular arrhythmias. *Progr. Cardiovasc. Diseases*, 37(4):225–242, 1995. Cited on page 18.

128] D. E. **Knuth**. *TEX: The Program*. Addison-Wesley, 1986. Volume B in the series Computers & Typesetting. Cited on page 205.

129] Donald E. **Knuth**. Literate programming. *The Computer Journal*, 27(1):97–111, 1984. Cited on pages 185 and 205.

130] Donald E. **Knuth**. *Literate Programming*. CSLI, Stanford University, 1992. CSLI Lecture notes no. 27. Cited on pages 185, 193, and 205.

131] Donald E. **Knuth**. *The Stanford Graphbase*. Addison-Wesley, 1993. Cited on page 205.

132] Donald E. **Knuth** and Silvio Levy. *The CWEB System of Structured Documentation*. Addison-Wesley, 1993. Cited on pages 186 and 205.

T. **Kobayashi**, see Yamada [282].

133] Teuvo **Kohonen**. Self-organized formation of topologically correct feature maps. *Biological Cybernetics*, 43:59–69, 1982. Cited on page 133.

134] Teuvo **Kohonen**. *Self-organizing maps*. Springer, Berlin, 1995. Cited on pages 133 and 147.

J. Mailen **Kootsey**, see Spach [246, 248, 249]. Harry **Kopelman**, see Calkins [29]. Thomas **Kordis**, see Eldar [63].

135] Fred **Kornreich**, Terrence J. Montague, Mikhail Kavadias, Joris Segers, Pentti M. Rautaharju, Milan B. Horacek, and Bruno Taccardi. Qualitative and quantitative analysis of characteristic body surface potential map features in anterior and inferior myocardial infarction. *Am. J. Cardiol.*, 60:1230–1238, 1987. Cited on page 18.

136] Fred **Kornreich**, Terrence J. Montague, Pentti M. Rautaharju, Mikhail Kavadias, Milan B. Horacek, and Bruno Taccardi. Diagnostic body surface potential map patterns in left ventricular hypertrophy during PQRST. *Am. J. Cardiol.*, 63:610–617, 1989. Cited on page 18.

Erol **Kosar**, see Khongphatthanayothin [125].

137] Antti **Koski**. Modelling ECG signals with hidden Markov models. *Artificial Intelligence in Medicine*, 8:453–471, 1996. Cited on page 102.

Olaf **Krueger**, see Van Rijen [220]. Anthony P. **Kuiper**, see Grimbergen [79] and MettingVanRijn [172]. M. **Kunt**, see Ligtenberg [147]. Teresa **Kus**, see Dubuc [54] and Molin [176].

138] Ad **Lagendijk**. De arrogantie van de fysicus. Inaugurele rede Universiteit van Amsterdam, September 1989. (Dutch language). Cited on page 13.

Jaap R. **Lahpor**, see De Bakker [10]. Kevin J. **Lang**, see Waibel [268].

139] A. **Latour**, C. A. Grimbergen, H. A. P. Peeters, A. C. Linnenbank, and A. Sippens Groenewegen. Quantitative algorithm for the localization of the origin of ectopic ventricular beats using catheter pace mapping. In *Proc. 18th Annu. Int. Conf. IEEE EMBS*, 1996. Cited on page 132.

140] Auke **Latour**. Een zoekalgoritme voor de lokalisatie van de oorsprong van hartritmestoornissen. Master's thesis, Faculteit der Werktuigbouwkunde en Maritieme Techniek, T.U. Delft: A-744-1 en -2, July 1995. Cited on page 132.

Ralph **Lazzara**, see Nakagawa [182]. I. J. **Le Grice**, see Nielsen [184]. Randall J. **Lee**, see SippensGroenewegen [238]. M. **Leiniö**, see Mäkijärvi [169].

141] L. Joshua **Leon** and B. Milan Horáček. Computer model of excitation and recovery in the anisotropic myocardium. I. Rectangular and cubic arrays of excitable elements. *J. Electrocardiol.*, 24(1):1–15, January 1991. Cited on page 149.

142] L. Joshua **Leon** and B. Milan Horáček. Computer model of excitation and recovery in the anisotropic myocardium. II. Excitation in the simplified left ventricle. *J. Electrocardiol.*, 24(1):17–31, January 1991. Cited on pages 111 and 178.

143] L. Joshua **Leon** and Francis X. Witkowski. Calculation of transmembrane current from extracellular potential recordings: A model study. *J. Cardiovasc. Electrophysiol.*, 6:379–380, May 1995. Cited on page 83.

Fabio **Leonelli**, see Natale [183]. Michael D. **Lesh**, see Eldar [63] and SippensGroenewegen [234, 238–240].

144] John **Levine**, Tony Mason, and Doug Brown. *Lex & Yacc*. O' Reilly, 2nd edition, October 1992. Cited on page 101.

Silvio **Levy**, see Knuth [132].

145] Cuiwei **Li**, Chongxun Zheng, and Changfeng Tai. Detection of ECG characteristic points using wavelet transforms. *IEEE Trans. Biomed. Eng.*, 42(1):21–28, January 1995. Cited on pages 100 and 104.

146] J. **Liebman**, J. A. Zeno, B. Olhansky, A. S. Geha, C. W. Thomas, Y. Rudy, R. W. Henthorn, M. Cohen, and A. L. Waldo. Electrocardiographic body surface potential mapping in the Wolff-Parkinson-White syndrome. Noninvasive determination of the ventricular insertion sites of accessory atrioventricular connections. *Circulation*, 83:886–901, 1991. Cited on page 18.

Jerome **Liebman**, see also Amoore [3] and Sun [254]. A. A. W. **van Lier**, see Durrer [56].

147] A. **Ligtenberg** and M. Kunt. A robust-digital QRS-detection algorithm for arrhythmia monitoring. *Comp. & Biom. Res.*, 16:273–286, 1983. Cited on pages 103 and 106.

148] A. C. **Linnenbank**, P. F. H. M. van Dessel, M. Potse, J. M. T. de Bakker, and N. M. van Hemel. Localization of late potentials using body surface mapping. *Biomed. Techn.*, 46(Erg. b. 2):204–206, 2001. Cited on page 20.

149] A. C. **Linnenbank**, J. G. C. Kemmelings, S. L. C. Muilwijk, A. Peper, and C. A. Grimbergen. An effective compression scheme for multilead ECG signals containing ectopic ventricular activation. In *Proc. 14th Annu. Int. Conf. IEEE EMBS*, pages 527–528, 1992. Cited on pages 5, 25, 37, 41, 43, 187, and 200.

150] A. C. **Linnenbank**, A. C. MettingVanRijn, C. A. Grimbergen, and J. M. T. de Bakker. Choosing the resolution in AD conversion of biomedical signals. In *Intern. Conf. on Electrocardiology*, pages 198–199, 1995. Cited on pages 5, 25, and 26.

151] A. C. **Linnenbank**, S. L. C. Muilwijk, A. SippensGroenewegen, and C. A. Grimbergen. Effect of baseline procedures on QRS integral patterns in body surface maps of ventricular tachycardia. In *Proc. 13th Annu. Int. Conf. IEEE EMBS*, pages 789–790, 1991. Cited on pages 5, 21, 25, 136, and 200.

152] A. C. **Linnenbank**, A. SippensGroenewegen, and C. A. Grimbergen. Artificial neural networks applied in multiple lead electrocardiography: rapid quantative classification of ventricular tachycardia QRS integral patterns. In *Proc. 12th Annu. Int. Conf. IEEE EMBS*, pages 1461–1462, 1990. Cited on pages 108, 109, and 112.

153] A. C. **Linnenbank**, A. SippensGroenewegen, and C. A. Grimbergen. Multiple lead ECG analysis using artificial neural networks: classification of ventricular tachycardia QRS integral patterns compared with correlation coefficients. *Circulation*, 82 Suppl:III–741, 1990. (abstract). Cited on pages 108, 109, and 112.

154] André C. **Linnenbank**. *On-site recording, analysis, and presentation of multichannel ECG data*. PhD thesis, University of Amsterdam, The Netherlands, August 1996. e-mail: a.c.linnenbank@amc.uva.nl. Cited on pages 13, 21, 23, 33, 61, 107, 129, 139, 192, and 200.

155] André C. **Linnenbank**, Jeroen G. Snel, Mélèze Hocini, Mark Potse, Jacques M. T. de Bakker, and Cornelis A. Grimbergen. Display of activation fronts on a 3D reconstruction of the left atrium of a dog. In *Proc. 20th Annu. Int. Conf. IEEE EMBS*, pages I–90–93, October 1998. Cited on pages 187, 188, 192, and 200.

André C. **Linnenbank**, see also De Bakker [12], Derksen [45], Van Dessel [47, 48], Grimbergen [79], Hocini [92, 93], Jessurun [118], Kawara [122], Kemmelings [123], Latour [139], MettingVanRijn [172], Peeters [194], Potse [197–201, 204, 206–214], SippensGroenewegen [240], and Willemsen [275, 276].

156] Zhiwei W. **Liu**, Jia Ping, Philip R. Ershler, Bruno Taccardi, Robert L. Lux, Dirar S. Khoury, and Yoram Rudy. Noncontact endocardial mapping: Reconstruction of electrograms and isochrones from intracavitary probe potentials. *J. Cardiovasc. Electrophysiol.*, 8:415–431, April 1997. Cited on page 81.

Cecilia **Lo**, see Morley [177]. James E. **Lock**, see Jenkins [117].

157] Peter **Loh**, Jacques M. T. de Bakker, Martin Borggrefe, and Michiel J. Janse. High resolution mapping of re-entrant activation in the AV node during ventricular echoes. *Circulation*, 100 Suppl. I(18):836, November 1999. (abstract). Cited on page 192.

158] Michel **Lorange** and Ramesh M. Gulrajani. A computer heart model incorporating anisotropic propagation: I. Model construction and simulation of normal activation. *J. Electrocardiol.*, 26(4):245–261, October 1993. Cited on pages 111 and 149.

Michel **Lorange**, see also Xu [280]. John D. **Lord**, see Dodge [49]. Richard **Luceri**, see Calkins [29].

159] Ching-Hsing **Luo** and Yoram Rudy. A dynamic model of the cardiac ventricular action potential; I. Simulations of ionic currents and concentration changes. *Circ. Res.*, 74(6):1071–1096, jun 1994. Cited on page 46.

Shen **Luo**, see Afonso [2].

160] R. L. **Lux**, M. J. Burgess, R. F. Wyatt, A. K. Evans, G. M. Vincent, and J. A. Abildskov. Clinically practical lead systems for improved electrocardiography: comparison with precordial grids and conventional lead systems. *Circulation*, 59:356–363, 1979. Cited on pages 15–17, and 139.

161] R. L. **Lux**, A. K. Evans, M. J. Burgess, R. F. Wyatt, and J. A. Abildskov. Redundancy reduction for improved display and analysis of body surface potential maps. I. Spatial compression. *Circ. Res*, 49:186–196, 1981. Cited on pages 91, 92, and 139.

162] Robert L. **Lux**, Creig R. Smith, Roland F. Wyatt, and J. A. Abildskov. Limited lead selection for estimation of body surface potential maps in electrocardiography. *IEEE Trans. Biomed. Eng.*, 25(3):270–276, May 1978. Cited on page 15.

Robert L. **Lux**, see also Abildskov [1], Anderson [4, 5], Green [76], and Liu [156]. Peter W. **Macfarlane**, see Willems [273, 274].

163] N. **Maglaveras**, F. J. L. van Capelle, and J. M. T. de Bakker. Wave propagation simulation in normal and infarcted myocardium: computational and modelling issues. *Medical Informatics*, 23(2):105–18, Apr–Jun 1998. Cited on page 48.

164] N. **Maglaveras**, T. Stamkopoulos, C. Pappas, and M. Strintzis. ECG processing techniques based on neural networks and bidirectional associative memories. *Journal of Medical Engineering & Technology*, 22(3):106–111, May–Jun 1998. Cited on page 109.

165] Nicos **Maglaveras**, Jacques M. T. de Bakker, Frans J. L. van Capelle, Costas Pappas, and Michiel J. Janse. Activation delay in healed myocardial infarction: A comparison between model and experiment. *Am. J. Physiol.*, 269:H1441–H1449, 1995. Cited on pages 46, 48, 53, 54, 58, and 83.

166] Nicos **Maglaveras**, Franklin Offner, Frans J. van Capelle, Maurits A. Allessie, and Alan V. Sahakian. Effects of barriers on propagation of action potentials in two-dimensional cardiac tissue. A computer simulation study. *J. Electrocardiol.*, 28(1):17–31, January 1995. Cited on page 48.

167] Nicos **Maglaveras**, Telemachos Stamkopoulos, Konstantinos Diamantaras, Costas Pappas, and Michael Strintzis. ECG pattern recognition and classification using non-linear transformations and neural networks: A review. *Int. Journ. Medical Informatics*, 52(1-3):191–208, Oct–Dec 1998. Cited on page 109.

168] Nicos **Maglaveras**, Telemachos Stamkopoulos, Costas Pappas, and Michael Gerassimos Strintzis. An adaptive backpropagation neural network for real-time ischemia episodes detection: development and performance analysis using the European ST-T database. *IEEE Trans. Biomed. Eng.*, 45(7):805–813, July 1998. Cited on pages 99 and 110.

Nicos **Maglaveras**, see also Stamkopoulos [253].

169] M. **Mäkijärvi**, J. Montonen, L. Toivonen, M. Leiniö, P. Siltanen, and T. Katila. High-resolution and signal-averaged electrocardiography to separate post-myocardial infarction patients with and without ventricular tachycardia. *Eur. Heart. J.*, 15:189–199, 1994. Cited on page 108.

David C. **Man**, see Rodriguez [221]. C. **Marchesi**, see Silipo [232]. Francis E. **Marchlinski**, see Cassidy [32] and Rodriguez [221]. Frank I. **Marcus**, see Green [76]. Tony **Mason**, see Levine [144]. Mokuo **Matsuhisa**, see Kamakura [121]. Gianfranco **Mazzocca**, see Willems [273, 274].

170] R. E. **McAllister**, D. Noble, and R. W. Tsien. Reconstruction of the electrical activity of cardiac Purkinje fibres. *J. Physiol.*, 251:1–59, 1975. Cited on page 46.

James H. **McClelland**, see Nakagawa [182]. James L. **McClelland**, see Rumelhart [226].

171] Mark A. **McGuire**, Jacques M. T. de Bakker, Jessica T. Vermeulen, Tobias Opthof, Anton E. Becker, and Michiel J. Janse. Origin and significance of double potentials near the atrioventricular node; correlation of extracellular potentials, intracellular potentials, and histology. *Circulation*, 89:2351–2360, 1994. Cited on page 71.

David D. **McPherson**, see Dove [50]. F. L. **Meijler**, see Durrer [60] and Van der Tweel [261]. Ronald **Menlove**, see Anderson [4].

172] Alexander C. **MettingVanRijn**, Anthony P. Kuiper, André C. Linnenbank, and Cornelis A. Grimbergen. Patient isolation in multichannel bioelectric recordings by digital transmission through a single optical fiber. *IEEE Trans. Biomed. Eng.*, 40(3):302–308, March 1993. Cited on pages 21, 25, 26, 139, and 181.

Alexander C. **MettingVanRijn**, see also Grimbergen [79], Hajer [86], Linnenbank [150], and Spekhorst [252]. Jürgen **Meyer**, see Willems [273, 274]. Jörg **Michaelis**, see Willems [273]. William M. **Miles**, see Klein [127].

173] Walter T. **Miller**, III and David B. Geselowitz. Simulation studies of the electrocardiogram; I. The normal heart. *Circ. Res.*, 43:301–315, August 1978. Cited on page 111.

Walter T. **Miller** III, see also Geselowitz [73] and Spach [249, 250]. Elizabeth **Miller-Jones**, see Spach [250].

174] Kei-ichiro **Minami**, Hiroshi Nakajima, and Takeshi Toyoshima. Real-time discrimination of ventricular tachyarrhythmia with fourier-transform neural network. *IEEE Trans. Biomed. Eng.*, 46(2):179–185, February 1999. Cited on pages 99, 108, and 110.

Y. **Mizuno**, see Yamada [282]. Makiko **Mizutani**, see Hayashi [90]. Michael D. **Mlynash**, see SippensGroenewegen [239].

175] Gordon K. **Moe**, Werner C. Rheinboldt, and J. A. Abildskov. A computer model of atrial fibrillation. *Am. Heart. J.*, 67:200–220, 1964. Cited on page 48.

176] Franck **Molin**, Pierre Savard, Marc Dubuc, Teresa Kus, Gaétan Tremblay, and Réginald Nadeau. Spatial resolution and role of pacemapping during ablation of accessory pathways. *PACE*, 20:683–694, March 1997. Cited on pages 18, 89, 136, and 149.

Franck **Molin**, see also Dubuc [54] and Xu [280]. Terrence J. **Montague**, see Kornreich [135, 136]. J. **Montonen**, see Mäkijärvi [169]. Emanuela **Monza**, see De Ambroggi [44].

177] Gregory E. **Morley**, Dhananjay Vaidya, Faramarz H. Samie, Cecilia Lo, Mario Delmar, and José Jalife. Characterization of conduction in the ventricles of normal and heterozygous Cx43 knockout mice using optical mapping. *J. Cardiovasc. Electrophysiol.*, 10(10):1361–1375, October 1999. Cited on pages 26 and 67.

Gregory E. **Morley**, see also Vaidya [267].

178] Jerry **Morrison**. EA IFF 85, January 1985. `ftp://mirrors.aol.com/pub/pc_games/programming/formats/iff.doc`. Cited on pages 41 and 187.

Hemmy **Morsink**, see Van Capelle [31] and Janse [116]. Charles E. **Mosher** Jr., see Spach [249].

179] S. L. C. **Muilwijk**. *Body Surface Mapping of Ventricular Arrhythmias*. PhD thesis, University of Amsterdam, The Netherlands, 1994. Cited on page 148.

S. L. C. **Muilwijk**, see also Kemmelings [123] and Linnenbank [149, 151]. A. **Murray**, see Clayton [33, 34]. Robin **Murray**, see Kadambe [120]. Ivaturi S. N. **Murthy**, see Udupa [262].

180] R. A. **Nadeau**, P. Savard, G. Faugère, M. Shenasa, P. Pagé, R. M. Gulrajani, R. A. Guardo, and R. Cardinal. Localization of pre-excitation sites in the Wolff-Parkinson-White syndrome by body surface potential mapping and a single moving dipole representation. In R. Th. **van Dam** and A. van Oosterom, editors, *Electrocardiographic Body Surface Mapping*, pages 95–98. Martinus Nijhoff, Dordrecht, The Netherlands, 1986. Cited on pages 18, 111, and 149.

Réginald A. **Nadeau**, see also Dubuc [54], Molin [176], Savard [228], and Xu [280]. Koonlawee **Nademanee**, see Khongphatthanayothin [125].

181] Seemantini K. **Nadkarni**, Derek R. Boughner, Maria Drangova, and Aaron Fenster. Three-dimensional echocardiography: Assessment of inter- and intra-operator variability and accuracy in the measurement of left ventricular cavity volume and myocardial mass. *Phys. Med. Biol.*, 45:1255–1273, 2000. Cited on page 179.

H. Troy **Nagle**, see Friesen [70].

182] Hiroshi **Nakagawa**, William S. Yamanashi, Jan V. Pitha, Mauricio Arruda, Xanzhung Wang, Kenichiro Ohtomo, Karen J. Beckman, James H. McClelland, Ralph Lazzara, and Warren M. Jackman. Comparison of in vivo tissue temperature profile and lesion geometry for radiofrequency ablation with a saline-irrigated electrode versus temperature control in a canine thigh muscle preparation. *Circulation*, 91(8):2264–2273, 1995. Cited on pages 18 and 177.

Hiroshi **Nakajima**, see Minami [174].

183] Andrea **Natale**, Keith H. Newby, Ennio Pisanó, Fabio Leonelli, Raffaele Fanelli, Domenico Potenza, Salwa Beheiry, and Gery Tomassoni. Prospective randomized comparison of antiarrhythmic therapy versus first-line radiofrequency ablation in patients with atrial flutter. *J. Am. Coll. Cardiol.*, 35(7):1898–1904, 2000. Cited on page 18.

Christoph **Naumann d'Alnoncourt**, see Janse [116]. Maria S. **Negroni**, see De Ambroggi [44]. Keith H. **Newby**, see Natale [183]. Truong Q. **Nguyen**, see Afonso [2]. Kim D. **Nielsen**, see Kemp [124].

184] P. M. F. **Nielsen**, I. J. Le Grice, B. H. Smaill, and P. J. Hunter. Mathematical model of geometry and fibrous structure of the heart. *Am. J. Physiol.*, 260:H1365–H1378, 1991. Cited on page 178.

Wiro J. **Niessen**, see Frangi [68]. Marianne **Nijsen-Karelse**, see Hauer [89]. D. **Noble**, see McAllister [170]. Floyd M. **Nolle**, see Cox [38, 39]. Franklin **Offner**, see Maglaveras [166]. Dan **Ohad**, see Eldar [63]. Tohru **Ohe**, see Kamakura [121]. Kenichiro **Ohtomo**, see Nakagawa [182].

185] Masahiko **Okada**. A digital filter for the QRS complex detection. *IEEE Trans. Biomed. Eng.*, 26(12):700–703, December 1979. Cited on page 103.

M. **Okajima**, see Yamada [282]. B. **Olhansky**, see Liebman [146]. G. Charles **Oliver**, see Cox [38, 39].

186] A. **van Oosterom**. Forward and inverse problems in electrocardiography. In A. V. **Panfilov** and A. V. Holden, editors, *Computational Biology of the Heart*, chapter 11, pages 295–343. Wiley, 1997. Cited on page 111.

187] A. **van Oosterom** and G. J. Huiskamp. The effect of torso inhomogeneities on body surface potentials quantified using 'tailored' geometry. *J. Electrocardiol.*, 22:53–72, 1989. Cited on page 111.

188] A. **van Oosterom** and J. Strackee. Computing the lead field of electrodes with axial symmetry. *Med. & Biol. Eng. & Comput.*, 21:473–481, July 1983. Cited on page 53.

Adriaan **van Oosterom**, see also Hoekema [95–98], Huiskamp [108, 112, 113], Nadeau [180], and Uijen [264–266]. Tobias **Opthof**, see De Bakker [6], De Groot [82], and McGuire [171]. Douglas **Packer**, see Calkins [29]. P. **Pagé**, see Nadeau [180].

189] Jiapu **Pan** and Willis J. Tompkins. A real-time QRS detection algorithm. *IEEE Trans. Biomed. Eng.*, 32(3):230–236, March 1985. Cited on pages 99, 103, and 104.

Alexandre **Panfilov**, see Gray [75] and Van Oosterom [186]. Costas **Pappas**, see Maglaveras [164, 165, 167, 168]. Jos **Pardaens**, see Willems [273]. Dave **Parish**, see Burbank [28]. Ragnar **Pascher**, see Gustavsson [85]. Katinka H. **Peels**, see Dambrink [42].

190] H. A. P. **Peeters**, A. SippensGroenewegen, R. N. W. Hauer, F. H. M. Wittkampf, E. F. D. Wever, M. Daniels, and E. O. Robles de Medina. Delayed ventricular depolarization and dispersion of ventricular repolarization in patients with idiopathic ventricular fibrillation. In *Intern. Conf. on Electrocardiology*, 1995. Cited on page 18.

191] H. A. P. **Peeters**, A. SippensGroenewegen, T. A. Simmers, E. F. D. Wever, F. H. M. Wittkampf, B. Schoonderwoerd, R. N. W. Hauer, and E. O. Robles de Medina. Identification of the target site for ablation of left-sided accessory pathways: body surface mapping compared with local electrocardiogram analysis. In *Intern. Conf. on Electrocardiology*, 1995. Cited on page 18.

192] Heidi A. P. **Peeters**, Arne SippensGroenewegen, Bas A. Schoonderwoerd, Eric F. D. Wever, Cornelis A. Grimbergen, Richard N. W. Hauer, and Etienne O. Robles de Medina. Body surface QRST integral mapping: Arrhythmogenic right ventricular dysplasia versus right ventricular tachycardia. *Circulation*, 95:2668–2676, 1997. Cited on pages 18 and 88.

193] Heidi A. P. **Peeters**, Arne SippensGroenewegen, Eric F. D. Wever, Mark Potse, Marcel C. G. Daniëls, Cornelis A. Grimbergen, Richard N. W. Hauer, and Etienne O. Robles de Medina. Electrocardiographic identification of abnormal ventricular depolarization and repolarization in patients with idiopathic ventricular fibrillation. *J. Am. Coll. Cardiol.*, 31(6):1406–1413, May 1998. Cited on pages 18, 88, 92, 94, and 192.

194] Heidi A. P. **Peeters**, Arne SippensGroenewegen, Eric F. D. Wever, Hemanth Ramanna, André C. Linnenbank, Mark Potse, Cornelis A. Grimbergen, Norbert M. van Hemel, Richard N. W. Hauer, and Etienne O. Robles de Medina. Clinical application of an integrated 3-phase mapping technique for localization of the site of origin of idiopathic ventricular tachycardia. *Circulation*, 99:1300–1311, March 1999. Cited on pages 18, 21, 99, 133, 136, 160, 165, 177, 182, 189, and 192.

Heidi A. P. **Peeters**, see also Latour [139], Potse [211, 212], and SippensGroenewegen [240]. Patricia A. **Penkoske**, see Witkowski [277, 278]. Olaf C. K. M. **Penn**, see Hauer [89]. A. **Peper**, see Grimbergen [79], Huigen [107], Kemmelings [123], and Linnenbank [149].

195] Marcello **Pera**. *The Ambiguous Frog: The Galvani–Volta Controversy on Animal Electricity*. Princeton University Press, Princeton, N.J., USA, 1992. Cited on page 14.

Arkady M. **Pertsov**, see Gray [75].

196] Nicholas S. **Peters**. Catheter ablation for cardiac arrhythmias; ablation is the safe and curative treatment of choice. *BMJ*, 321:716–717, September 2000. (editorial). Cited on page 18.

Karun **Philip**, see Dove [50]. Jia **Ping**, see Liu [156]. Ennio **Pisanó**, see Natale [183]. Jan V. **Pitha**, see Nakagawa [182]. Robert **Plonsey**, see Witkowski [277, 278]. Siegfried **Pöppl**, see Willems [273]. Domenico **Potenza**, see Natale [183].

197] M. **Potse**, R. Hoekema, A. C. Linnenbank, A. SippensGroenewegen, J. Strackee, J. M. T. de Bakker, and C. A. Grimbergen. Conversion of left ventricular endocardial positions from patient-independent co-ordinates into biplane fluoroscopic projections. *Med. & Biol. Eng. & Comput.*, 40(1):41–46, 2002. Cited on pages 10, 24, and 165.

198] M. **Potse** and A. C. Linnenbank. Maplab version 1.44, 2001. Copyrighted software. Cited on page 43.

199] M. **Potse**, A. C. Linnenbank, P. F. H. M. van Dessel, A. SippensGroenewegen, and C. A. Grimbergen. Integration of body surface mapping and biplane fluoroscopy for guidance of catheter ablation of ventricular tachycardia. *Biomed. Techn.*, 46(Erg. b. 2):210–212, 2001. Cited on pages 8, 23, and 97.

200] M. **Potse**, A. C. Linnenbank, A. SippensGroenewegen, and C. A. Grimbergen. Continuous localization of ectopic left ventricular activation sites by means of a two-dimensional representation of body surface QRS integral maps. In *Proc. 18th Annu. Int. Conf. IEEE EMBS*, 1996. Cited on page 112.

201] M. **Potse**, A. C. Linnenbank, A. SippensGroenewegen, and C. A. Grimbergen. Continuous localization of ventricular tachycardia exit sites in patients with previous myocardial infarction. *Biomed. Techn.*, 46(Erg. b. 2):82–84, 2001. Cited on pages 9, 23, and 151.

202] Mark **Potse**. The Webfiles package, version 0.5.39, 1999. Free software. Available from the CTAN archives [41] in the directory `web/webfiles`. Cited on page 186.

203] Mark **Potse**. MWEB (Matlab web) version 2.10, 2000. Free software. Available from the CTAN archives [41] in the directory `web/matlabweb`. Cited on pages 186, 205, 206, and 211.

204] Mark **Potse**, Pascal F. H. M. van Dessel, André C. Linnenbank, Norbert M. van Hemel, Cornelis A. Grimbergen, and Jacques M. T. de Bakker. Properties of unipolar electrograms recorded with a multielectrode basket catheter. *J. Electrocardiol.*, 37:1–10, 2004. Cited on pages 7 and 69.

205] Mark **Potse** and others. Literate programming and scripting languages. *In preparation*. Cited on pages 11 and 205.

206] Mark **Potse**, André C. Linnenbank, Pascal F. H. M. van Dessel, Norbert M. van Hemel, and Cornelis A. Grimbergen. The use of simultaneous multichannel endocardial and surface electrocardiograms for verification of exit site localization using body surface mapping. In *Proc. 20th Annu. Int. Conf. IEEE EMBS*, pages I–75–78, October 1998. Cited on pages 9, 21, 24, 151, 192, and 200.

207] Mark **Potse**, André C. Linnenbank, and Cornelis A. Grimbergen. MAP$_{\text{L}}$AB: An extensible software package for analysis of multichannel ECG recordings. In *Proc. 20th Annu. Int. Conf. IEEE EMBS*, pages I–59–62, October 1998. Cited on pages 24, 33, 42, 62, 71, 104, and 105.

208] Mark **Potse**, André C. Linnenbank, and Cornelis A. Grimbergen. Software design for analysis of multichannel intracardial and body surface electrocardiograms. *Comp. Meth. Progr. Biomed.*, 69:225–236, 2002. Cited on pages 10, 11, 24, 33, 42, 62, 71, 104, 105, 107, 181, and 205.

209] Mark **Potse** and André C. Linnenbank. MAP$_{\text{L}}$AB *Introduction and User's Manual*. University of Amsterdam, AMC, Med. Phys. Dept., Meibergdreef 15, 1105 AZ Amsterdam, The Netherlands. Cited on page 105.

210] Mark **Potse** and André C. Linnenbank. MAP$_{\text{L}}$iB *Sourcebook*. University of Amsterdam, AMC, Med. Phys. Dept., Meibergdreef 15, 1105 AZ Amsterdam, The Netherlands. e-mail: `m.potse@amc.uva.nl`. Cited on page 104.

211] Mark **Potse**, André C. Linnenbank, Heidi A. P. Peeters, and Cornelis A. Grimbergen. Nondipolar content of body surface QRS and QRST integral maps. In *World Congress on Medical Physics and Biomedical Engineering*, September 1997. Cited on pages 7, 85, 91, 92, 189, and 192.

212] Mark **Potse**, André C. Linnenbank, Heidi A. P. Peeters, Arne SippensGroenewegen, and Cornelis A. Grimbergen. Continuous localization of cardiac activation sites using a database of multichannel ECG recordings. *IEEE Trans. Biomed. Eng.*, 47(5):682–689, May 2000. Cited on pages 9, 22, 23, 99, 112, 133, 135, 151, 159, 161, 182, 189, 191, 192, and 200.

213] Mark **Potse**, André C. Linnenbank, Arne SippensGroenewegen, and Cornelis A. Grimbergen. Conversion from left ventricular cylinder coordinates to radiographic projections during ECG-guided catheter ablation of cardiac arrhythmias. In *Chicago 2000 World Congress on Medical Physics and Biomedical Engineering*, July 2000. Cited on pages 22 and 24.

214] Mark **Potse**, André C. Linnenbank, Arne SippensGroenewegen, and Cornelis A. Grimbergen. Influence of chronic myocardial infarction on exit site localization of ventricular tachycardia using paced body surface map databases. In *Chicago 2000 World Congress on Medical Physics and Biomedical Engineering*, July 2000. Cited on pages 9, 23, 24, and 151.

Mark **Potse**, see also De Bakker [12], Derksen [45], Van Dessel [47, 48], Hocini [93], Linnenbank [148, 155], Peeters [193, 194], Van Rijen [220], and Willemsen [275, 276].
M. J. **Pratt**, see Faux [64].

215] William H. **Press**, Saul A. Teukolsky, William T. Vetterling, and Brian P. Flannery. *Numerical Recipes in C; The Art of Scientific Computing*. Cambridge University Press, Cambridge, NY, second edition, 1992. Cited on pages 37, 43, 91, and 132.

Stephen R. **Quint**, see Friesen [70].

216] Lawrence R. **Rabiner**. A tutorial on hidden markov models and selected applications in speech recognition. *Proc. IEEE*, 77(2):257–286, 1989. Cited on page 102.

Charles E. **Rackley**, see Rogers [222].

217] Charulatha **Ramanathan** and Yoram Rudy. Electrocardiographic imaging: I. Effect of torso inhomogeneities on body surface electrocardiographic potentials. *J. Cardiovasc. Electrophysiol.*, 12(2):229–240, 2001. Cited on page 111.

218] Charulatha **Ramanathan** and Yoram Rudy. Electrocardiographic imaging: II. Effect of torso inhomogeneities on noninvasive reconstruction of epicardial potentials, electrograms, and isochrones. *J. Cardiovasc. Electrophysiol.*, 12(2):241–252, 2001. Cited on page 111.

Hemanth **Ramanna**, see Peeters [194] and Wittkampf [279]. Pentti M. **Rautaharju**, see Kornreich [135, 136]. David **Rawling**, see Yanowitz [283].

219] Eric S. **Raymond**, editor. *The New Hacker's Dictionary*. MIT Press, 1991. Cited on page 35.

Bernard C. **Reardon**, see Willems [273]. Judd E. **Reed**, see Dove [50]. Susan L. **Reiser**, see Ideker [114]. Carol Ann **Remme**, see De Groot [81, 82]. H. **Reuter**, see Beeler [19]. Werner C. **Rheinboldt**, see Moe [175].

220] Harold V. M. **van Rijen**, Toon A. B. van Veen, Marjan J. A. van Kempen, Francien J. G. Wilms-Schopman, Mark Potse, Olaf Krueger, Klaus Willecke, Habo J. Jongsma, and Jacques M. T. de Bakker. Impaired conduction in the bundle branches of mouse hearts lacking the gap junction protein connexin40. *Circulation*, 103:1591–1598, 2001. Cited on pages 67 and 192.

Henk J. **Ritsema van Eck**, see Willems [273, 274]. Fernand A. **Roberge**, see Drouhard [51, 52] and Savard [228]. Etienne O. **Robles de Medina**, see Hauer [88, 89], Peeters [190–194], Simmers [233], SippensGroenewegen [240], Willems [273, 274], and Wittkampf [279]. Angel **Rodrigues-Santiago**, see Dubuc [53].

221] Enrique **Rodriguez**, David C. Man, Robert F. Coyne, David J. Callans, Charles D. Gottlieb, and Francis E. Marchlinski. Type I atrial flutter ablation guided by a basket catheter. *J. Cardiovasc. Electrophysiol.*, 9:761–766, July 1998. Cited on pages 19, 69, and 70.

Jack M. **Rogers**, see Bayly [18].

222] William J. **Rogers**, Peter R. Bream, Richard Smith, Steve E. Williams, Charles E. Rackley, and Richard O. Russell, Jr.. A better look at the left ventricle: a comparison of conventional and axial oblique biplane angiography. *Circulation*, 59/60 Supp II:II–262, October 1979. Cited on page 180.

Franz X. **Roithinger**, see SippensGroenewegen [234, 238, 239]. Agostinho C. **Rosa**, see Kemp [124].

223] David S. **Rosenbaum**, Lance E. Jackson, Joseph M. Smith, Hasan Garan, Jeremy N. Ruskin, and Richard J. Cohen. Electrical alternans and vulnerability to ventricular arrhythmias. *The New England Journal of Medicine*, 330(4):235–241, January 1994. Cited on page 108.

224] Frank **Rosenblatt**. *Principles of neurodynamics: perceptrons and the theory of brain mechanisms*. Spartan Books, Washington, DC, 1962. Cited on page 109.

Zeev **Rotstein**, see Eldar [63]. Denis **Roy**, see Dubuc [53]. Paul **Rubel**, see Willems [273]. Yoram **Rudy**, see Amoore [3], Liebman [146], Liu [156], Luo [159], and Ramanathan [217, 218].

225] Rodolphe **Ruffy**, Mir A. Imran, Donald J. Santel, and J. Marcus Wharton. Radiofrequency delivery through a cooled catheter tip allows the creation of larger endomyocardial lesions in the ovine heart. *J. Cardiovasc. Electrophysiol.*, 6(12):1089–1096, 1995. Cited on page 18.

F. Paul **van Rugge**, see Schalij [229]. John A. **Rumberger**, see Dove [50].

226] D. E. **Rumelhart** and D. Zipser. Feature discovery by competitive learning. In D. E. **Rumelhart** and James L. McClelland, editors, *Parallel Distributed Processing: Explorations in the Microstructure of Cognition*, volume 1. MIT Press, 1988. Cited on page 109.

Jeremy N. **Ruskin**, see Rosenbaum [223] and Smith [243]. Richard O. **Russell** Jr., see Rogers [222]. Alan V. **Sahakian**, see Maglaveras [166]. Hidehiko **Saito**, see Hayashi [90].

227] Guy **Salama**, Anthony Kanai, and Igor R. Efimov. Subthreshold stimulation of Purkinje fibers interrupts ventricular tachycardia in intact hearts; experimental study with voltage-sensitive dyes and imaging techniques. *Circ. Res.*, 74(4):604–619, April 1994. Cited on page 67.

Faramarz H. **Samie**, see Morley [177] and Vaidya [267]. Harold **Sandler**, see Dodge [49]. Donald J. **Santel**, see Ruffy [225]. José **Santos Reyes**, see Duro [55]. Iwao **Sato**, see Kamakura [121]. J. Philip **Saul**, see Jenkins [117].

228] Pierre **Savard**, Alexandre Ackaoui, Ramesh M. Gulrajani, Reginald A. Nadeau, Fernand A. Roberge, Robert Guardo, and Bruno Dube. Localization of cardiac ectopic activity in man by a single moving dipole. Comparison of different computation techniques. *J. Electrocardiol.*, 18(3):211–222, 1985. Cited on pages 17 and 150.

Pierre **Savard**, see also Dubuc [54], Molin [176], Nadeau [180], and Xu [280]. Naresh **Saxena**, see Wiener [271]. Leslie A. **Saxon**, see SippensGroenewegen [238].

229] Martin J. **Schalij**, F. Paul van Rugge, Machiel Siezenga, and Enno T. van der Velde. Endocardial activation mapping of ventricular tachycardia in patients: First application of a 32-site bipolar mapping electrode catheter. *Circulation*, 98:2168–2179, November 1998. Cited on pages 19, 69, and 70.

Melvin M. **Scheinman**, see Eldar [63] and SippensGroenewegen [238]. D. B. **Scholtz**, see SippensGroenewegen [234]. L. **Schoo**, see Van der Tweel [261]. Bas A. **Schoonderwoerd**, see Peeters [191, 192]. Heike **Schuster**, see Gerhardt [72]. Peter J. **Schwartz**, see De Ambroggi [44]. Randal L. **Schwarz**, see Wall [269]. Joris **Segers**, see Kornreich [135]. Gerald A. **Serwer**, see Spach [246]. Dipen **Shah**, see Hocini [93]. Syed Ismail **Shah**, see Shusterman [231]. M. **Shenasa**, see Nadeau [180]. Kiyohiro **Shikano**, see Waibel [268]. Katsuro **Shimomura**, see Kamakura [121].

230] Shlomo **Shpun**, Lior Gepstein, Gal Hayam, and Shlomo A. Ben-Haim. Guidance of radiofrequency endocardial ablation with real-time three-dimensional magnetic navigation system. *Circulation*, 96:2016–2021, September 1997. Cited on pages 149, 166, 179, 197, and 202.

231] Vladimir **Shusterman**, Syed Ismail Shah, Anna Beigel, and Kelley P. Anderson. Enhancing the precision of ecg baseline correction: Selective filtering and removal of residual error. *Comp. & Biom. Res.*, 33:144–160, April 2000. Cited on page 99.

Machiel **Siezenga**, see Schalij [229].

232] R. **Silipo**, M. Gori, A. Taddei, M. Varanini, and C. Marchesi. Classification of arrhythmic events in ambulatory electrocardiogram, using artificial neural networks. *Comp. & Biom. Res.*, 28(4):305–318, August 1995. Cited on page 99.

P. **Siltanen**, see Mäkijärvi [169].

233] Timothy A. **Simmers**, Fred H. M. Wittkampf, Richard N. W. Hauer, and Etienne O. Robles de Medina. In vivo ventricular lesion growth in radiofrequency catheter ablation. *PACE*, 17:523–531, 1994. Cited on pages 18 and 177.

Timothy A. **Simmers**, see also De Bakker [13] and Peeters [191]. Edward V. **Simpson**, see Bollacker [23] and Ideker [114]. M. B. **Simson**, see Breithardt [25].

234] A. **SippensGroenewegen**, F. X. Roithinger, D. B. Scholtz, P. R. Steiner, and M. D. Lesh. Body surface mapping during left atrial pace mapping: Evaluation of spatial differences in P-wave configuration. *J. Am. Coll. Cardiol.*, 31 suppl. A:46A, 1998. (abstract). Cited on page 111.

235] A. **SippensGroenewegen**, H. Spekhorst, N. M. van Hemel, J. H. Kingma, R. N. W. Hauer, J. M. T. de Bakker, C. A. Grimbergen, M. J. Janse, and A. J. Dunning. Value of body surface mapping in localizing the site of origin of ventricular tachycardia in patients with previous myocardial infarction. *J. Am. Coll. Cardiol.*, 24(7):1708–1724, 1994. Cited on pages 18, 21, 112, and 135.

236] A. **SippensGroenewegen**, H. Spekhorst, N. M. van Hemel, J. H. Kingma, R. N. W. Hauer, M. J. Janse, and A. J. Dunning. Body surface mapping of ectopic left and right ventricular activation: QRS spectrum in patients without structural heart disease. *Circulation*, 82:879–896, 1990. Cited on pages 18, 21, 22, 88, 99, 105, 111–119, 121–123, 127, 129, 132, 135–140, 142–144, 146, 147, 149, 151, 156, 158, 169, 171, 189, 191, and 201.

237] A. **SippensGroenewegen**, H. Spekhorst, N. M. van Hemel, J. H. Kingma, R. N. W. Hauer, M. J. Janse, and A. J. Dunning. Body surface mapping of ectopic left ventricular activation: QRS spectrum in patients with prior myocardial infarction. *Circ. Res.*, 71(6):1361–1378, 1992. Cited on pages 18, 21, 99, 111, 112, 129, 132, 135, 149, 151, 156, 158–160, 163, and 201.

238] Arne **SippensGroenewegen**, Michael D. Lesh, Franz X. Roithinger, Willard S. Ellis, Paul R. Steiner, Leslie A. Saxon, Randall J. Lee, and Melvin M. Scheinman. Body surface mapping of counterclockwise and clockwise typical atrial flutter: A comparative analysis with endocardial activation sequence mapping. *J. Am. Coll. Cardiol.*, 35(5):1276–1287, 2000. Cited on page 111.

239] Arne **SippensGroenewegen**, Michael D. Mlynash, Peter G. Guerra, Franz X. Roithinger, Bernhard Tilg, and Michael D. Lesh. Atlas of paced body surface P wave integral maps for localization of focal left atrial arrhythmias. *PACE*, 23 part II:556, 2000. (abstract). Cited on pages 18 and 189.

240] Arne **SippensGroenewegen**, Heidi A. P. Peeters, Emile R. Jessurun, André C. Linnenbank, Etienne O. Robles de Medina, Michael D. Lesh, and Norbert M. van Hemel. Body surface mapping during pacing at multiple sites in the human atrium: P-wave morphology of ectopic right atrial activation. *Circulation*, 97:369–380, February 1998. Cited on pages 18, 111, 149, 189, and 192.

241] Arne **SippensGroenewegen**, Hans Spekhorst, Richard N. W. Hauer, Norbert M. van Hemel, Petro Broekhuijsen, and Arend J. Dunning. A radiotransparent carbon electrode array for body surface mapping during cardiac catheterization. In *9th Annu. Conf. IEEE EMBS*, pages 178–181, November 1987. Cited on pages 21 and 139.

242] Arne **SippensGroenewegen**, Hans Spekhorst, Norbert M. van Hemel, J. Herre Kingma, Richard N. W. Hauer, Jacques M. T. de Bakker, Cornelis A. Grimbergen, Michiel J. Janse, and Arend J. Dunning. Localization of the site of origin of postinfarction ventricular tachycardia by endocardial pace mapping: Body surface mapping compared with the 12-lead electrocardiogram. *Circulation*, 88(5):2290–2306, 1993. Cited on pages 18, 112, and 135.

Arne **SippensGroenewegen**, see also Dambrink [42], Van Dessel [47], Kemmelings [123], Latour [139], Linnenbank [151–153], Peeters [190–194], Potse [197, 199–201, 212–214], and Spekhorst [252]. Emmanuel **Skordalakis**, see Trahanias [259]. B. H. **Smaill**, see Nielsen [184]. C. **Smallpeice**, see Holt [99]. Creig R. **Smith**, see Lux [162].

243] Joseph M. **Smith**, Edward A. Clancy, Robert Valeri, Jeremy N. Ruskin, and Richard J. Cohen. Electrical alternans and cardiac electrical instability. *Circulation*, 77(1):110–121, 1988. Cited on page 108.

Joseph M. **Smith**, see also Rosenbaum [223]. Michael F. **Smith**, see Eldar [63] and Greenspon [78]. Richard **Smith**, see Rogers [222].

244] William M. **Smith** and Roger C. Barr. The forward and inverse problems: What are they, why are they important, and where do we stand? *J. Cardiovasc. Electrophysiol.*, 12(2):253–255, 2001. Cited on page 111.

William M. **Smith**, see also Bayly [18], Bollacker [23], and Ideker [114]. Jeroen G. **Snel**, see Linnenbank [155]. Joachim R. **Sommer**, see Spach [249]. I. **Sotohata**, see Yamada [282].

245] Madison S. **Spach** and Roger C. Barr. Analysis of ventricular activation and repolarization from intramural and epicardial potential distributions for ectopic beats in the intact dog. *Circ. Res.*, 37:830–843, 1975. Cited on page 151.

246] Madison S. **Spach**, Roger C. Barr, Gerald A. Serwer, J. Mailen Kootsey, and Edward A. Johnson. Extracellular potentials related to intracellular action potentials in the dog purkinje system. *Circ. Res.*, 30(5):505–519, May 1972. Cited on pages 50 and 56.

247] Madison S. **Spach** and Paul C. Dolber. Relating extracellular potentials and their derivatives to anisotropic propagation at a microscopic level in human cardiac muscle. *Circ. Res.*, 58:356–371, 1986. Cited on page 46.

248] Madison S. **Spach** and J. Mailen Kootsey. Relating the sodium current and conductance to the shape of transmembrane and extracellular potentials by simulation: Effects of propagation boundaries. *IEEE Trans. Biomed. Eng.*, 32:743–755, October 1985. Cited on pages 50 and 70.

249] Madison S. **Spach**, Walter T. Miller, III, Paul C. Dolber, J. Mailen Kootsey, Joachim R. Sommer, and Charles E. Mosher, Jr.. The functional role of structural complexities in the propagation of depolarization in the atrium of the dog. *Circ. Res.*, 50:175–191, 1982. Cited on pages 47 and 50.

250] Madison S. **Spach**, Walter T. Miller, III, Elizabeth Miller-Jones, Robert B. Warren, and Roger C. Barr. Extracellular potentials related to intracellular action potentials during impulse conduction in anisotropic canine cardiac muscle. *Circ. Res.*, 45:188–204, 1979. Cited on page 50.

Madison S. **Spach**, see also Barr [15–17] and Geselowitz [73].

251] H. **Spekhorst**. *Body surface mapping of induced regional transmural ischemia*. PhD thesis, University of Amsterdam, 1990. Cited on page 18.

252] H. **Spekhorst**, A. SippensGroenewegen, G. K. David, A. C. MettingVanRijn, and P. Broekhuijsen. Radiotransparent carbon electrode for ECG recordings in the catheterization laboratory. *IEEE Trans. Biomed. Eng.*, 35:402–406, 1988. Cited on pages 16 and 17.

Hans **Spekhorst**, see also SippensGroenewegen [235–237, 241, 242]. Scott R. **Spielman**, see Josephson [119]. Ralph W. **Stacy**, see Cox [39].

253] Telemachos **Stamkopoulos**, Konstantinos Diamantaras, Nicos Maglaveras, and Michael Strintzis. ECG analysis using nonlinear PCA neural networks for ischemia detection. *IEEE Trans. Signal Processing*, 46(11):3058–3067, November 1998. Cited on page 110.

Telemachos **Stamkopoulos**, see also Maglaveras [164, 167, 168]. William **Stanford**, see Dove [50]. G. **Steinbeck**, see Breithardt [25]. Paul R. **Steiner**, see SippensGroenewegen [234, 238]. Richard M. **Stern**, see Coast [36]. William **Stevenson**, see Calkins [29]. D. **Stilli**, see Hoekema [98]. J. **Strackee**, see Van Oosterom [188] and Potse [197]. Michael **Strintzis**, see Maglaveras [164, 167, 168] and Stamkopoulos [253]. G. **Stroink**, see Hren [102, 103]. J. **Sugenoya**, see Yamada [282]. S. **Sugiyama**, see Yamada [282].

254] G. **Sun**, C. W. Thomas, and J. Liebman. QRS onset and offset detection accuracy improvement by additional spatial information in body surface potential maps. *J. Electrocardiol.*, pages 293–300, 1990. Cited on pages 105 and 107.

Ying **Sun**, see Suppappola [255].

255] Seth **Suppappola** and Ying Sun. Nonlinear transforms of ECG signals for digital QRS detection: A quantitative analysis. *IEEE Trans. Biomed. Eng.*, 4:397–400, April 1994. Cited on pages 101, 103, and 107.

David K. **Swanson**, see Eldar [63].

256] Bruno **Taccardi**. Distribution of heart potentials on the thoracic surface of normal human subjects. *Circ. Res.*, 12:341–352, 1963. Cited on pages 25 and 32.

Bruno **Taccardi**, see also Kornreich [135, 136] and Liu [156]. A. **Taddei**, see Silipo [232]. Changfeng **Tai**, see Li [145]. Kazuhide **Takami**, see Hayashi [90]. Mario **Talajic**, see Dubuc [53]. Jan L. **Talmon**, see Willems [273]. Jean-Claude **Tardif**, see Dubuc [53]. Sara **Tasseron**, see De Bakker [6, 10, 12], Derksen [45], and Kawara [122]. Saul A. **Teukolsky**, see Press [215]. Bernard **Thibault**, see Dubuc [53]. C. W. **Thomas**, see Liebman [146] and Sun [254].

257] L. **Thoraval**, G. Carrault, and J. J. Bellanger. Heart signal recognition by hidden Markov models: The ECG case. *Meth. Inf. Med.*, 33(1):10–14, 1994. Cited on page 102.

Bernhard **Tilg**, see SippensGroenewegen [239].

258] Bryan S. **Todd** and David C. Andrews. The identification of peaks in physiological signals. *Comp. & Biom. Res.*, 32:322–335, 1999. Cited on page 103.

L. **Toivonen**, see Mäkijärvi [169]. Gery **Tomassoni**, see Natale [183]. Willis J. **Tompkins**, see Afonso [2], Hamilton [87], Hu [105], Pan [189], and Xue [281]. J. **Toyama**, see Yamada [282]. H. **Toyoshima**, see Yamada [282]. Takeshi **Toyoshima**, see Minami [174].

259] Panagiotis **Trahanias** and Emmanuel Skordalakis. Syntactic pattern recognition of the ECG. *IEEE Trans. Patt. Analysis & Mach. Intell.*, 12(7):648–657, July 1990. Cited on pages 100–102.

Gaétan **Tremblay**, see Dubuc [54] and Molin [176]. Janet **Trusso**, see Calkins [29]. R. W. **Tsien**, see McAllister [170]. Ingeborg **van der Tweel**, see Hauer [88].

260] L. H. **van der Tweel**. Van hoofd en hart. Inaugural lecture, University of Amsterdam, December 1963. (in Dutch). Cited on page 13.

261] L. H. **van der Tweel**, L. Schoo, R. M. Heethaar, and F. L. Meijler. Elektrisch demonstratiemodel van de prikkelgeleiding van het hart [electronic heart model for teaching purposes]. *Ned. T. Geneesk.*, 118(24):908–913, 1974. Cited on pages 48 and 49.

L. H. **van der Tweel**, see also Durrer [57–59]. John J. **Tyson**, see Gerhardt [72].

262] Jayaram **Udupa** and Ivaturi S. N. Murthy. Syntactic approach to ECG rhythm analysis. *IEEE Trans. Biomed. Eng.*, 27(7):370–375, 1980. Cited on pages 101 and 102.

Haruyoshi **Uematsu**, see Hayashi [90].

263] G. J. H. **Uijen**. *The information content of the electrocardiogram*. PhD thesis, Katholieke Universiteit Nijmegen, Geert Grooteplein 21, Nijmegen, The Netherlands, december 1991. Cited on page 88.

264] G. J. H. **Uijen** and A. van Oosterom. On the detection of the number of signals in multilead ECGs. *Meth. Inf. Med.*, 31:247–255, 1992. Cited on page 15.

265] G. J. H. **Uijen** and A. van Oosterom. The performance of information-theoretic criteria in detecting the number of independent signals in multilead ECGs. *Meth. Inf. Med.*, 31:256–262, 1992. Cited on page 15.

266] G. J. H. **Uijen** and A. van Oosterom. The number of signals in multilead ECGs in individuals. *J. Electrocardiol.*, 26(2):107–116, 1993. Cited on page 15.

G. J. H. **Uijen**, see also Hoekema [95–98]. José L. **Urrusti**, see Hu [105].

267] Dhananjay **Vaidya**, Gregory E. Morley, Faramarz H. Samie, and José Jalife. Reentry and fibrillation in the mouse heart; a challenge to the critical mass hypothesis. *Circ. Res.*, 85(2):174–181, July 1999. Cited on pages 26, 49, 50, and 67.

Dhananjay **Vaidya**, see also Morley [177]. Robert **Valeri**, see Smith [243]. M. **Varanini**, see Silipo [232]. Alpo **Värri**, see Kemp [124]. Joseph A. **Vassallo**, see Cassidy [32]. Toon A. B. **van Veen**, see Van Rijen [220]. Enno T. **van der Velde**, see Schalij [229]. Marieke W. **Veldkamp**, see Wilde [272]. Zvi **Vered**, see Eldar [63]. Freddy E. E. **Vermeulen**, see De Bakker [9]. Jessica T. **Vermeulen**, see De Bakker [10] and McGuire [171]. William T. **Vetterling**, see Press [215]. Max A. **Viergever**, see Frangi [68]. G. M. **Vincent**, see Lux [160]. Michael J. **Vonesh**, see Dove [50]. M. **Wada**, see Yamada [282].

268] Alexander **Waibel**, Toshiyuki Hanazawa, Geoffrey Hinton, Kiyohiro Shikano, and Kevin J. Lang. Phoneme recognition using time-delay neural networks. *IEEE Trans. Acoust. & Signal Proc.*, 37(3):328–339, March 1989. Cited on pages 108 and 109.

Gregory P. **Walcott**, see Bollacker [23]. A. L. **Waldo**, see Liebman [146]. Richard **Walker**, see Anderson [4, 5].

269] Larry **Wall**, Tom Christiansen, and Randal L. Schwarz. *Programming Perl*. O' Reilly, second edition, 1996. Cited on page 186.

Edward P. **Walsh**, see Jenkins [117]. Xanzhung **Wang**, see Nakagawa [182]. Robert B. **Warren**, see Spach [250]. Shinji **Watabe**, see Hayashi [90]. Bruce D. **Waxman**, see Cox [39].

270] Harvey L. **Waxman** and Mark E. Josephson. Ventricular activation during ventricular endocardial pacing: I. Electrocardiographic patterns related to the site of pacing. *Am. J. Cardiol.*, 50:1–10, 1982. Cited on pages 151 and 201.

Harvey L. **Waxman**, see also Josephson [119]. Eric F. D. **Wever**, see Van Dessel [47], Peeters [190–194], and Wittkampf [279]. Lewis **Wexler**, see Burbank [28]. J. Marcus **Wharton**, see Calkins [29] and Ruffy [225]. James G. **Whayne**, see Eldar [63].

271] Isaac **Wiener**, Joseph Yamashita, Naresh Saxena, and Thomas Comer. Intramural activation of the human ventricle: Findings in normal and abnormal myocardial segments in patients with coronary artery disease. *Am. Heart. J.*, 111(2):258–261, 1986. Cited on page 151.

David **Wilber**, see Calkins [29].

272] Arthur A. M. **Wilde** and Marieke W. Veldkamp. Ion channels, the QT interval, and arrhythmias. *PACE*, 20:2048–2051, 1997. (Review). Cited on page 46.

Arthur A. M. **Wilde**, see also De Bakker [6, 11], Kléber [126], and Wittkampf [279]. Klaus **Willecke**, see Van Rijen [220].

273] Jos L. **Willems**, Pierre Arnaud, Jan H. van Bemmel, Peter J. Bourdillon, Christian Brohet, Sergio Dalla Volta, Jens Damgaard Andersen, Rosanna Degani, Bernard Denis, Michel Demeester, Joachim Dudeck, Frits M. A. Harms, Peter W. Macfarlane, Gianfranco Mazzocca, Jürgen Meyer, Jörg Michaelis, Jos Pardaens, Siegfried Pöppl, Bernard C. Reardon, Henk J. Ritsema van Eck, Etienne O. Robles de Medina, Paul Rubel, Jan L. Talmon, and Christoph Zywietz. Assessment of the performance of electrocardiographic computer programs with the use of a reference data base. *Circulation*, 71(3):523–534, 1985. Cited on pages 101–103, and 107.

274] Jos L. **Willems**, Pierre Arnaud, Jan H. van Bemmel, Peter J. Bourdillon, Rosanna Degani, Bernard Denis, Frits M. A. Harms, Peter W. Macfarlane, Gianfranco Mazzocca, Jürgen Meyer, Henk J. Ritsema van Eck, Etienne O. Robles de Medina, and Christoph Zywietz. Establishment of a reference library for evaluating computer ECG measurement programs. *Comp. & Biom. Res.*, 18:439–457, 1985. Cited on page 101.

275] Jeroen R. **Willemsen**, André C. Linnenbank, Pascal F. H. M. van Dessel, Mark Potse, Cornelis A. Grimbergen, and Norbert M. van Hemel. A new method for detecting late potentials using multichannel ECGs. In *Proc. First Joint BMES/EMBS Conf.*, October 1999. Cited on pages 20 and 192.

276] Jeroen R. **Willemsen**, André C. Linnenbank, Mark Potse, and Cornelis A. Grimbergen. Signal averaging of non-stationary noise. In *Proc. First Joint BMES/EMBS Conf.*, October 1999.

Steve E. **Williams**, see Rogers [222]. Francien J. G. **Wilms-Schopman**, see Coronel [37], De Groot [81, 82], Janse [116], Kléber [126], and Van Rijen [220].

277] Francis X. **Witkowski**, Katherine M. Kavanagh, Patricia A. Penkoske, and Robert Plonsey. In vivo estimation of cardiac transmembrane current. *Circulation*, 72:424–439, 1993. Cited on pages 26, 49, 54, 57, and 83.

278] Francis X. **Witkowski**, Robert Plonsey, Patricia A. Penkoske, and Katherine M. Kavanagh. Significance of inwardly directed transmembrane current in determination of local myocardial electrical activation during ventricular fibrillation. *Circ. Res.*, 74:507–524, 1994. Cited on pages 54, 57, and 58.

Francis X. **Witkowski**, see also Leon [143].

279] Fred H. M. **Wittkampf**, Eric F. D. Wever, Richard Derksen, Arthur A. M. Wilde, Hemanth Ramanna, Richard N. W. Hauer, and Etienne O. Robles de Medina. LocaLisa: New technique for real-time 3-dimensional localization of regular intracardiac electrodes. *Circulation*, 99:1312–1317, March 1999. Cited on pages 149, 166, 179, 197, and 202.

Fred H. M. **Wittkampf**, see also Peeters [190, 191] and Simmers [233]. Patrick D. **Wolf**, see Ideker [114]. R. F. **Wyatt**, see Lux [160,161]. Roland F. **Wyatt**, see Lux [162].

280] Zhenyao **Xu**, Ramesh M. Gulrajani, Franck Molin, Michel Lorange, Bruno Dubé, Pierre Savard, and Réginald A. Nadeau. A computer heart model incorporating anisotropic propagation: III. Simulation of ectopic beats. *J. Electrocardiol.*, 29(2):73–90, April 1996. Cited on pages 149, 161, and 202.

281] Qiuzhen **Xue**, Yu Hen Hu, and Willis J. Tompkins. Neural-network-based adaptive matched filtering for QRS detection. *IEEE Trans. Biomed. Eng.*, 39(4):317–329, April 1992. Cited on page 104.

Seitaro **Yabe**, see Hayashi [90].

282] K. **Yamada**, J. Toyama, M. Wada, S. Sugiyama, J. Sugenoya, H. Toyoshima, Y. Mizuno, I. Sotohata, T. Kobayashi, and M. Okajima. Body surface isopotential mapping in Wolff-Parkinson-White syndrome: noninvasive method to determine the localization of the accessory atrioventricular pathway. *Am. Heart. J*, 90:721–734, 1975. Cited on page 18.

William S. **Yamanashi**, see Nakagawa [182]. Joseph **Yamashita**, see Wiener [271].

283] Frank **Yanowitz**, Plato Kinias, David Rawling, and Harry Fozzard. Accuracy of a continuous real-time ECG dysrhythmia monitoring system. *Circulation*, 50:65–72, July 1974. Cited on pages 99–102.

A. K. **Yates**, see Holt [99]. Stanford L. **Yates**, see Friesen [70]. J. A. **Zeno**, see Liebman [146]. Chongxun **Zheng**, see Li [145].

284] Henry A. **Zimmerman** and Herman K. Hellerstein. Cavity potentials of the human ventricles. *Circulation*, 3:95–104, January 1951. Cited on page 81.

Douglas D. **Zipes**, see De Bakker [13]. D. **Zipser**, see Rumelhart [226]. Michel T. W. **de Zwart**, see Hauer [88, 89].

285] Chr. **Zywietz**. Zum Informationsgehalt von EKG-Ableitungssystemen [on the information content of ECG lead systems]. *Biomediz. Techn.*, 23:16–22, 1978. Cited on page 15.

Christoph **Zywietz**, see also Willems [273, 274].

Samenvatting

Inleiding

De samentrekking van spieren wordt in gang gezet door zeer kleine elektrische stroompjes. Dit verschijnsel, dat al in de zeventiende eeuw bekend was, werd aan het einde van de achttiende eeuw nauwkeurig onderzocht door de arts Galvani en de fysicus Volta. Hun werk was cruciaal voor de ontwikkeling van de fysiologie en tegelijk voor die van de fysica: het is te danken aan Volta dat we het begrip "elektrische stroom" kennen en de ontdekkingen van Galvani kunnen begrijpen.

De stroom die wordt gegenereerd door één enkele spiercel, is zo klein dat deze slechts met zeer gevoelige apparatuur kan worden gemeten. Alleen wanneer grote aantallen cellen tegelijk *geactiveerd* worden, ontstaat een stroom die relatief eenvoudig gemeten kan worden aan het lichaamsoppervlak. Omdat het hart gecoördineerd moet samentrekken om zijn taak te kunnen verrichten, treedt bij elke hartslag een dergelijke meetbare stroom op. Daardoor kon al in 1902 door de nederlandse arts Einthoven het eerste betrouwbare *elektrocardiogram* (ECG) geregistreerd worden. Einthoven en zijn tijdgenoten toonden vervolgens aan dat het ECG van grote waarde is voor de diagnose van hartziekten. Met name hartritmestoornissen, afwijkingen in de elektrische activatie van het hart, kunnen met behulp van het ECG goed worden vastgesteld.

Behalve aan het lichaamsoppervlak, worden ook in het hart zelf elektrische signalen gemeten. Men kan met behulp van endocardiale catheters—dunne slangetjes die door een kleine snee in de lies of schouder, via een ader of slagader worden opgevoerd naar het hart—aan de binnenkant van het hart meten. Ook kan men direct aan de buitenkant en binnenkant van het hart meten tijdens open-hartoperaties. Tenslotte wordt voor wetenschappelijke doeleinden ook gemeten aan geïsoleerde harten, en zelfs aan kleine stukjes hartweefsel.

Veelkanaals elektrocardiografie

Voor alle vormen van meting van de elektrische hartactiviteit, aan het lichaamsoppervlak, in het hart, of op het hart, geldt dat soms gemeten wordt met een groot aantal meetelektroden. Deze elektroden worden vaak zo aangebracht dat ze een zeker oppervlak bestrijken. Deze methode heet *veelkanaals elektrocardiografie* of elektrocardiografische *mapping*, en wordt zowel in het hart als aan het lichaamsoppervlak toegepast. In het laatste geval spreekt men van *body surface mapping*.

Het is pas sinds enkele jaren mogelijk om met een catheter veelkanaals elektrogrammen te meten in het hart van een patiënt. Met de "Constellation Basket" catheter, die in gebruik is in het St.-Antoniusziekenhuis in Nieuwegein, kan met 64 elektroden tegelijk worden gemeten. Uniek in de wereld is de mogelijkheid die dit ziekenhuis heeft om tegelijk met deze endocardiale signalen een 64-kanaals body surface map (BSM) op te nemen. Een dergelijke simultane meting wordt *integrated mapping* genoemd.

Dit proefschrift behandelt de analyse van veelkanaals ECGs gemeten in het hart, op het hart en aan het lichaamsoppervlak, en met name de analyse van integrated mapping gegevens. Het is één van de eerste publicaties waarin het gebruik van *integrated mapping* data wordt beschreven: in hoofdstuk 4 worden eigenschappen van signalen van de Constellation Basket catheter onderzocht. Uit vergelijking met signalen verkregen tijdens openhartoperaties blijkt dat de aanwezigheid of afwezigheid van bloed in de hartkamer tijdens catheter-mapping de analyse van basketsignalen moeilijker maakt, maar dat desondanks de signalen goed interpreteerbaar zijn. De verschillen tussen beide situaties kunnen grotendeels verklaard worden door de afwezigheid van bloed tijdens open-hartoperaties. De verschillen worden echter niet volledig begrepen. Met behulp van computersimulaties zou een goede verklaring gevonden kunnen worden, en zouden we een beter begrip kunnen verkrijgen van endocardiale elektrogrammen.

Programmatuur

Het grote aantal signalen waaruit een veelkanaals elektrocardiogram bestaat, maakt het gebruik van computers noodzakelijk voor de verwerking van de meetgegevens. De analysemethoden voor deze gegevens verschillen nogal van die voor gewone ECGs. De ontwikkeling van deze methoden is nog in volle gang. Eén van de onderwerpen van dit proefschrift is dan ook de ontwikkeling van een software-pakket voor de verwerking van veelkanaals ECGs. Dit pakket, MAP$_{\text{L}}$AB, dat wordt beschreven in hoofdstuk 10, is bijzonder omdat het geschikt is gemaakt voor de analyse van bijna alle soorten van veelkanaals ECG metingen. Dit maakt het mogelijk

dat de software wordt gebruikt door veel verschillende onderzoeksgroepen, zodat minder tijd besteed hoeft te worden aan het ontwikkelen van software voor allerlei verschillende onderzoeksdoeleinden.

Een andere bijzondere eigenschap van dit softwarepakket is dat het geheel geschreven is met behulp van de "literate programming"-techniek (Appendix A) [129, 130]. Met deze techniek schrijft men programma en documentatie in één enkele computerfile. Bovendien wordt de volgorde van presentatie van het programma niet gedicteerd door de eisen van de programmeertaal. Daardoor kan een programma veel beter beschreven worden dan met traditionele software-documentatie. De software die nodig is voor literate programming in de MATLAB programmeertaal, waarin MAPLAB is geschreven, is in het kader van dit project ontwikkeld, en later vrij beschikbaar gemaakt [203].

Het MAPLAB pakket heeft een grote rol gespeeld bij de analyse van de integrated-mappinggegevens die in het St.-Antoniusziekenhuis verkregen zijn, en wordt wereldwijd gebruikt in meer dan tien onderzoekscentra. Verwacht wordt dat het gebruik van dit pakket nog zal toenemen, en dat in verband daarmee voortdurende ontwikkeling gewenst is.

Eén van de algoritmes die in MAPLAB worden gebruikt, is beschreven in hoofdstuk 3. Dit betreft een verbeterde methode voor het automatisch tekenen van isochroon-kaarten (figuur 3.7 en 3.8). Dit is een weergavetechniek die bij de analyse van endocardiale maps gebruikt wordt om een activatiepatroon weer te geven. Isochronen zijn lijnen die punten met gelijke activatietijd verbinden. Ze zijn te vergelijken met hoogtelijnen op een landkaart. Het bijzondere van het gepresenteerde algoritme is onder meer dat het rekening houdt met lijnen van "block", het equivalent van een afgrond of verticale wand in een landkaart.

Localisatie van ventriculaire ritmestoornissen

Een tweede belangrijk aandachtspunt van dit proefschrift is het localiseren van hartritmestoornissen die ontstaan in de linkerkamer (ventrikel) van het hart. Het gaat hierbij met name om de localisatie van ventriculaire tachycardie (VT), een situatie waarin het hart met een ritme van 200 tot 300 slagen per minuut veel sneller klopt dan normaal. Dit leidt tot een verminderde pompfunctie van het hart en kan dodelijk zijn door het ontaarden in ventrikelfibrilleren. VT kan optreden in een normaal gezond hart, bijvoorbeeld als gevolg van een infectie. Dergelijke "idiopathische" VT's zijn echter zeldzaam. Meer voorkomend zijn VT's die optreden na een hartinfarct. Deze zijn het gevolg van dunne bundels overlevende spiercellen in een infarctlitteken.

VT is in principe te genezen door met een endocardiale catheter op de juiste plaats een stukje spierweefsel dat voor het onderhouden van de ritmestoornis essentieel is, uit te schakelen. Om deze plaats te vinden, kan men eerst met de catheter op zoek gaan naar de plaats waar de te vroege activatie van de hartspier duidelijk tevoorschijn komt. Deze plaats, de "exit-site", kan worden voorspeld met behulp van het ECG. In de afgelopen jaren is hiervoor de "drie-fasenmapping"-methode ontwikkeld [194]. De eerste fase bestaat uit het voorspellen van de exit-site met behulp van een BSM. De catheter wordt dan naar deze plek geleid. In de tweede fase wordt doormiddel van "pace-mapping" de catheter dichter bij de exit-site gebracht. Pace-mapping is het elektrisch prikkelen van de hartspier op een bepaalde plaats, waardoor een extra slag ontstaat met een ECG dat hetzelfde is als dat van een VT-slag met een exit-site op dezelfde plaats. Door herhaaldelijk de nieuwe BSM te vergelijken met die van de VT zelf en de catheter te verplaatsen, totdat een BSM gevonden wordt die goed genoeg lijkt op die van de VT, kan men de catheter zeer nauwkeurig naar de exit-site brengen. In de derde fase van de procedure wordt vanuit de exit-site gezocht naar een geschikte plaats om weefsel onschadelijk te maken. Deze laatste stap valt buiten het bestek van dit proefschrift.

Voor VT-localisatie in de eerste twee fasen van de procedure, wordt gebruik gemaakt van signalen die gemiddeld zijn over het QRS interval van het ECG. Het patroon van de resulterende "QRS integraalmap" (QRSI) (figuur 1.2) is zeer specifiek voor de exit-site (hoofdstuk 6). Met behulp van een "atlas" of "database" van QRSI's van geïnduceerde slagen waarvan de exit-sites goed bekend zijn, kan uit het patroon afgeleid worden waar de exit-site zich bevindt [236]. Een nadeel van deze methode is dat de atlas een beperkt aantal exit-site segmenten kent; 25 voor de linkerventrikel.

In hoofdstuk 6, 7, en 8 is een methode gepresenteerd voor *continue localisatie*: berekening van precieze coördinaten van de exit-site. Deze methode is gebaseerd op gegevens uit de atlas. Met behulp van deze methode kan zeer nauwkeurig catheter-verplaatsingsadvies worden gegeven gedurende de tweede fase van de procedure.

Tot nu toe worden de localisatieresultaten aan de behandelende arts gepresenteerd in een schematisch diagram van de ventrikel. Een verbeterde presentatiemethode is beschreven in hoofdstuk 9. Met deze methode kan het catheter-verplaatsingsadvies direct worden weergegeven op de beeldschermen van de röntgeninstallatie die wordt gebruikt om de catheterpositie te observeren (figuur 1.4b).

Het is te verwachten dat met deze methoden tezamen de drie-fasenmapping procedure efficiënter kan worden gemaakt, waardoor deze korter en dus minder belastend wordt voor de patiënt, en wellicht ook kan worden gebruikt voor de behandeling van 'moeilijkere' VT's.

Dankwoord

Zeer veel dank ben ik verschuldigd aan mijn co-promotor André Linnenbank, die voor, gedurende en na mijn promotie-onderzoek zowel mijn begeleider als, zonodig, mijn linker- en rechterhand is geweest. Zonder zijn hulp zou dit werk, en dat van vele collega's, grotendeels onmogelijk zijn geweest. Ook hartelijk dank aan Marijke, voor het lenen.

Mijn beide promotoren, Kees Grimbergen en Jacques de Bakker, dank ik voor het feit dat ze altijd bereikbaar waren voor een dringende vraag of om nog snel even een manuscript te lezen, voor de vrijheid die ze me geboden hebben bij het richting geven aan mijn werk en voor hun wijsheid die me geholpen heeft om een paar jaar werk om te zetten in een proefschrift.

Zonder het baanbrekend werk van co-promotor Arne Sippens Groenewegen had mijn onderzoek vanzelfsprekend niet bestaan. Ook hem dank ik hartelijk voor zijn steun en voor het onvermoeibaar corrigeren van vele manuscripten. I thank Arne and his co-founders of Cardiac Focus Inc.: Terry Ransbury and Michael Mlynash, for the inspiring cooperation on the new generation of body surface mapping equipment.

Zeer veel dank aan Jan en Annelies Strackee, samen het wiskundig en taalkundig geweten van de afdeling Medische Fysica, voor alles wat er wel deugt aan dit proefschrift.

Rudi Hoekema, prof. Van Oosterom en hun collega's dank ik hartelijk voor de samenwerking die uitmondde in hoofdstuk 9 van dit proefschrift, en voor vele nuttige discussies.

Het was een genoegen om samen te werken met onze afstudeerders: Auke Latour, Vincent Verdult en Jeroen Willemsen.

Samenwerking met artsen en biomedische onderzoekers is van groot belang voor medisch-technisch onderzoek als hier beschreven. Hartelijk dank daarom aan Doctor Pascal van Dessel en zijn promotor prof. Van Hemel, Heidi Peeters, Hemanth Ramanna, prof. Hauer, Fred Wittkampf, Jan-Henk Dambrink, Sylvia Muilwijk, Chantal Conrath, Harold van Rijen, Peter Loh,

Francien Wilms, Joris de Groot, Sara Tasseron, Richard Derksen, Mélèze Hocini en Emile Jessurun.

Ook zonder spullen gaat het niet. Dank daarom aan de vennoten van BioSemi: Coen Metting van Rijn, Robert Honsbeek en Ton Kuiper, voor het bouwen van hun uitstekende acquisitie-systemen.

Bij het verkennen van de oude software en file-formaten heb ik veel hulp gehad van Jaap van Hulst en Frans van Capelle; hartelijk dank daarvoor.

Jeroen Haak dank ik voor zijn kwaliteiten als UNIX guru en als één van de weinigen die begrijpen wat "faciliteit" eigenlijk betekent.

De afgelopen jaren heb ik met groot plezier gewerkt bij de afdeling Medische Fysica van het AMC. Het bestaan van deze afdeling is in de eerste plaats te danken aan oprichter prof. Van der Tweel. Voor de prettige 'huisstijl' van de afdeling dank ik alle medewerkers, in het bijzonder de professoren Estevez, Grimbergen, Spaan, Spekreijse, en Strackee. Het functioneren van de afdeling is, in de tijd dat ik hier werkte, echter vooral te danken geweest aan Marijke Lensing-Kooiman en Jetty Stam; hartelijk dank voor jullie steun!

Henk Venema, Robert Numan, Remmet Jonges, Jeroen Snel en Marcel van Straaten dank ik voor vele nuttige discussies en praktische adviezen over programmeren en voor hun bijdragen aan mijn werk.

Ook de andere collega's en 'gang-genoten' van Medische Fysica: Aart, Ab, Alina, Annemiek, Bernard, Boaz, Dirk, Ed, Erik, Ester, Geert, Hans, Isabelle, Jan-Arie, Jenny, Josette, Jurgen, Leo, Marc, Maria, Matthijs, Michiel, Mirella, Nico, Niels, Oana, Paul, Pier, Piet, Pim, Radha en Wouter; het was een genoegen om temidden van jullie te werken.

Het was me een eer en een genoegen om regelmatig te gast te zijn bij de afdeling Experimentele Cardiologie; dank daarvoor aan alle medewerkers.

De grafici Cees Hersbach en John Nunumete dank ik voor vele malen levensreddend werk in de laatste dagen voor een congres.

Dit onderzoek is grotendeels gefinancierd door Stichting Technische Wetenschappen, STW. Dank aan onze program officer, mw Kemper, voor het op de rails houden van de formele kant van dit project.

Heel veel dank aan mijn paranimfen, Ruud en Maarten, voor alles wat hen nog te wachten staat na het verschijnen van dit proefschrift.

Bij het vormgeven van dit proefschrift heb ik veel geleerd van de adviezen van Richard Kuin, Peter Lowie, en Chris Bor; veel dank daarvoor.

Traditioneel als laatste maar niet als minste, dank ik Nanda voor het nodige tegenwicht, en mijn ouders voor hun geduld en hun steun.

Index

In this index, an italic page number in the entry for an acronym refers to a page where the acronym is defined.

W